



---

Graduate Theses, Dissertations, and Problem Reports

---

2022

## Combustion Feature Characterization using Computer Vision Diagnostics within Rotating Detonation Combustors

Kristyn B. Johnson May  
*West Virginia University*, kkjohnson@mix.wvu.edu

Follow this and additional works at: <https://researchrepository.wvu.edu/etd>

 Part of the [Energy Systems Commons](#), and the Heat Transfer, Combustion Commons

---

### Recommended Citation

Johnson May, Kristyn B., "Combustion Feature Characterization using Computer Vision Diagnostics within Rotating Detonation Combustors" (2022). *Graduate Theses, Dissertations, and Problem Reports*. 11216.  
<https://researchrepository.wvu.edu/etd/11216>

This Dissertation is protected by copyright and/or related rights. It has been brought to you by the The Research Repository @ WVU with permission from the rights-holder(s). You are free to use this Dissertation in any way that is permitted by the copyright and related rights legislation that applies to your use. For other uses you must obtain permission from the rights-holder(s) directly, unless additional rights are indicated by a Creative Commons license in the record and/ or on the work itself. This Dissertation has been accepted for inclusion in WVU Graduate Theses, Dissertations, and Problem Reports collection by an authorized administrator of The Research Repository @ WVU. For more information, please contact [researchrepository@mail.wvu.edu](mailto:researchrepository@mail.wvu.edu).

# **Combustion Feature Characterization using Computer Vision Diagnostics within Rotating Detonation Combustors**

**Kristyn B. Johnson May**

**Dissertation submitted  
to the Benjamin Statler College of Engineering  
at West Virginia University**

**in partial fulfillment of the requirements for the degree of**

**Doctor of Philosophy in  
Mechanical Engineering**

**Andrew C. Nix, Chair, Ph.D., Chair  
Donald Adjeroh, Ph.D.  
V'yacheslav Akkerman, Ph.D.  
Cosmin Dumitrescu, Ph.D.  
Donald Ferguson, Ph.D.**

**Department of Mechanical and Aerospace Engineering**

**Morgantown, West Virginia**

**2022**

**Keywords: Rotating Detonation Engine, Pressure Gain Combustion, Machine Learning, Real-time  
Diagnostics**

**Copyright 2022 Kristyn B. Johnson May**

# Abstract

## Combustion Feature Characterization using Computer Vision Diagnostics within Rotating Detonation Combustors

Kristyn B. Johnson May

In recent years, the possibilities of higher thermodynamic efficiency and power output have led to increasing interest in the field of pressure gain combustion (PGC). Currently, a majority of PGC research is concerned with rotating detonation engines (RDEs), devices which may theoretically achieve pressure gain across the combustor. Within the RDE, detonation waves propagate continuously around a cylindrical annulus, consuming fresh fuel mixtures supplied from the base of the RDE annulus. Through constant-volume heat addition, pressure gain combustion devices theoretically achieve lower entropy generation compared to Brayton cycle combustors. RDEs are being studied for future implementation in gas turbines, where they would offer efficiency gains in both propulsion and power generation turbines. Much diagnostic work has been done to investigate the detonative behaviors within RDEs, including point measurements, optical diagnostics, thrust stands and other methods. However, to date, these analysis methods have been limited in either diagnostic sophistication or to post-processing due to the computationally expensive treatment of large data volumes. This is a result of the substantial data acquisition rates needed to study behavior on the incredibly short time scale of detonation interactions and propagation.

As laboratory RDE operations become more reliable, industrial applications become more plausible. Real-time monitoring of combustion behavior within the RDE is a crucial step towards actively controlled RDE operation in the laboratory environment and eventual turbine integration. For these reasons, this study seeks to advance the efficiency of RDE diagnostic techniques from conventional post-processing efforts to lab-deployed real-time methods, achieving highly efficient detonation characterization through the application of convolutional neural networks (CNNs) to experimental RDE data.

This goal is accomplished through the training of various CNNs, being image classification, object detection, and time series classification. Specifically, image classification aims to classify the number and direction of waves using a single image; object detection detects and classifies each detonation wave according to location and direction within individual images; and time series classification determines wave number and direction using a short window of sensor data. Each of these network outputs are used to develop unique RDE diagnostics, which are evaluated alongside conventional techniques with respect to real-time capabilities. Those real-time capable diagnostics are deployed and evaluated in the laboratory environment using an altered experimental setup via a live data acquisition environment.

Completion of the research tasks results in overarching diagnostic capability developments of conventional methods, image classification, object detection, and timeseries classification applied to experimental RDE data. Each diagnostic is employed with varying strengths

with respect to feasibility, long-term application, and performance, all of which are surveyed and compared extensively. Conventional methods, specifically detonation surface matrices, and object detection are found to offer diagnostic feedback rates of 0.017 and 9.50 Hz limited to post-processing, respectively. Image classification using high-speed chemiluminescence images, and timeseries classification using high-speed flame ionization and pressure measurements, achieve classification speeds enabling real-time diagnostic capabilities, averaging diagnostic feedback rates of 4 and 5 Hz when deployed in the laboratory environment, respectively. Among the CNN-based methods, object detection, while limited to post-processing usage, achieves the most refined diagnostic time-step resolution of 20  $\mu$ sec compared to real-time-capable image and timeseries classification, which require the additional correlation of a sensor data window, extending their time-step resolutions to 80 msec.

Through the application of machine learning to RDE data, methods and results presented offer beneficial advancement of diagnostic techniques from post-processing to real-time speeds. These methods are uniquely developed for various RDE data types commonly used in the PGC community and are successfully deployed in an altered laboratory environment. Feedback rates reported are expected to be satisfactory to the future development of an RDE active-control framework. This portfolio of diagnostics will bring valuable insight and direction throughout RDE technological maturation as a collective early application of machine learning to PGC technology.

*To my greatest supporter and friend, my dear husband, Jason William*

*And to those who raised me with more love and direction than any square-headed kid  
could ever dream, Mom and Dad*

*"If you're prepared and the opportunity comes up, it's your good fortune to have been in the  
right place at the right time and to have been prepared for the job." -Katherine Johnson*

# Acknowledgments

THE GRATITUDE AND THANKS OWED to those who have created and fostered my path and progress are well beyond what I could attempt to express in the words below, or what could be written with ink that could fill a hundred books. This document is a result of a collective fostering by family, community, and mentors, of which I have been the most fortunate recipient. Among the first category, I would like to thank my husband, Jason, for his enduring support, love, and friendship. Amidst many other things, his extroversion, humility and outrageous appetite for wit are my anchor point for seeing and experiencing the many joys of this life. The foundational members of the primary category, my parents, deserve my sincerest thanks for their unwavering love and dedication. Their guidance, devotion, and nurturing have been the most consistent themes of my life. To have two remarkable parents who have shaped my character and personality, each in their own unique way, is an incredible blessing. I am gracious to be a product of a kind, competitive, humorous, and driven environment, forged especially for me by my loving parents.

An individual's growth does not occur in a vacuum; fortunately, mine has been against the backdrop of family and community who have shown unparalleled commitment and benevolence towards myself and others. Although none could be thanked enough, extraordinary educators, from the earliest of grades to graduate education, deserve my deepest gratitude. To name just one, Mr. Thomas Bane redefined my career's path by introducing me to the beauties of engineering years before I ever thought it would be within reach. His impact is not in solidarity, as he stands amongst a dense crowd of teachers who poured into me at each and every step; an investment far beyond what was warranted.

Along the way, a collective of strong friends maintained my focus and set a common standard of excellence; a standard I hope to achieve and maintain alongside their own. As was better stated by C.S. Lewis, "*Friendship is unnecessary... It has no survival value; rather, it is one of those things which give value to survival.*"

A unique fortune is to find friendship among mentors and colleagues. In this thought, I would like to express my greatest thanks to my advisor, Dr. Andrew C. Nix, whose teaching sparked my interests for research and whose guidance led me to this current benchmark. Throughout these few years, Dr. Nix has challenged and enabled me through countless discussions, all while showing great respect for my work and research interests. In addition to

his mentorship and friendship, I have very been privileged enough to work alongside him as a colleague in our work at NETL.

Pressure gain combustion was a delightfully unexpected research opportunity, for which, according to Katherine Johnson, it was my *"good fortune to have been in the right place at the right time and to have been prepared for the job.* Specifically, it was a research opportunity granted as an appointment under Dr. Donald Ferguson, for which I extend my warmest gratitude. Under Don's tutelage, I have carved out a space for machine learning work within our rotating detonation engine work. His vision and the autonomy he has given me over these past few years have had a profound effect on me as a researcher.

In addition to Don and Dr. Nix, I would like to thank my research colleagues at NETL: Todd Sidwell, Justin Weber, Pete Strakey, Clint Bedick and Andrew Tulgestke. All of efforts would be in vain if not for the support from our colleagues Jeff and Rich. I would also like to thank the members of my committee for their support in this process.

Finally, I would like to acknowledge all the female scientists and engineers who came before me; each one contributing to the gradual but continuous paving and broadening of the road forward. My hope is that I may contribute to this cause in my career, involving and, at best, inspiring the future female scientists who should come after me. Each one is needed to best address the issues that we have yet to encounter.

*To God be the glory,*

*Kristyn B. Johnson May*

# Contents

ABSTRACT	I
LIST OF FIGURES	xi
LIST OF TABLES	xii
NOMENCLATURE	xiii
1 INTRODUCTION	I
1.1 Scientific Background . . . . .	3
1.2 Objective . . . . .	32
1.3 Scope of Work . . . . .	35
1.4 Outline of the Manuscript . . . . .	37
2 DATA ACQUISITION AND TREATMENT	40
2.1 NETL Uncooled Experimental RDE . . . . .	42
2.2 NETL Water-Cooled RDE . . . . .	46
2.3 Image Acquisition and Real-Time Adaptation . . . . .	51
2.4 Image Treatment . . . . .	61
3 SURVEY OF CONVENTIONAL METHODS	69
3.1 Detonation Surfaces . . . . .	70
3.2 Average Wave Behavior . . . . .	74
3.3 Modal Changes . . . . .	75
3.4 Auto-Correlation Method . . . . .	76
3.5 Outcomes . . . . .	79
4 RDE IMAGE CLASSIFICATION	81
4.1 CNN Methodology . . . . .	84
4.2 Performance Comparison of Five Image Classification CNNs . . . . .	87
4.3 Preferred CNN Architecture Selection (SqueezeNet) . . . . .	89
4.4 Performance of Preferred CNN: SqueezeNet . . . . .	90

4.5	Extension of Evaluated Modes: Counter-rotating and Deflagration . . . . .	93
4.6	Practical Application of SqueezeNet Network . . . . .	97
4.7	Outcomes of RDE Image Classification . . . . .	99
<b>5</b>	<b>REAL-TIME CHARACTERIZATION: SQUEEZE NET ADAPTATION</b>	<b>100</b>
5.1	Time Series Data Integration . . . . .	103
5.2	Toward Real-Time Processing & Lab Integration . . . . .	105
5.3	Lab Acquisition Results . . . . .	107
5.4	Overview of outcomes . . . . .	115
<b>6</b>	<b>OBJECT DETECTION</b>	<b>117</b>
6.1	Network Development . . . . .	119
6.2	Baseline Network Performance . . . . .	126
6.3	Annotation Size Refinement . . . . .	128
6.4	Consideration of Linearized Network . . . . .	133
6.5	Wave Speed Calculations . . . . .	135
6.6	Uncertainty Analysis . . . . .	139
6.7	Summary of RDE YOLO Outcomes . . . . .	141
<b>7</b>	<b>TIME SERIES CLASSIFICATION OF ION PROBE AND PRESSURE DATA</b>	<b>144</b>
7.1	Dataset Creation and Normalization . . . . .	147
7.2	RDE TSC Network Development . . . . .	150
7.3	TSC Network Selection and Usage . . . . .	151
7.4	Parametric Consideration of TSC Network Performance . . . . .	154
7.5	Outcome of TSC Effort . . . . .	164
<b>8</b>	<b>DIAGNOSTIC EVALUATION AND COMPARISON</b>	<b>167</b>
8.1	Evaluation of External Images . . . . .	168
8.2	Overall Model Comparison and Requirements . . . . .	178
8.3	Limitations of Usage . . . . .	184
8.4	Survey of AI Methods and Future Work . . . . .	186
<b>9</b>	<b>CONCLUSION</b>	<b>192</b>
<b>APPENDIX A ENLARGED AND EXPANDED FIGURES</b>		<b>197</b>
<b>APPENDIX B MODEL SUMMARIES</b>		<b>204</b>
<b>REFERENCES</b>		<b>223</b>

# Listing of figures

1.1	PGC Device Process Comparison (PDE & RDE) . . . . .	9
1.2	RDE Characteristics . . . . .	11
1.3	Brayton and Humphrey Cycles . . . . .	12
1.4	RDE Unwrapped Anatomy . . . . .	13
1.5	Simple Convolutional Kernel Operation . . . . .	17
1.6	Convolutional Kernel with Stride 2 . . . . .	18
1.7	Convolutional Kernel with Stride 1 . . . . .	19
1.8	Max Pooling and Average Pooling Illustration . . . . .	19
1.9	SqueezeNet Architecture . . . . .	22
1.10	SqueezeNet Feature Maps - Class 3 . . . . .	24
1.11	SqueezeNet Feature Maps - Class 6 . . . . .	26
1.12	YOLO Architecture . . . . .	28
1.13	YOLO Unified Detection . . . . .	29
1.14	TSC Data Framework . . . . .	31
1.15	Data Flow Visualization throughout Publications . . . . .	36
2.1	NETL Uncooled RDE Cross-section Geometry . . . . .	43
2.2	NETL Uncooled RDE Test Facility . . . . .	43
2.3	Instrumentation Nomenclature, Uncooled RDE . . . . .	44
2.4	ITP Power Spectrum . . . . .	45
2.5	ITP Spectrogram Examples . . . . .	45
2.6	Water-Cooled NETL RDE . . . . .	47
2.7	Water-Cooled NETL RDE Cross Section . . . . .	48
2.8	Water cooled detonation channel profile . . . . .	49
2.9	Radial and axial air injectors . . . . .	51
2.10	Imaging Component Transmission Curves . . . . .	53
2.11	High-Speed Camera Setup . . . . .	54
2.12	Down-axis Imaging of Various Wave Modes . . . . .	55
2.13	Optical Obstruction Proportions within Annulus . . . . .	56
2.14	Wave Profile Pixel Intensities . . . . .	58
2.15	Water cooled LECTR profile - Real Time Acquisition . . . . .	60

2.16	Live data acquisition hardware . . . . .	61
2.17	Standard Image Treatment . . . . .	64
2.18	YOLO Image Treatment . . . . .	66
2.19	Linearized channel image . . . . .	68
3.1	Multi-wave Detonation Surfaces . . . . .	72
3.2	Detonation Surface with Hough Transform . . . . .	73
3.3	Average Wave Frequencies . . . . .	75
3.4	Modal Transition Detonation Surface . . . . .	76
3.5	Average Modal Behaviors . . . . .	77
3.6	Autocorrelation Data and Time Lag . . . . .	78
4.1	Down-axis images - six classifications . . . . .	85
4.2	Image Classification Flow Chart . . . . .	86
4.3	CNN Image Classificaiton Accuracies . . . . .	88
4.4	SqueezeNet Training & Validation Accuracies . . . . .	91
4.5	SqueezeNet Confusion Matrix . . . . .	92
4.6	SqueezeNet Confusion Matrix, Normalized . . . . .	93
4.7	Downstream RDE Images, Complex Modes . . . . .	94
4.8	Extended Dataset Confusion Matrix, Normalized . . . . .	96
5.1	Real-time Diagnostic Flow Chart . . . . .	104
5.2	Real-time Diagnostic Data Arrangement . . . . .	106
5.3	Butterworth Filter Frequency Response . . . . .	107
5.4	Real-time Diagnostic, 2CW ( $T_{air}=320^{\circ}\text{F}$ , $\Phi=0.75$ , $P_{back}=0 \text{ psig}$ ) . . . . .	109
5.5	Real-time Diagnostic, 3CW ( $T_{air}=400^{\circ}\text{F}$ , $\Phi=0.75$ , $P_{back}=0 \text{ psig}$ ) . . . . .	110
5.6	Real-time Diagnostic, 2CCW ( $T_{air}=320^{\circ}\text{F}$ , $\Phi=0.75$ , $P_{back}=0 \text{ psig}$ ) . . . . .	111
5.7	Real-time Diagnostic, 3CW, Down-axis Ion Probe . . . . .	113
5.8	Real-time Diagnostic, 2CW Optical Interference . . . . .	114
5.9	Real-time Diagnostic, 3CW Optical Depreciation . . . . .	114
6.1	YOLO CNN Development Flowchart . . . . .	119
6.2	Example YOLO Annotation Outputs . . . . .	121
6.3	Intersection Over Union Visualization . . . . .	123
6.4	YOLO Velocity Calculation Geometry . . . . .	125
6.5	YOLO Loss Across 100 Epochs . . . . .	127
6.6	YOLO Velocity Calculation Geometry . . . . .	129
6.7	YOLO Annotation Style Variation . . . . .	130
6.8	YOLO Annotation Taubin Fit . . . . .	132
6.9	YOLO Annotation Area Feature Coverage . . . . .	133
6.10	Linearized Channel Image with Annotation Binning . . . . .	135

6.11	Velocity via S <sub>3</sub> Annotations . . . . .	137
6.12	Velocity via R <sub>2</sub> Annotations . . . . .	137
6.13	Velocity via Lin Annotations . . . . .	138
6.14	Linearized Images with YOLO Annotations . . . . .	139
7.1	TSC Data Framework . . . . .	147
7.2	Example Optical & Point Measurement Data . . . . .	148
7.3	Time series Classification Flowchart . . . . .	150
7.4	Residual Block Schematic . . . . .	153
7.5	Univariate Encoder Training Accuracy . . . . .	156
7.6	Univariate FCN Training Accuracy . . . . .	157
7.7	Univariate ResNet Training Accuracy . . . . .	157
7.8	Multivariate Network Training Accuracies . . . . .	158
7.9	Global Performance Variation with Sample Length . . . . .	159
7.10	Global Performance, Classification Speeds . . . . .	163
8.1	External Images - Distortion Correction . . . . .	170
8.2	External Images - TU Berlin RDE . . . . .	171
8.3	External Images - Detonation Surface . . . . .	172
8.4	External Images - SqueezeNet Classifications . . . . .	173
8.5	External Images - YOLO S <sub>3</sub> Annotations . . . . .	174
8.6	External Images - YOLO S <sub>3</sub> Velocity Results . . . . .	176
8.7	External Images - YOLO Lin Annotations . . . . .	177
A.1	Water-Cooled NETL RDE Cross Section, Large . . . . .	198
A.2	Water cooled LECTR profile - Real Time Acquisition, Large . . . . .	199
A.3	YOLO S <sub>3</sub> Output (1) . . . . .	200
A.4	YOLO S <sub>3</sub> Output (2) . . . . .	201
A.5	YOLO Linear Output (1) . . . . .	202
A.6	YOLO Linear Output (2) . . . . .	203
B.1	SqueezeNet Model Summary . . . . .	205
B.2	SqueezeNet Model Summary Cont. . . . .	206
B.3	Encoder Summary - Univariate 200 Sample Length . . . . .	207
B.4	Encoder Summary - Multivariate 500 Sample Length . . . . .	208
B.5	FCN Summary - Univariate 500 Sample Length . . . . .	209
B.6	FCN Summary - Multivariate 200 Sample Length . . . . .	209
B.7	ResNet Summary - Multivariate 200 Sample Length . . . . .	210

# **Listing of tables**

2.1	RDE Operating Conditions . . . . .	50
2.2	RDE Geometric variations . . . . .	51
4.1	Image Classification CNN Architecture Training Results . . . . .	89
6.1	Annotation style statistics . . . . .	132
7.1	TSC Network Performance . . . . .	155
7.2	TSC Network Performance Rank . . . . .	161
8.1	Diagnostic Comparison - Application . . . . .	179
8.2	Diagnostic Comparison - Performance . . . . .	183
8.3	RDE Operating Conditions, Restated . . . . .	186

# Nomenclature

## Roman Symbols

$A_{3,1}$	air injector area
$A_{3,2}$	combustor channel area
$A_8$	nozzle exit area
$\text{CH}^*$	excited state Methylene
$\text{C}_2^*$	excited state diatomic carbon
$d_i$	linear distance between centroids in frames $i$ and $i+1$ (pixels)
$d_{\text{nom}}$	nominal Annulus Diameter
$D_{\text{RDE}}$	nominal annulus diameter
fps	frames per second
FR	frame rate (fps)
FWHM	full width-half max (nm)
$f_{\text{CJ}}$	Chapman-Jouguet frequency
$f_{\text{det}}$	detonation wave rotational frequency
$f_{\text{ion}}$	ion probe frequency
GT	area of ground truth annotation (pixels)
$i$	iteration count or frame at current time step
$i+1$	frame at future time step
IoU	Intersection over Union
$L(\theta, \hat{r}_i, n)$	linearized image stack of $n$ images
$m$	average wave number
$m_{\text{CNN}}$	CNN wave number classification
$n$	number of data points (frames)
$N_K$	total number of images within image stack $k$
$\text{OH}^*$	excited state Hydroxyl

P	area of the predicted annotation (pixels)
$P_{\text{back}}$	backpressure
$p_k(x,y,n)$	down-axis image stack k of n images
$\bar{p}_k$	average image of image stack k
$p_{k_{\text{corr}}}(x,y,n)$	corrected down-axis image stack of n images
r	radius (m)
R <sub>1</sub>	rectangular annotation style 1
R <sub>2</sub>	rectangular annotation style 2
RoI	region of interest
$\hat{r}_i$	incremental radius value for image linearization
r <sub>RDE</sub>	RDE annulus radius (m)
r <sub>Taub</sub>	Taubin radius (pixels)
s	arc length (rad)
S <sub>1</sub>	square annotation style 1
S <sub>2</sub>	square annotation style 2
S <sub>3</sub>	square annotation style 3
SR	sampling rate
T <sub>air</sub>	preheat air temperature
t <sub>i</sub>	time at increment i
U <sub>CJ</sub>	Chapman-Jouguet velocity
U <sub>W</sub>	individual detonation wave speed (m/sec)
V	wave velocity (m/sec)
V <sub>Bias</sub>	wave velocity bias uncertainty (%)
V <sub>Precision</sub>	wave velocity precision uncertainty (%)
V <sub>Uncertainty</sub>	wave velocity total uncertainty (%)
x <sub>i</sub>	x dimension of centroid in frame i (pixels)
x <sub>i,Z</sub>	Z-normalized data point i
x <sub>i+1</sub>	x dimension of centroid in frame i+1 (pixels)
x <sub>Taub</sub>	x dimension of centroid in frame i+1 (pixels)
y <sub>i</sub>	y dimension of centroid in frame i (pixels)
y <sub>i+1</sub>	y dimension of centroid in frame i+1 (pixels)
y <sub>Taub</sub>	y dimension of centroid in frame i+1 (pixels)

## Greek Symbols

$\beta_n$	image correction factor for n images
$\Delta$	annulus gap width (pixels)
$\Delta t_{Ci}$	calculation time duration
$\Delta T_{Si}$	sample window time length
$\theta$	azimuthal coordinate
$\theta_i$	angle of rotation between frames (rad)
$\Theta$	detonation wave matrix
$\mu_{\text{global}}$	global mean
$\sigma_{\text{global}}$	global standard deviation
$\tau$	cross-correlation time shift
$\varphi$	pixel intensity
$\Phi$	equivalence ratio
$\psi$	noise reduction matrix

## Abbreviations

AB	Allen Bradley
AFRL	Air Force Research Laboratory
CAML	Center for Artificial Intelligence and Machine Learning
CCW	Counterclockwise
CJ	Chapman-Jouget detonation wave speed
CNN	convolutional neural network
CR	counterrotating
CTAP	Continuous tube attenuated pressure
CW	clockwise
DNN	deep neural network
DOE	Department of Energy
FCN	fully convolutional network
FFT	Fast Fourier Transform

GAP	global average pooling
HT	Hough transform
ITP	Infinite tube pressure
LECTR	Low Emission Combustor Test and Research facility
NETL	National Energy Technology Laboratory
NLP	natural language processing
NN	nearest neighbor
ORISE	Oak Ridge Institute for Science and Education
PGC	pressure gain combustion
PReLU	parametric rectified linear unit
PSD	power spectral density
R-CNN	region-based convolutional neural network
RDE	Rotating Detonation Engine
ReLU	rectified linear unit
RMSE	root-mean-square error
SGD	stochastic gradient descent
SVM	support vector machine
TRL	technology readiness level
TSC	time series classification
UV	ultraviolet
YOLO	You Only Look Once network

*Understand well as I may, my comprehension can only be  
an infinitesimal fraction of all I want to understand.*

Ada Lovelace, English mathematician and pioneer of  
modern computer science

# 1

## Introduction

PRESSURE GAIN COMBUSTION OFFERS AN ALTERNATIVE STRATEGY for advancing the thermodynamic efficiency of gas turbine engines. Historically, the approach to increased gas turbine efficiency has relied on increasing turbine inlet temperatures. However, even with advanced cooling strategies, material limitations restrict maximum sustained temperatures. Conventional gas turbines are also limited by the occurrence of a pressure loss across the combustor due to the usage of subsonic combustion. Pressure gain combustion (PGC)

technologies, through development of devices such as rotating detonation engines (RDEs), have the potential to increase the pressure across the combustor through detonation without the need for extracting additional work from the compressor. RDEs provide advantages to the turbine of not only elevated pressure, but also the same high temperatures permitted by advanced materials consistent with conventional gas turbine engines. Within RDEs, detonation waves travel at supersonic speeds around a cylindrical annulus, consuming a detonable fuel-oxidizer mixture, and creating a complex flow field<sup>1</sup>. To capture and evaluate the unsteady detonation behavior within the RDE, high-speed image and conventional point-measurements are recorded. These data types are analyzed using diagnostics that historically require post-test processing to provide useful information. However, as RDEs move closer to an applied technology, there is a greater need for diagnostics that function at time scales more suitable operational engines as opposed to those common to advanced research. Utilization of methods common in machine learning and computer vision can assist with the transitioning of RDE diagnostics into an operational / production time scale. As volumes of recorded RDE down-axis images and high-frequency time series data continue to grow, benefits of incorporating machine learning capabilities into RDE diagnostics become more apparent. Using computer vision techniques such as image classification and object detection, as well as a deep learning approach to time series classification, this study aims to train neural networks capable of discerning detonation wave behavior within an experimental RDE at speeds reaching real-time or near-real-time.

Each network is to be fully developed into a diagnostic framework and evaluated as a potential real-time RDE diagnostic. The network-based diagnostics will each independently provide information regarding detonation wave number, direction, velocity, and frequency, parameters vital to characterizing RDE operability, stability, and performance. Networks

will be evaluated and compared according to different benefits, complexities, and potential longevity throughout future stages of RDE technology maturation. As a whole, this work poses a first attempt to create and implement real-time RDE diagnostics, which are believed to be a vital component to the continued development of RDE technology towards active control and eventual turbine integration.

This document serves as a dissertation in fulfillment of the requirements of the degree of Doctor of Philosophy in Mechanical Engineering submitted to West Virginia University Benjamin M. Statler College of Engineering and Mineral Resources, Department of Mechanical and Aerospace Engineering. This research is supported by an appointment under Dr. Donald Ferguson at the National Energy Technology Laboratory Professional Internship Program, sponsored by the U.S. Department of Energy (DOE), and administered by the Oak Ridge Institute for Science and Education (ORISE).

### 1.1 SCIENTIFIC BACKGROUND

Modernization throughout the millennia across humanities, transportation, military technologies, and practically every other aspect of present-day life, may in large part be attributed to widespread energy production by consumption of combustibles. As an irreplaceable, historically significant contributor to energy production, gas turbines have revolutionized both aviation and land-based power generation schemes. Gas turbines to date make use of standard, highly reliable deflagration, or subsonic combustion. Combustion devices within gas turbines have evolved over the span of decades to positively influence thermal efficiencies, leading to substantial fuel savings and environmental impact. However, as increases in thermal efficiency become increasingly evasive and expensive, incremental technological adaptations applied to existing turbine components will not likely achieve step-change efficiency

improvements. Instead, it is believed that such progress may be realized by a radically different sub-component which exploits the more powerful combustion form: continuous detonation.

### 1.1.1 DETONATION

Detonation is a radically different form of combustion, distinguishable by extraordinary propagation and energy conversion speeds. An established detonation front consists of a strong shock wave which by compression drastically heats the gases beyond the spontaneous thermal ignition temperature. The elevated gas temperature results in a chemical reaction, forming a combustion zone that closely follows the shock front. The heat of the shock-induced combustion process then supports the continued propagation of the shock front<sup>2</sup>.

Detonation consumes material many orders of magnitude ( $10^3$ ) times faster than an ordinary plane flame front<sup>3</sup>. For example, hydrogen-air mixtures are associated with flame burning velocities of 320 cm/sec which is orders of magnitude slower than detonation front velocities in the same mixture which typically range from 1500 to 3500 m/sec. This discrepancy is a result of differing driving factors among the two combustion forms. While an ordinary flame's velocity is mainly dependent on chemical process, detonation velocity is almost entirely dependent on the local speed of sound within the burnt gas region, as well as heat available from the chemical reaction <sup>2</sup>.

Across the detonation wave front, temperature, pressure and density experience sharp increases imposed by the shock front. The reaction region behind the shock front further increases temperature, resulting in immediately decreasing pressure and density values. Therefore, maximum temperature is experienced at the end of the reaction zone, which is deemed the *equilibrium or final state*.

Concerned with the properties at the equilibrium state, and relying on the conservation of mass, momentum, and energy alongside the equation of state, the Rankine-Hugoniot relation describes the possible solutions of pressure and density in the equilibrium state region given initial reactant properties and heat release. For a given initial state, wave velocity may be calculated for each possible solution described by the Rankine-Hugoniot relation. In 1899, Chapman<sup>4</sup> postulated that the solution of the equilibrium state corresponded to the minimum velocity consistent with the Rankin-Hugoniot relation. His historic one-dimensional hypothesis satisfies a singular solution of conservation laws and was later substantiated by Jouget<sup>5</sup>. Early success in experimental velocity predictions solidified the theory and the minimum velocity point is thus coined the Chapman-Jouguet (CJ) detonation velocity<sup>2,3</sup>. In addition to the CJ detonation velocity, there exists a similarly derived CJ deflagration velocity. CJ deflagration speed is roughly half of the corresponding CJ detonation speed, where ignition is not sustained behind the leading shock due to lower static temperatures<sup>6</sup>. Throughout the remainder of the work, unless specified otherwise, CJ velocity refers specifically to the more relevant CJ detonation speed.

Although it represents a small portion of RDE operation, specifically at startup, the deflagration to detonation transition (DDT) process should be noted. The most fundamental and intuitive means of demonstrating DDT phenomena may be within the closed-end shock tube filled with an explosive mixture. If near the closed end of the long tube, a localized reaction by a spark source is introduced, the flame will undergo DDT through the following generalized steps: a small spherical flame expands the surrounding gases due to heating; as the flame front approaches the confining sidewalls, expansion becomes restricted to the axial direction, increasing velocity; expansion along the non-slip walls results in a non-uniform flow, which promotes a curved flame shape (finger flame), increasing burning surface area and thereby

rapidly increasing velocity; the accelerating flame front forces a shock ahead of the reaction zone; gas compression slows the flame front to a quasi-steady flame speed (Chapman-Jouguet deflagration speed); the strengthened shock heats reactants ahead of flame front, leading to an explosion; the shock and coupled reaction zone form a self-supporting detonation wave<sup>2,7</sup>.

The development of the finger flame contributes to the very early moments of burning and therefore has little effect on DDT of slow, hydrocarbon flames. However, for fast flames more closely related to the current study such as hydrogen-oxygen mixtures, finger-flame acceleration in a closed-end tube may accelerate flame propagation up to sonic values<sup>7</sup>. DDT may also be promoted by intentional or natural introduction of obstacles, turbulence<sup>8</sup>, wall friction<sup>9</sup>, and increased local equivalence ratio among other factors. Although detonation is currently being explored for energy benefits due to its rapid energy conversion provocation, detonation also poses extreme dangers in confined spaces such as tunnels, subways and mines. To mitigate DDT in those potentially hazardous structures, a combination of vented ends, smooth walls, decreased equivalence ratios and acoustics should be considered.

As mentioned previously, the Chapman-Jouguet theory relating deflagration and detonation speeds with initial state properties was a historic step in combustion research. Early velocity measurements which coincided with CJ predictions enforced the one-dimensional simplification in the absence of density and pressure measurement techniques, which would have shown consequential discrepancies. Acknowledgement of three-dimensional phenomenon in detonative flows observed in experimental gaseous systems quickly stunted the broad application of the CJ theory. Half way through the 20<sup>th</sup> century, a comprehensive comparison of the CJ theory with three-dimensional measurements was performed by a myriad of researchers. Divergence in theoretical and experimental values was clarified by the time-dependent, corrugated wave front that was otherwise considered a one-dimensional discon-

tinuity plane. As is the case in many experimental settings, the state values reported were representative of an average intrinsically associated with the experimental facility/apparatus<sup>3</sup>.

Still yet, the simple CJ theory offers valuable calculations for simple combustion fields, and combustion classification insights relative to the combustion interests of today. Specifically, the theory outlines three detonation distinctions, being strong detonation, CJ detonation, and weak detonation<sup>2</sup>. Consideration of RDE technology, which is thoroughly detailed in the following subsections, with respect to these detonation types is valuable to the understanding of detonative performance and loss mechanisms. For this reason, CJ velocity is commonly used as a benchmark for individual wave velocity throughout the RDE research community. While some detonation devices experience wave speeds at or above ideal CJ values, RDEs built and operated with varying geometric ratios, fuel types, and facility integration schemes all experience velocity and peak pressure deficiencies compared to their respective ideal CJ state<sup>10,11,12</sup>. As described by Anand<sup>13</sup>, this suggests that RDEs are not likely experiencing weak detonations, but instead are a "type of near-limit detonation phenomena." Anand supports this claim by comparison to spinning detonations, a substantially similar near-limit phenomena.

Velocity deficits vary across RDE studies, and increase with the number of waves present in the RDE annulus, suggesting some dependence on injector back-flow, and fill height among other persistent loss mechanisms. Strakey<sup>14</sup> computationally quantified a portfolio of losses within RDEs, finding that enhanced deflagration in the fill region, mixing effectiveness, and reactant dilution caused by injector back-flow were major contributors to decreased detonation wave pressure and speed. In the same study among others, heat transfer to the combustor wall and wall friction are reported as secondary loss mechanisms. Paxson<sup>15</sup> reported an unstable loss mechanism of reaction zone enlargement due to turbulence, ordained uniquely

by the physical constraints of RDE annular geometry. The presence of reaction zone enlargement and subsequent reduction in chemical reaction rate<sup>15</sup> implies that RDEs, being vulnerable to both<sup>13</sup> boundary interaction losses and flowfield chemistry losses reported by Strakey<sup>14</sup>, will likely never reach ideal CJ detonation velocities. Despite velocity and pressure deficits compared to the CJ state, RDEs remain a viable topic of interest as a potential means of pressure gain combustion, afterburner envelope reduction, and adoption of cleaner non-hydrocarbon fuels.

### 1.1.2 PRESSURE GAIN COMBUSTION

Propagating detonation waves offer unique benefits for gas turbine and rocket engines compared to conventional subsonic combustors. Through the use of detonation, pressure gain combustion devices applied to gas turbines introduce a theoretical thermodynamic benefit due to increased thermal availability for the downstream turbine<sup>16</sup>. While pressure gain combustion has become host to renewed research interests in the last two decades<sup>17,18,19</sup>, use of detonation in a propulsion device was first proposed in 1940 by Hoffman<sup>20</sup>. By 1960 Voitsekhovskii<sup>21</sup> successfully sustained spin detonation in an annular channel. Following the early demonstration, Nichols et al.<sup>22</sup> conducted experiments to stabilize gaseous detonation waves and consider the feasibility of such devices in ram-jet and rocket motors.

Upon reviewing pressure gain combustion devices, two primary topics consume a majority of research efforts: pulsed detonation engines<sup>23,24</sup> and rotating detonation engines<sup>25,14</sup>. Both designs rely on the propagation of a detonation wave through a region of fresh reactants. The pulse detonation engine ignites a pre-filled reactant mixture within a long tube. The ignition results in deflagration which quickly transitions to an individual detonation wave via DDT. The detonation wave then propagates axially towards the open end of the

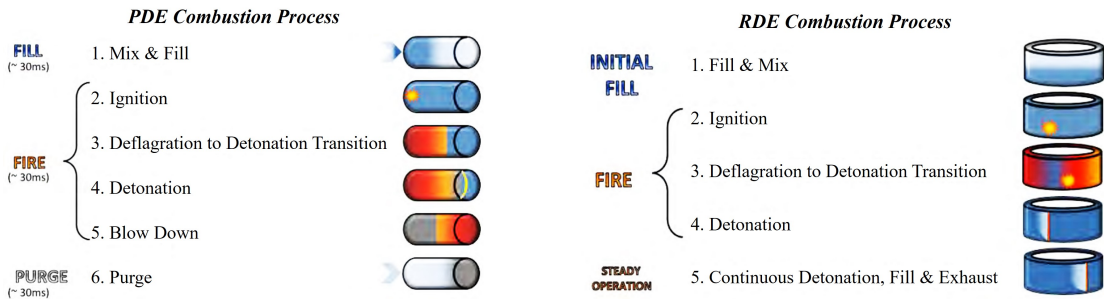


**Figure 1.1:** Pulsed Detonation Engine Combustion Process (left) and Rotating Detonation Engine Combustion Process (right)<sup>26</sup>

tube. The hot products left from detonation must be purged between each ignition event to avoid premature burning of the fresh reactants designated for the upcoming wave. This process, illustrated in Figure 1.1(left), requires a large schematic footprint, and six action steps for each detonation wave. Therefore, the cyclic frequency is limited to a range of 100-200 Hz<sup>26</sup> due to the practical limits of high-speed valves.

Like the pulsed detonation engine, the rotating detonation engine must first be filled with a reactant mixture and ignited. The ignited mixture again results in deflagration which immediately transitions to a supersonic detonation wave. Unlike the pulsed detonation engine, sequential firing steps are not required. Once a detonation wave is established, it continuously propagates circumferentially around a cylindrical annulus. Fresh reactants are simultaneously supplied at the base of the combustor. The detonation wave consumes the fresh reactants as it travels around the annulus and exhausts axially at the open end of the combustor. This process, illustrated in Figure 1.1(right), requires a less complex, smaller design footprint. The absence of a recurring firing sequence due to the uninterrupted presence of the detonation wave offers a cyclic frequency range of 1-10 kHz without the presence of check valves<sup>26</sup>. For these reasons among others, the RDE has become the most widely studied pressure gain combustion device in academic, government, and private sector research for

applications in aviation, rocket propulsion, and the overarching thrust of the current work: land-based electric power generation. As a potential means to realize a step-change in efficiency within combustion gas turbines, RDEs are the sole pressure gain combustion device studied throughout this manuscript. Details of the experimental RDE facilities at the U.S. Department of Energy's National Energy Technology Laboratory (NETL) are presented in Chapter 2.

Detonation with subsequent pressure gain offers an alternative to the ideally isobaric deflagrative combustion process that currently occurs in conventional gas turbine and rocket engines. The RDE offers a practical realization of detonation combustion with potential for improved thermodynamic performance<sup>27,28,29</sup>. A geometrically simple device, shown in Figure 1.2, the RDE consists of a narrow annular gap combustion chamber, with fuel and air injected into the restricted upstream end of the annulus and products of combustion exhausted through the throttled (nozzle/diffuser) downstream end. During operation, a detonation, consisting of a coupled shock wave and reaction front, continuously propagates circumferentially around the upstream end of the combustor, generating a significant, although spatially isolated, temperature and pressure rise, producing a rise in total pressure within the combustor that can result in greater thermodynamic availability for power production in the turbine.

The thermodynamic cycle of pressure gain combustion devices can be approximated as the Humphrey cycle, which is a constant volume heat addition process. This is due to the high-pressure region which trails the supersonic flame and subsequent shock wave<sup>26</sup>. Compared to the constant pressure of the ideal Brayton cycle, the thermal efficiency of the ideal Humphrey cycle is superior at all temperature ratios<sup>30</sup>. The T-s and P-v diagrams for both cycles are shown in Figure 1.3<sup>26</sup>. The increase between states 1 and 2 is due to the pressure

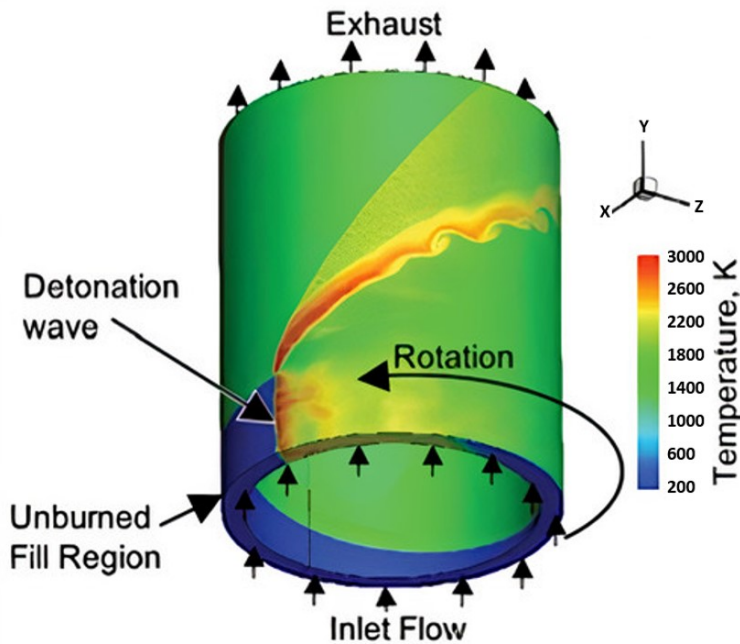


**Figure 1.2:** General rotating detonation characteristics<sup>1</sup>

gain in constant volume combustion systems, which increases the total area under the curve and therefore allows more work extraction from the process<sup>31</sup>.

While an inherently unsteady process, the rapid progression of the detonation wave(s) within the combustor combined with optimized flow control produces an exhaust flow that could be introduced to turbomachinery with minimal impact to individual component efficiencies<sup>32,33,34</sup>. Increased research over the last 5-10 years has advanced RDE technology from concept exploration to mechanism research<sup>35</sup>.

Figure 1.4 displays the unwrapped, generic anatomy of a quasi-steady rotating detonation wave. Fresh reactants are supplied by nozzles at the base (F). The detonation wave (A) travels azimuthally, consuming the fresh reactants. The supersonic wave creates an oblique shock wave (B) of freshly detonated products. The presence of older products (D) causes a slip line (C) between the two regions<sup>30</sup>. The operational characteristics of the RDE encom-

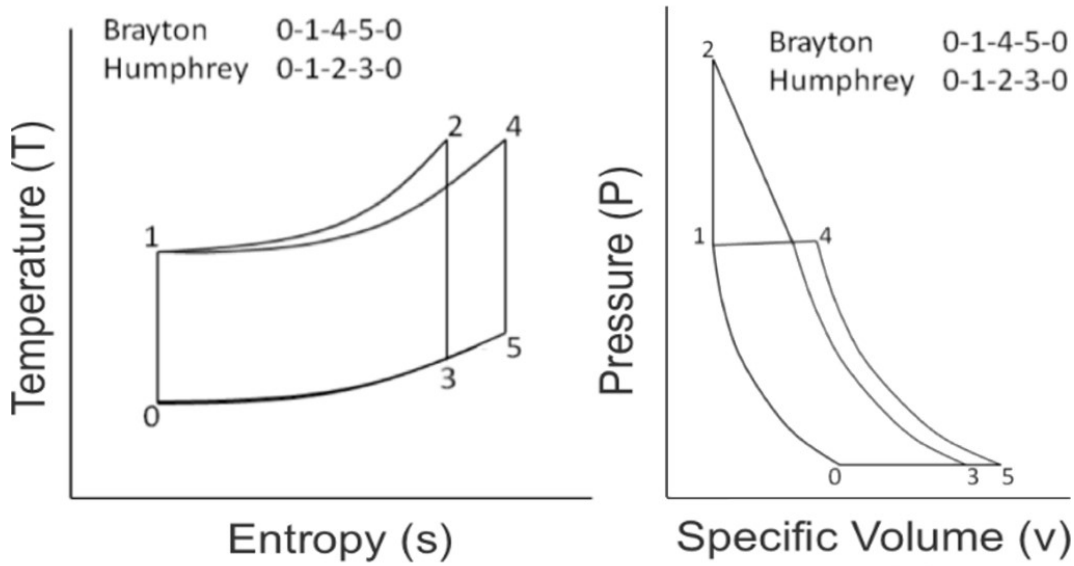


**Figure 1.3:** T-s diagram comparing ideal Brayton and Humphrey Cycles (left); P-v diagram comparing Brayton and Humphrey Cycles<sup>26</sup>

pass both stable and unstable behaviors. Even within the realm of stable operation, the RDE may experience momentary or seemingly permanent mode changes with regards to the number and direction of both co- and counter-rotational detonation waves. Unstable modes may also consist of co- or counter-rotating detonation waves, as well as longitudinal pulse detonation and deflagration. While attempts have been made to control the operational mode and characteristics of the RDE<sup>36</sup>, the ability to exercise active control leading to a desired change in behavior has not been fully demonstrated<sup>30</sup>.

The number and direction of waves propagating through the RDE annulus are described as the wave mode or modal operation. Given the varied nature of performance from the RDE, the ability to quantify its modal response is paramount to understanding the underlying physics that controls combustion behavior. Various techniques have been developed to characterize the modal properties of the detonation waves that occur in an RDE. Because det-

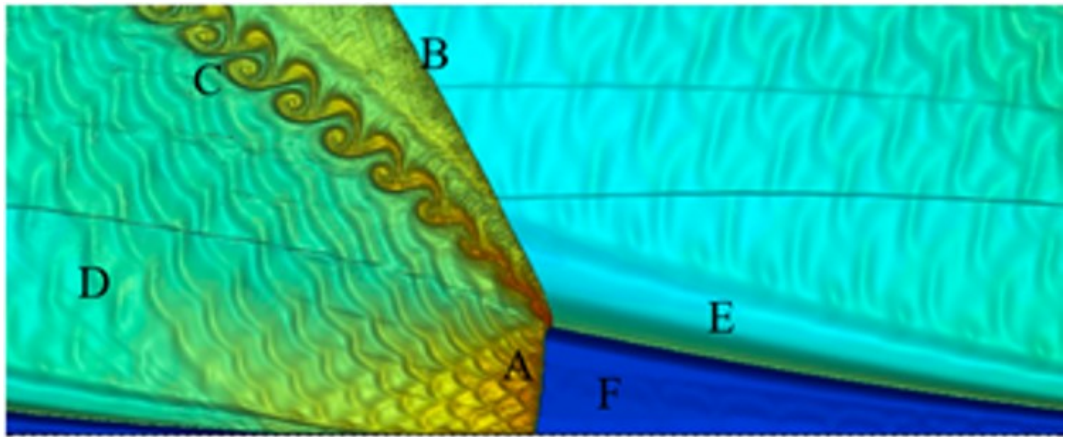


**Figure 1.4:** Generic anatomy of a quasi-steady rotating detonation wave, unwrapped<sup>30</sup>

onation wave speeds are on the order of 1 to 2 km/sec<sup>37,38</sup> high-speed measurements are necessary to resolve the behaviors associated with the detonation wave(s). Several research groups have developed techniques that utilize high-speed chemiluminescent imagery acquired from the end-view of the RDE, referred to as down-axis<sup>39,40,41</sup>. These images, when acquired appropriately, provide definitive details regarding the average and instantaneous wave speed, direction, number, and mode. However, acquisition of high-speed imagery at an adequate resolution requires expensive hardware. Less expensive alternatives rely on transducer measurements (i.e. pressure and ionization) to perform time-of-flight or frequency-based analysis to evaluate detonation wave behaviors. While this may provide a measure of wave speed, determining the number of waves relies on a comparison with an assumed theoretical Chapman-Jouguet (CJ) detonation wave speed such that measured values greater or less than a proportion of theoretical values would be presumed to define the number of waves present in the combustor. Determining wave mode (co- vs counter rotation) is less trivial, requiring techniques such as cross-correlation of multiple transducers<sup>10,42,43</sup>. The number of waves is more often compared against high-speed imaging to offer spatial, and visual modal certainty.

In order to observe the detonation wave behavior within an RDE, many optical techniques have been studied. Down-axis images, defined as those captured downstream of the exhaust section and aligned with the center axis of the annulus, are commonly used to study wave propagation through time, which is done by concatenating polar pixel intensities to generate detonation surfaces, sometimes referred to as  $\theta$ -t or X-t plots<sup>39,41,44</sup>. Other optical studies rely on transverse images, which are captured perpendicular to the annulus center axis<sup>40,45</sup>. In each of the mentioned studies, as well as the current work, images are captured with high frame rates at or above 50,000 frames per second (fps), or 20  $\mu$ s timestep resolution. High framerates, necessary to capture detonation waves traveling short distances between frames, result in an abundance of images, which typically require extensive processing times using conventional methods like detonation surfaces. The discernible variation in pixel intensity along different detonation modes as well as the abundance of available image data with known classifications are two factors supporting the application of computer vision to perform similar analyses at significantly more efficient rates<sup>46</sup>.

The complexities of the RDE require extensive fundamental and applied research. Progression of the technology has been substantial throughout recent years thanks to the efforts of a diligent research community committed to a broad scope of technological hurdles such as cooling<sup>47</sup>, inlet backflow<sup>48</sup>, down-axis turbine integration<sup>45</sup>, flight demonstrations<sup>49</sup>, and many more<sup>11,50,51</sup>. It is believed that machine learning may enable a new wave of progress in each of these sub-fields.

#### 1.1.3 MACHINE LEARNING

Computer vision, a field within artificial intelligence, aims to equip computers so that they may interpret and infer information from images similar to that which is capable by humans.

As a part of this broad effort, machine vision looks to analyze images and videos to facilitate automated machine decisions based on image content. According to a 1980's era description, "computer vision is the construction of explicit, meaningful descriptions of physical objects from images" and differs dramatically from conventional image processing<sup>52</sup>. Major improvements have been made in the field in recent years. Like many technological areas, improved computing capabilities have contributed to widespread advances. Computer vision, however, has specifically benefited from an exponential growth in available image datasets from smartphones, aerial and satellite imaging, video feeds, laboratory optical techniques, and many other sources. Applications of computer vision are becoming more commonly recognized by the public as adoption of the technologies is widening across many industries such as self-driving cars, facial expression recognition, and 3D medical imaging<sup>53,54,55</sup>.

Convolutional neural networks are a type of deep learning network that excel at analyzing images for categorical classification. When considering images, CNNs have been widely developed, applied and proven over the course of decades across many industries. CNNs are arguably the most well-known subset of machine learning as subsequent technologies, such as facial and handwriting recognition, become more commonly used by the public. Analysis is accomplished by taking an input image and applying a set of trainable weights and biases to various aspects in the image, allowing the network to differentiate between the various features of an image. In this application, those features indicate differences between varying wave direction and number. The strength of CNNs over traditional neural networks is the application of convolutional layers which work by sliding a filter over a finite pixel region and taking the dot product between filters and regions of an image to produce an activation map. As the CNN becomes deeper with multiple convolutional layers, the dot product of the deeper layers inherits dot products of the previous convolutional layers allowing low-level

features to be built into high-level features. In this type of network each artificial neuron is connected to only a small part of the input volume, but they all have the same weights. The sharing of weights is referred to as parameter sharing and allows the CNNs to be locally connected rather than fully connected as is common in a traditional neural network. The ability of these networks to perform parameter sharing while having local connectivity reduces the number of trainable parameters in the system, i.e. neuron weights, leading to a more computationally efficient system.

CNN designs are inspired by the connectivity patterns of neurons in the human brain as the architectures attempt to simulate human visual cortices. Images are broken down into discrete areas known as receptive fields in which neurons respond to stimuli only in that field. These fields are overlapped together to cover the entire visual area. By breaking down the image into these fields it is possible to draw out the spatial and temporal dependencies in an image by applying relevant filters.

CNNs have been proven to outperform all other types of classification algorithms in the ImageNet object identification challenge<sup>56,57,58,59</sup>. These networks are highly flexible and have been applied to a variety of specialized applications, including combustion and gas turbines. Dering et al.<sup>60</sup> showed that CNNs could be used to predict a products function given its form. Mao et al.<sup>61</sup> utilized CNNs to predict unsteady wave forces on bluff bodies due to the free-surface wave motion. CNNs have also been used in conjunction with sensors to diagnose faults in rotating machinery as shown by Xia et al.<sup>62</sup>.

The arrangement and specification of convolutional, max pooling and other layers is referred to as the CNN architecture. There are a multitude of unique architectures that exist in the literature consisting of various combinations of filters, layers, neurons and other trainable parameters, termed hyperparameters, that all attempt to achieve the same goals as quickly and

Data	2x2	Dot	Scalar
region	Kernel	Product	Output
$\begin{matrix} 1 & 7 \\ 3 & 1 \end{matrix}$	$\begin{matrix} 1 & 0 \\ 0 & 1 \end{matrix}$	$= \underbrace{(1*1) + (7*0) + (3*0) + (1*1)}_{\text{Dot Product}} = 2$	

**Figure 1.5:** Illustration of simple 2x2 convolutional kernel applied to 2x2 sample space

efficiently as possible. CNN architectures employed throughout the text will be detailed in the following subsections. CNN Hyperparameters are tunable parameters that can significantly affect the performance of a CNN. Typical hyperparameters are learning rate, activation function, kernel initializers, stride length, kernel size, and pooling size.

Although the capabilities of CNNs are vast and complex, the mathematical functions occurring within are more simplistic. While these networks may contain a variety of layer types, they are uniquely identified by the inclusion of convolutional layers. Convolutional layers include a series of kernels which are passed across an input to create feature maps. The passage of the input data region through each kernel involves a single convolution, or more simply a dot product, as visualized in Figure 1.5. Kernels can be one, two or three-dimensional matrices, and include weights which are randomly initialized at the beginning of network training and tuned to detect valuable features which minimize network loss.

Figure 1.5 shows the kernel mathematical operation for an equally sized data region. As input sizes and dimensions increase, kernel size is not increased to maintain a single convolution. Instead, the kernel steps across the entire input data region, and the scalar outputs at each location are logged to the feature map. The distance the kernel moves between evaluations is referred to as the stride length. Utilizing the same kernel weights shown in Figure 1.5, an example of a 2x2 kernel with a stride length of 2 passed over a 6x4 input data region is shown in Figure 1.6. Within this illustration, kernel locations are outlined in the color of the

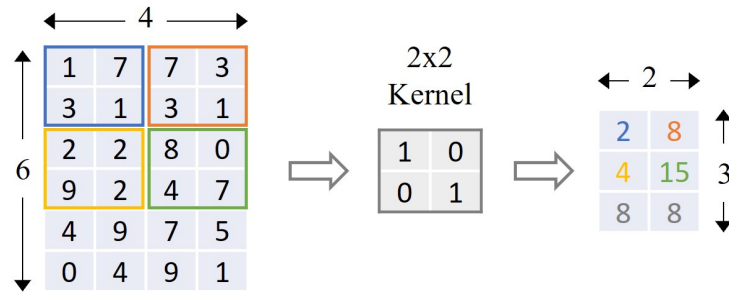


**Figure 1.6:** Illustration of simple  $2 \times 2$  convolutional kernel applied to  $6 \times 4$  sample space with stride of 2

corresponding scalar output. This data and kernel arrangement results in a feature map, also referred to as an activation map, of size  $2 \times 3$ .

Because the stride length in Figure 1.6 is equal to the kernel width and height, there is no overlap in the kernel application locations. More often, stride lengths are not equal to kernel dimensions intentionally creating overlapping convolution operations. To the same sample space, the same kernel is applied with a reduced stride length of 1 in Figure 1.7. Because the overlapping kernel locations are not as easily visualized, the feature map formation is shown in the four initial steps as the kernel progresses across the sample space, left to right, top to bottom, at steps of 1. Here again, the color outlining kernel application locations corresponds to the scalar output in the feature map. Due to the reduced stride length, the resultant feature map is larger than the previous example with dimensions  $3 \times 5$ . Feature map sizes and dimensions are directly related to that of the input data, and inversely related to those of the kernel and stride length.

Another important aspect of CNNs is the use of pooling layers which reduce the spatial dimensionality of an input image. Pooling layers play a key role in the computational efficiency of CNNs by reducing the dimensionality of the input data resulting in fewer parameters and thereby lesser computational expense. Pooling layers operate as independent

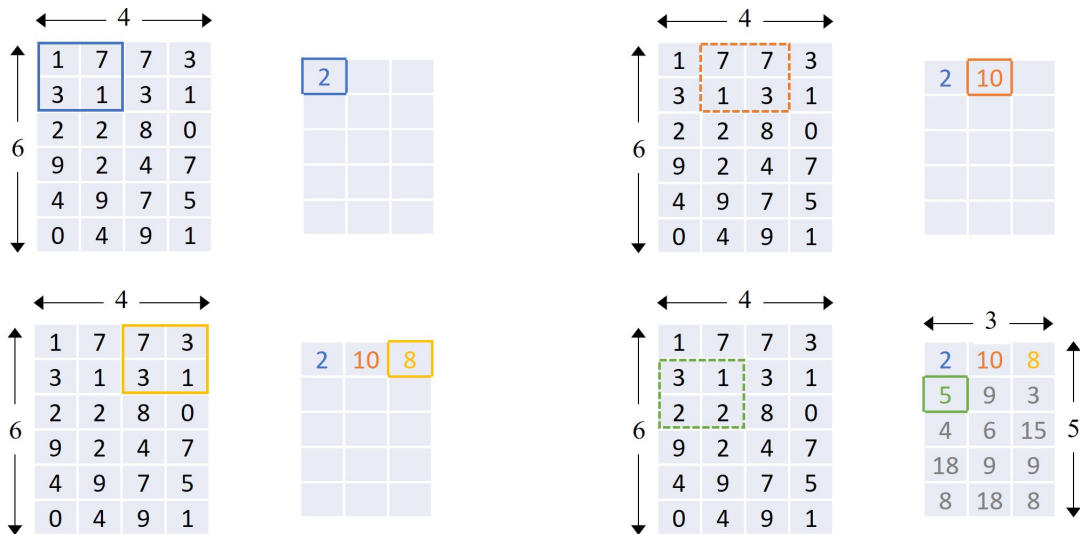


**Figure 1.7:** Illustration of simple  $2 \times 2$  convolutional kernel applied to  $6 \times 4$  sample space with stride of 1

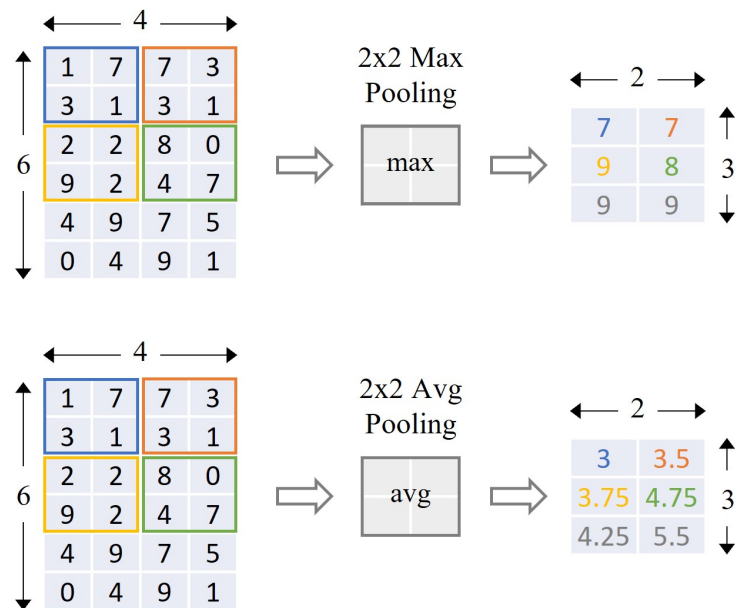


**Figure 1.8:** Illustration of  $2 \times 2$  max pooling (top) and  $2 \times 2$  average pooling (bottom) applied to  $6 \times 4$  sample space with stride of 2

layers from the convolutional layers. Within CNNs, pooling layers are often used to further reduce the output of convolutional layers. Two common examples are maximum (max) pooling, and average pooling. Much like the previous examples, max pooling and average pooling are performed with specified kernel sizes and stride lengths. Instead of performing the dot product, the max and average pooling kernels output the local maximum and average, respectively. Using the same input data, kernel size, and stride length as that in Figure 1.6, the application of max pooling and average pooling and their respective feature maps is shown in Figure 1.8. Max pooling and average pooling may also be applied globally, where the kernel size is equal to that of the input data. In those instances, global max pooling or global average pooling result in a single scalar value summarizing the respective input space. Note that none of the feature maps across these simplified examples is the same for any kernel location. This emphasizes the incredibly large variety of possible data representations resulting from architecture design and kernel weights, leading to CNNs' abilities to generalize large datasets according to both high and low level features without complex algorithms.

It is important to note that the examples shown in Figures 1.5 through 1.8 are simplified for the fundamental illustration of CNN calculations in the forward pass. Within a single convolutional layer, a multitude of kernels are tuned to generate the same quantity of feature maps. For example, the SqueezeNet and You Only Look Once networks, summarized in later subsections, train 96  $7 \times 7$  and 64  $7 \times 7$  kernels, respectively, in their first convolutional layers alone. Computations in the backward pass where errors are passed through activation functions and kernels to tune network parameters are more complex. The full coverage of these topics does not fall within the scope of the current work, which aims to apply CNNs as a tool for RDE monitoring. The following three sections highlight the three CNN types used: image classification, object detection, and time series classification.

### 1.1.3.1 IMAGE CLASSIFICATION

A common and widely developed capability within the field of CNNs is image classification, which is trained to predict a single label for a given image. Image classification capabilities have proven useful in a variety of engineering applications, most often through the use of neural networks. As an expected result of the sophisticated imaging techniques among RDE studies, image classification has proven to be a beneficial means of classifying detonation wave number and direction using a convolutional neural network (CNN). In a study outlined in Chapter 4<sup>46</sup>, a CNN is trained to classify ten different wave modes within individual high-speed images at >95% accuracy.

The network employed throughout the RDE image classification effort detailed in Chapter 4<sup>46</sup> and utilized in Chapter 5, SqueezeNet, is a unique architecture in the CNN design space, as it was developed to achieve the same accuracy as other popular architectures, but with fewer parameters and a smaller model size by incorporating a building block referred to as a *fire module*. SqueezeNet is illustrated with an expanded view of the namesake fire module in Figure 1.9. The architecture is comprised of a single convolutional input layer followed by 8 fire modules and ending with another single convolution layer. The fire module, whose microarchitectural view is expanded in Figure 1.9, utilizes a squeeze layers of 1x1 convolutional filters to reduce parameter volume as well as decrease the number of input channels to the downstream expand layers of 3x3 convolutional filters. Max pooling is performed after the 1<sup>st</sup>, 4<sup>th</sup> and 8<sup>th</sup> layers, and a global average pooling after the final convolutional layer, each at a stride of 2 pixels. The output is fed to a softmax function, typical for classification problems. Further information detailing the SqueezeNet architecture can be found in the original literature<sup>63</sup>, and in the model summary in Appendix B.

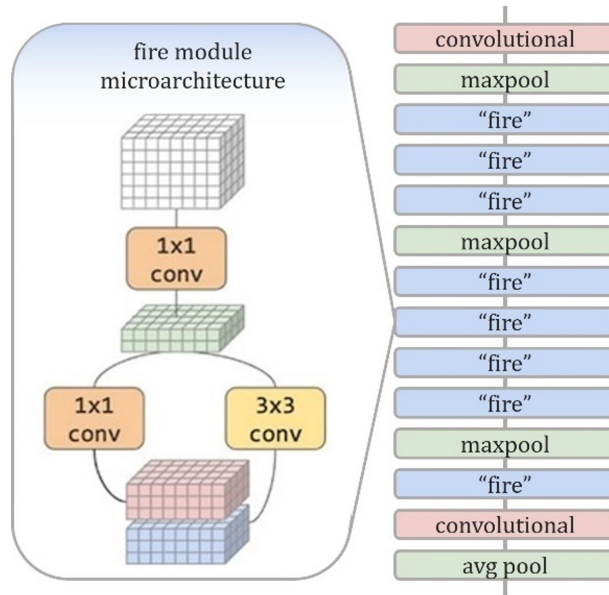


**Figure 1.9:** SqueezeNet fire module (left) expanded from SqueezeNet architecture visualization (right)<sup>63,64</sup>

Calling on the basic understanding of convolutional and pooling layers described in the text surrounding Figures 1.5- 1.8, examination of feature maps gives basic but valuable insight into the inner workings of the network. Recall that each layer passes the input through a number of filters, all of which are tuned throughout the network training process. Chapter 4 details the training of a 6-class SqueezeNet model, which is used to generate the feature maps in Figures 1.10 and 1.11. Because networks train a large number of filters at each layer, it is not practical to plot every feature map, even from a single layer. The first six feature maps from five layers of interest (Convolution 1, MaxPool 1, MaxPool2, Fire Module 8, and Convolution 2, named according to model summary detailed in Appendix B) are plotted for an input image containing 2CW waves in Figure 1.10. Again, feature maps in Figure 1.10 represent a small portion of the filter collection at each layer. For example, the first layer, Convolution 1, trains 96 filters alone. Still, sophisticated treatment of the wave profiles to-

wards increasingly abstract representation can be seen through incrementally deeper layers, left to right.

The final convolutional layer outputs a reduced number of feature maps, equal in quantity to the number of possible classifications. In the case of the 6-class network used to generate Figures 1.10 and 1.11, the final feature space is  $6 \times 3 \times 3$  matrices, each corresponding to one of the possible classifications. Average global pooling is applied to each of the 6 final feature maps, resulting in a 6-integer probability distribution overlaid as white numeric text in Figures 1.10 and 1.11. Through the application of a softmax function, the probability distribution is translated to a 6-Boolean vector where the largest value among the probability distribution results in a value of 1, and the rest values of 0. The index of the unity value within the Boolean vector corresponds to the final network classification. To more practically rephrase, the maximally activated output channel, which appears visually as the brightest, is selected via the softmax operation.

For both Figures 1.10 and 1.11, the class list associated with the ground truth training data is vector: [’1CW’, ’1CCW’, ’2CW’, ’2CCW’, ’3CW’, ’3CCW’]. A maximum value of 63.19 output by global average pooling for the example within Figure 1.10 results in a true prediction for the the third index whose channel is outlined in yellow. Therefore, relating the maximally activated output channel to the third component within the class list vector, the network output for this specific example is Class 3, or ’2CW’.

Similarly, an image depicting a 3CCW wave mode is input to the trained 6-class network, for which the same sub-sampling of feature maps is shown in Figure 1.11. Here the global average pooling of the final convolutional layer output results in a maximum value of 89.09 at the sixth channel, outlined in yellow. The softmax function therefore assigns a value of

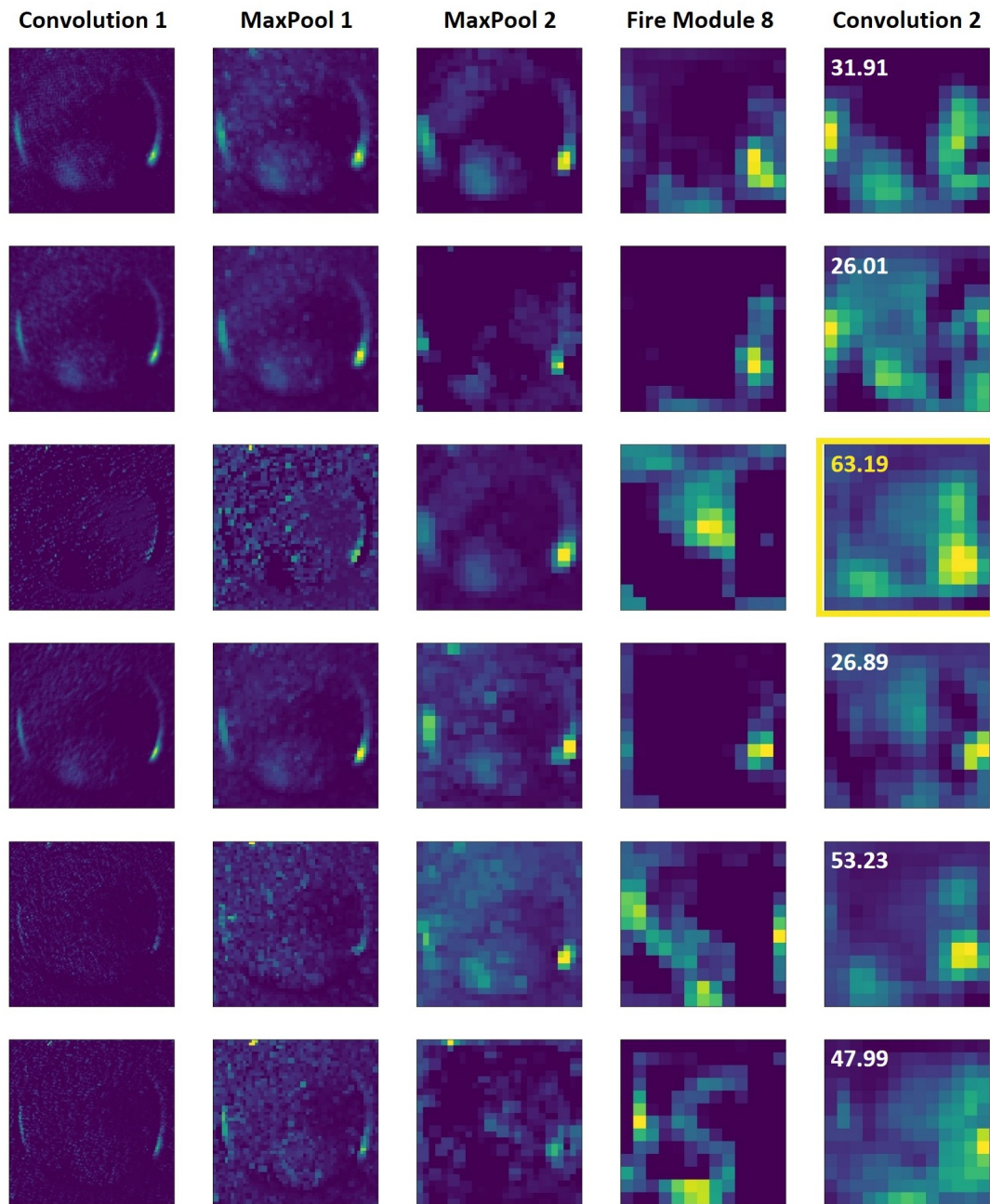


**Figure 1.10:** Extracted SqueezeNet feature maps from various trained network layers, with global average pooling values overlaid in white text and the maximally activated channel outlined in yellow (Class 3: zCW)

unity in the sixth index of the Boolean classification vector, resulting in a network output of Class 6, or '3CCW'.

Feature maps shown in Figures 1.10 and 1.11 represent correct classifications. Comparison of global average pooling values, listed in white text, offers insight into activation levels of near misclassifications. For similar reasons, evaluation of trained filters and resulting feature maps throughout network training can lead to valuable understanding of network function, progress, and feature evaluation. Further consideration of feature maps does not lie within the scope of the current work, but serves to demonstrate the inner workings of a CNN as well as the describable and accessible nature of a method often mistakenly referred to as a "black box". To that end, CNNs behave in a way that is reproducible according the design of the layered architecture, which remains malleable to the needs of the user, as is demonstrated by the portfolio of networks surveyed throughout Chapters 4 through 7.

Compared to conventional image processing techniques, image classification offers distinct advantages in computational efficiency and time-scale independence. In order to obtain those metrics reliant on time-scale such as wave velocity and frequency, correlation of simultaneously recorded sensor data is performed. Still yet, image classification has the distinct disadvantage of only predicting a single label for each image, which becomes an issue when a new arrangement of objects is present in an image that are not included in the training set. This issue can be addressed through the use of a more sophisticated computer vision technique such as object detection.

#### 1.1.3.2 OBJECT DETECTION

Object detection attempts to locate observable objects within an image, constrain them with bounding boxes, then identify each detected object, which leads to more robust capabilities

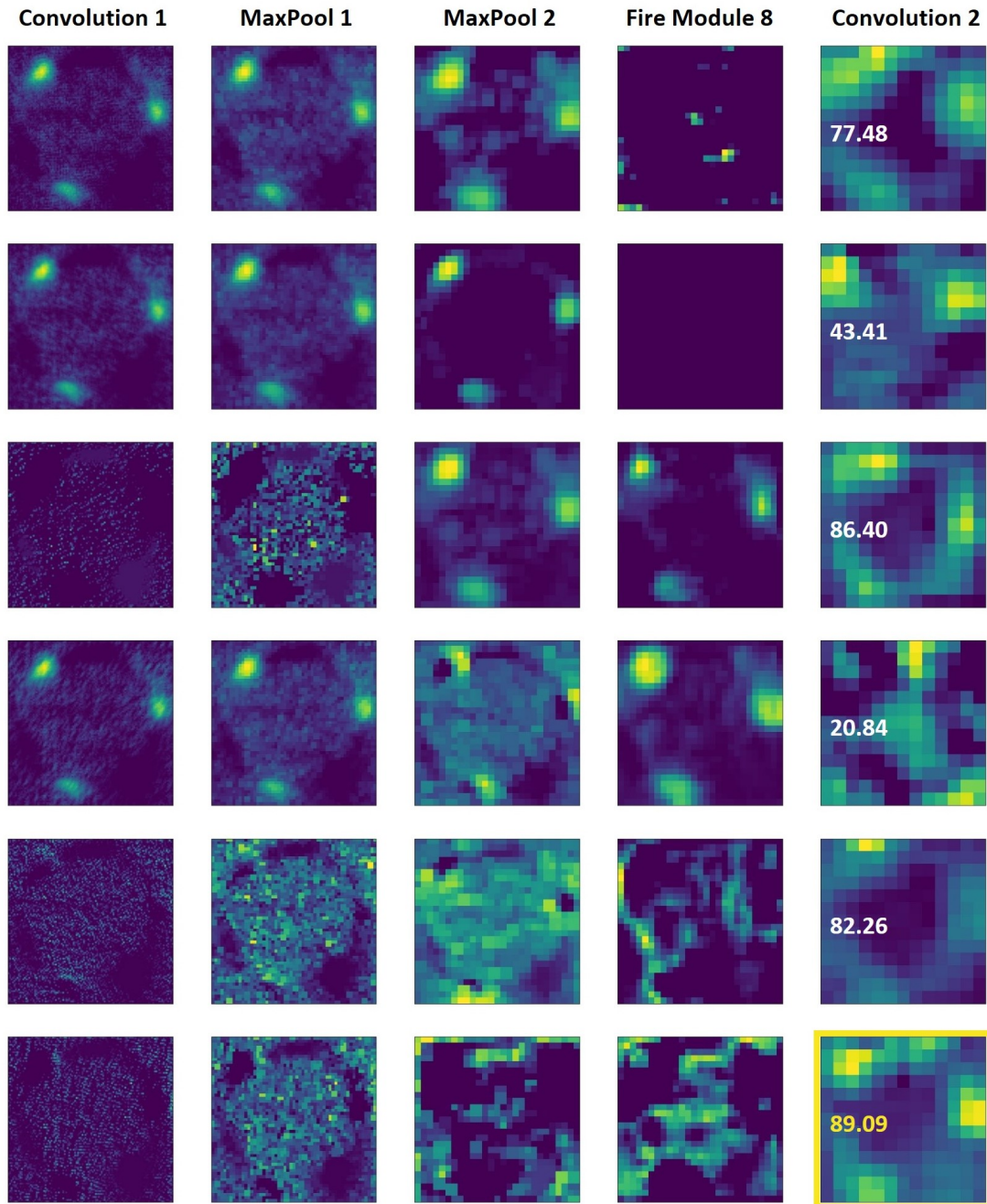


**Figure 1.11:** Extracted SqueezeNet feature maps from various trained network layers, with global average pooling values overlaid in white text and the maximally activated channel outlined in yellow (Class 6: 3CCW)

and the ability to discern information in images containing a new arrangement of objects. Object detection was shown to accurately locate key features of analog multimeters to automated readings from a live-video source by Chen et al.<sup>65</sup>, and continues to offer valuable insight to medical imaging<sup>66</sup>, radar imaging<sup>67</sup>, agriculture<sup>68</sup>, automated driving systems<sup>69</sup> and many other industries. A family of model types that accomplishes this task is region-based convolutional neural networks (R-CNNs), which scan an image to detect objects, then use a conventional CNN on each of those detected regions of interest (RoIs) to predict the label of each object<sup>69</sup>. The use of a CNN for each identified object proved to introduce issues impacting efficiency, which was later addressed with the development of Fast R-CNN, a new model type which performs feature extraction prior to detecting RoIs<sup>70</sup>. Shortly after the development of Fast R-CNN, Faster R-CNN was introduced and showed higher accuracy and speed performance than its predecessors. Faster R-CNNs outpaced those predecessors by using a pre-trained CNN to propose regions of interest (RoIs) and the objects within RoIs, which were then fed to a Fast R-CNN<sup>71</sup>.

A later type of object detection model, referred to as the You Only Look Once (YOLO) model, was created to specifically enhance object detection speeds. Unlike other object detection methods which use sliding windows or region proposal methods to first detect potential bounding boxes and then run regions through separately trained classifiers, YOLO achieves drastically reduced detection speeds by performing unified detection and labeling entirely with one neural network. The YOLO architecture, shown in Figure 1.12<sup>72</sup>, relies on 24 convolutional layers feeding to 2 fully connected layers. Unified detection considers object presence in relation to the global image information. To do so, the YOLO network first parses an image into a grid within which each cell grid is used to separately predict possible bounding boxes and conditional class probability. The network's confidence in the size

and location of a bounding box whose centroid lies within a given grid cell is multiplied by the class confidence of that same grid cell, resulting in final class-specific confidence scores. Final detections with class-specific confidence scores falling above the user-defined confidence threshold are output as object detection annotations. An example of YOLO unified detection from the original work is shown in Figure 1.13<sup>72</sup>. The effects of confidence thresholding and annotation ground truth sizes will be discussed in Sections 6.2 and 6.3, respectively. The ability to perform all necessary tasks within a single network pushes the YOLO architecture to real-time object detection capabilities.

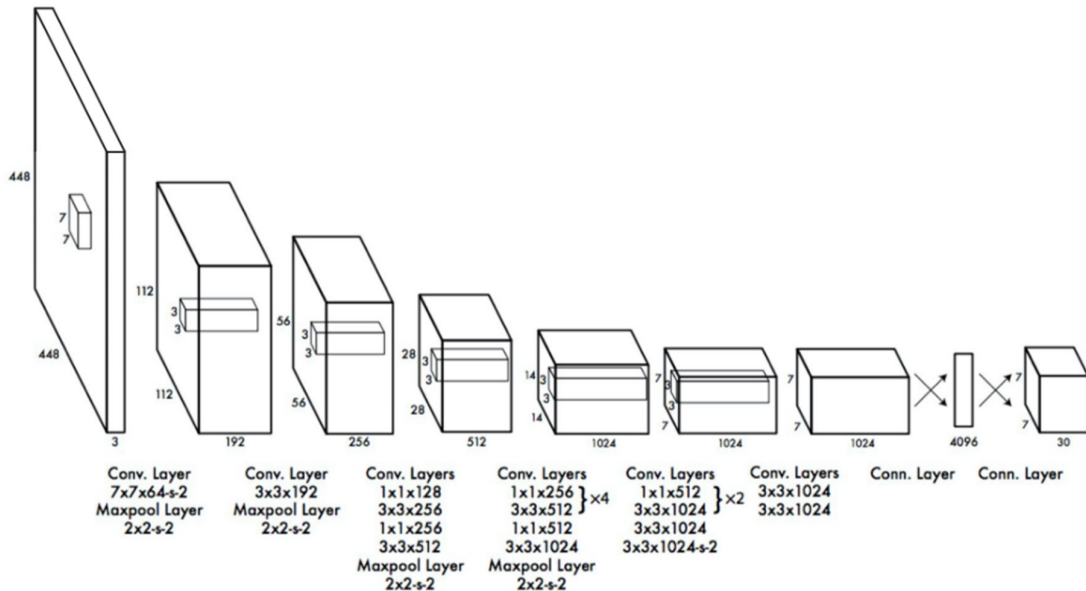


**Figure 1.12:** You Only Look Once (YOLO) network architecture<sup>72</sup>

It is important to note that while YOLO is often considered a solution for real-time object detection, processing speeds are adequate for standard streaming video which is orders of magnitude slower than imaging speeds within the RDE community as well as the timescale of detonation wave progression. For this reason the RDE YOLO network proposed within this work cannot accomplish real-time RDE monitoring, but remains beneficial as a means

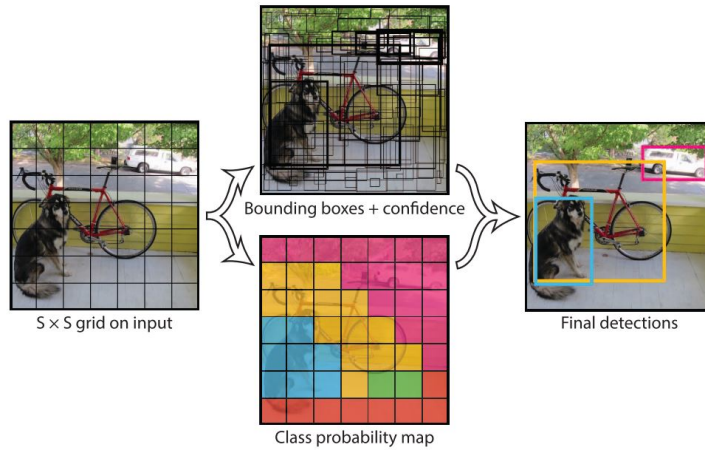


**Figure 1.13:** YOLO unified detection example<sup>72</sup>

to improve data processing speeds and offer highly resolved frame-to-frame velocities. The network will be trained to detect and identify individual detonation waves according to the rotational direction. Compared to other object detection methods, YOLO learns representations of objects that are more generalizable due to the contextual consideration of the entire image, making it less likely to fail if applied to varied down-axis RDE imaging techniques across multiple labs.

Using computer vision object detection, this study aims to train a neural network to detect, locate, and label individual detonation waves within an image according to their rotational direction. Coordinates of each wave can be tracked to evaluate individual wave speeds and frequencies in co- and counter-rotational modes.

#### 1.1.3.3 TIME SERIES CLASSIFICATION

Although the previous and ongoing machine learning approaches to RDE imaging are promising and offer significant reduction in computational time, their application beyond an experimental phase of RDE development may be limited by equipment availability and optical ac-

cess. While this is not an immediate concern as experimental RDEs are expected to be studied for many years to come, it does highlight the need for a similar machine learning application to data more readily available in a turbine-integrated arrangement. It should be noted that like optical techniques, temporal data analyses have been studied at length within the RDE community. Time series data from pressure probes, ion probes, and other sensors have been analyzed to determine wave modes and dynamics by way of fast Fourier transform<sup>11</sup>, auto-correlation<sup>44</sup>, cross-correlation<sup>43,42</sup> and other adapted methods<sup>10</sup>. However, consideration of temporal data is done alongside or verified by optical techniques which offer the confidence of spatial resolution. The current study aims to fully incorporate the advantages of imaging certainty by creating a labeled dataset of input-output pairs where pressure and ionization current data serves as an input and wave mode classification derived from down-axis images serve as the corresponding output. These datasets will be used to develop a collection of time series classification (TSC) networks.

Time series classification is a longstanding challenge in data mining which aims to probabilistically determine the correct label of univariate or multivariate time series. Univariate datasets can be generalized as a collection of vectors containing data from a single sensor throughout time. Multivariate datasets are structured as matrices where in addition to the dimension of time, a second dimension is added for the inclusion of additional sensors. This data structure is illustrated in Figure 1.14. As an example, a univariate datapoint with a sample length of 200 samples would have dimensions of  $1 \times 200$ , while a multivariate datapoint of equal sample length that includes two sensors has dimensions of  $2 \times 200$ . As the number of sensors increases, so does the size of the multivariate set by stacking traces recorded simultaneously along the time axis. In the current study, as is the case in many TSC efforts, the benefit of multivariate datasets is a result of added spatial resolution as well as varying sensor

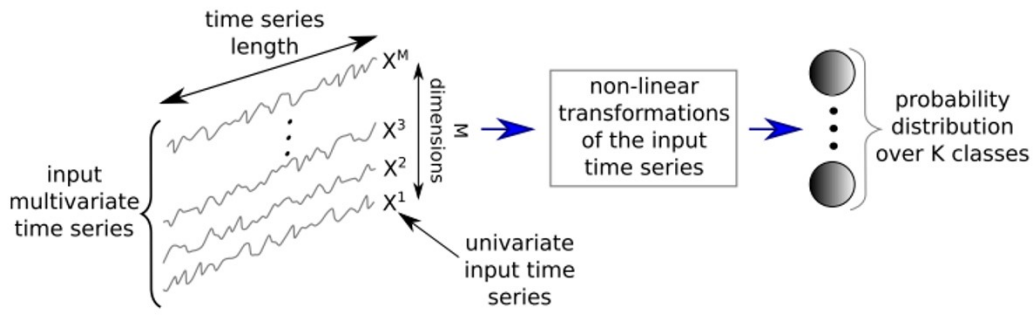


**Figure 1.14:** Generic DNN TSC framework for multivariate time series<sup>74</sup>

type. Due to the prevalence of time series data in a wide range of fields, a vast number of methods to solve time series classification have been developed and considered. Some examples of popular and traditional solutions included nearest neighbor (NN) classifiers joined with a distance function, decision trees, support vector machines (SVM), HIVE-COTE<sup>73</sup>, and many others<sup>74</sup>. With increased accuracy, however, the time complexity of each traditional method increases significantly sometimes to the point of impracticality. Therefore, deep learning, which has revolutionized computer vision and has shown success in natural language processing (NLP) and speech recognition, is considered as an alternative solution for TSC. In this study, deep neural networks (DNN) will be used to perform TSC on experimental RDE pressure and ionization data recorded at 250 kHz. Multiple datasets will be created to determine the advantages of univariate and multivariate time series. The DNN will work according to the DNN TSC framework shown in Figure 1.14. The time series, either univariate or multivariate is fed to the DNN which performs non-linear transformations according to the prescribed architecture resulting in a probability distribution over the classes present in the dataset.

While the use of a CNNs for experimental RDE data is novel, the increasing benefits of machine learning techniques have been utilized in a variety of studies across the combustion

community. As a very early example, Santos-Victor et al. <sup>75</sup> showed that flames within a glass furnace can be classified via computer vision to determine the number of active burners as well as the reactant flow rate. Neural networks were applied in the field of gas turbines through the work of Tong et al. <sup>76</sup> where the effectiveness of using machine learning to predict core sizes of high efficiency turbofan engines was displayed. Grogan and Ihme <sup>77</sup> investigated the probability of predictive parameters for irregular combustion regimes and detonation sensitivity to heat release with machine learning. With possible application to RDEs, Barwey et al. <sup>78</sup> presented a data-driven approach to combustion regime classification within the complex structure of detonation waves using artificial neural networks. Using a different data mining technique, Rezzag et al. <sup>79</sup> investigated instantaneous detonation wave speeds in post-processing using k-means clustering. The current work further extends the usage of CNNs within pressure gain combustion via a heavy reliance on the broader collection of previous machine learning development efforts.

## 1.2 OBJECTIVE

Known for their simplistic design and continuous detonation, RDEs constitute a majority of current pressure gain combustion (PGC) research efforts. Increased research over the last 5-10 years has advanced RDE technology from concept exploration to mechanism research<sup>35</sup>. A major contributor to this progression, experimental RDE operation times have been continuously extended through the use of rig cooling techniques, such as the NETL water-cooled rig used in a portion of this study. As the window of observable behavior is expanded, and as the technology matures toward eventual integration within gas turbines, monitoring techniques must evolve to better match industrial diagnostics. Various techniques have been developed to characterize the modal properties of the detonation waves that occur in rotat-

ing detonation engines (RDEs). Traditional feature extraction and image analysis are time consuming and computationally expensive processes. For studies of time dependent processes, such as progressing detonation wave(s), extracting temporal details such as operating frequency requires a large number of images exceeding 1000 frames or a large window of time series data. Additionally, while transducer-based methods are well understood, they often rely on underlying assumptions, such as an assumed Chapman-Jouguet wave speed, to quantify detonation wave properties and draw physical conclusions. Further verification of their ability to quantify the desired properties is often performed through image analysis which offers spatial resolution. As such, these methods are only performed in post-processing and therefore cannot be considered for real-time applications. High-speed processing of large data quantities on a time scale comparable to that of the detonation speed will likely only be accomplished through the use of machine learning. Machine learning offers many benefits to the study of RDEs due to its proven successes in consideration of the two major data types recorded and studied in experimental RDE facilities: images and time series data. In order to realize RDE engineering application, there is a need for the development of a real-time diagnostic portfolio, and subsequent ability to control and predict detonation wave behaviors during operation. This body of work aims to address these needs by accomplishment of the overall objective:

*Advance the efficiency of RDE diagnostic techniques from conventional post-processing efforts to lab-deployed real-time methods, achieving highly efficient detonation characterization through the application of machine learning to experimental data.*

Conventional diagnostic techniques for defining the wave speed, number of waves and propagation direction have included analysis of high-speed imagery, as well as frequency based and time of flight correlations of transducer signals such as dynamic pressure or flame ionization (chemi-ionization). In order to advance RDE diagnostics, deep learning techniques are applied to experimental RDE data. Convolutional neural networks (CNNs) consisting of varying architectures are used for image classification, object detection, and time series classification applied to experimental RDE high-speed images and sensor data. To conclude the work, a final comparison of the three networks alongside conventional methods according to classification accuracy, output speed, and experimental setup is performed.

The steps to execute the outlined objective in full are listed in the following section as six unique research tasks, all of which have been detailed in coinciding publications. The presented work offers a framework in which significant detonation diagnostic capabilities are accomplished by CNNs, adapted to analyze RDE operational characteristics of interest, and successfully deployed in an adapted experimental setup. As an early application of machine learning within pressure gain combustion research, established real-time diagnostic capabilities will certainly play a vital role in the development of active control practices necessary to the continued advancement of RDE technology towards turbine integration.

### 1.3 SCOPE OF WORK

As discussed in the previous section, the objective of this work is to:

*Advance the efficiency of RDE diagnostic techniques from conventional post-processing efforts to lab-deployed real-time methods, achieving highly efficient detonation characterization through the application of machine learning to experimental data.*

This goal is to be accomplished through the completion of six research tasks which are proposed below.

- (A) *Analyze image and pressure data using conventional techniques: AFRL detonation surface and auto-correlation of pressure signals<sup>44</sup>*
- (B) *Develop and train RDE image classification CNNs<sup>80,46</sup>*
- (C) *Develop live image and data acquisition system and deploy in lab<sup>81</sup>*
- (D) *Develop and train object detection CNN for individual wave detection and tracking; Apply secondary calculations to CNN outputs to determine wave velocity<sup>82</sup>*
- (E) *Create time-series classification CNN for pressure data<sup>83</sup> and deploy in lab*
- (F) *Compare 3 methods for real-time application and survey additional AI methods applicable to experimental RDEs*

Following the coverage of conventional techniques, methods of three machine learning applications including image classification, object detection, and time series classification are

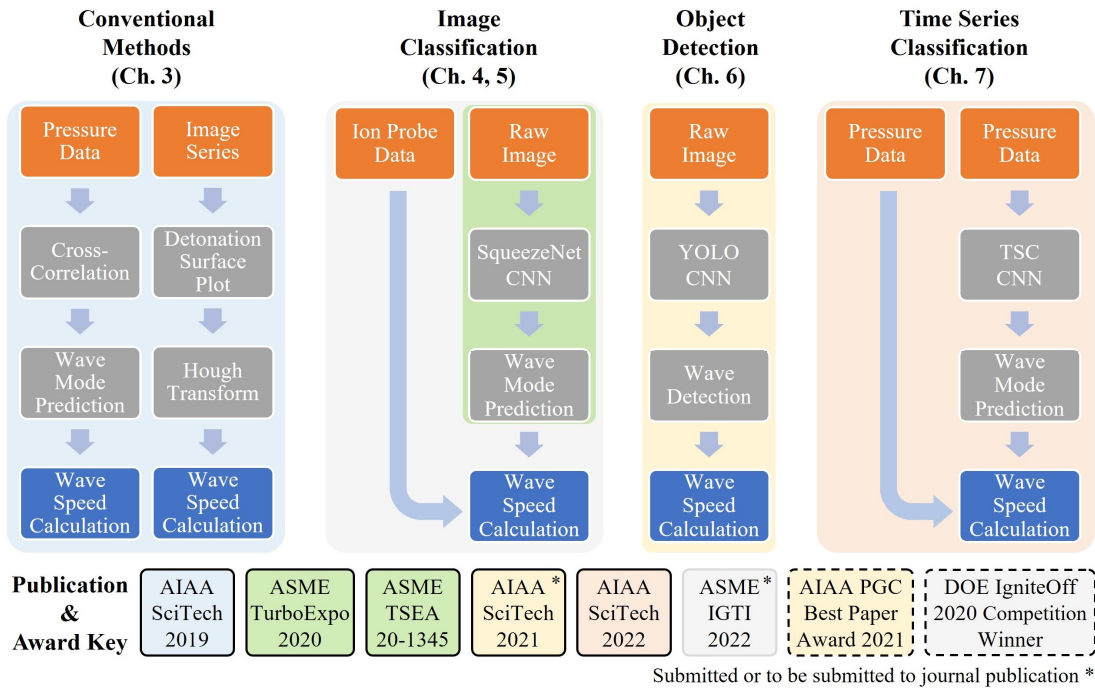


**Figure 1.15:** Visualization of data flow in various tasks paired with publication key where outlined boxes indicate published work, non-outlined boxes indicate upcoming accepted publications, and dashed outlines indicate awards received

to be developed, lab-integrated, and compared. To visualize the major efforts outlined in Section 1.2, Figure 1.15 outlines the data flow used in conventional methods, image classification, object detection and time series classification applied to RDE data. Figure 1.15 includes a publication and award key depicting the publication in which each body of work is documented according to colors matching those behind each technical effort. Within the publication key, black-outlined boxes indicate papers already published, a box with no outline corresponds to an upcoming publication which has been accepted, but not yet published, and boxes with dashed outlines indicate awards won for a subsection of the current work. Specifically, training of an object detection network for individual detonation wave detection and tracking (yellow) was documented in a publication(AIAA-2021-1382<sup>82</sup>) at AIAA SciTech 2021, a publication which was later awarded the *2021 AIAA PGC Best Paper Award*.

In a similar fashion, the overall RDE image classification adapted for real-time measurement contributed to multiple publications<sup>80,46,81</sup>, and was the topical coverage of a presentation awarded top prize at the *2019 DOE IgniteOff Competition*. For additional insight, asterisks\* indicate publications submitted or to be submitted to journal publications.

#### 1.4 OUTLINE OF THE MANUSCRIPT

Each research task is addressed in a designated chapter. Specifically, Chapters 3- 8 constitute coverage of Tasks (A)-(F) in succession. Chapter 2 outlines experimental facilities and data treatment relevant throughout the remaining text. To further correlate the research tasks to the four major efforts outlined in Figure 1.15 as well as coverage throughout the manuscript:

**Task (A)** corresponds to Conventional Methods, highlighted in blue and covered in Chapter 3<sup>44</sup>; **Task (B)** corresponds to the green portion of Image Classification, specifying the training of the CNN prior to lab integration, and is detailed in Chapter 4<sup>80,46</sup>; **Task (C)** addresses the grey portion of Image Classification, being the lab-integration of the network employed as a real-time diagnostic within Chapter 5<sup>81</sup>; **Task (D)** completes Object Detection efforts, denoted in yellow and designated to Chapter 6<sup>82</sup>; **Task (E)** encompasses Time Series Classification, including lab deployment, demonstrated in Chapter 7<sup>83</sup>; and finally **Task (F)** compares the strengths and long-term feasibility of the four major efforts within Chapter 8.

Prior to the coverage of research task content, the following chapter discusses data acquisition and treatment applied throughout the manuscript. Similar to the treatment of CNN architectures within this chapter, shared details regarding experimental setup, image acquisition, real-time arrangement, and image treatment techniques within Chapter 2 are outlined once, in detail, and referenced accordingly throughout the remaining chapters. Of particular interest is the coverage and comparison of two experimental RDEs operated at NETL Mor-

gantown, differentiated as uncooled and water-cooled geometries. Data collected from both arrangements is used to generate training sets throughout the present work, resulting in an inherent strength of data variety expected to result in network tolerance of externally acquired data. Data variety implies a level of consignable application in other laboratory environments without additional training. This level has not been explored by physical relocation, but by analysis of external data. The likelihood of successful model sharing as a component of the real-time monitoring framework further broadens the significance of the highly efficient detonation characterization work.

The following publications have resulted from the work contained herein, and are listed with their corresponding reference number:

- [44] **Johnson KB**, Ferguson DH, Nix A. 2020 Validation of Cross-Correlation Detonation Wave Mode Identification Through High-Speed Image Analysis. In: *AIAA Scitech 2020 Forum*. (doi:10.2514/6.2020-1179).
- [46] **Johnson KB**, Ferguson DH, Tempke RS, Nix AC. 2021 Application of a Convolutional Neural Network for Wave Mode Identification in a Rotating Detonation Combustor Using High-Speed Imaging. *Journal of Thermal Science and Engineering Applications* **13**, 6, 1–11. (doi:10.1115/1.4049868).
- [80] **Johnson KB**, Ferguson DH, Tempke RS, Nix AC. 2020 Application of a Convolutional Neural Network for Wave Mode Identification in a Rotating Detonation Combustor Using High-Speed Imaging. In: *ASME 2020 Turbomachinery Technical Conference & Exposition*, pp. 1–12. (doi:10.1115/GT2020-15676).
- [81] **Johnson KB**, Ferguson DH, Nix AC. 2022 Use of Convolutional Neural Network Image Classification and High-Speed Ion Probe Data Towards Real-Time Detonation Characterization in a Water-Cooled Rotating Detonation Engine. In: *Proceedings of the ASME*

*2022 Turbomachinery Technical Conference & Exposition.* To be published, manuscript accepted.

- [82] **Johnson KB**, Ferguson DH, Nix AC. 2021 Individual Wave Detection and Tracking within a Rotating Detonation Engine through Computer Vision Object Detection applied to High-Speed Images. In: *AIAA SciTech 2021 Forum*. (doi:10.2514/6.2021-1382).
- [83] **Johnson KB**, Ferguson DH, Nix AC. 2022 Time Series Classification within a Rotating Detonation Engine through Deep Convolutional Neural Networks applied to High-Speed Pressure Data. In: *AIAA SciTech 2022 Forum*. (doi:10.2514/6.2022-2371)

*I was just excited to have challenging work to do and smart people to work with.*

Katherine Johnson, West Virginian mathematician and orbital spaceflight pioneer

# 2

## Data Acquisition and Treatment

Data utilized and presented throughout the document was collected from two experimental RDE configurations over a time frame ranging from 2016 to 2022. Earlier data was collected by Donald Ferguson, Ph.D from the NETL uncooled experimental RDE. Data from the NETL water-cooled RDE was collected in more recent years by the author. Both configurations are designed to support a range of research efforts targeting pressure gain combustion within the Thermal Sciences Team at DOE NETL Morgantown. Data acquisition techniques and instrumentation are similar across both rigs, which separately incorporated

various annulus geometries. Details of each facility are detailed in Sections 2.1 through 2.3. Data treatment, detailed in Section 2.4, and analysis techniques are functionally transferable between the two settings. Consideration of differing data collections in development of conventional techniques and generation of CNN training data sets bolsters each effort and its potential impact in various experimental and industrial settings throughout future RDE development.

A horizontal arrangement of the uncooled was studied from August 2016 to August 2018. The uncooled RDE was previously oriented in a vertical position. Vertical arrangement data is not used in the current study, and will therefore not be detailed in the same manor. The water-cooled RDE is also positioned horizontally, and is utilized in studies from August 2019 to the present time of publication. All NETL RDEs to date are annular combustors with solid centerbodies and ducted exhausts, combusting hydrogen-air mixtures. Natural gas is occasionally introduced in small proportions to assist optical measurement efforts. Combustion of natural gas, formed primarily of methane, results in additional OH\*, CH\*, and CO<sub>2</sub>\* chemiluminescence. CH\* emittance is not captured due to bandpass filtering, and CO<sub>2</sub>\* contributes to the background of the total signal, at small fractions around the OH\* 310 nm wavelength and larger scales at the CH\* 435 nm wavelength which is neglected by filtering<sup>84</sup>. Therefore, the addition of small amount of natural gas enhances the OH\* chemiluminescence emitted by the detonation wave, which is captured by the imaging setup. Further consideration of CH\* imaging and chemiluminescent responses to varying proportions of natural gas addition in the RDE should be considered in a future work.

Data treatment and network training are performed using NETL's cloud computing facility, WATT. WATT is a part of the NETL Center for Artificial Intelligence and Machine Learning (CAML), offering 24 40-core Intel Skylake nodes (384 GBs of RAM and four

Nvidia P100 GPUs), and 40 PBs of raw storage. WATT hardware achieves 50 TFLOPs performance across all CPUs, and 323 TFLOPs performance across GPUs. The OpenStack software platform enables deep learning training and consideration of large datasets, tailored to the exploration of problems in machine learning such as the current study<sup>85</sup>.

## 2.1 NETL UNCOOLED EXPERIMENTAL RDE

The annulus design employed in the NETL uncooled experimental RDE, shown in Figure 2.1, is based on the 6-inch (15.24 cm) Air Force Research Laboratory (AFRL) geometry that has been widely examined in many academic studies<sup>86,87,12,88</sup>. Tests are performed in the high-pressure (2.0 MPa) Low Emission Combustor Test and Research (LECTR) facility at the US Department of Energy, NETL<sup>25</sup> shown in Figure 2.2. The 100-mm long combustor annulus has an outer diameter of 149 mm with a combustor gap width of 5 mm, and an air injector to combustor area ratio of 0.2. Unlike other experimental RDE facilities, the combustor in the NETL facility is connected to a ducted exhaust that incorporates a downstream high-temperature valve. The valve permits adjusting the operating pressure independent of the combustor exit geometry. This ability is beneficial for studies interested in simulating integration of the RDE with turbomachinery<sup>89,33,90</sup>. As tests are performed on an uncooled rig, high temperatures exceeding 1,700 K, associated with the detonation, limit the test duration to 6 to 10 seconds to prevent damage to the experimental facility and sensitive instrumentation.

A number of conventional measurements, such as dynamic and static pressure, OH\* chemiluminescence via a UV bandpass filtered Photomultiplier Tube, ion probes to measure chemi-ionization from the detonation wave, and thermocouples are placed at various axial and azimuthal locations throughout the combustor. Time-dependent measurements such as pres-

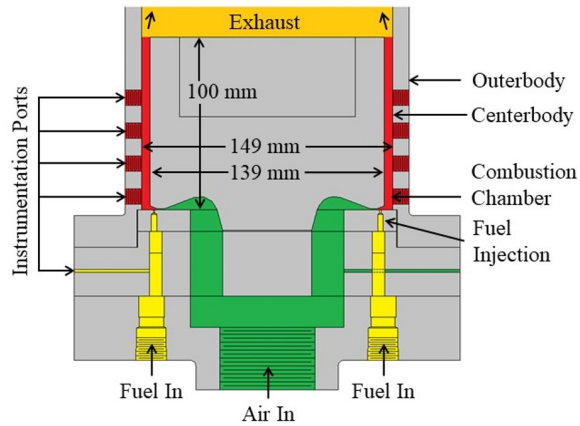


**Figure 2.1:** NETL RDE Cross-section Geometry

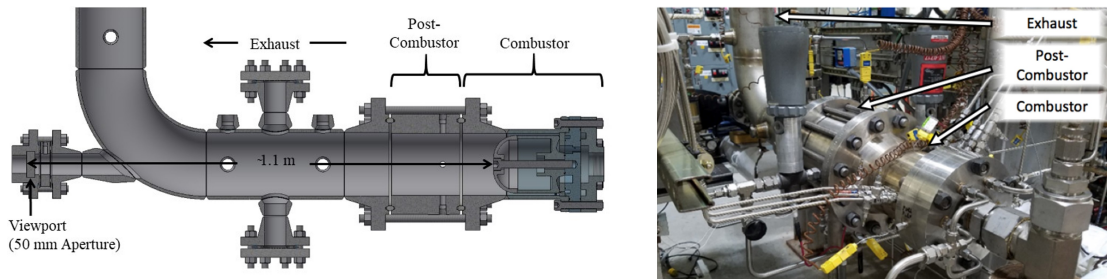


**Figure 2.2:** (a) Rotating detonation engine design and (b) test facility

sure (measured using a semi-infinite tube pressure coil (ITP) and PCB model CA102Bo4/CA102B15 pressure transducers), OH\* and chemi-ionization are recorded at 250 kHz through a National Instruments PXI data acquisition system and provide a means to quantify the performance of the detonation with regards to wave speed, number of waves and wave direction. Figure 2.3 illustrates the location of instrumentation ports in the RDE and port location nomenclature. PCB pressure transducers sample dynamic pressure at port locations B1 and C1. These port locations are an axial distance of 10.8 mm from the base of the RDE and are separated circumferentially by 130°, and are used directly in Chapter 3.

To ascertain the average detonation wave speed across a run, the power spectral density (PSD) of the time-based signals determines the dominant frequency which is used to define

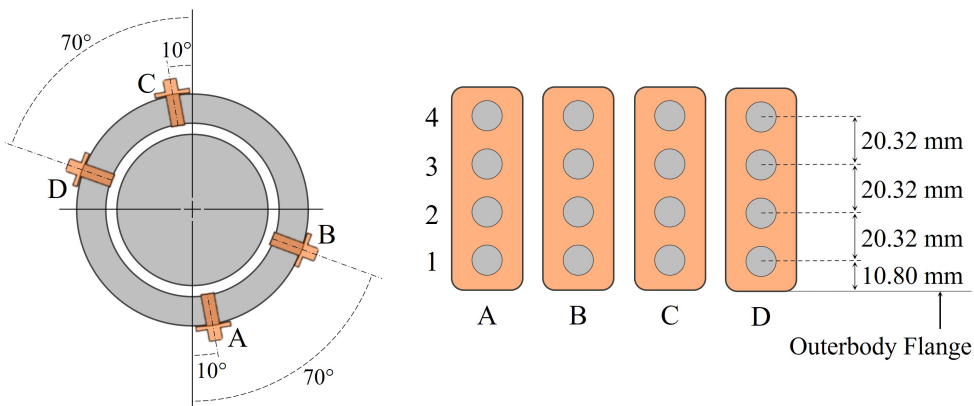


**Figure 2.3:** Nomenclature of NETL RDE instrumentation ports

the detonation wave speed. However, this commonly used methodology for defining wave speed relies on approximating the number of waves that are present in the combustor as well as their direction of rotation. An example of the PSD for dynamic pressure measured 10 mm downstream of the injection plane is shown in Figure 2.4. The dominant frequency is defined by the maximum peak amplitude (energy per frequency) with lesser peaks associated with additional periodic content or harmonics of the dominant mode. For the example shown in Figure 2.4, the dominant frequency is determined to be 7.1 kHz. The theoretical Chapman-Jouguet (CJ) wave frequency for the test RDE at the experimental conditions is found to be 4.45 Hz using the SDToolbox<sup>91</sup> and Cantera<sup>92</sup>. As the theoretical CJ frequency is less than the measured dominant frequency, it is assumed that there are multiple waves present in the combustor. Individual waves in the combustor typically operate at approximately 80%  $U_{CJ}$ , suggesting a two-wave frequency of 3.55 kHz. Quantifying the wave speed and number provides a comparison for later methods based solely on image analysis that do not rely on underlying assumptions such as theoretical CJ wave speed.

Although the uncooled NETL RDE does not achieve run times as extensive as the water cooled facility outlined in the next section, test durations of 6 to 10 seconds still exceed

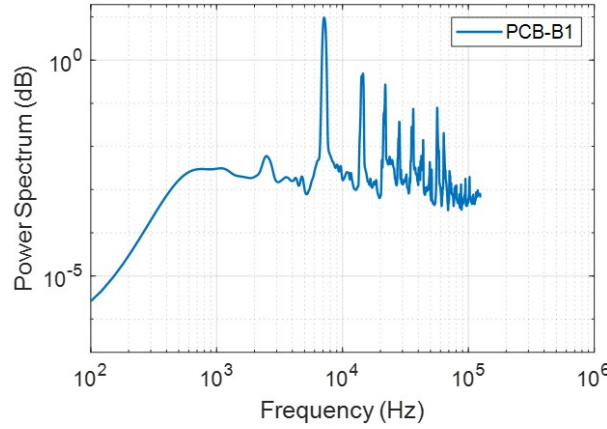


**Figure 2.4:** Power spectrum for dynamic pressure (measured with ITP) at port B<sub>1</sub>, 10 mm downstream of injection plane

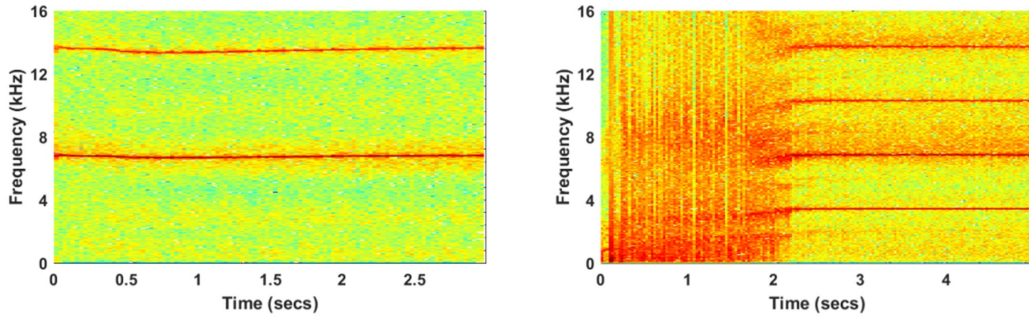


**Figure 2.5:** Example spectrograms for filtered dynamic pressure (measured with ITP) at port C<sub>1</sub>, 10 mm downstream of injection plane showing (left) stable 2-wave operation and (right) delayed ignition after 2 secs followed by stable detonation

capabilities of many RDEs studied elsewhere in the PGC community. A method more applicable across extended run times is through calculation of a spectrogram, which visualizes the varying frequencies of a signal through time. Compared to Figure 2.4 which is indicative of average behavior, the spectrogram displays modal variation at smaller timesteps across the entire operational window. Two example spectrograms are plotted in Figure 2.5, where the first depicts a steady 2-wave case with no mode changes, and the second indicates an issue with delayed ignition just after 2 seconds and subsequent detonation.

In order to study detonation behaviors more representative of future turbine applications reaching thermal equilibrium, a new water-cooled arrangement enables longer run times reaching approximately 30 seconds.

## 2.2 NETL WATER-COOLED RDE

A portion of data for this study was collected from experiments conducted in the water-cooled, ducted-exhaust RDE which is fully integrated within the LECTR facility at NETL Morgantown. A graphic of the experimental rig is shown in Figure 2.6, and a cross-section in Figure 2.7. The detonation channel, which is outlined in black in Figure 2.7, is further detailed in Figure 2.8. Because Figure 2.7 is densely detailed, limiting dimension text resolution, the water-cooled cross-section is also plotted in larger proportion in Appendix A. Water-cooling of the RDE along with a portion of the exhaust permits operating the system for an indefinite period of time at fuel-lean conditions. Test duration is typically limited to 20 to 30 seconds in order to conserve fuel. This is sufficient to bring the combustor to a thermally stable state, as determined by the cooling water reaching a steady temperature, although material temperatures of the exhaust downstream of the RDE continue to rise throughout the test, causing a continued increase in exhaust pressure above the combined pre-combustion setpoint and pressure as a result of sustained detonation. The combination of ducted exhaust and backpressure control valve allows the pre-combustion pressure to be regulated in the exhaust at pressures ranging from ambient to 20 bar.

The exhaust duct immediately following the RDE has an internal diameter of 154 mm and is water-cooled for a length of approximately 3.8 m. Here water-cooling gives way to a refractory-lined duct with an increase in diameter to 273 mm for approximately 1 m through the sampling cross. At the exit of the cross, the refractory-lined duct increases in diameter

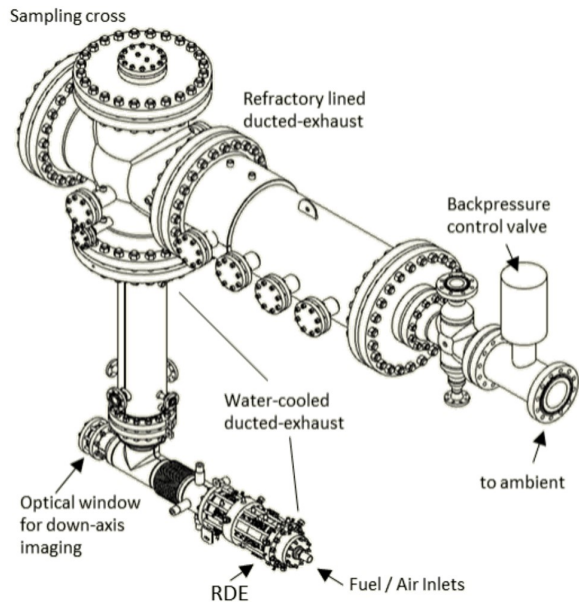


**Figure 2.6:** High-pressure, water-cooled, ducted-exhaust RDE at NETL

to 431 mm for approximately 1.84 m before gradually decreasing in diameter to 216 mm. The exhaust flow passes through a secondary cross, which permits fine tuning of the system backpressure (valve not shown), before encountering the primary back-pressure control valve (Valtek Mark One globe control valve), which is located approximately 7 m downstream from the RDE exit. The valve provides a means of simulating downstream loads from components such as a turbine, as well as controlling pre-combustion pressure in the RDE combustion channel independent of the RDE exit nozzle<sup>25,50</sup>. Downstream of the primary control valve the flow continues through pipe of length 216 mm before passing through an exhaust muffler, irrelevant of back-pressure, before leaving to the atmosphere.

The 119.5 mm long RDE utilizes an axial air injection configuration with an injection area,  $A_{3.1}$ , of 16.23 cm<sup>2</sup>, an outer diameter of 149 mm, and a combustion channel width of 10 mm, resulting in a ratio of injector area to channel area ( $A_{3.1}/A_{3.2}$ ) of 0.37. At the end of the combustor is an exit nozzle, choking the flow by applying additional pressure in

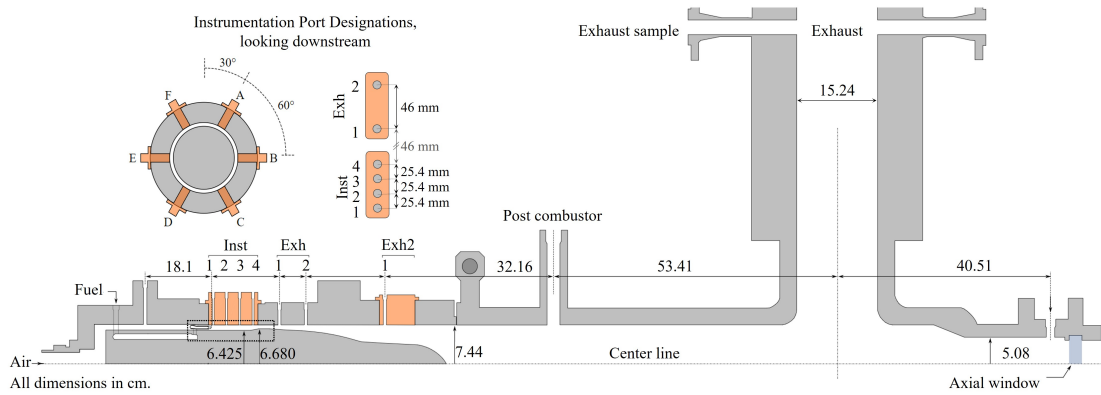


**Figure 2.7:** Cross-section water-cooled RDE showing axial injection, sampling port circumferential and axial nomenclature, exit nozzle, and downstream diffuser. Box indicates boundary for Figure 2.8

the combustion channel independent of the backpressure control valve. The exit nozzle has a minimum area of  $33.8 \text{ cm}^2$ , creating an exit area to channel area ratio ( $A_8/A_{3.2}$ ) of 0.76. Immediately downstream of the exit nozzle is an exhaust diffuser whose purpose is to slow the flow from the RDE to a hypothetical turbine inlet. Additional details on the diffuser are not provided as its influence is not significant to this study, although it was installed while testing. Hydrogen fuel is injected through 120 evenly spaced jets on both sides of the air inlet, totaling 240 jets, located just downstream of the air inlet throat where the cross-sectional area is minimal. Each jet has a diameter of 0.75 mm offering a total fuel injection area of  $1.06 \text{ cm}^2$ .

Four sample ports, designated Inst. 1 through 4, are located along the length of the RDE, and two sample ports just downstream of the RDE exhaust, designated Exh. 1 and 2, are positioned at six circumferential locations, A through F, as shown in the upper-left portion of Figure 2.7. A detailed view of the detonation channel is shown in Figure 2.8. These sample ports are used for both Infinite Tube Pressure (ITP – PCB model CA102Bo6) and Capillary Tube Averaged Pressure (CTAP – Omega PX309-100G5V), as well as ion probe data and

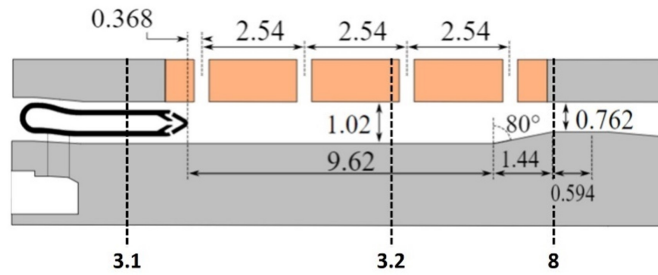


**Figure 2.8:** Profile view of axial air injection, combustion channel and exit nozzle with station designations at the air injector throat (3.1), combustion channel gap (3.2) and exit nozzle throat (8)<sup>93</sup>

band-pass OH\* chemiluminescence. Specific locations of parameters relevant to each portion of the outlined work are detailed in their respective chapters.

Combustion air is provided by an on-site compressor capable of providing a maximum flow of 1 kg/sec at a pressure of 1.4 MPa. A separate natural gas-fired air heater (1.17 MW<sub>th</sub>) can heat the air to a maximum of 600 K, although excessive heating reduces the allowable run times due to limits on vessel temperatures. The RDE is fueled by hydrogen or mixtures of natural gas and hydrogen, which are available at maximum flow rates of 55 g/s and 13 g/s, respectively. All gas flows are metered individually by Coriolis meters located approximately 3 meters upstream of the RDE inlet. Although the Coriolis meters are not capable of measuring the dynamic response of the flow at the RDE injector, they do provide an accurate (< 0.5%) measure of the flow, sampled at 5 kHz. A natural gas-air burner is located approximately 0.5 m downstream from the exit of the RDE to prevent a combustible mixture accumulating in the exhaust duct during start-up or in the event of blow-out in the combustor. This burner also provides ignition of the RDE, as opposed to a commonly used detonation tube whose exit is located just downstream of the injectors, as the combustion wave quickly transitions to detonation for the conditions considered in this study. Control of the facilities is provided through an Allen Bradley (AB) control system while high-speed data acquisition is

performed by a National Instruments PXIE 1082 chassis with multiple analog input/output cards using a custom National Instruments LabView program. The AB records facility operating conditions at a sampling rate of 1 Hz, while the NI hardware samples at rates ranging from 5kHz to 1 MHz depending upon the desired signal.

Air mass flow rate	0.52-0.7 kg/sec
Equiv. Ratio	0.5 - 0.9
Pressure (Pre-Combustion)	0 - 310 kPa
Temperature (Inlet Air)	340 - 480 K

**Table 2.1:** RDE operating conditions utilized for TSC study

The accompanying objective throughout the manuscript is to collect data at as many wave modes as permitted by the RDE. To accommodate this requirement, a range of operating conditions, detailed in Table 2.1, were tested across multiple RDE configurations, summarized in Table 2.2. The dataset includes data from both radial AFRL-style, and axial pindle/"sting" injectors<sup>94</sup>, both depicted in Figure 2.9. The "Sting" injector configuration permits axial air flow along both sides of the injector with fuel injection occurring through 120 rearward-facing angled orifices on each side of the sting injector tip, each with a diameter of 0.75 mm. Tests with the radial injector geometry included variable air injector areas as outlined in Table 2.2. Station designations as defined by Brophy et al.<sup>93</sup> are illustrated in Figure 2.8 for the axial air injection RDE used in this study. The radial air injection RDE has similar station designations. These stations provide convenient reference locations for area ratio comparisons including an air injection area to combustor channel area ( $A_{3,1}/A_{3,2}$ ) and nozzle exit area to combustor channel area ( $A_8/A_{3,2}$ ).

Delineations of RDE geometric parameters are not present throughout the manuscript, as each dataset encompasses varying degrees of parameter variety in order to train a network which is agnostic to the RDE configuration. In other words, the purpose of including data

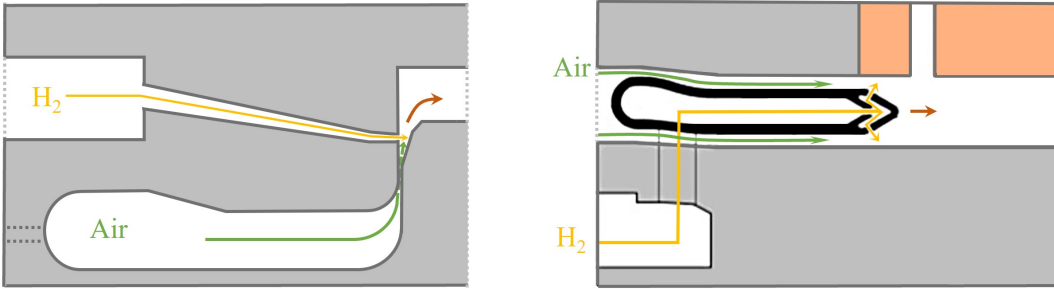


**Figure 2.9:** Radial (left) and axial (right) air injectors utilized in this study. Radial injector geometry was also changed as per Table 2.2

Combustor	RDE Diameter inner/outer (mm)	Combustor Gap Size (mm)	Air Injector Area (mm <sup>2</sup> )	$A_{3,1}/A_{3,2}$	$A_8/A_{3,2}$
<b>AFRL-1</b>	134/149	7.5	306	0.1	1
<b>AFRL-2</b>	134/149	7.5	679	0.2	1
<b>AFRL-3</b>	134/149	7.5	1086	0.33	1
<b>String Inlet</b>	129/149	10	1623	0.37	0.76

$A_{3,0}$  = Fuel inlet area,  $A_{3,1}$  = Air inlet area,  $A_{3,2}$  = Combustor annulus area,  $A_8$  = Exit nozzle area

**Table 2.2:** Geometric variations of the RDE utilized for TSC study

across a variety of combustor geometries, gap widths, and injector schemes is to create CNNs which generalize experimental data well beyond low level features influenced by such physical changes.

### 2.3 IMAGE ACQUISITION AND REAL-TIME ADAPTATION

Due to the progress in high frame rate digital cameras and data storage capacities, high-speed imaging has become a widely applied and valuable means of combustion diagnostics<sup>95</sup>. Moreover, high-speed imaging explores behaviors and measurements within timescales which were previously too brief to consider. Application of high-speed imaging has enabled a wealth of new understanding across many combustion topics such as deflagration-to-detonation transition<sup>96</sup>, turbulent boundary layers<sup>97</sup>, jet flow mixture fractions<sup>98</sup>, and many others.

Non-intrusive combustion diagnostic techniques, including laser-integrated high speed imaging in more optically accessible or simplistic combustion devices compared to the current study, are often associated with high costs and added experimental complexities due to the use of high repetition rate lasers, flow seeding, and other factors. To avoid some of these issues, a simpler method which still provides insights on burning conditions termed chemiluminescence<sup>99</sup> is employed throughout the study. Flame chemiluminescence imaging is a longstanding combustion diagnostic technique in which the radiation emitted by excited radicals within the combustion reaction zone is captured. To do so, hydrogen or carbon-based flames are imaged via bandpass filtering around narrow spectrum emittance bands uniquely associated with targeted species such as OH\* and CH\*, with primary wavelengths of 310 and 435 nm respectively.

The specific strength of high speed chemiluminescence applied to the current research is rooted in the primary presence of the OH\* radical within the hydrogen-air flame. Unlike combustion of hydrocarbon-air mixtures, which present an abundance of multiple excited radicals (OH\*, CH\* and C<sub>2</sub>\* ) across the near-UV and visible spectra<sup>99</sup>, hydrogen-air flames can be characterized in the absence of a carbon-based fuel by OH\*, the major intermediate species present. Emission spectrums at the detonation plane dominated by OH\* have been measured experimentally<sup>100</sup> and computed<sup>101</sup> across a range of operating conditions, centered at approximately 310 nm. In addition to the insights produced throughout the current work, high speed OH\* chemiluminescence images have been used throughout the RDE community to study acoustic/detonative modes<sup>102</sup>, heat release distributions<sup>103</sup>, injection backflow and recovery<sup>104</sup>, and a host of additional detonation interactions<sup>105,106,107</sup>.

In order to capture chemiluminescence images, imaging components with appropriate transmission and responses must be paired. Images presented or leveraged throughout the

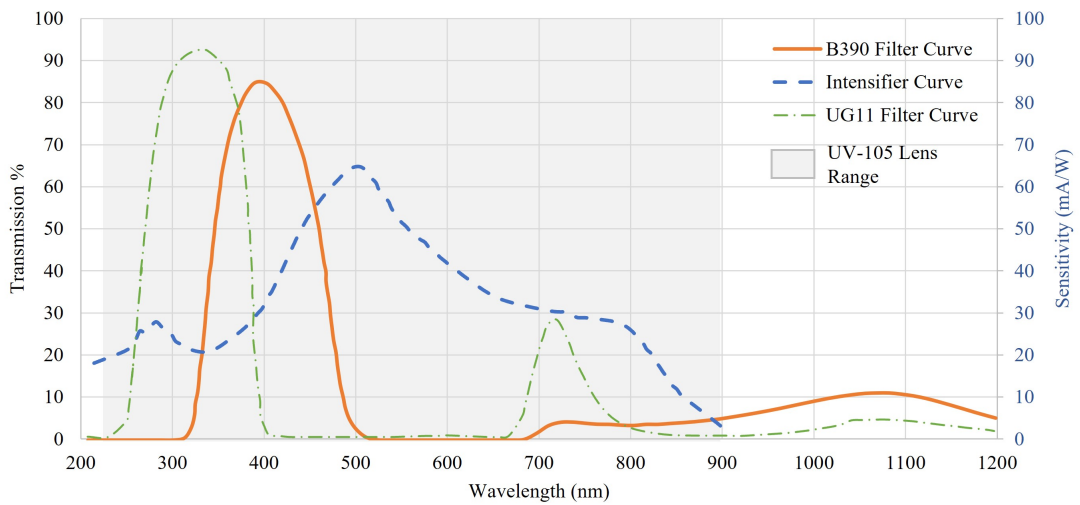


**Figure 2.10:** Transmission and response curves for individual components of high-speed imaging setup<sup>108,109,110</sup>

manuscript, excluding those plotted in Chapter 5, are captured using a Photron FASTCAM SAZ high-speed digital camera. Images throughout Chapter 5 are acquired using a low-speed camera within the real-time acquisition arrangement, which is detailed in the following section. Both camera types are used in conjunction with an Invisible Vision UVi 2550-10-S25 intensifier, a Nikkor UV-105mm lens and a bandpass filter. The bandpass filter corresponds to either a UG11 filter with a center wavelength of 325 nm, and full width-half max (FWHM) of 110 nm, or a B390 filter with a center wavelength of 390 nm and FWHM of 125 nm. Response curves and ranges for the UV-105 lens, UVi intensifier, and bandpass filters are plotted in Figure 2.10.

All images reported throughout the manuscript are down-axis images. A fused quartz window is located approximately one meter downstream of the RDE exit just past a 90° elbow in the main exhaust duct to permit imaging of the detonation wave. Viewport diameters are 50mm and 90mm for the uncooled and water-cooled RDEs, respectively. To protect the camera in the event of potential viewport glass failure, the camera equipment is not aligned

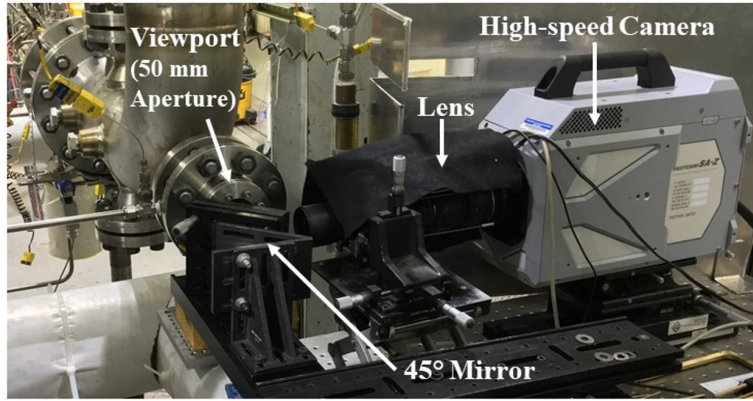


**Figure 2.11:** Rotating Detonation Engine test facility with camera integration at NETL

with the RDE center axis. Instead, as shown in Figure 2.11, a mirror fixed at  $45^\circ$  reflects an image to the camera, which is mounted perpendicular to the RDE. Images acquired for the uncooled RDE are captured at 50,000 frames per second (fps) with a resolution of 600x640 pixels. Because only a portion of the frame is filled with the RDE geometry, the annulus is captured with a represented resolution of 301x301 pixels. In an effort to increase both time and pixel resolution, images of the water-cooled RDE are captured at 60,000 fps a resolution of 512 x 512 pixels, and an annulus represented resolution of 501x501 pixels.

Detonation waves appear as high intensity regions within the image and are constrained by the annular gap within the RDE. The number and direction of detonation waves present in the annulus of an RDE is referred to as the mode. Possible modes commonly seen in RDEs include one or multiple waves traveling in the same rotational direction, either clockwise (CW) or counterclockwise (CCW), as well as counter-rotational (CR) and longitudinal pulse behavior.

Throughout the text, a common naming convention will be used when referring to a specific mode, in which the wave quantity is directly followed by the wave direction. For example, when three counterclockwise detonation waves are present, the proper label is 3CCW.

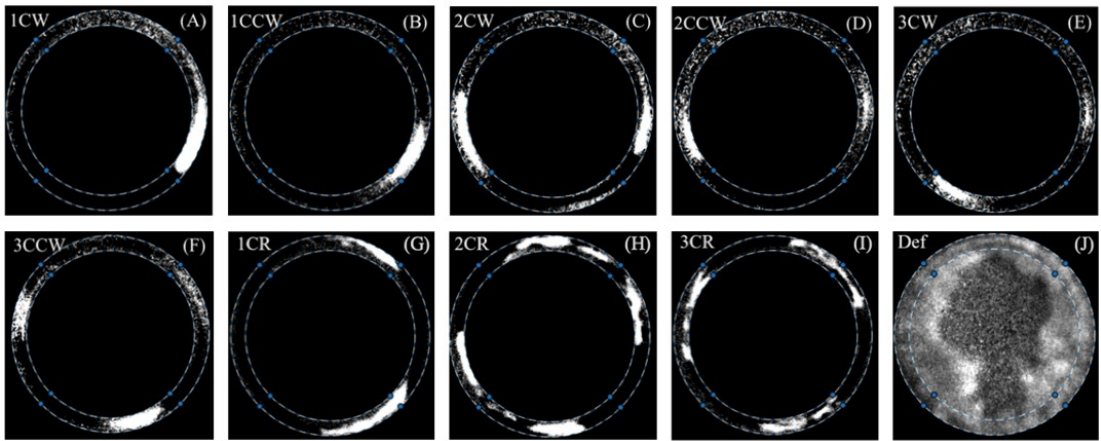


**Figure 2.12:** Examples of successfully classified modes by CNN in Chapter 4

An exception of deflagration, where no discernable detonation waves are formed, is referred to simply as Def. Modes considered at length in this text include wave multiples from 1 to 7 waves, co-rotational and counter-rotation, and Def. Specific modes considered in each portion of the study are specified in each respective chapter. Example images of co-rotational modes with 1, 2, and 3 waves is shown alongside a deflagrative mode in Figure 2.12 with the annular gap overlaid for visual reference.

It should be noted that pixel intensities of the detonation waves in Figure 2.12 are scaled, and the noise filtered to improve human readability of the figure. Even with scaling, it is apparent that variations exist in the pixel intensity, such that as the total number of waves increases, overall pixel intensities decrease. This is due in part to a reduced fill height and a subsequent lesser volume of reactants available for each wave. An additional hindrance to wave visibility that occurs in the upper portion of the annulus.

Images in Figure 2.12 were captured on the uncooled RDE. In the specific experimental setup of the uncooled RDE, a protruding weld interferes with a portion of the imaging region of interest. Specifically, due to a protruding weld in the exhaust section of the RDE, the downstream view of the upper portion of the annulus is obstructed. Therefore, a portion of

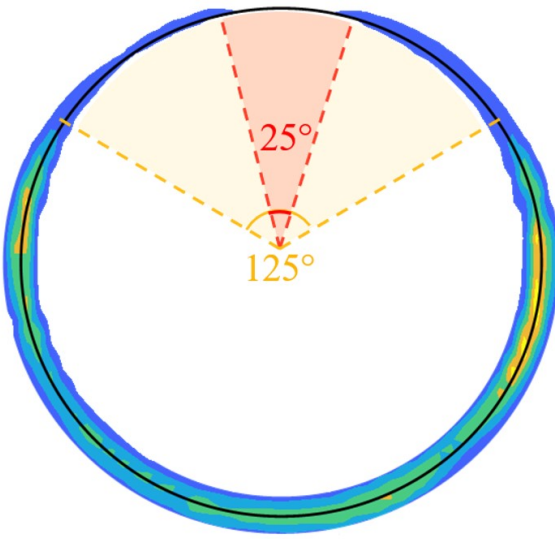


**Figure 2.13:** Contour of maximum Fourier coefficients of local pixel intensities throughout 100 images with annulus center radius overlaid as black line

the annulus is consistently represented by lower pixel intensities. This behavior is represented in Figure 2.13, which displays a contour of the maximum Fourier coefficient at each pixel region throughout a sample of 100 frames. Approximately  $25^\circ$  of the upper portion of the annulus will not be visible while an additional  $50^\circ$  in each upper quadrant is only partially visible. The view obstruction is not present in the water-cooled RDE.

However, even when a wave is out of view, the radial spacing of waves can be used to infer the presence of a wave occupying the annulus space not visible to the down-axis camera. Specifically, multiple waves are spaced somewhat evenly around the annulus circumference. For example, Figure 2.12(E) shows an image where three waves are present, but only two are visible. Because the two visible waves are spaced at approximately  $120^\circ$ , instead of a  $180^\circ$  spacing expected of a two-wave mode, the third wave's presence is known. This concept is leveraged during image processing and while performing manual classification of data sets. In cases of galloping, where wave separation oscillates around an even spacing through time,

extremely non-uniform wave spacing may complicate manual classification if two waves are tightly grouped in the obstructed portion of the down-axis view. However, in galloping modes analyzed to date at NETL, wave spacing typically oscillates within a  $\pm 10^\circ$  window around the uniformly spaced location. This implies that 10 co-rotational waves would need to be present in the annulus before two waves could be simultaneously obstructed in the  $25^\circ$  weld region.

While human detection of detonation waves quantities among images in Figure 2.12 may be innately simple, discerning wave direction is much more difficult. Unlike other RDE image processing methods which use a collection of sequential images offering time dependencies, the application of machine learning for image classification and object detection aims to draw conclusions from a single image. Although differences in some images depicting CW and CCW behavior are not obvious, detonation waves present themselves with distinct luminosity profiles which clearly suggest angular direction. These profiles are most clearly seen when only one detonation wave is present in either direction, as shown in Figure 2.14A and Figure 2.14C.

To further acknowledge the profile differences of each wave direction, pixel intensities along the center radius of the annulus are plotted against azimuthal location in Figure 2.14B and Figure 2.14D. Intensity profiles for each rotational direction are similar in structure, but profile characteristics occur in a reversed order along the azimuthal path, indicating opposite directions. In both instances, an abrupt spike in intensity caused by the blunt face of the detonation front is followed by a slow decay caused by the trailing profile. Although the general features are similar across waves, the appearance of waves throughout various operational periods, even a constant wave number, will vary due to wave strength, chemiluminescent emission intensity, local equivalence ratio and many other factors. As an example,

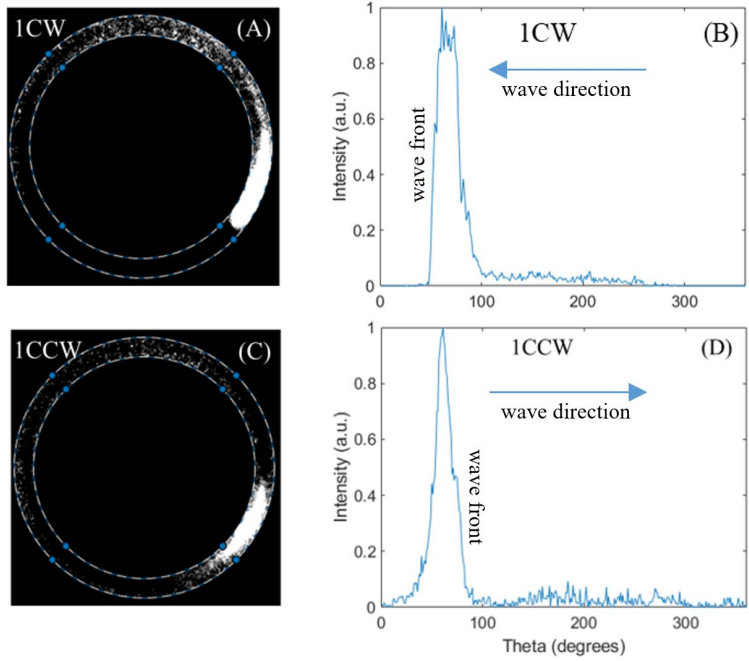


**Figure 2.14:** Downstream images of modes (A) 1CW and (C) 1CCW, paired with pixel intensity along center radius of annulus plotted against theta for (B) 1CW and (D) 1CCW

Figure 2.14 shows two similar wave modes, but the CW wavefront is not as clearly defined as the CCW wavefront, due to varying operating conditions. The ability to discern these subtle differences across images by analyzing both low- and high-level features is the strength and goal of the applied neural networks.

It is important to note that the intensity trends plotted in Figure 2.14 (B) and (D) are not utilized in any of the upcoming methodologies. Instead, the profile variations simply suggest the existence of differing wave profile features, which will foster feature extraction performed by each proposed CNN.

### 2.3.1 REAL-TIME DATA ACQUISITION

Imaging of the RDE annulus is typically performed with the high-speed Photron FASTCAM SAZ camera at 50 or 60 kfps in conjunction with the intensifier, UV lens, and bandpass fil-

ter, as detailed in the previous subsection. High-speed images are utilized throughout the work to create labeled datasets with modal certainty for image classification, object detection, and time series classification CNN training. In order to adopt the trained image classification network for real-time RDE monitoring capabilities which are outlined in Chapter 5, a real-time data acquisition framework is defined. For the real-time test series, the Photron camera is replaced with a 10-bit Basler Ace acA640-750um area scan camera with a maximum resolution of 640 x 480 pixels. The camera is connected to an Invisible Vision UVi 2550-10-S25 intensifier, a Nikkor UV-105mm lens and a 390 nm bandpass filter with a full width-half maximum of 125 nm to primarily limit observation to OH\* chemiluminescence that dominates the combustion wave. The intensifier amplifies the low-intensity information transmitted through the bandpass filer, and regulates gate width. Although the camera has a maximum frame rate of 751 fps, the camera is triggered intermittently at each diagnostic iteration. Within the broad exposure time of the low-speed camera, around 1.3 msec, the detonation wave makes multiple passes around the annulus, which would result in an image offering no valuable insights of instantaneous wave shape or location. In order to prevent such smearing of the detonation wave, images are improved by an intensifier gate width limited to 12  $\mu$ s, essentially "freezing" the wave within a timescale comparable to that of image at high-speed images acquired with the Photron SA-Z camera. Within this exposure time, a wave traveling at 1,800 m/sec travels 21.6 mm. This is not an insignificant distance, but provides the wave profile of interest in both intermittently triggered and high-speed images. A similar gate width across framerates and imaging arrangements ensures similarity across image sets.

The experimental configuration of the water-cooled RDE permits the installation of a variety of transducers with data sampling rates of 1.25 Hz (very slow-speed), 5 kHz (slow-speed),

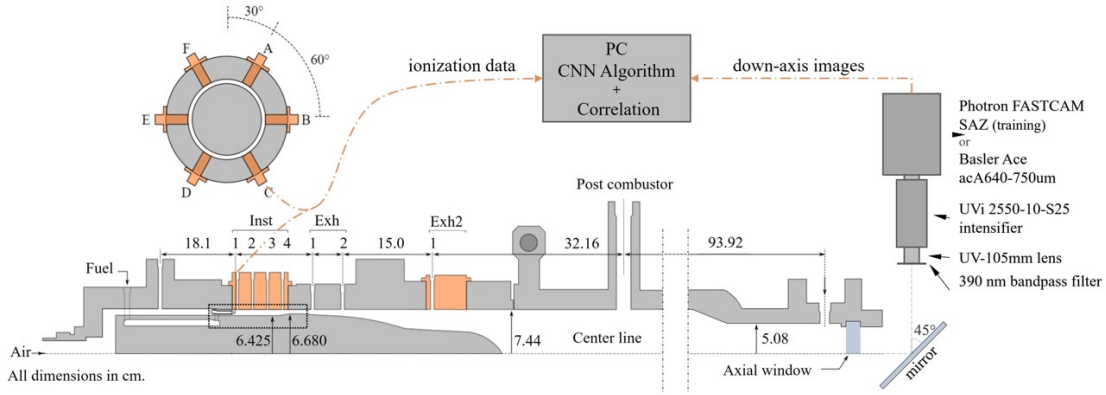


**Figure 2.15:** Cross-section water-cooled RDE showing axial injection, sampling port nomenclature, exit nozzle, downstream diffuser, camera alignment, and data acquisition setup. Box indicates boundary for Figure 2.8

250 kHz (mid-speed) and 1 MHz (high-speed). Relevant to this study is the use of an ion probe to measure ionization current, sampled at 250 kHz, centered approximately 4 mm downstream of the tip of the axial air injector, permitting sampling within the detonation wave. Output from the ion probe, measuring chemi-ionization from the detonation wave, is acquired using a National Instruments cDAQ-9188 chassis and NI 9223 module which is independent from the primary data acquisition performed with a NI PXIe-1082DC chassis and NI PXIe-8880 controller along with a series of NI analog input modules. Arrangement of ionization time series and image collection needed for real-time monitoring, fed to the CNN and correlation algorithm is depicted in Figure 2.15. Figure 2.15 closely resembles Figure 2.7, with an abbreviation of the exhaust section to allow for the depiction of the imaging equipment downstream of the axial window. A larger depiction of Figure 2.15 is included in Appendix A for enhanced dimension resolution.

Image and ion data collection is triggered and performed using the Basler Pylon<sup>111</sup> and PyDAQmx<sup>112</sup> libraries, respectively, within a Python environment throughout RDE operational windows. The current study relies on the partially modified experimental setup,



**Figure 2.16:** Basler Ace acA640-750um area scan camera (left), and National Instruments cDAQ-9188 chassis (right) utilized for live data acquisition

but intends to develop a monitoring technique feasible for ongoing studies and future adaptations for active control using instrumentation widely available within the existing experimental water-cooled RDE facilities. While instrumentation schemes of production engines remain unclear, the current structure of high-speed data fed to machine learning algorithms is expected to remain applicable throughout industrial integration of RDE technology. Hardware added to the experimental setup to allow live data acquisition is shown in Figure 2.16.

#### 2.4 IMAGE TREATMENT

Because annulus representation in high-speed images is not perfectly uniform across frame rates, experimental setups, or realignment efforts, a standardized image treatment process is necessary. The steps outlined below are similar in nature to the image treatment process outlined by Bennewitz et al.<sup>113</sup>, where raw images are corrected with a Beta factor, a Cartesian mesh is generated to determine integrated pixel intensities, and a Taubin fit used to locate the annulus geometry for later polar conversion. The current method does not immediately filter images due to the higher proportion of surrounding pixels to annulus pixels in some configurations. Instead, an uncropped raw image stack of 100 images,  $p_k$ , defined in Equation 2.1

is used throughout the annulus detection and cropping steps, and filtering is conducted as a final step.

$$p_k = p_k(x, y, n) \quad (2.1)$$

A Cartesian mesh of the image space is defined using Equations 2.2 and 2.3, specifying no pixel overlap across cells. An example mesh grid is overlaid on a raw image in Figure 2.17(a). In this particular example which analyzes images captured at 50fps and a resolution of 600x640 pixels, cell dimensions  $\Delta x$  and  $\Delta y$  are globally set to 6 pixels. The determination of appropriate cell dimensions typically scales with pixel width, where smaller values result in finer Taubin center approximations at higher computational costs, but larger values distort the inner and outer annulus perimeters.

$$(x_1, x_2) = ((i - 1)\Delta x, i\Delta x) \quad (2.2)$$

$$(y_1, y_2) = ((j - 1)\Delta y, j\Delta y) \quad (2.3)$$

Once the mesh is determined, Equation 2.4 is used to calculate the integrated pixel intensity,  $I$ , within each cell at indexed location  $(i, j)$  in image  $(n)$ . Specifically, a trapezoidal numerical integration function is applied to individual two-dimensional cell matrices extracted from raw image  $p_k(:, :, n)$ . Once evaluated across each cell, integrated pixel intensities can be plotted for each image in the stack, with reduced dimensions proportional to the cell dimensions, as is illustrated in Figure 2.17(b). The pixel intensity stack is a three-dimensional matrix, where the value of a single cell can be tracked through time, as vector  $I(:, :, n)$ . An illustration of a cell value time series is shown in Figure 2.17(b).

$$I(i,j,n) = \int_{y_1}^{y_2} \int_{x_1}^{x_2} p_k(x,y,n) dx dy \quad (2.4)$$

Maximum Fourier amplitudes are calculated for each cell time series to generate a single annulus representation, as is shown in Figure 2.17(c). The top 50 to 100 cells from the final two-dimensional matrix is fed to the Taubin circle fit<sup>114,115</sup> to estimate the annulus center coordinates and Taubin radius. The image stack is then cropped before undergoing Beta-factor correction. Many studies conduct this procedure for defined image intervals, which may be a portion of an image collection across a single run to account for camera movement from vibrations. Within the experimental setup of both NETL RDEs, the camera is fixed to an independent optical table downstream of the ducted exhaust, and does not experience alignment issues often associated with cameras positioned downstream of ambient-exhausting RDEs. Therefore, annulus location steps outlined in Figure 2.17(a)-(b) are conducted only once for a collection of images absent of camera alterations, typically throughout a day of operation or 20 to 30 20-second runs. Annulus center coordinates and Taubin radius are stored and applied across the similar images to reduce post-processing times.

The steps outlined in Figure 2.17(a) through (c) and Equations 2.2 to 2.4 may be bypassed in some scenarios by calculating an average image to replace the maximum Fourier amplitude matrix. However, if any pixels are consistently illuminated by other experimental bodies, the Taubin fit will become skewed. Images acquired from the water-cooled NETL RDE often capture a heated thermocouple emitting broadband radiation in later runs. Although the thermocouple is present in all images, the maximum Fourier amplitude is minimal and does not influence the Taubin fit, reinforcing the benefits of a standard image treatment process which is sufficiently capable across varying imaging issues.

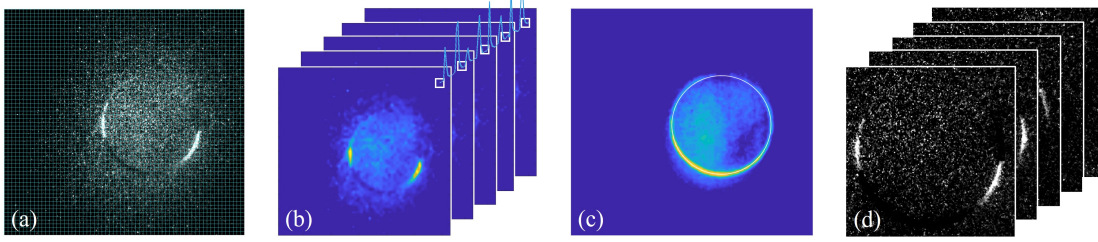


**Figure 2.17:** Standardized Image Treatment: (a) raw image with Cartesian grid overlaid; (b) stack of Cartesian cell integrated pixel intensities,  $I(i,j,n)$ , with pixel trace illustrated; (c) maximum Fourier amplitudes of Cartesian cells with Taubin fit circle overlaid; (d) corrected image stack

A cropped image stack may now be filtered using the AFRL Beta correction factor<sup>113</sup> by first determining an average image,  $\bar{p}_k$ , across  $N_k$  images using Equation 2.5. The Beta factor scalar for image ( $n$ ),  $\beta_n$ , is defined in Equation 2.6 as a ratio of the average image pixel summation to the image stack pixel summation. The corrected image stack,  $p_{k,corr}$ , is created by scaling each image ( $n$ ) by its respective beta factor, and subtracting the average image, according to Equation 2.5. A corrected image stack is shown in Figure 2.17.

$$\bar{p}_k = \frac{1}{N_k} \sum_{n=1}^{N_k} p_k(x,y,n) \quad (2.5)$$

$$\beta_n = \frac{\sum_{x,y} \bar{p}_k(x,y)}{\sum_{x,y} p_k(x,y,n)} \quad (2.6)$$

$$p_{k,corr}(x,y,n) = \beta_n p_k(x,y,n) - \bar{p}_k(x,y) \quad (2.7)$$

The standardized image treatment process is the baseline treatment for all images shown and inspected throughout the current work. Individual applications, such as conventional methods outlined in Chapter 3 or unique CNN datasets such as those in Chapters 4 and 6,

make additional alterations according to the needs and strengths of each particular method, but all begin with the canon method as an initial step.

It is worth noting that this filtering process can not be executed for a single image. For generation of detonation surface plots or ground truth datasets, this is not an issue. However, real-time image classification, the subject matter of Chapter 5, requires capture and probing of individual images captured throughout the RDE operational period. For that particular case, where a CNN was trained on Beta factor-corrected images, an average image from a previous but similar run may be used to produce an image mask. Alternatively, standard filtering and contrast adjustments determined by comparison can be sufficient for neural network inference.

#### 2.4.1 YOLO IMAGE TREATMENT

To prepare the image set for training, raw images are pre-processed identically according to the method outlined in the previous section. An example raw image is shown in Figure 2.18(a). A short series of images are first used to generate an average image, shown in Figure 2.18(b). From the distribution of pixel intensities in the average image, a Taubin fit is used to algebraically fit a circle to the data<sup>115</sup>. The circle is inherently associated with the mean radius of the RDE annulus and is used to crop each image to a reduced size of 301x301 pixels centered about the annulus. Once cropped, each image is multiplied piecewise by a scaled, noise reduction matrix,  $\Psi$ , to reduce pixel magnitudes outside of the area of interest. The noise reduction matrix is created using Equation 2.8 in polar coordinates, where  $r_{Taub}$  is the annulus radius found using the Taubin fit and  $\Delta$  is the annulus gap width in pixels. For the current image set,  $r_{Taub}$  and  $\Delta$  were found to be 130 and 20 pixels, respectively. The contour of the resultant noise reduction matrix,  $\Psi$ , is shown in Figure 2.18(c).

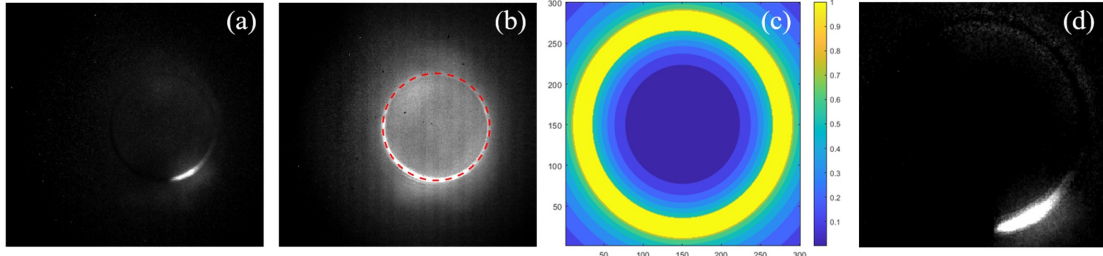


**Figure 2.18:** Image treatment process: (a) an example raw image, (b) an average image with Taubin fit circle overlaid, (c) Noise Reduction Matrix ( $\Psi$ ) contour plot, and (d) the final cropped and filtered example image

$$\Psi(r, \theta) = \begin{cases} \left(\frac{r}{r_{\text{Taub}}}\right), & r \leq r_{\text{Taub}} - \frac{\Delta}{2} \\ \left(\frac{r_{\text{Taub}}}{r}\right), & r \geq r_{\text{Taub}} + \frac{\Delta}{2} \\ 1, & r_{\text{Taub}} - \frac{\Delta}{2} < r < r_{\text{Taub}} + \frac{\Delta}{2} \end{cases} \quad (2.8)$$

Once pixel intensities have been reduced outside the region of interest, images are filtered with a basic contrast adjustment which linearly maps pixel intensities such that the lowest and highest 1% of all pixel values are saturated. The resultant filtered example image is shown in Figure 2.18(d). Each step of the outlined image treatment process requires minimal computational effort. However, this treatment sufficiently prepares each image for feature extraction within the neural network.

#### 2.4.2 YOLO LINEARIZED IMAGE TREATMENT

A secondary image style is created to address annotation uncertainties associated with the YOLO network output and successive velocity calculations. Linearized images attempt to "unwrap" RDE annulus region to a rectangular collection of pixel intensity data to reduce total pixel volume and eliminate unrelated pixels such as those representing the RDE centerbody. Construction of linearized images does not involve any mathematical operations to

alter pixel values, but instead rearranges pixels according to Equation 2.9, where  $i$  and  $j$  are iterated values,  $\Delta r$  and  $\Delta\theta$  are set increments of radial and azimuthal locations, and  $r_{in}$  is the inner radius pixel value. Values from the square image stack,  $p_{k,corr}(x, y, n)$  from Eqation 2.7, are rearranged to form the linearized image stack  $L(\theta, r, n)$ . For the specific application to the YOLO dataset, Equation 2.9 converts square RDE images which are sized 301x301 pixels to a new size of 32x736 pixels. In order to create the linearized images, pixels are extracted at radius locations spanning  $\pm 16$  pixels from the annulus radius, stated previously as 130 pixels, and at 736 azimuthal locations, as described in Equation 2.10. Those locations correspond to radial angular spacing values specified in Equation 2.11. An example image is displayed with azimuthal lines overlaid in Figure 2.19, zoomed to the lower-right quadrant to visualize the heavily condensed azimuthal lines. By stacking the pixels along each line, shown in cyan, the annulus is “unwrapped” to a resultant format with x- and y-axes corresponding to  $\theta$  and  $(\hat{r}_i - r_{in})$ , respectively. Coordinates calculated by sine and cosine functions within Equation 2.9 result in non-integer indices, which cannot be accomdated by the image matrix. Therefore, endpoints of azimuthal lines are assigned to pixels nearest to the exact coordinates, resulting in the uneven pacing of azimuthal lines in Figure 2.19. An alternative solution to the non-integer indices would be interpolation. However, selection of nearest pixels is more computationally efficient, better fitting the objective of the body of work. Trade offs associated with pixel loss and image dimension are discussed in Section 6.4. The example quadrant is linearized in the lower portion of Figure 2.19. A reiteration of Figure 2.19 is presented in Section 6.4 with the additional illustration of bounding box translation.

$$L(\theta, \hat{r}_i, n) = L(i, j, n) = p_{k,corr}([(j \Delta r + r_{in}) \cos(i \Delta\theta)], [(j \Delta r + r_{in}) \sin(i \Delta\theta)], n) \quad (2.9)$$

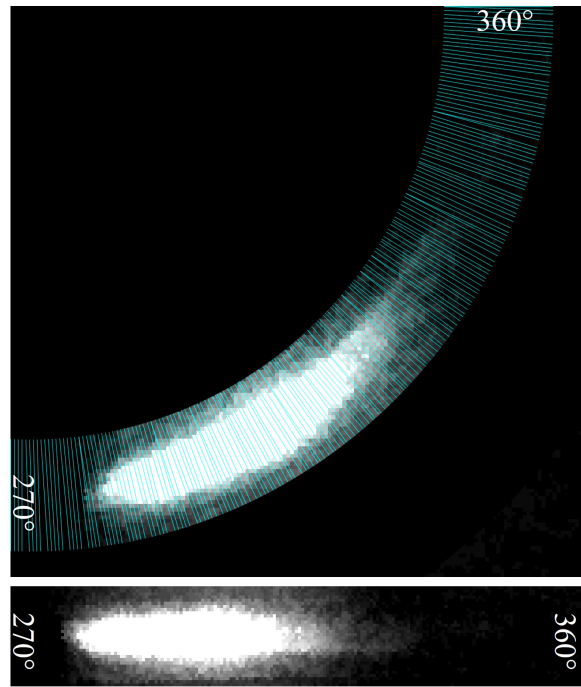


**Figure 2.19:** Example quadrant unwrapped to linearized image

$$i = [1, 2, \dots, 31, 32] \quad j = [1, 2, \dots, 735, 736] \quad (2.10)$$

$$\Delta r = 1 \text{ pixel} \quad \Delta\theta = 0.00856 \text{ radians} \quad (2.11)$$

*I am among those who think that science has great beauty.*

Marie Curie, Polish physicist and chemist,

Nobel laureate

# 3

## Survey of Conventional Methods

VARIOUS TECHNIQUES HAVE BEEN DEVELOPED TO CHARACTERIZE the modal properties of the detonation waves that occur in rotating detonation engines (RDEs). Primary techniques for defining the wave speed, number of waves, propagation direction and mode (co- vs counter-rotating) have included analysis of high-speed imagery, as well as frequency based and time of flight correlations of transducer signals such as dynamic pressure or flame ionization (chemi-ionization). Although high speed imagery (even in the visible spectrum) can

provide insightful quantitative data regarding the performance of the detonation wave(s), it can be challenging to acquire in an application that would have both upstream and downstream turbomachinery. For these applications, transducer-based methods coupled with signal processing methodologies to characterized operation may be more appropriate. While transducer-based methods are well understood, they often rely on assumptions to draw physical conclusions and verification of their ability to quantify the desired properties must be performed. Previous studies have proposed the use of a cross-correlation method to measure wave properties and modes in an RDE. While these techniques appear to have proposed logical results they rely on underlying assumptions, such as an assumed Chapman-Jouguet wave speed, to quantify detonation wave properties and modes, some means of verifying their performance must be considered. This section will utilize a modified version of an automated image process method developed at the Air Force Research Laboratory (AFRL) to validate a previously published multi-transducer cross-correlation algorithms used to characterize the operational state of an RDE. Calculated wave number and wave speeds are compared across a modal change to evaluate agreement between techniques as well as individual strengths of each.

### 3.1 DETONATION SURFACES

According to the AFRL method proposed by Bennewitz<sup>39</sup>, a polar mesh centered about the annulus is generated for the corrected down-axis image set,  $p_{k,cor}$ , summarized in Equation 3.1. Azimuthal bins of equally spaced regions along the radius of the annulus are defined, encompassing the full annulus width. Annulus size and centering locations are determined uniquely for each detonation surface according to the method outlined in Section 2.4. The binning dimensions may be altered according to the RDE geometry, physical pixel width,

and user preference for angular resolution. The plots presented are generated using 200 polar bins, each spanning  $1.8^\circ$ , and a RDE gap width of 24 pixels, stated in Equation 3.2. Integrated polar pixel intensities for a given azimuthal bin,  $\varphi_Z$ , are determined for each image,  $n$ , by integrating pixel values according to Equation 3.4. Integrated intensities of each bin,  $\varphi_Z$ , are then concatenated into a detonation surface matrix,  $\Theta(z, n)$ , in the manner shown in Equation 3.4<sup>39</sup>, where each row ( $z$ ) represents a radial location from the first to the  $Z^{th}$  bin and each column ( $n$ ) represents an image frame up to the Nth frame in the time interval of interest.

$$\rho_k(r, \theta, n) = p_{k,cor}(x, y, n) \quad (3.1)$$

$$\Delta\theta = 1.8^\circ \quad \Delta r = 24 \text{ pixels} \quad (3.2)$$

$$\varphi_Z(n) = \int_{r_1}^{r_2} \int_{\theta_2}^{\theta_1} \rho_k(r, \theta, n) d\theta dr \quad (3.3)$$

$$\Theta(z, n) = \begin{bmatrix} \varphi_{1_1} & \varphi_{1_2} & \varphi_{1_3} & \cdots & \varphi_{1_N} \\ \varphi_{2_1} & \varphi_{2_2} & \varphi_{2_3} & \cdots & \varphi_{2_N} \\ \vdots & \vdots & \vdots & \ddots & \vdots \\ \varphi_{Z_1} & \varphi_{Z_2} & \varphi_{Z_3} & \cdots & \varphi_{Z_N} \end{bmatrix} \quad (3.4)$$

To visualize the trace of each wave throughout a time increment as it travels radially, a contour plot of the detonation surface matrix can be generated. Examples of this detonation surface plot are shown in Figure 3.1a and 3.1c for a 2-wave CCW mode as well as a 3-wave CW mode. Information from individual images, like those in Figure 3.1b and 3.1d, is represented as incremental columns of the detonation surfaces. Each trace is an indication

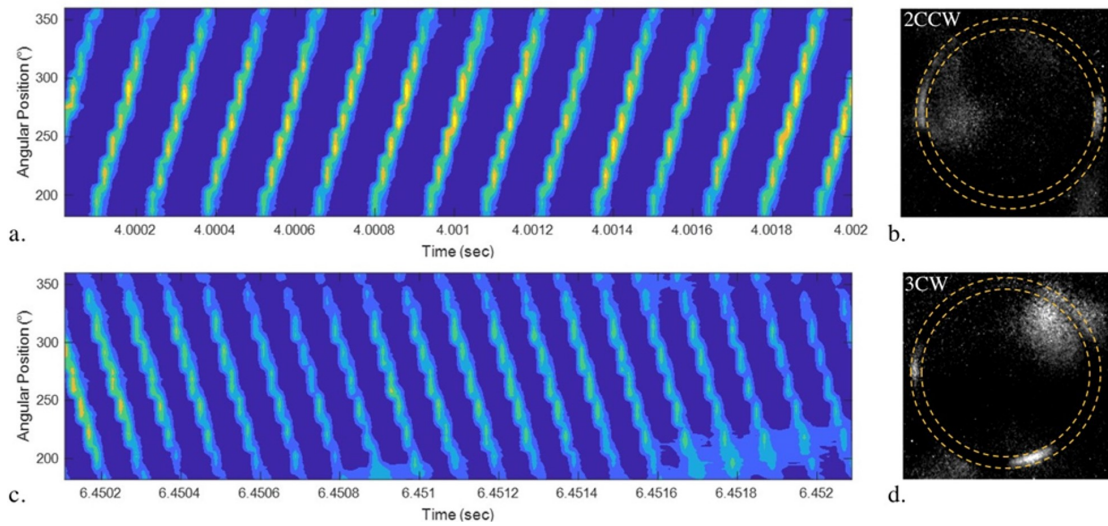


**Figure 3.1:** Detonation surfaces in lower portion of annulus (a) 2-wave CCW operational period, (c) 3-wave CW operational period as well as example images of (b) 2 CCW waves and (d) 3CW waves

of a wave's azimuthal location throughout consecutive frames, such that positive and negative slopes correspond to counterclockwise and clockwise behavior respectively. The slope of each trace represents angular progression through time, or wave speed. The distance a wave travels between captured frames presents itself as a step-like progression along each trace. The uniformity of detonation trace intensity improves with increasing the frame rate.

Many studies, including the foundational AFRL work, apply the two-dimensional fast Fourier transform (FFT) to extract average wave behaviors. The FFT limits the resolution to which the wave frequency can be estimated, driving the need for large image quantities. To determine wave properties within shorter operational windows than what is required by an FFT, the Hough Transform is used to determine average wave property values. Hough Transforms are commonly used in image processing to detect lines or edges within an image and have previously been used in similar RDE image processing efforts<sup>41,116</sup>. The Hough

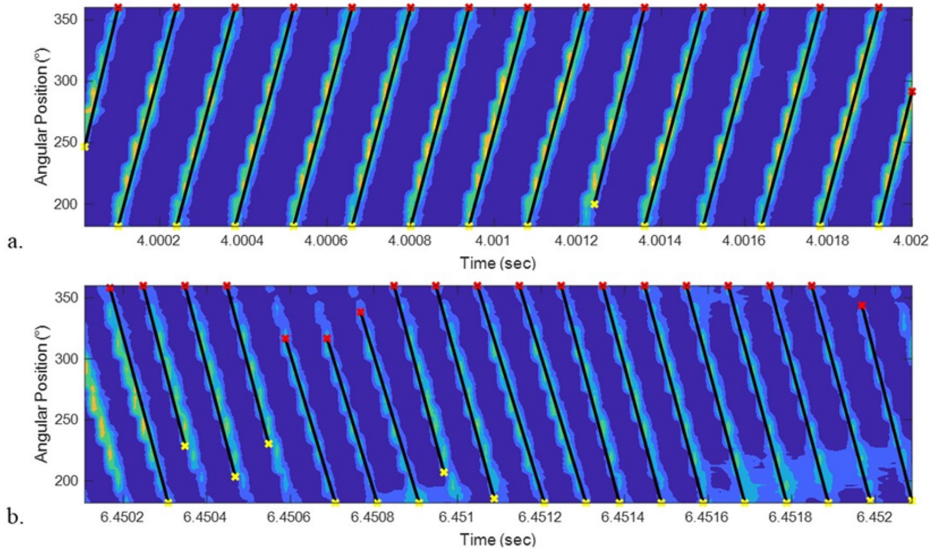


**Figure 3.2:** Detonation surface with overlaid Hough Transform lines used to identify modal characteristics (a: 2-wave CCW operational period, b: 3-wave CW operational period)

Transform of the detonation wave matrix associates the trace of each wave with an identified line, which can be seen in Figure 3.2.

Once the Hough Transform identifies the wave features within the detonation surface, the properties of each line is associated with detonation wave propagation characteristics. Line slopes indicate the direction and speed of each wave, where lines with positive and negative slopes trace counter-clockwise waves and clockwise waves, respectively. Generated lines can now be used for average wave behavior calculations independent of the detonation surface plots. Lines of each directionality are transferred to one of two binary matrices designated for a specific wave direction, either clockwise or counterclockwise. The binary matrices will be used throughout the remainder of the image processing efforts to ascertain modal information. This separation allows bi-directional wave detonation surfaces to be processed as two single-direction binary matrices, eliminating intersecting wave traces.

### 3.2 AVERAGE WAVE BEHAVIOR

Using the binary Hough Transform matrices, the average wave number, direction, frequency and speed can be determined for a set of images. Intuitively, the slope of the detected lines corresponds to the wave direction, speed and frequency. Nonuniformities in the magnitude in each detonation line can cause slight variations in the slopes of the Hough Transform lines, creating a variance in the estimated frequencies as well. Frequencies predicted by this inconsistent behavior for the 2-wave CW mode in Figure 3.2b are illustrated by the approximate frequencies shown in Figure 3.3a as hollow data points. For this reason, the average slope across a time increment was used only to approximate the average wave number and direction. Using the wave number prediction and a known framerate, a second calculation of frequency,  $f_{det}$ , and subsequent wave speed,  $U_W$ , is performed by analyzing the time series of a single azimuthal bin across each Hough Transform matrix (CW and CCW). This back-calculation, plotted as solid data points in Figure 3.3a, eliminates the variability introduced by the Hough Transform line detection, and provides a better representation of consistent wave behavior. Frequencies calculated using this method can be compared to the power spectra of the corresponding pressure signal in Figure 3.3b.

With 2-wave behavior known (from image processing), a maximum spectrum value at 7.11 kHz corresponds to a single-wave frequency of 3.56 kHz which compares extremely well with the 3.57 kHz calculated using the image processing method. This provides a more reliable indication of the number of waves as the use of the dynamic pressure signal power spectrum to estimate the number of waves relies on the assumption of the theoretical Chapman-Jouguet (CJ) wave speed. For example, the theoretical CJ wave speed for the test shown in Figure 3.3 based on the fuel / air flow rates, as well as the operating temperature and pressure is  $U_{CJ} = 1,990$  m/s. This is equivalent to wave propagation frequency of 4.45 kHz. Because the

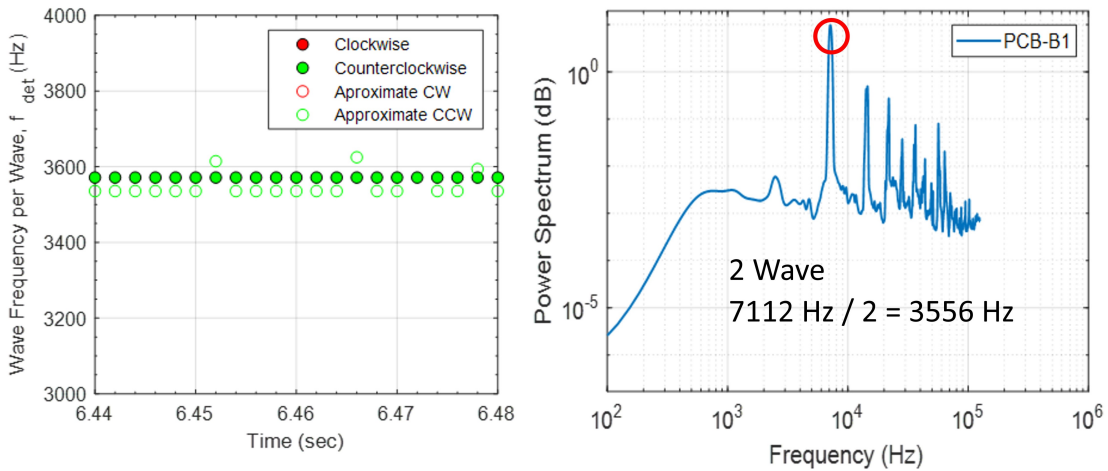


**Figure 3.3:** (a) Average wave frequency per wave,  $f_{det}$ , for time increments of  $2 \mu\text{s}$ , and (b) Power Spectrum of corresponding pressure signal

calculated single-wave frequency is less than the measured dominant frequency based on the dynamic pressure, it is assumed that there is more than one wave. Without verification, this approach could prove inadequate for estimating the number of waves when the measured dominant frequency is relatively close to the theoretical single wave value.

### 3.3 MODAL CHANGES

During quasi-steady operation, the number and/or direction of waves often changes unexpectedly. While the cause of this behavior is not yet fully understood, the detection of wave mode changes is essential as the design of downstream turbomachinery will likely require quantification of the modal behavior in the RDE. Successive calculation of wave modes offers the ability to detect modal changes in the RDE. An example mode change, shown in Figure 3.4, where RDE operation experiences a sudden transition from a 2-wave CW mode to a 3-wave CW mode, which seems to be introduced by a counter-rotating instability. The previously described relationship between wave number and contour magnitude is displayed

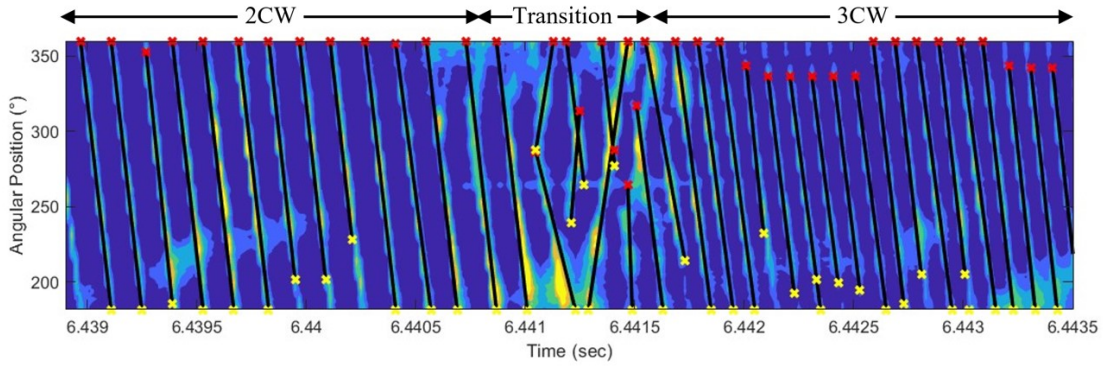


**Figure 3.4:** Detonation surface including modal transition from 2-wave CW to 3-wave CW

within a single detonation surface as the increase in the number of waves present from two to three decreases the integrated pixel intensities along individual detonation traces.

Average wave numbers  $m$ , frequencies  $f_{det}$ , and wave speeds  $U_W$ , are plotted for consecutive time increments in Figure 3.5, including the mode change depicted in Figure 3.4. Because modal characteristics are calculated as an average behavior across 100 frames, the behavior in Figure 3.4 is only represented by a single data point at 6.442 seconds in Figure 3.5. The momentary presence of the CCW wave, lasting approximately 500  $\mu\text{s}$  in Figure 3.4, is also represented in Figure 3.5. Average wave numbers are plotted according a convention in which CCW waves are positive, and CW waves are negative.

### 3.4 AUTO-CORRELATION METHOD

A method of auto-correlation can be used to confirm the modal properties found using the image processing technique. The pressure recorded by individual sensors can be analyzed to determine time lag between successive pressure peaks<sup>10,42</sup>. This analysis makes use of pressure data from instrumentation locations B1 and C1, whose locations are described in Figure 2.3.

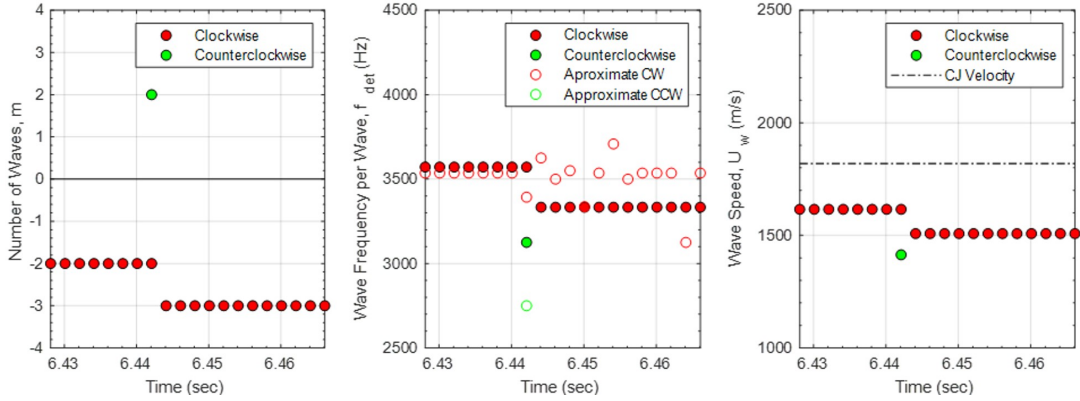


**Figure 3.5:** Average modal properties (number of waves,  $m$ , wave frequency per wave,  $f_{det}$ , and wave speed  $U_W$ ) for time increments of  $2 \mu\text{s}$ , suggesting modal change event at approximately 6.442 seconds

The incremental auto-correlation of a time series determines the time between similar pressure peaks, known as time lag, as illustrated in Figure 3.6a. Similar to the efforts of the University of Cincinnati<sup>10</sup>, each time lag calculation is performed for a data window of approximately three waves. This is accomplished by adaptively adjusting the data window to a width three times that of the previous time lag. The adaptive data window specifically accommodates mode changes and signal amplitude irregularities. Pressure data collected during the modal change seen in Figures 3.4 and 3.5 is analyzed to determine time lags experienced at each port location. Time lag values plotted in Figure 3.6b suggest a modal change at a time interval consistent with that in Figure 3.5.

The time lag,  $\tau$ , of each signal can be compared to that expected of a single wave traveling at the ideal Chapman-Jouguet wave speed, a value of 1,819 m/sec for these operating conditions. This relationship points to the number of waves present,  $m$ , and therefore wave speed,  $U_W$ , as functions of time and nominal annulus diameter,  $d_{nom}$ , is known. Wave speed values can be calculated and compared to those suggested by the image processing technique by Equation 3.5.

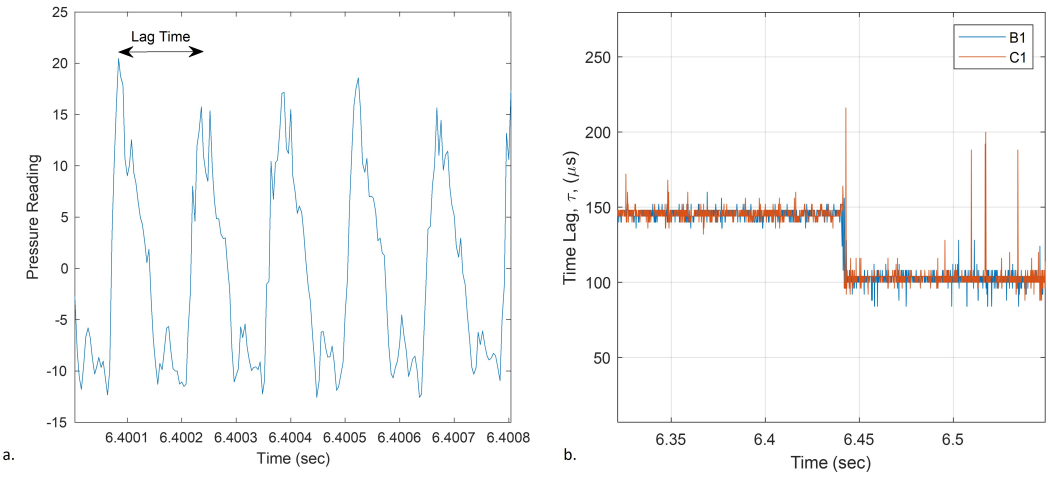


**Figure 3.6:** (a) Example window of pressure reading used in auto-correlation to estimate lag time and (b) the time lag found for pressure data from locations B<sub>1</sub> and C<sub>1</sub>

$$U_w = \pi d_{\text{nom}} (m\tau)^{-1} \quad (3.5)$$

The first modal behavior shows an average time lag of 143  $\mu$ s, which corresponds to 2 waves and an average wave velocity of 1,582 m/s. The second modal behavior shows an average time lag of 100  $\mu$ s, which suggests an average wave velocity of 1,508 m/s. Both classifications correspond well to those predicted in Figure 3.5 with the advantage of an almost instantaneous identification of a modal change. While the cross-correlation technique displays a more urgent response to modal changes, the minor presence of a counter-rotating mode is not obvious in the time lag data. Further investigation of individual pressure trace structure is believed to offer better understanding of modal direction as well as possible prediction of modal changes. Nevertheless, correlation of pressure data can be difficult to translate in complex modal state and should be compared with image classification whenever possible.

### 3.5 OUTCOMES

In summary, the image-based detonation surface and sliding cross-correlation techniques are common among the RDE community and offer valuable data in the post-processing stages. To illustrate the similarities and unique strengths of each, both techniques are applied to data that was recorded during a modal change. Auto-correlation of dynamic pressure measurements determined wave speeds of 1,582 and 1,508 m/s for 2-wave and 3-wave behaviors respectively, which agreed well with values of 1,616 and 1,520 m/s obtained using high-speed image analysis. Cross-correlation calculations can be executed for each pressure peak compared to average calculations across 100 images, therefore offering more immediate response to modal changes. However, while evaluation of pressure signals responded more quickly to a modal change, a brief presence of a counter-rotating wave was not reflected well in the cross-correlation results.

In an experimental setting both techniques should be employed to ensure full understanding of modal behavior in post processing. Images offer spatial resolution, while pressure data offers reduced data dimensionality and volume. In an industrial setting, where downstream turbomachinery is fully integrated, image analysis may be difficult or impossible. In these settings, cross-correlation or other analysis of transducer-based data may offer adequate understanding of modal behavior. Time series classification by a convolutional neural network is proposed in Chapter 7 as a means to understand modal behavior with more spatial certainty. Regardless of setting, modal discernment identification methods must be improved towards real-time speeds to enable active control and monitoring. To address the need for modal feedback during RDE operation, machine learning is applied to both data types via convolutional neural networks.

The aim of this chapter was to survey conventional methods for transducer signal and high-speed image analysis in determining modal variations within an RDE. An automated high-speed image analysis methodology which expands on the work of AFRL by utilizing a Hough Transform to detect wave traces is presented as the baseline method for data labeling and validation of computer vision approaches outlined in the following chapters.

*What we find is that if you have a goal that is very, very far out, and you approach it in little steps, you start to get there faster. Your mind opens up to the possibilities.*

Mae Jemison, American engineer, physician, and

NASA astronaut

# 4

## RDE Image Classification

UTILIZING A NEURAL NETWORK, INDIVIDUAL DOWN-AXIS IMAGES of combustion waves in a Rotating Detonation Engine (RDE) can be classified according to the number of detonation waves present and their directional behavior. While the ability to identify the number of waves present within individual images might be intuitive, the further classification of wave rotational direction is a result of the detonation wave's profile, which suggests its angular direction of movement. The application of deep learning is highly adaptive and therefore can be

trained for a variety of image collection methods across RDE study platforms. In this section of the work, a supervised approach is employed where a series of manually classified images is provided to a neural network for the purpose of optimizing the classification performance of the network. These images, referred to as the training set, are individually labeled as one of ten modes present in an experimental RDE. Possible classifications include deflagration, clockwise and counterclockwise variants of co-rotational detonation waves with quantities ranging from one to three waves, as well as single, double and triple counter-rotating detonation waves.

After training the network, a second set of manually classified images, referred to as the validation set, is used to evaluate the performance of the model. The ability to predict the detonation wave mode in a single image using a trained neural network substantially reduces computational complexity by circumnavigating the need to evaluate the temporal behavior of individual pixel regions throughout time. Results suggest that while image quality is critical, it is possible to accurately identify the modal behavior of detonation waves based on only a single image rather than a sequence of images or signal processing. Successful identification of wave behavior using image classification serves as a steppingstone for further machine learning integration in RDE research and development of comprehensive real-time diagnostics.

This chapter outlines the workflow to develop and train a data-driven model utilizing a CNN for the purpose of rapidly assessing the detonation mode in an RDE. This model is considered a data-driven model as it is trained on images that have been manually classified based on the known wave mode. It is important to note, that while it may take tens or hundreds of thousands of images to train the model, once trained the user is able to identify the detonation mode (wave number and direction) from a single image. When coupled with

high-speed pressure data, an accurate real-time diagnostic for the wave mode, including wave number, direction, velocity and frequency, becomes possible in the following chapter. Furthermore, a trained model stemming from the algorithm described here consists of two files (model and parametrized weights) which can easily be shared and implemented by others operating similar experiments by writing only a few lines of code.

As a first step, the current chapter is limited to outlining the algorithm followed to develop and train the data-driven CNN model to identify wave number and direction. Approximately one hundred thousand images were acquired, manually classified by visual inspection and then divided into sets for training and validation. The training set consisted of a randomized series of classified images that define the mode of the detonation wave in the combustor. These images were used to optimize the parameterized weighting functions within the neural network using TensorFlow and Keras libraries in Python<sup>117</sup>. Once the network was trained, the validation image set is used to characterize the performance of the CNN. The validated CNN is then available for practical usage in rapid mode classification detecting quasi-steady modal behavior as well as unsteady behavior and modal changes.

Classifying wave modes through image analysis has been the goal of multiple studies in the RDE community<sup>41,113,44</sup>, but this method is the first to do so using individual images, reducing computational time significantly. At this time, possible benefits of different wave modes such as reduced losses or ease of high-pressure turbine integration are not yet fully understood by the RDE community. It is possible that a preference may arise between co- or counter-rotational modes, while it may also be possible to optimize annulus fill heights for a known number of waves. Although the value of this information is not yet fully known, it is apparent that being able to accurately classify these modes at speeds closer to the timescale of the RDE is comparatively beneficial.

#### 4.1 CNN METHODOLOGY

Images considered in this effort are recorded by a Photron FASTCAM SA-Z, at a rate of 50,000 fps and a gate width on the intensifier of 20  $\mu$ sec. Depending on the detonation wave speed and the number of waves present, this framerate captures waves at 10-15 azimuthal locations throughout each revolution. Images considered in the initial development of this methodology include six classifications or wave modes. Those modes are CW and CCW variants of single, double and triple co-rotational wave behaviors. Examples of each mode are displayed in Figure 4.1

Figure 4.2 represents the algorithm used to train the CNN model which includes manual classification, or labeling, of the images according to the number of waves present in the annulus as well as their direction. Images can be classified in several ways. Visual classification of a series of images while the RDE maintains a quasi-steady mode is performed. Classified images are then split, as depicted in Figure 4.2, into two sets labeled Training Image Set and Validation Image Set for separate use in CNN Training and CNN Validation processes respectively.

In training the selected CNN architecture, it is important to shuffle training images beforehand to ensure the CNN is incrementally considering small training batches that are representative of each possible classification. Shuffling removes the time-dependency by separating sequential images prior to classification. Randomized training does not prevent the future use of the trained CNN as a temporally resolved diagnostic, but just reduces the potential of bias error in the derivation of the model.

The incremental performance of the network is evaluated as an ability to accurately classify labeled validation images each time the network has updated its trainable weights for the entire set of training data. Since neural networks are global approximators this approach

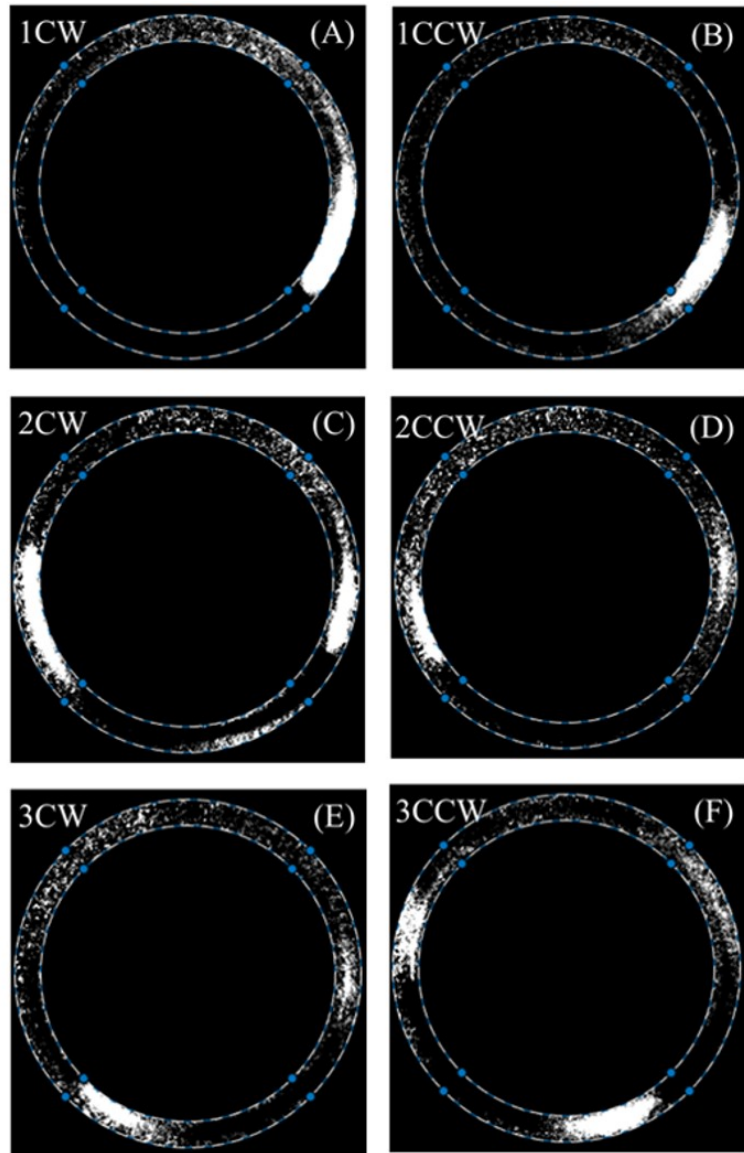


**Figure 4.1:** Down-axis images of modes: (a) 1CW, (b) 1CCW, (c) 2CW, (d) 2CCW, (e) 3CW, and (f) 3CCW

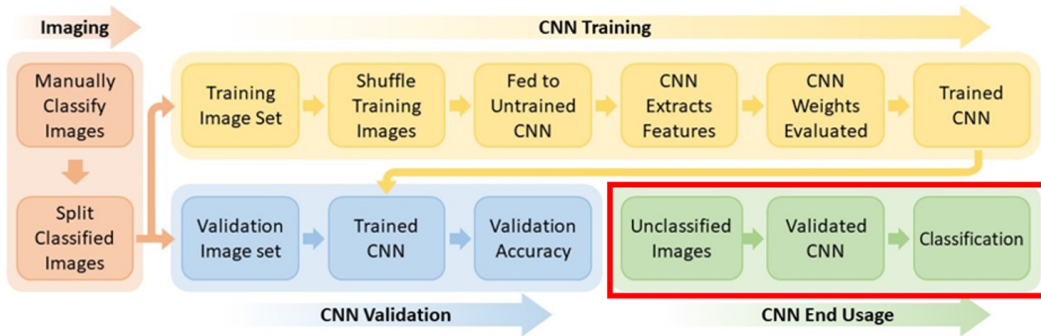


**Figure 4.2:** Image Classification CNN Development Methodology Flow Chart

ensures that a CNN does not overfit the system to just the set of images used for training. This process is repeated for several iterations, or epochs, until a desired validation accuracy is reached. Once the proper validation accuracy of the Trained CNN is achieved, the CNN is considered to be a Validated CNN which is suitable for end usage. In this stage, shown in green and enclosed in a red box in Figure 4.2, newly recorded images can be fed to the Validated CNN for classification of the wave mode. A user of the trained/validated CNN would only need to follow the last three steps (red box) of the algorithm illustrated in Figure 4.2 in order to classify an image recorded during a test. This process significantly reduces the time required to determine the wave mode and when ultimately coupled with instantaneous sensor data, real-time determination of wave mode and speed could be possible.

While it is possible to design an entirely unique CNN architecture, previously successful architectures designed for image classification are incredibly valuable to the practitioner. This effort will adapt some of the most notable, publicly available architectures including AlexNet<sup>57</sup>, VGG16<sup>57</sup>, ResNet<sup>59</sup>, LeNet<sup>118</sup> as well as a lesser known architecture such as SqueezeNet<sup>63</sup>, and adapt them to best fit the needs of high-speed multi-wave and bidirectional image classification. In each case, architectures are fully accessible and adjustable unlike other machine learning platforms often categorized as black box algorithms.

Networks considered in the present chapter were mostly designed for classification using images in the ImageNet database. Thus, certain parameters need to be changed before training could be achieved. This requirement is due to the greater similarity among the RDE images compared to those used in the ImageNet database i.e. dog, plane, zebra etc. For example, differences between two images showing 1CW wave behavior and 1CCW wave behavior are incredibly small compared to differences between two images of a cat and that of a boat. The ImageNet competition factors in a top 5 classification error score in choosing a winner so the CNNs were designed to maximize that score. However, within the RDE initially considered in this effort, there are only six classes, so the architecture should aim to maximize only the top 1 classification.

In order to compensate for the similarity of the different RDE image classes the learning rate of the system was reduced to  $10^{-6}$ , where a traditional learning rate is on the order of  $10^{-3}$ . Adjusting the learning rate allows the network to learn slower making smaller changes to the weights of the system, thereby not missing out on the finer details of the system. The smaller learning rate coupled with a “he normal” kernel initializer for the initial distribution of weights allowed for the network to capture finite changes between wave directionality, as exemplified in Figure 2.14. A unique advantage of the dataset used in this environment is that because RDE detonation waves rotate around an annulus each image could be rotated  $360^\circ$  and still represent a possible true image. These synthetically created images allowed the CNN to visualize each class of wave at all positions around the annulus.

## 4.2 PERFORMANCE COMPARISON OF FIVE IMAGE CLASSIFICATION CNNs

For training, classified images were shuffled randomly into a training set and validation set consisting of 65,600 and 16,400 images respectively. For each architecture, a different num-

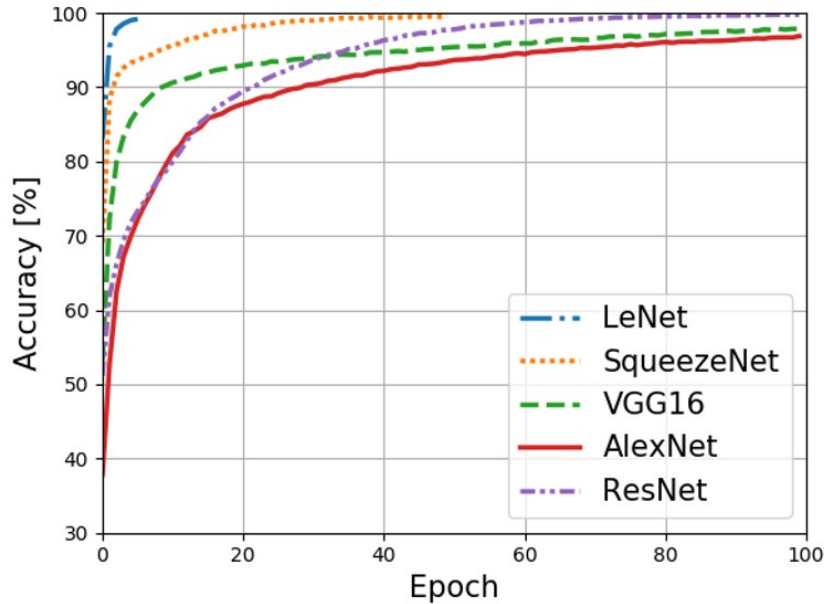


**Figure 4.3:** Training accuracies of five trained neural network architectures against epochs

ber of epochs was needed to reach accuracy convergence. The accuracies for each architecture are shown in Figure 4.3. The number of epochs at which the accuracy plateaus depends heavily on the number of convolutional layers included in the structure of the network as well as the subsequent volume of trainable parameters. As seen in Figure 4.3, a deeper network such as AlexNet may require 100 training epochs while a shorter network such as LeNet requires just six. A reduced number of necessary training epochs results in a lower upfront computational effort, saving time and computing resources during training. The number of required epochs is considered when selecting a preferred network to optimize initial training time as well as validation speed.

The final training and validation accuracies achieved by each model and their associated epochs are summarized in Table 4.1. An additional parameter is also tabulated to represent the speed at which the fully trained network can classify individual images from the valida-

Architecture	Training Accuracy	Validation Accuracy	Training Epochs	Speed [sec/frame]
AlexNet	96.9	95.5	100	0.0585
VGG16	97.9	95.4	100	0.4136
<b>SqueezeNet</b>	<b>99.6</b>	<b>98.</b>	<b>50</b>	<b>0.0299</b>
LeNet	98.0	99.5	6	0.0550
ResNet	99.8	98.8	100	0.3542

**Table 4.1:** Training results for five texted neural network architectures

tion dataset. The speed was recorded using a local desktop HP EliteDesk 800 G2 DM 65W computer with an Intel® core (TM i5-6500 CPU @ 3.2GHz and 16.0 GB of RAM). Due to the fact that each architecture achieves accuracies above 95%, the number of required training epochs as well as the classification speed are the driving factors when selecting the preferred architecture.

For both measures, SqueezeNet and LeNet surpass the performance of the remaining architectures with low epochs and efficient classification speeds. Although LeNet achieves similar accuracies using only a fraction of the epochs used by SqueezeNet, SqueezeNet's improved classification speed provides a practical efficiency that is realized each time new images must be classified. This faster classification speed is an expected advantage of the fire modules which are unique to the SqueezeNet architecture. In an experimental setting, SqueezeNet's 45% improvement in classification speed over LeNet will result in significant time savings, with little sacrifice in accuracy, and is therefore chosen as the preferred neural network throughout the remainder of this text.

#### 4.3 PREFERRED CNN ARCHITECTURE SELECTION (SQUEEZE NET)

SqueezeNet, detailed in Section 1.1.3.1 and visualized in Figure 1.9, is a unique architecture in the CNN design space. It was developed to achieve the same accuracy as AlexNet but with

fewer parameters and a smaller model size. SqueezeNet is unique among CNNs because it incorporates a building block referred to as a fire module. Fire modules are built using three different strategies: maximizing  $1 \times 1$  convolutional filters, reducing the input channels when using  $3 \times 3$  filters and downsampling on the backend of the network in order to increase the networks activation map size. These three strategies are utilized in the fire module by the creation of a squeeze convolution layer comprised of only  $1 \times 1$  filters which feeds an expanded layer with a mixture of both  $1 \times 1$  and  $3 \times 3$  layers. By limiting the hyperparameters in the fire module, the architecture reduces the number of trainable parameters making the model smaller and more computationally efficient. By using these strategies, SqueezeNet can achieve a comparable accuracy with 50 times fewer parameters and a model size that is less than 0.5 MB compared to larger architectures like AlexNet which has a model size of 255 MB. These changes proved advantageous to the total amount of time needed to classify the images. The smaller architecture size is less computationally expensive to run, while the fewer parameters results in less mathematical computations being run. Since the accuracy is on par with more computationally expensive models such as AlexNet or ResNet, the main benefit is the speed and accuracy at which images can be classified.

#### 4.4 PERFORMANCE OF PREFERRED CNN: SQUEEZENET

The learning curve of the SqueezeNet training process can be seen in Figure 4.4 which shows the training and validation accuracy as a function of epoch. While the training accuracy is seen to exhibit smooth behavior in Figure 4.4, the validation accuracy does not always improve with each additional epoch. The somewhat sporadic behavior of the validation accuracy implies that the weights associated with the final epoch may not offer the highest validation accuracy. The magnitudes and effects of this behavior vary between architectures. For

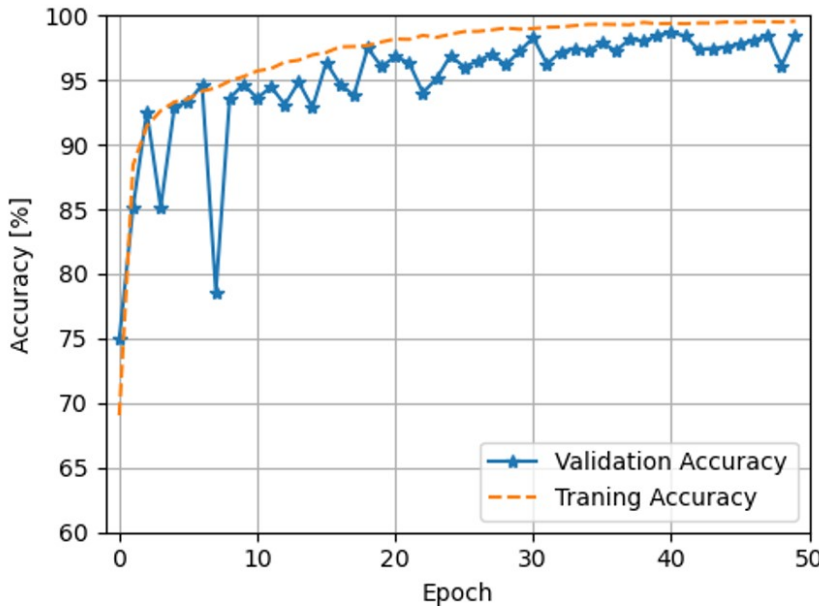


**Figure 4.4:** Training and validation accuracies of chosen SqueezeNet architecture against epochs

this reason, it is imperative to record and use the model weights associated with the highest of both accuracies, which is common practice in the application of CNNs.

To visualize the final performance of SqueezeNet, a confusion matrix is compiled in Figure 4.5. This matrix tabulates the number of each predicted classification for a given true classification. For example, Figure 4.5 shows that 3,900 1CW images are classified as 1CW by the network with 0 images being incorrectly classified as any other modes, which shows a 100% accuracy of the network on 1CW images. Figure 4.5 also displays lesser performances, such as the evaluation of 4,000 images of known 3CW behavior in which a great majority of images are predicted correctly except for one and three images labeled as 2CW and 3CCW, respectively. These errors are a result of previously predicted visibility issues and directional confusion but remain insignificant.

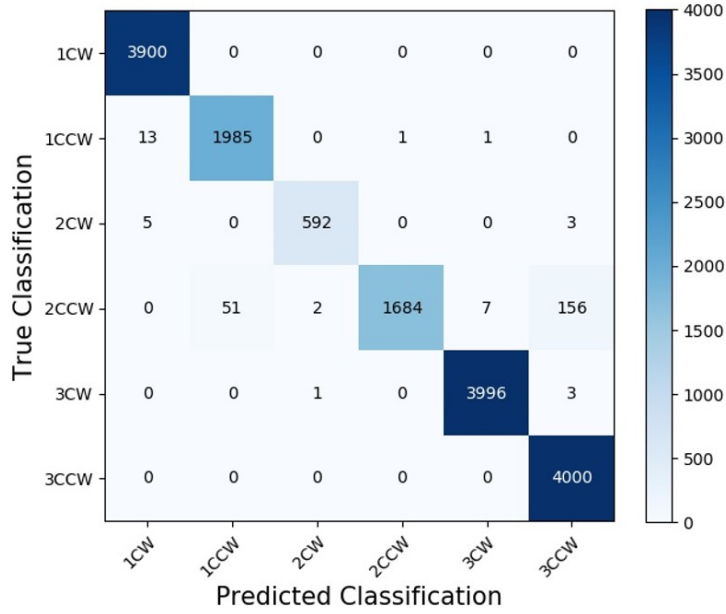


**Figure 4.5:** SqueezeNet confusion matrix comparing predicted classifications against true classifications of validation data set

To understand the performance of the model with respect to the number of images available in each classification set, a normalized confusion matrix is shown in Figure 4.5. In this configuration, cells in each row display the percent of predictions of a given subset, totaling 100%. Intuitively, the ideal confusion matrix should have maximum intensity across the diagonal as a result of perfect classification of every image.

Other misclassifications of 2CW and 2CCW images are likely a result of a low sampling density, which is depicted in Figure 4.5 showing that the total number of images present in the data subset is significantly lower than other classification subsets. Although this could likely be resolved with an increase of 2CW and 2CCW images in the training data set, infrequent misclassifications are negligible due to the practical understanding of RDE operation.

Accuracy improvements would be achieved if the architecture instead classified experimental images free from obstruction. With a full view of the annulus gap, identifying the

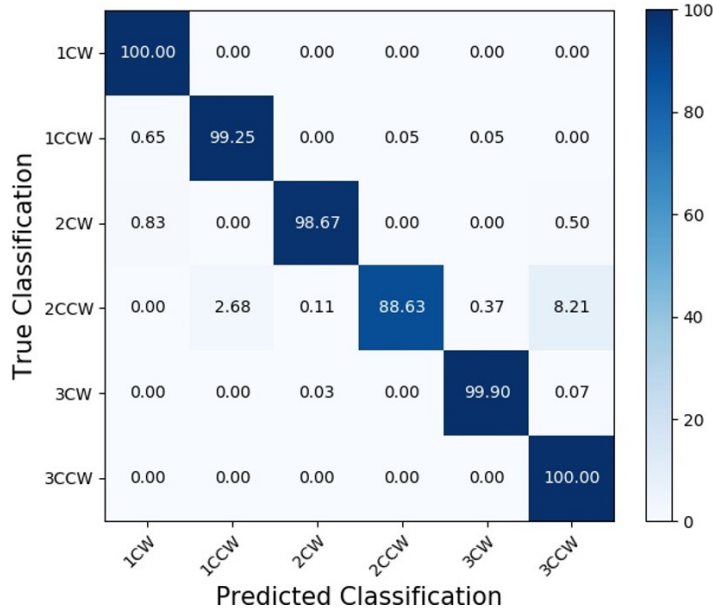


**Figure 4.6:** Normalized SqueezeNet confusion matrix comparing predicted classifications against true classifications of validation data set

number of waves present would become further trivial while classification of wave direction would improve as a result of more visible profile features. This improvement in experimental setup addresses the error associated with 86% of the total image misclassifications. Additionally, a more uniform sampling density across each classification type would likely increase lesser accuracies that were seen in modes 2CW and 2CCW.

#### 4.5 EXTENSION OF EVALUATED MODES: COUNTER-ROTATING AND DEFLAGRATION

As noted throughout the text, modes experienced in the studied RDE are limited as they do not include counter-rotating behaviors. Figure 4.5, discussed previously, confirmed proper CNN feature extraction for high-speed images containing co-rotating detonation waves within an RDE. To evaluate a more complex range of modal behaviors representative of those seen throughout the RDE community, an extended data set is created and subjected to the

same process steps outlined in Figure 4.2. Images capturing deflagrative behavior, or operation including no establishment of detonation waves, are added as an additional classification. A lack of detonation waves does not directly correspond to the adopted naming convention and will therefore be referred to simply as Def. Images recorded down-axis of another well-studied RDE at Purdue University<sup>119,94,120</sup> containing single, double, and triple counter-rotating waves are utilized as well. According to the naming convention, these are denoted as 1CR, 2CR, and 3CR respectively. Examples of the four new modes are shown in Figure 4.7.

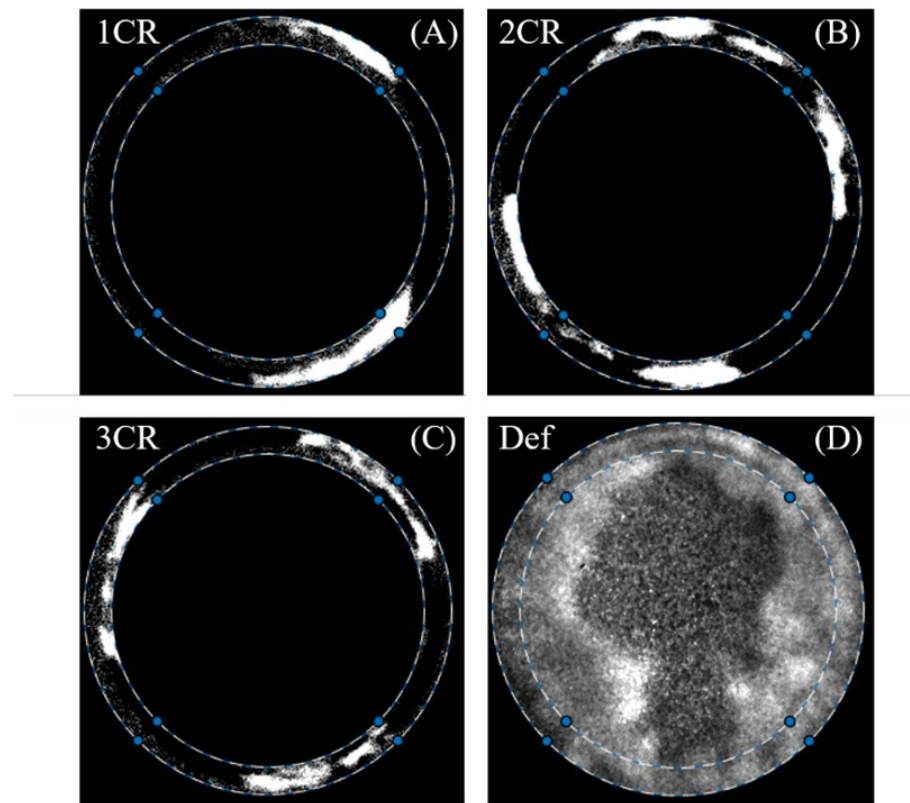


**Figure 4.7:** Downstream images of additional modes (A) 1CR, (B) 2CR, (C) 3CR, and (D) Def

When acquiring a set of images for the purpose of training a CNN, two common sampling types are generally favored: experimental images recorded using an identical setup, or images recorded under vastly dissimilar conditions. Results presented in Figures 13 and 14 represent the former due to consistent origin, experimental set up and pixel dimensions across the dataset. An example of the latter would be represented by a database encompassing various designs, framerates, filters and other imaging factors associated with several RDE studies. Combining two unique datasets (NETL and Purdue) falls between either preferred dataset structure but serves to show that complex modes can be accurately classified by the network. Therefore, some inherent confusion between the two datasets is expected.

Nonetheless, the performance of the CNN trained on the extended dataset, summarized using a normalized confusion matrix in Figure 4.8, serves as proof of an overarching ability to simultaneously classify complex and co-rotational modes.

In both cases of notable error, specifically the misclassification of 2CCW and 3CW as 1CR, confusion between the two datasets is a major contributor. This confusion accounts for 14% and 7% error in 2CCW and 3CW classifications, respectively, and would be significantly reduced if the data set better conformed to one of the preferred sampling strategies.

Network performance on the extended dataset shows network ability to discern features captured from another experimental facility. Network transferability is considered further in Chapter 8. Since extension of the dataset was primarily performed to study the response of the CNN when exposed to complex modes, it is most important to note the high accuracies associated with those modes. Those values are indicated within the four lower-right cells in the diagonal. Deflagration, although not a mode of detonation, is perfectly classified across the dataset. Similarly, 1CR and 2CR images are each correctly classified with 99% accuracies.

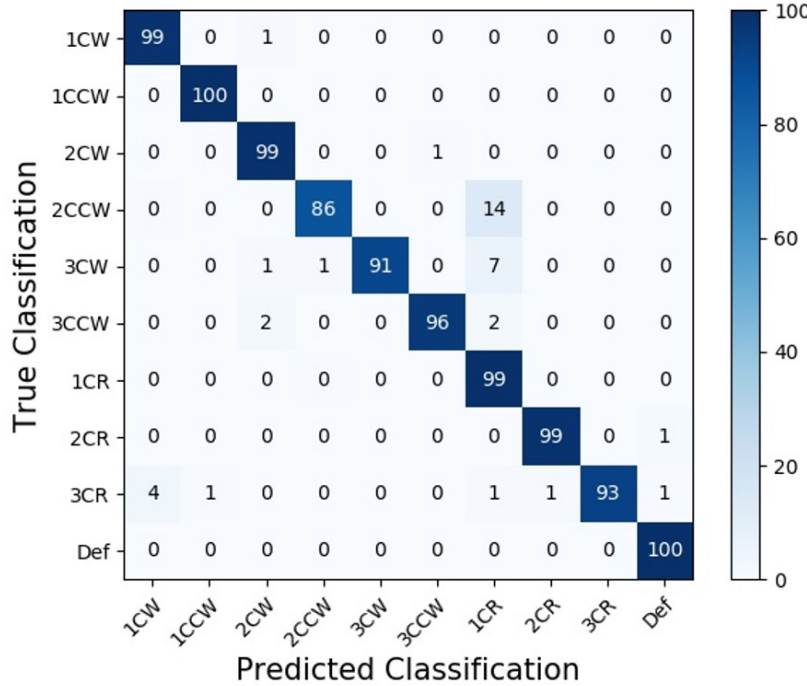


**Figure 4.8:** Normalized confusion matrix of extended dataset containing counter-rotating waves and deflagrative behaviors

Less accurate classification of 3CR images is in part a result of lower overall pixel intensity due to the presence of six detonation waves and a subsequent reduced fill height within the annulus. This trend is consistent with images previously presented in Figure 4.1, and is the cause of a lesser defined wave profile in Figure 4.7(C). However, the poorest performance among the complex modes of 93% classification within the 3CR subset exceeds the lowest performance among the purely co-rotational analysis, and therefore proves the ability classify complex modes by way of feature extraction.

To increase the performance of SqueezeNet on the RDE images, several image processing techniques could be applied when training. In addition to rotating images  $360^\circ$  around the annulus, sheer intensity could be added to each picture to account for different lighting conditions. Gaussian noise could also be applied to the images to help bolster the network

and its ability to interpret noisier images captured under different conditions. These changes could help the network approximate better to other environmental conditions and make the system more robust, however they likely will come at some cost to overall accuracy.

Classification of the number and direction of detonation waves present in a rotating detonation engine (RDE) annulus during combustor operation is critical to advancing the control and integration of RDEs in gas turbine engines. A methodology for wave behavior classification was demonstrated in this work through analysis of individual downstream high-speed images using a convolutional neural network (CNN). The goal of this work was to use CNNs to classify wave number and direction in multi-wave modal behavior in an experimental RDE. Classified modes included clockwise and counterclockwise variants of one, two and three co-rotational detonation waves, single, double and triple counter-rotating detonation waves as well as deflagration. Direct high-speed images of detonation waves were collected down-axis of experimental RDEs at the US Department of Energy (DOE) National Energy Technology Laboratory (NETL) and Purdue University using high-speed digital cameras, then manually classified for application of CNN architectures.

#### 4.6 PRACTICAL APPLICATION OF SQUEEZENET NETWORK

Proper implementation of the proposed methodology results in a validated CNN which is easily employed as a diagnostic tool offering high accuracies, processing speeds, and possible data acquisition integration for real-time classification. End usage of the validated CNN, accentuated by a red outline in Figure 4.2, can be applied to time sequential images. Therefore, modal changes and instabilities can be observed through a series of frames. While the CNN will not directly report these behaviors, continuous classification of each frame will make them innately obvious to the practitioner. For example, if consistent 2CW classifications are

suddenly followed by consistent 3CCW classifications, it is apparent that a mode change has occurred. Similarly, if classifications constantly alternate between multiple modes, it is reasonable to assume unsteady modal behavior within the annulus. While the ability to detect mode changes may seem contrary to the previously suggested negligence of misclassification outliers, the timescale in which mode changes are experienced is much longer than that of a single frame. Therefore, relying on this practical understanding of the RDE, one outlier of 3CCW in a stable series of 2CW classifications is easily identified as a sparse error. Recognition of these phenomenon can be easily automated if of significant interest.

With an established ability to classify wave modes quickly and accurately with a CNN trained using the proposed methodology, it is now possible to integrate that information with existing pressure correlation techniques to improve wave speed calculations as the focus of a future work. While methods to calculate wave speed using pressure data already exist, those point measurements lack spatial resolution and may therefore confuse more complex modes or secondary behaviors. Additionally, those methods which rely only on pressure traces may require large sampling sizes and will therefore be unlikely to reach real-time feedback capabilities. However, with wave number and direction known, smaller windows of pressure traces may be quickly analyzed to determine wave frequency. To do so in real-time, only a camera with improved triggering and data communication speeds, and a single sensor is needed to find the wave velocity and frequency. It is important to note that this technique does not aim to analyze every image or every pressure reading. Instead, a single image captured at the beginning of a simultaneous pressure data sample window will be acquired. Both operations of data acquisition and processing shoudl be optimized for accuracy as well as processing speeds.

#### 4.7 OUTCOMES OF RDE IMAGE CLASSIFICATION

After surveying and successfully training five publicly available CNN architectures, SqueezeNet was chosen for its classification speed of 0.0229 sec/frame. Achieving training and validation accuracies of 99.6% and 98.5% respectively, SqueezeNet demonstrated the ability to consistently classify the number of waves present as well as their direction in individual images, and did so in a fraction of the time required by other common methods. This capability extends the application of this method to a variety of RDE imaging techniques regardless of framerate limitations. The one-time execution of the training methodology results in a trained and validated CNN available for unlimited end usage, classifying modes experienced in newly captured images.

Although image classification offers crucial modal information at excellent classification speeds, the method **does not independently provide wave speeds**. To address this shortcoming, two diagnostic approaches which evaluate all targeted detonation wave details are pursued and documented. The first extends the method outlined within this chapter alongside conventional high-speed sensor data to achieve real-time detonation wave classification capabilities, including wave frequency, and is addressed in Chapter 5. The second is a unique application of an object detection CNN with the ability to actively track individual detonation waves around the annulus. Object detection applied to RDE images, and subsequent frame-to-frame velocity calculations are presented in Chapter 6.

The demonstrated image classification approach offers a very early example of CNN applications aiding in the development of RDE technologies.

*I was attracted both by the sheer idea and the fact that it  
had never been done before.*

Margaret Hamilton, American computer scientist, and  
NASA software engineering pioneer

# 5

## Real-Time Characterization: SqueezeNet

### Adaptation

As RDE TECHNOLOGIES PROGRESS IN MATURITY, the importance of monitoring methods progressing towards development of active control becomes more critical. This chapter aims to develop and deploy a real-time monitoring technique which integrates flame image clas-

sification by a convolutional neural network (CNN) and ionization current signal analysis with the goal of determining detonation wave number, direction, frequency, and individual wave speeds throughout experimental RDE operational windows. Wave mode identification through single image CNN classification bypasses the need to evaluate sequential images and offers instantaneous identification of the wave mode present in the RDE annulus. The output of the existing CNN is utilized alongside a correlation of ion probe data to generate diagnostic outputs. The diagnostic acquires live data using a modified experimental setup as well as Pylon and PyDAQmx libraries within a Python data acquisition environment. Lab-deployed diagnostic results are presented across a variety of wave modes, operating conditions, and data quality, currently executed at 4-5 Hz with a variety of iteration speed optimization options to be considered as future work. These speeds exceed that of conventional techniques and offer a proven structure for real-time RDE monitoring, which will play a vital role in the development of active control necessary to the extension of operational capabilities and RDE technology maturation toward industrial integration

The methodology used in this chapter consists of three distinct portions: training of a CNN for image classification, integration of ion probe data, and advancement of data acquisition and processing techniques toward real-time data processing and reporting. Of these three, the final effort of advancement towards real-time monitoring and outputting of RDE modal behavior in the laboratory environment is the primary thrust of the current study. The first portion is completed by a previously developed CNN, where a CNN was trained to classify the number and direction of counter- and co-rotational detonation waves in individual images of an uncooled RDE<sup>46</sup>. The preferred network developed in that preliminary study is an architecture named SqueezeNet, which was trained to classify 10 RDE wave modes from down-axis images. The finalized architecture and weights are used in the CNN infer-

ence mode throughout the current chapter. A brief functional overview of the steps taken to generate the utilized CNN are presented here, while a more in-depth discussion of the theory, dataset generation, training method, and architecture selection recommendations can be found within the previous chapter.

While many unique architectures could perform the task at hand, selection of the SqueezeNet architecture<sup>63</sup> is based on a classification speed which far exceeds that of other networks trained on the same image set<sup>46</sup>. Briefly reviewing process of CNN image classification, to begin the Imaging phase, a set of down-axis high-speed images must be manually labeled, or classified, according to their wave number and direction. The classified images are then partitioned into two subsets, the Training Image Set and the Validation Image Set, which contain 70% and 30% of the classified images, respectively. The next phase, CNN Training, begins by shuffling the training images. This process is imperative as it is dual purposed: ensuring the model is incrementally analyzing images across the classification range, which limits possible bias towards individual classifications; and creates a nonsequential dataset, eliminating time dependencies from image to image. Shuffled images and their labels are then fed to the untrained CNN which executes feature extraction and updates its trainable weights. After every epoch, which is one complete evaluation of the entire set of training images by the CNN, the subsequent training accuracies are evaluated.

Simultaneously, the CNN Validation phase works to evaluate the incrementally trained CNN by attempting classification of the validation image set without labels. The incrementally trained CNN predicts labels for each of the images, which are then compared to the known label to determine validation accuracy. Once the training and validation accuracies are found to be acceptable, the CNN is considered trained and validated, and can then be used indefinitely to evaluate unclassified images. It is important to emphasize that the first

three phases indicated in Figure 4.2 must only be performed once to develop an production CNN which can be used indefinitely as a tool to classify new, unlabeled relevant images.

### 5.1 TIME SERIES DATA INTEGRATION

Analysis of high-speed time series data, such as pressure or ion probe, is commonly used to determine detonation wave behavior<sup>10,42,121</sup>. This process typically relies on cross-correlation or power spectral density analyses, which are then related to an estimated ideal velocity via Chapman-Jouguet (CJ) theory, a classical theory describing a thin detonation wave with infinite chemical reaction rate, to determine wave number and frequency<sup>4</sup>. As mentioned in the previous section, point measurements lack complete spatial resolution and may therefore confuse more complex modes or secondary behaviors. Additionally, those methods which rely only on time series traces may require large sampling sizes and will therefore be unlikely to reach real-time feedback capabilities.

However, with wave number and direction supplied by the image classification CNN, time series data may be quickly and certainly analyzed to determine wave frequency. To accomplish this, CNN image classification and time series data evaluation techniques can be integrated. First, using autocorrelation for a 200 sample-length window of ion probe data collected at a sampling rate,  $SR$ , of 250 kHz, the sample lag,  $\tau$ , can be found. Using Equation 5.1, the frequency of the ion probe signal,  $f_{ion}$ , can be found. While the frequency of RDE time series data is commonly found using an FFT, the resolution of an FFT is drastically reduced by shortened sample lengths. Autocorrelation resolution is proportional only to the sampling rate and is therefore more well suited for analysis of brief data windows, which are of interest due to the pursuit of a real-time diagnostic. Using Equation 5.2, the wave number

output from the CNN,  $m_{CNN}$ , is used alongside ion probe frequency and the nominal RDE annulus diameter,  $d_{nom}$ , to determine individual wave speed,  $U_W$ .

$$f_{\text{ion}} = SR/\tau \quad (5.1)$$

$$U_W = \pi d_{nom} f_{\text{ion}} / m_{CNN} \quad (5.2)$$

To visualize the proposed diagnostic data flow, a diagram is shown in Figure 5.1, where upon determining detonation wave number and rotation type from an individual image, a very short sampling of ion probe data is needed to find the wave velocity and frequency. Inevitably, the CNN will produce sporadic misclassifications. To address this issue, either a rolling or sliding window median of wave number can be used in place of  $m_{CNN}$  within Equation 5.2. The results presented in the next section plot both median types and utilize a sliding window median with a width of 7 iterations to calculate individual wave speed.

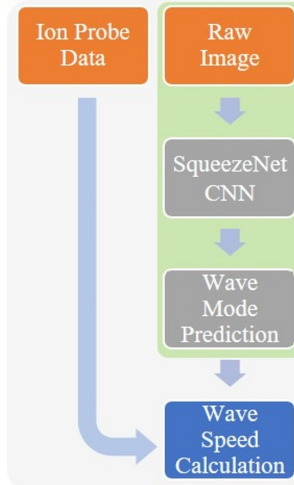


**Figure 5.1:** Diagnostic data flow diagram

## 5.2 TOWARD REAL-TIME PROCESSING & LAB INTEGRATION

The data flow process illustrated in Figure 5.1 is simple in nature after a CNN is trained for the specified outputs, and can be used as a post processing technique to evaluate RDE detonation wave behaviors within operational windows much shorter than other techniques. However, the objective of the current study is to develop a real-time RDE diagnostic. Therefore, the ability to collect data and execute the process in Figure 5.1 while the RDE is running is imperative. It is important to note that this technique does not aim to analyze every image or every time series reading. Instead, for each iteration  $i$ , a single image is captured by the Basler camera at  $t_i$  and ion probe data acquired within a sample window of length  $\Delta T_{S_i}$ . Throughout this study, sample window length  $\Delta T_S$  is equal to 200 samples at 250 kHz, or 0.8 msec. The time needed to acquire the data from the camera and sensor, image classification and calculations will be performed, taking the time indicated as  $\Delta t_C$  in Figure 5.2.

Using the single image and the short window of time series data, the diagnostic will output wave number, direction, frequency and individual wave speed at each iteration. The next iteration will acquire the most recent data for the next loop, beginning at  $t_{i+1}$ . In general, this means that only one image at the beginning of each loop will be considered, and the ion probe data in the highlighted section is not considered. The summation of sample window length and calculation time,  $(\Delta T_S + \Delta t_C)$ , is the period at which the diagnostic output is reported. Therefore, the feedback frequency is equal to  $1/(\Delta T_S + \Delta t_C)$ . Reducing either time parameter directly improves feedback frequency with unique challenges and drawbacks. Decreasing sample window length,  $\Delta T_S$ , is the simpler alteration, but reduces accuracy of the time series correlation.

In an effort to optimize both operations for accuracy as well as processing speeds, data treatment is kept to a minimum. Images fed to the CNN are adjusted using only a median

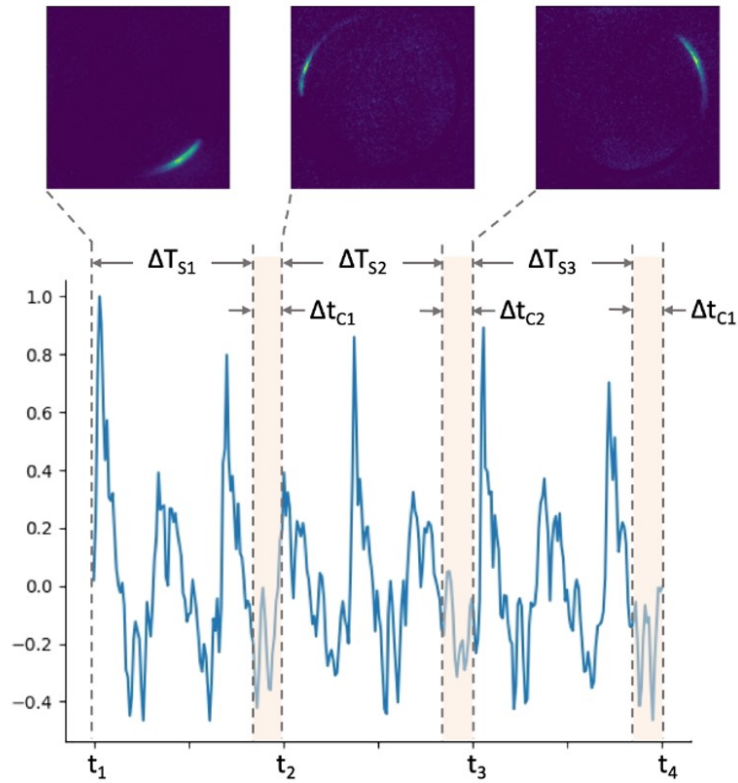


**Figure 5.2:** Data sampling for image and time series data integration

blur digital filter. Prior to autocorrelation, ion probe data windows are filtered using a Butterworth digital filter with a filter order of 5 and a critical frequency of 6000 Hz normalized by the Nyquist frequency, being 125 kHz or half of the sampling rate. The critical frequency is the frequency at which the response of the filter is equal to the square root of 0.5. The filter gain response is plotted in Figure 5.3.

Finally, this technique is adapted to be executable within a Python environment during RDE operation. The hardware used to acquire live data is detailed in the earlier Experimental Setup section. Prior to each diagnostic run, the environment session is established and prepared with all operations that precede diagnostic execution. Connections to the Basler camera, via the USB 3.0 connection, as well as the NI cDAQ chassis, via ethernet connection,

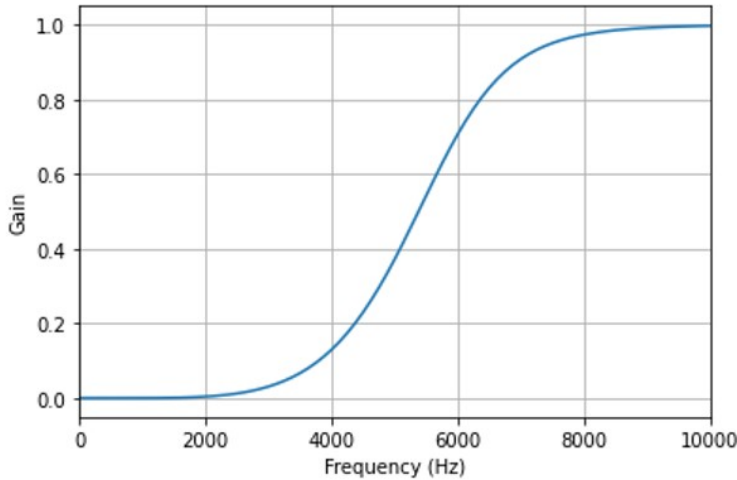


**Figure 5.3:** Frequency response of digital Butterworth filter

are established and configured using Pylon and PyDAQmx libraries respectively. Empty variables are created to store incremental diagnostic outputs and performance metrics, and the CNN model and weights are loaded into the environment. The completed CNN, as discussed in the previous work, is small in memory space and can be uploaded and utilized with only a few lines of code. After initialization measures are complete, the environment session is prepared to perform the diagnostic during RDE operation. Throughout operation, all raw data as well as calculated values and timing metrics are recorded. Recorded data is saved after each run, and the environment session reinitialized. Intuitively, these efforts will target the minimization of the shaded areas, or  $\Delta t_{Ci}$ , in Figure 5.2 for higher feedback frequencies which is a crucial step in optimizing the system with the goal of achieving real-time monitoring within the RDE flow field.

### 5.3 LAB ACQUISITION RESULTS

The diagnostic requires short-gate,  $10 \mu\text{s}$ , intensified down-axis images and short windows of ion probe data. By executing the method described in the previous section, each iteration

provides wave number, wave direction (not plotted), iteration time, wave frequency, and individual wave velocity. Each of these values are recorded over individual RDE runs, and plotted alongside example images and ion probe data in the figures to follow. It is important to note, that because this study is concerned with the performance of a real-time diagnostic, no post-processing or digital filtering has been performed to the presented results. All classifications and calculations plotted represent the output of the diagnostic during live RDE operation. In each subplot, overall medians are plotted as red lines, and the sliding window median of wave number is plotted as a blue line. The sliding window median is used to relate ion probe frequency, calculated through auto correlation, to the individual wave velocity using Equation 5.2. A single image and ion probe window are recorded for each iteration. However, a sub-sampling of four images and one ion probe window is plotted in each diagnostic example.

Figure 5.4 shows a diagnostic output for a quasi-steady 2 wave run whose operating conditions are an air temperature,  $T_{air}$ , of 320°F, equivalence ratio,  $\Phi$ , of 0.75, and initial back-pressure,  $P_{back}$ , of 0 psig. Images in Figure 5.4 on the upper right show a clear 2 CW wave mode, with an addition point of pixel intensity associated with a thermocouple. Images are 640x480 pixels with pixel depth of 10 bits. The utilized image classification CNN was trained on images from a Photron FASTCAM SAZ with a cropped size of 301x301 pixels. Therefore, images captured by the Basler camera are cropped to square proportions centered about the RDE annulus, and resized to match the size and format of the desired CNN input.

The classification of wave number experiences occasional misclassifications of 1 wave, often when the pixel intensity and apparent size of the second wave is significantly less than the first. Even in the instances of misclassification, the sliding window median (blue line)

reflects the true mode present with only a few points of error across a 17 second sampling (60 iterations).

Ion probe signals exposed to less extreme operating conditions and more stable wave modes display clean, well-defined peaks (lower right). This type of ion trace results in stable frequency outputs across the entire run, like what is seen in Figure 5.4. The sliding window median is used to relate the frequency values, to individual wave speeds, averaging 6492 Hz and 1623 m/sec respectively, and plotted in the bottom-middle portion of Figure 5.4. The iteration time across this run averaged around 0.28 seconds, or 3.57 Hz, which is slightly higher than experienced across runs presented in Figures 5.5- 5.7.

The diagnostic has been evaluated over more than one hundred runs. Figures 5.4- 5.9 serve as a sampling of diagnostic outputs with the purpose of displaying the diagnostic performance across varying operating conditions, measurement quality, and wave modes. Figure 5.5 mirrors the format of Figure 5.4, displaying the diagnostic output across a steady 3 wave operational window with conditions  $T_{air} = 400^{\circ}\text{F}$ ,  $\Phi = 0.75$ , and  $P_{back} = 0 \text{ psig}$ . Again,

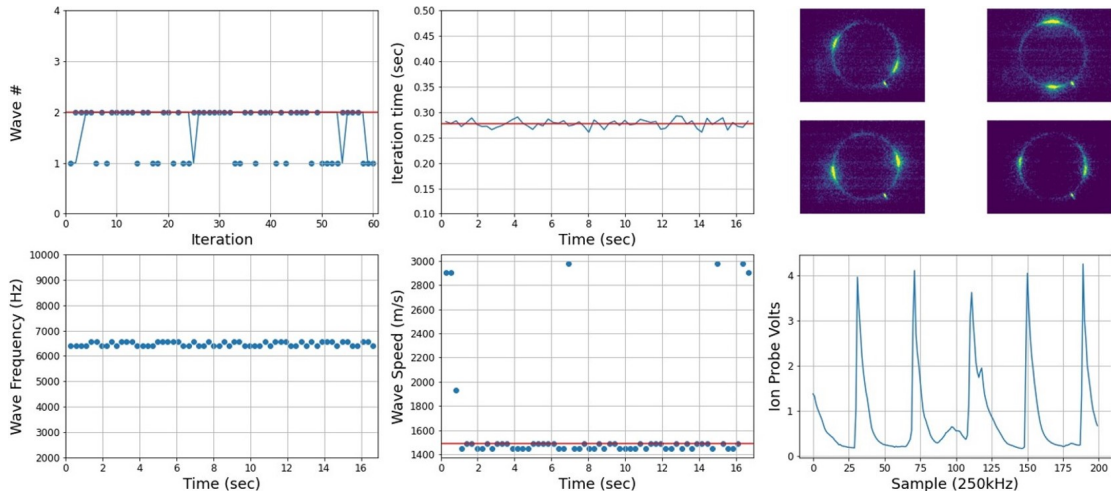


**Figure 5.4:** Diagnostic output monitoring 2 CW steady waves with operating conditions:  
 $T_{air}=320\text{F}$ ,  $\Phi=0.75$ ,  $P_{back}=0 \text{ psig}$

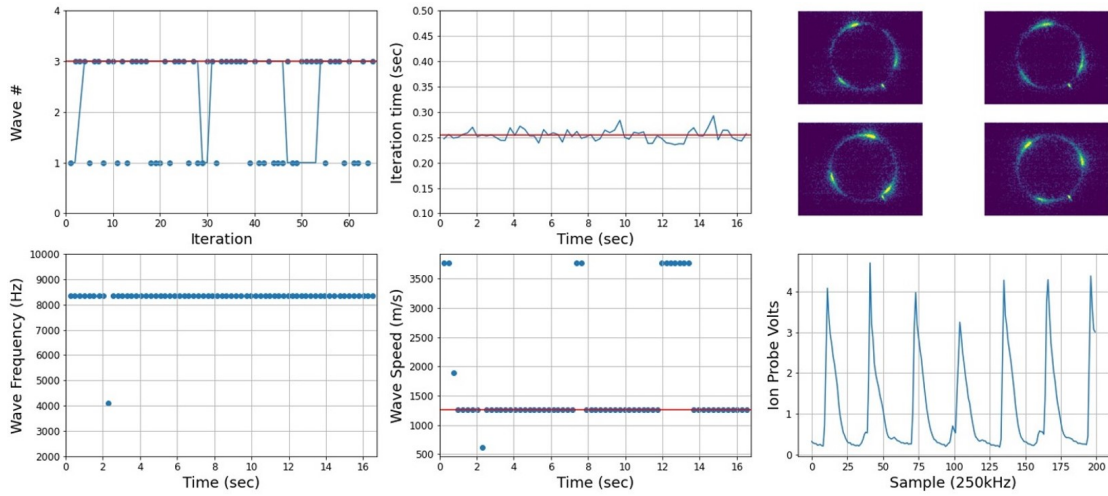


**Figure 5.5:** Diagnostic output monitoring 3 CW steady waves with operating conditions:  
 $T_{air}=400^{\circ}\text{F}$ ,  $\Phi=0.75$ ,  $P_{back}=0 \text{ psig}$

the images show a fairly clear wave mode, which is classified by the CNN with a fair degree of accuracy. In most cases of error, the sliding window median corrects the wave count. Misclassification of higher wave counts is expected as pixel intensity decreases with a decreasing wave strength given a constant gain setting on the intensifier. Autocorrelation of the ion signal results in a very steady wave frequency of 8333 Hz and resultant wave speed of 1257 m/sec. Iteration times averaging 0.25 sec led to a diagnostic feedback rate of 4 Hz.

Results presented have shown the performance across extended run times allowed by the water-cooled rig. Although the feedback rate could be improved, it still offers valuable information across shorter runs. Diagnostic outputs across a 5 second run with 2 waves present throughout are shown in Figure 5.6. Operating conditions are  $T_{air} = 320^{\circ}\text{F}$ ,  $\Phi = 0.75$ , and  $P_{back} = 0 \text{ psig}$ . Across the shortened run time, 20 iterations are performed offering calculated values of 6410 Hz and 1488 m/sec for ion probe frequency and individual wave speed, respectively. These calculations were performed at an average iteration time of 0.27 sec and feedback frequency of 3.71 Hz. While improvement of iteration speeds is necessary moving

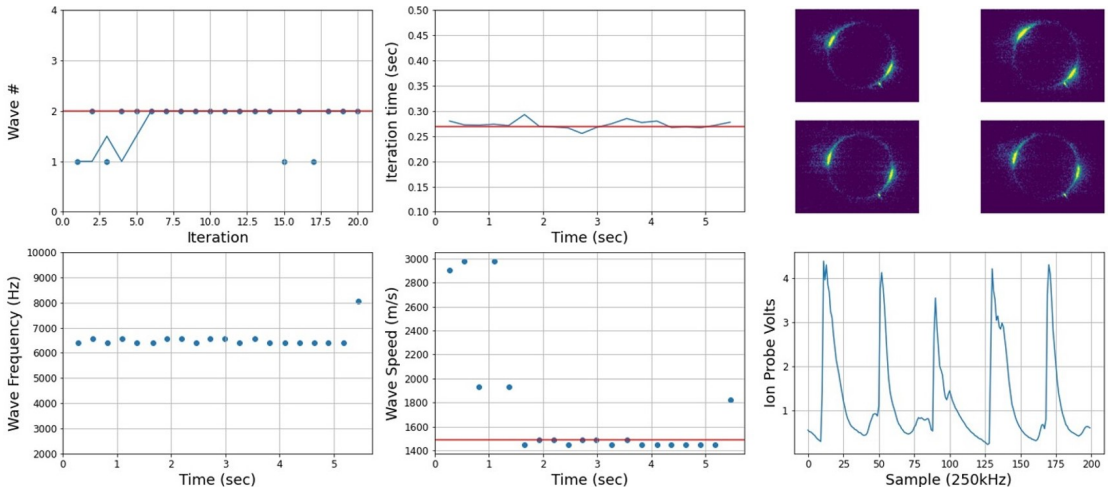


**Figure 5.6:** Diagnostic output monitoring 2 CCW steady waves across short run of with operating conditions:  $T_{air}=320^{\circ}\text{F}$ ,  $\Phi=0.75$ ,  $P_{back}=\text{opsig}$

forward, these results show the useful application of the proposed method on shorter runs more common throughout the RDE community, even considering the preliminary state of the method.

In every example of diagnostic output, an initial error of wave classification is present during the first two seconds, or more generally during startup because detonation waves are more sporadic and more difficult to image during startup as the system attempts to stabilize. Because this method is developed as a tool to accompany technology maturation as well as offer a potential means of active control in the experimental setting, startup conditions are of less interest than the ability to monitor steady conditions.

The quality of ion probe measurements has expected effects on diagnostic outputs. Clarity of the signal can be impacted by backpressure, port location, probe condition, and other factors. Results to this point have been generated using ion probe data from a port located 2.5 cm downstream of the injector and the anticipated detonation plane. Additionally, these results reflect runs with no initial backpressure. Diagnostic outputs for a run utilizing an

ion probe located 5 cm from the injector are plotted in Figure 5.7. Operating conditions for this 3-wave run are  $T_{air} = 400^{\circ}\text{F}$ ,  $\Phi = 0.6$ , and  $P_{back} = 0 \text{ psig}$ . The ion probe signal is visibly noisy, and the passing of wave fronts is less distinct. Therefore, as seen in the wave frequency plot, autocorrelation inherits a large degree of uncertainty. Unlike the previous subplots, Figure 5.7 includes a spectrogram of recorded pressure, with transducer in an infinite tube pressure (ITP) configuration, in place of iteration time enabling the comparison at a similarly located port and the output of the diagnostic. Like the current method, the spectrogram results at startup are not immediately stable. It can be seen that although the diagnostic frequency output shows more dispersion than the previous results, a similar behavior of deviation and secondary frequency can be seen in the spectrogram. Still yet, the autocorrelation of the downstream probe doesn't properly distinguish primary and secondary frequencies resulting in the underestimation of frequency and subsequent calculations of uncharacteristically low wave speeds. For this reason, further use and development of an RDE diagnostic should use data recorded at optimal locations to cleanly define the detonation wave in the absence of more computationally expensive time series data analysis.

Although the results in Figure 5.7 are presented to highlight the impact of ion data quality, the image quality remains satisfactory. Four images from the run are shown in the subplot and show a distinct 3 CW wave mode with little pixel intensity outside of detonation wave profiles, offering contrast surpassing that of previous images. In fact, only four misclassifications occur after startup, all of which are negated by the sliding window median. The effects of image quality should be similarly considered with respect to classification accuracy.

Similar to ion probe signals, image quality may be affected by backpressure, preheat temperature, filtering, and camera and intensifier settings. Two examples of poor image quality and the resulting classifications are shown in Figures 5.8 and 5.9. Because these examples

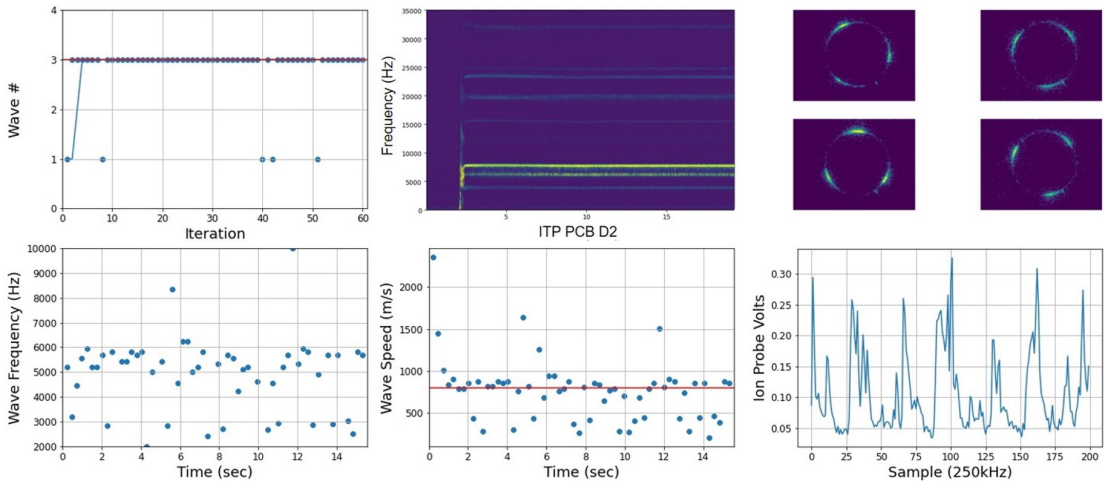


**Figure 5.7:** Diagnostic output monitoring 3 CW steady waves with down-axis ion data at operating conditions:  $T_{air}=400^{\circ}\text{F}$ ,  $\Phi=0.6$ ,  $P_{back}=0 \text{ psig}$

serve to specifically demonstrate effects of image quality, the full diagnostic outputs are not shown. Figure 5.8 specifically shows unfocused images where two thermocouples, circled and labeled in first image, consistently appear across all iterations. Without further digital filtering or masking to remove the thermocouples, the CNN classification of wave number remains accurate beyond startup, suggesting a higher resilience for image quality compared to ion data.

A second example of lesser image quality is shown in Figure 5.9 where a backpressure of 15 psig resulted in significantly reduced pixel intensities. Because the wave mode within these images is more difficult to discern, only two images are shown in the state at which they are fed to the CNN. For the benefit of the reader, further digital filtering was performed on those two images to highlight the 3-wave mode present. Again, the CNN is able to classify the number of waves present in the annulus despite a heavily deteriorated image quality. Ultimately, this resilience is due to the presence of similarly poor images within the training image set, which spans a variety of operating conditions including elevated backpressure. Unlike the

images shown in Figure 5.8, which are out of focus, images in Figure 5.9 do fall within the RDE's operational domain. In addition to the implications of image quality, Figure 5.9 also benchmarks an additional set of operating conditions,  $T_{air} = 345^{\circ}\text{F}$ ,  $\Phi = 0.45$ , and  $P_{back} = 15$  psig at which the diagnostic adequately performs.

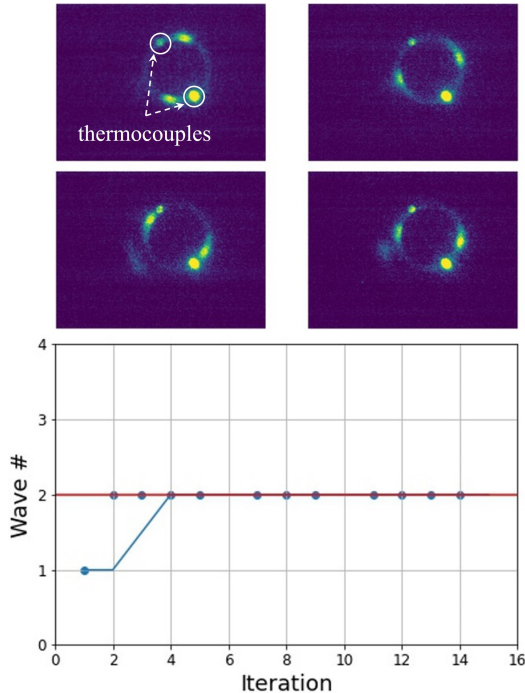


**Figure 5.8:** Diagnostic output monitoring 2 steady waves with visible thermocouples at operating conditions:  
 $T_{air}=295^{\circ}\text{F}$ ,  $\Phi=0.77$ ,  $P_{back}=0$  psig

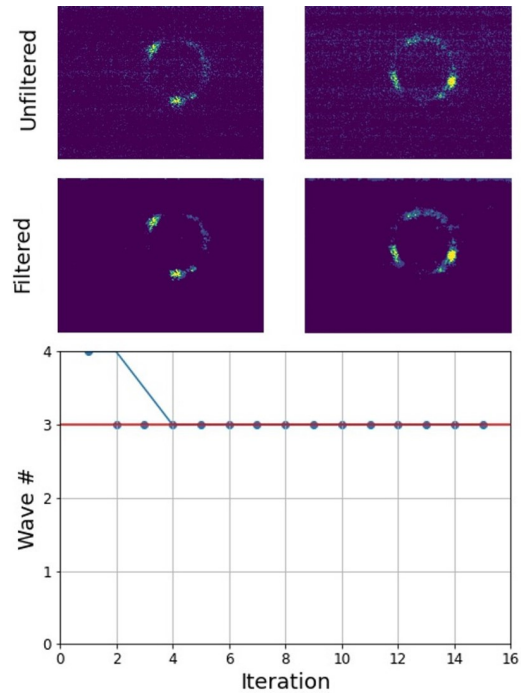


**Figure 5.9:** Diagnostic output monitoring 3 steady waves with images affected by backpressure at conditions:  
 $T_{air}=345^{\circ}\text{F}$ ,  $\Phi=0.45$ ,  $P_{back}=15$  psig

In each presented case, iteration times showed averages around 0.25 seconds. Storing all outputs of the diagnostic as well as data used to monitor the diagnostic accounts for a significant portion of overall calculation time. To reduce this time and further improve the diagnostic, the volume of saved data beyond raw images and ion probe data can be reduced or completely eliminated. However, classification and calculation time accounts for approximately 20% of total iteration time, meaning sample window times and data acquisition requires 80%

of the current diagnostic time. Therefore, additional options to increase diagnostic speeds by reducing acquisition time, including reduction of image size, shortened time series windows and improved hardware should be considered. Each of these means of improvement will be considered as future work.

A second diagnostic using a time series classification (TSC) network<sup>83</sup> trained in Chapter 7 will also be deployed in the lab environment and compared to the results of the current method. Eventually, the output of the superior diagnostic may be used to achieve active control of equivalence ratio for a preferred wave mode or wave speed. At this time, a preferred wave mode or wave speed based on RDE operating conditions are not abundantly clear. However, development of diagnostics and control schemes will inevitably be necessary. It is believed that the speeds of machine learning techniques will be a necessary component of data processing nearing a time scale comparable to what will be required by eventual RDE industrial integration.

#### 5.4 OVERVIEW OF OUTCOMES

Increased operation times in facilities equipped with cooling strategies, such as the water-cooled rig used in this study, facilitate the development of highly efficient detonation characterization techniques which may be optimized for real-time detonation wave monitoring. A real-time RDE diagnostic was developed utilizing a convolutional neural network (CNN) developed to classify wave modes from individual down-axis images and a correlation technique applied to an ionization current, or ion probe data. Live image collection was performed using a common area-scan camera operating at very low speeds relative to conventional RDE high-speed imaging, paired with an intensifier, and live ion probe data was acquired via an NI cDAQ chassis. Data acquisition within the Python diagnostic environment relied on Pylon

and PyDAQmx Python libraries. The diagnostic code was integrated and deployed in the RDE lab environment for use during live runs.

Across a variety of operating conditions and wave modes, the developed method was evaluated and found to offer beneficial outputs as a result of combining the spatial certainty of down-axis images, classification speeds of the CNN and high-quality ion probe measurements. Although the current study utilized ion probe data, the proposed method could be employed with other point measurement time series data, such as ITP pressure transducer data or any other high-frequency sensor signal. However, any reduction in data quality or clarity of wave fronts drastically reduces the accuracy of the correlation technique, as was shown in the previous section. Poor image quality showed lesser impact than ion data affected by port locations. Sporadic misclassifications of wave mode were mostly bypassed by a sliding window median used to inform later calculations. Reported diagnostic feedback rates around 3-4 Hz exceed existing methods with comparable mode certainty. Improvement of diagnostic accuracy and speed will be considered within future work. The presented method achieves live RDE monitoring in the laboratory environment independent of post-processing, which is believed to be a crucial step towards intelligent RDE active control. This new capability will contribute to future RDE maturation studies of turbine integration, and serves as a new milestone of machine learning and computer vision techniques applied to RDE technology.

*I like to think of ideas as potential energy. They're really wonderful, but nothing will happen until we risk putting them into action.*

Mae Jemison, American engineer, physician, and  
NASA astronaut

# 6

## Object Detection

TO REDUCE DATA PROCESSING TIME AND OFFER REDUCED INTERVAL wave velocity data compared to that of traditional image analysis techniques, a computer vision object detection methodology is proposed to quickly detect individual detonation waves within a single down-axis image. Detonation waves are detected in individual images by implementing a You Only Look Once (YOLO) object detection network trained using RDE high-speed camera images. The location and rotational direction of each wave is detected, and locations are

tracked to calculate frame-to-frame wave velocity across a series of frames. Analysis of the effect of annotation box size is presented for standard image proportions, demonstrating lower uncertainty in wave speed calculation with smaller bounding boxes, while larger bounding boxes more accurately predict wave direction. An additional network is trained on linearized images which unwrap the RDE annulus pixel region to a reduced image size. Linearized annotations are produced for new experimental images at 9.5 frames per second. Uncertainty analysis estimates a total uncertainty of  $\pm 3.8\%$  for detonation wave frame-to-frame velocity calculations, using the linearized annotation boxes. This new method offers great reductions in data processing times, as a step toward improved monitoring of detonation waves within an RDE.

The process presented in this section includes three distinct efforts. The first effort is dedicated to the creation and treatment of an image data set spanning a variety of wave modes and operating conditions. The second major effort develops and trains a neural network based on the YOLO family<sup>122</sup>, which can detect and classify each individual detonation wave within an image. The third and final effort processes the output of the network to determine wave mode, velocity and frequency. It should be noted that steps one and two only need to be performed once, as the trained neural network would be applied to future datasets without the need for additional training thus providing a rapid means of quantifying detonation wave performance.

#### 6.0.1 IMAGE TREATMENT

In order to adequately train an object detection network, a dataset of images must be selected. To prevent overfitting to features that can be associated with artifacts of specific test dates or wave modes, variety in images is a necessity. The image set created for this study includes

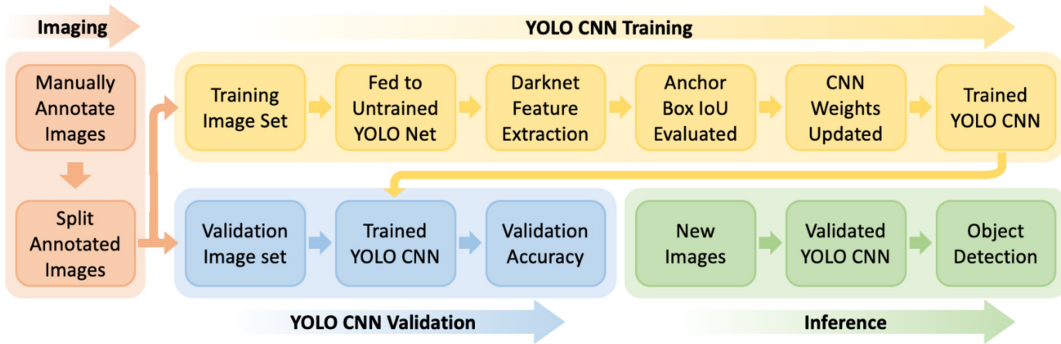


**Figure 6.1:** YOLO CNN Development Method Flowchart

500 images which were captured across various dates, operating conditions, and experimental locations including NETL and Purdue University<sup>119,94,120</sup>. While 500 images may seem like a low threshold of data volume compared to what is required by other artificial intelligence techniques, many images containing multiple detonation waves will provide multiple annotations in the Network Development effort.

## 6.1 NETWORK DEVELOPMENT

As mentioned in an earlier section, object detection, the goal of the current study, varies significantly from image classification. However, the phases of development are very similar for both techniques due to their shared reliance on CNNs, leading to a methodology flowchart similar to those used in previous studies<sup>44</sup>. However, differences among sub-steps should be recognized and regarded with great significance. The current method, outlined in Figure 6.1, includes four major phases: Imaging, YOLO CNN Training, YOLO CNN Validation, and Inference.

### 6.1.1 IMAGING PHASE

To begin the Imaging phase, images from the created data set should be manually annotated. Manually annotating images, which is arguably the most crucial step of this process, includes identifying each detonation wave present in an image, creating a bounding box around each ROI, and labelling each bounding box according to wave direction. The process of annotation can be accomplished using a custom annotation tool, or one of several publicly available annotation platforms. Object detection models are commonly configured to detect as many as 20-80 object category labels such as a plane or a dog, as required by popular competitions<sup>123,124</sup>. Annotations for this study, however, will be labeled as one of only two object categories: clockwise (CW) or counterclockwise (CCW) detonation waves. Examples of wave annotations are shown in Fig. 6.2 such that annotations of CW waves are shown with green bounding boxes while those of CCW waves are shown with orange bounding boxes. To again highlight the major difference between this work and the previous study, predicted image classification labels that include wave number as well as direction of rotation are shown in the top left corner of each example image. Image classification labels differ drastically from the bounding boxes predicted by the current object detection method. In images (a) and (b) image classification labels are 1CCW and 2CW, respectively. Annotation boxes still inform wave number and direction while providing additional information regarding the location of each wave. The previous image classification network would identify and assign a single label to images (c) and (d) containing counter-rotating (CR) detonation waves, while object detection identifies each detonation wave and its specific rotational direction<sup>46</sup>. The ability to properly identify and analyze CR wave modes, occurring when one or more pairs of CW and CCW waves are present, is critical to the previous and the current work. All wave modes in the studied RDE are a variation of only CW waves, CCW waves, or both to create

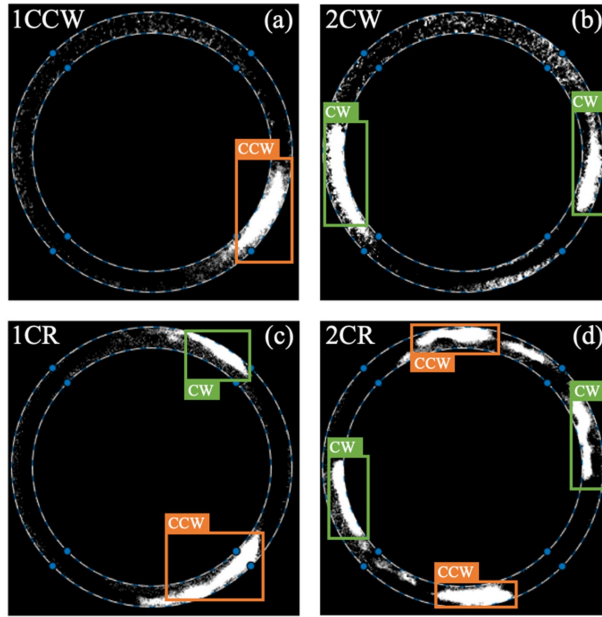


**Figure 6.2:** Annotation of RDE down-axis images of (a) 1CCW (b) 2CW (c) 1CR and (d) 2CR modes <sup>46,119</sup>

a CR mode. Therefore, the use of bounding boxes also results in the ability to properly analyze wave modes not present in the training set, which was otherwise not possible with image classification. It is important to note that the annotations must be performed manually to generate an annotated image set which is then split into training and validation image sets.

#### 6.1.2 CNN TRAINING PHASE

Once split into respective image sets, the YOLO CNN Training phase may begin. As is common with most applications of neural networks, training is initialized with pre-trained weights that are tuned to the data set of interest. The pretrained weights used in this study are associated with Darknet, an open source feature extraction framework <sup>72</sup>. Utilizing pre-trained weights, which is a common form of transfer learning, shortens the training process by initializing weights that have previously trained on similar object detection tasks. To train

the network for this specific problem, images and their annotations are first fed to the initialized YOLO network. As the network repeatedly evaluates the entire image set, referred to as an epoch, parameterized weights are internally updated. At each update, predicted annotation locations, sizes and wave classifications are compared to values associated with manual annotations. Unlike the previous study, a standard accuracy measurement is not possible since the size and location of the YOLO prediction must be compared. To evaluate both outputs, Intersection over Union ( $IoU$ ) is calculated for each predicted annotation. The  $IoU$  metric is widely used in object detection <sup>125</sup> and is calculated using Equation 6.1 where  $GT_i$  represents the area of the ground truth annotation and  $P_i$  represents the area of the predicted annotation. The spatial significance of  $IoU$ , or Equation 6.1, is illustrated in Figure 6.3. While  $IoU$  is calculated for each annotation box, an overall measurement of performance is calculated at each epoch using the multi-part YOLO loss function <sup>72</sup>. The YOLO loss function is a sum-squared error approach, accounting for classification loss, localization loss, and confidence loss. Once the performance meets a desired threshold, specifically when the validation loss does not improve over 10 epochs, the weights are finalized, and the network is deemed a trained network.

$$IoU = \frac{GT_i \cap P_i}{GT_i \cup P_i} \quad (6.1)$$

### 6.1.3 CNN VALIDATION PHASE

Once training is complete, the YOLO CNN Validation phase can be performed. To validate the model, the validation image set is fed to the trained YOLO CNN without annotations. The trained CNN is used to perform object detection, and again the loss and  $IoU$  of predicted anchor box locations, sizes and object classifications can be evaluated. If performance exceeds

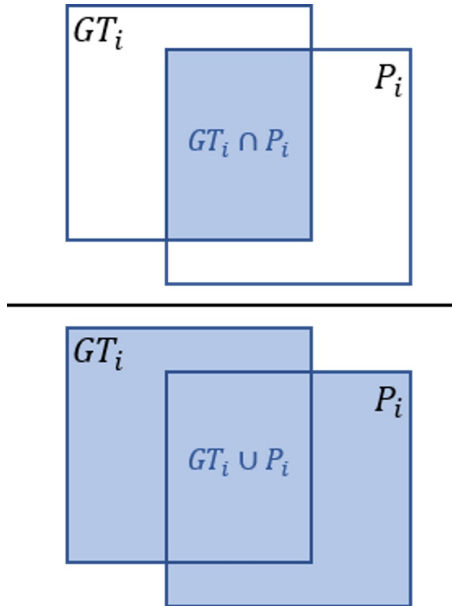


**Figure 6.3:** Visualization of Intersection over Union (IoU)

the desired threshold, the trained network is then considered to be a trained and validated YOLO network.

#### 6.1.4 INFERENCE

From the point of network validation, the trained network is able to call on finalized weights and therefore available to detect CW and CCW waves and their respective locations in new laboratory images. That is to say the phase of Inference is treated as a tool which can be utilized indefinitely although detection is limited by training, so for example a network trained on detonation objects could not predict the presence of deflagration. Detections output dimension clusters which include four coordinates for each anchor box as well as the object classification and the network confidence of prediction. This is unique to the current object detection method, where the previous image classification method only output a single classification of the entire image. Although the network is finalized, the Inference technique is

further refined in two distinct ways, both ensuring the output of the network meets the determined standard required by the current study. The first alteration increases the threshold of confidence required for a predicted annotation to be reported. The second refinement calls on the *IoU* formulation to enable non-maximum suppression. Non-maximum suppression is a computer vision technique used to prevent the reporting of multiple, overlapping bounding boxes for a single object <sup>126</sup>. In simplest terms, when the network attempts to predict two annotations of the same label that are overlapping, *IoU* of the two boxes is calculated and when that *IoU* exceeds a chosen threshold, the annotation with the lower confidence is discarded. Due to the physical understanding of detonation waves in the RDE, the improbability of two waves of the same rotational direction overlapping in an image allows the non-maximum *IoU* threshold to be significantly increased. Under these conditions, anchor boxes predicted by the proposed object detection method can be used in the following effort of wave speed calculation.

#### 6.1.5 NETWORK OUTPUT PROCESSING

Once objects are located and the number of waves and wave mode are determined, post processing can be performed to determine individual wave speed. Progression of each detonation wave can be tracked from image to image using the dimension cluster output of the Inference phase of the YOLO CNN. Although the network will not associate objects from one frame to the next, high framerates ensure that wave progressions between frames remain minimal. Therefore, a simple assumption can be made such that when multiple waves are detected, each wave corresponds to the wave in the next frame that is closest to the original position. Because the waves detected are also classified as CW or CCW, counter-rotating waves are less likely to be incorrectly labeled. Additionally, CW and CCW waves within a counter-rotating

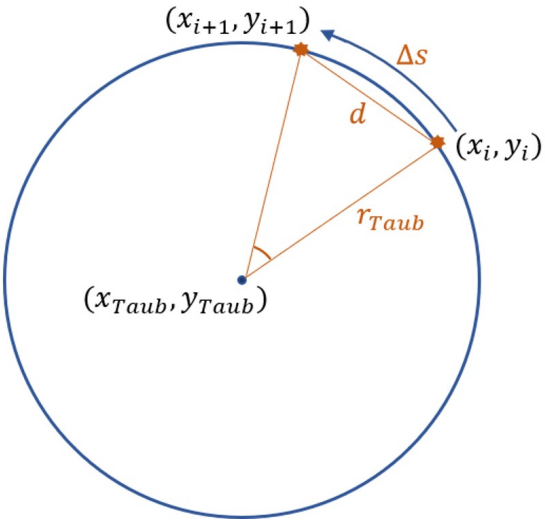


**Figure 6.4:** Geometric relationship leveraged for wave velocity calculation

wave pair can be tracked independently to compare velocity variations between oppositely rotating wave groupings. In each case, the progression of each wave can be compared to the framerate and nominal annulus diameter to determine wave velocity. The process is initiated by first finding the linear distance,  $d_i$ , between the centroids of two bounding boxes in successive frames using Equation 6.2 where the annotation centroids in frames  $i$  and  $i + 1$  are located at coordinates  $(x_i, y_i)$  and  $(x_{i+1}, y_{i+1})$  respectively. Assuming both centroids lie along the annulus circle with calculated radius  $r_{Taub}$ , the angle of rotation between frames,  $\theta_i$ , can be calculated using Equation 6.3. To finally calculate the velocity of the wave, the true distance traveled along the circumference of the annulus must be determined according to the geometric relations outlined in Figure 6.4.

By relating the angle of rotation and the annulus physical radius,  $r_{RDE}$ , to the traveled arc length,  $\Delta s$ , Equation 6.4 can be used to calculate wave velocity,  $\vec{V}_i$ , for a given frame. Additionally, successive frames can be used to correct sparse errors of detected wave direction.

$$d_i = \sqrt{(x_{i+1} - x_i)^2 + (y_{i+1} - y_i)^2} \quad (6.2)$$

$$\theta_i = 2 \sin^{-1} \left( \frac{d_i}{2r_{Taub}} \right) \quad (6.3)$$

$$\vec{V}_i = \Delta s FR = r_{RDE} \theta_i FR \quad (6.4)$$

## 6.2 BASELINE NETWORK PERFORMANCE

To prepare for the training of the network, an image set of 500 images were manually annotated. Although this is a relatively small collection of images compared to the data volume collected from the high-speed camera, the costs of manual annotation were minimized to that which was required to successfully train the networks. Among the 500 images, a variety of wave modes, dates and operating conditions were covered. Due to multiple waves being present in many images, a total of 771 annotation boxes were manually created and labeled. Those annotations were converted to a text-based YOLO format which calls on the specified image file path and associates that image with the dimension cluster of each annotation. With the inputs available, the network can begin to train the parameterized weights. As mentioned in a previous section, the loss of the updated network is evaluated and recorded after each epoch. The behavior of the loss reduction over the process of training is shown in Figure 6.5. The YOLO loss function computes the sum-squared error of classification loss, localization (coordinate) loss and confidence loss between the incremental network output and ground truth data.

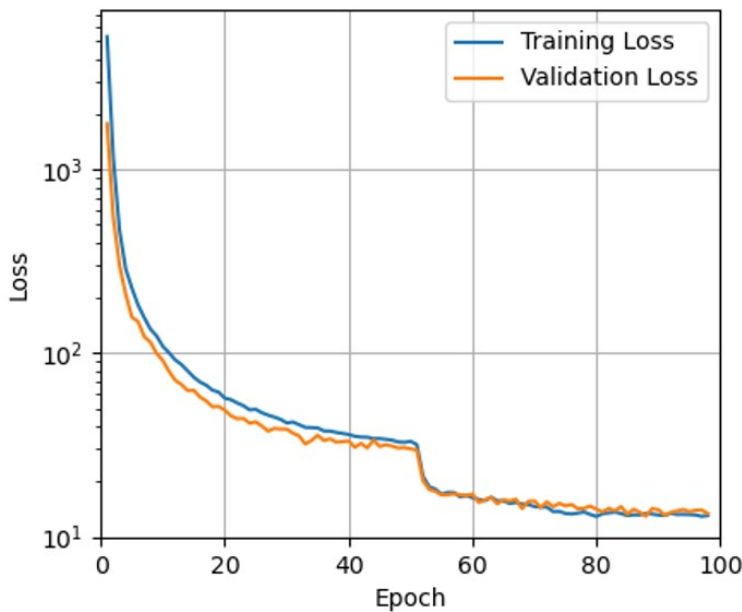


**Figure 6.5:** YOLO training and validation loss across 100 epochs

In this figure, training loss and validation loss are both shown to decrease considerably in the first 20 epochs, which is expected as the network begins to understand features extracted from the image set. The initially decreasing loss is followed by a near-plateau around 50 epochs and then a sharp decrease is experienced in both trends at the 52<sup>nd</sup> epoch. The major and instantaneous improvement in loss is due to a significant reduction in batch size from 32 to 4 images. Neural networks attempt to minimize a loss function of the training parameters. At a smaller batch size, the gradient of the loss function is updated using fewer images. Therefore, model parameters are updated in smaller “steps” toward the loss minimum resulting in the refinement of the network over the final 48 epochs. Larger batch sizes are used in the early epochs as an effort to avoid converging to local minima while also optimizing of computational budgeting. Unlike a percent accuracy measurement, there is no given or accepted threshold of loss. Instead, its slope is used as a measure of progressing learning, informing reduced learning rates and early stopping to prevent overfitting of the model.

Once the network weights are finalized, the network is available for inference efforts. However, as mentioned earlier, confidence and IoU thresholds must be altered to ensure proper results and to perform non-maximum suppression. Appropriately altering each threshold is done by simply feeding new, unseen images to the trained YOLO network, performing inference at low thresholds of confidence and IoU, and increasing each threshold independently until the results are satisfactory. Examples of the resulting improvement are shown in Figure 6.6 where non-maximum suppression and confidence thresholding have direct impacts on network output respectively. Specifically, Figure 6.6(a) shows an example image where 2 clockwise (CW) waves are present, but 3 bounding boxes are predicted. It can be seen that two of the predicted bounding boxes are overlapping on the same wave and can therefore be resolved by increasing the *IoU* threshold. Once the *IoU* threshold is increased to a value that encompasses the scenario of these two overlapping boxes, the box with the lower confidence score, displayed right of each classification, is disregarded, resulting in a more accurate output, shown in Figure 6.6(b). Figure 6.6(c and d) displays an instance where confidence thresholding plays a major role in network output. In Figure 6.6(c) an image containing 1 counterclockwise (CCW) wave is present, but an additional CW bounding box is predicted. The confidence of the incorrect prediction corresponds to a very low confidence value of 0.19 and can be disregarded by simply increasing the confidence threshold value. The optimal values of confidence and IoU thresholding vary between image types and network iterations but are easily altered with minimal effort.

### 6.3 ANNOTATION SIZE REFINEMENT

Having demonstrated that an object detection network can be trained to accurately locate and label individual detonation waves, it is possible to further refine the network for im-

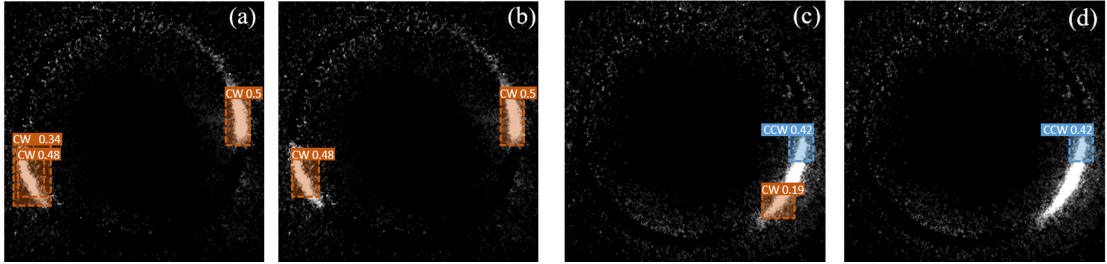


**Figure 6.6:** Results of Non-maximum Suppression: (a) example image before  $IoU$  thresholding, (b) example image after  $IoU$  thresholding Results of Confidence Thresholding: (c) example image before confidence thresholding, (d) example image after confidence

proved end usage. Because velocity calculations, not solely successful object detection, are the end goal of this study, it is beneficial to study the impact of annotation geometries. As with any supervised learning endeavor, the output of the network inherits the form of the input created by the practitioner. Therefore, the variation in annotation size and location associated with the training data set will be directly reflected in the network predictions, which has direct implications on the upcoming velocity calculation. Specifically, irregularly sized and larger annotation boxes are found to create larger errors in velocity calculations while smaller, uniform bounding boxes result in reduced classification accuracy of rotational direction, which is shown in a later section. In order to form a more encompassing understanding of these relationships, multiple networks were trained with various annotation styles. Examples of each style are depicted on a sample image in Figure 6.7.

The example image in Figure 6.7(a) shows two clockwise waves. The initial annotation style in Figure 6.7(b) encompasses the entire detonation wave, and has a strong ability to properly identify wave direction. The second iteration in Figure 6.7(c) attempts to reduce average annotation area to refine velocity calculations. However, simply reducing average annotation area did not fully resolve the issue of large velocity fluctuations as the centroid location relative to the wave front remains inconsistent from frame to frame. The final iteration

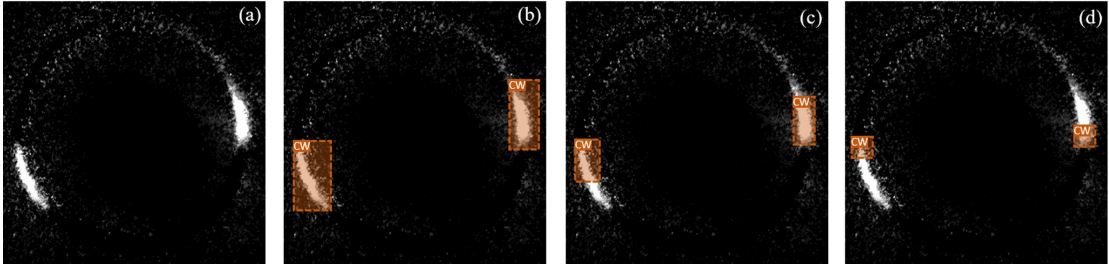


**Figure 6.7:** Progression of manual annotation variations on an image containing 2 CW waves

of annotation style shown in Figure 6.7(d) utilizes small square annotation boxes consistently centered about a location just behind the wave front. A consistent relationship between wave profile geometry and annotation centroid results in a more accurate and stable velocity calculation.

For variation of each annotation style shown in Figure 6.7, a network is trained according to the proposed methodology. In order to better evaluate the expected improvements in velocity calculations resulting from varying annotation styles, each network was used to perform predictions on a test image set. The centroids of the annotation boxes were then used to generate a best-fit circle using the Taubin fit algorithm. Finally, the root-mean-square error,  $RMSE$ , is calculated for each centroid radius,  $\hat{r}_i$ , relative to the Taubin center point,  $(x_{Taub}, y_{Taub})$ , and the Taubin radius,  $r_{Taub}$ , using Equations 6.5 and 6.6. As a general rule, as Taubin RMSE decreases, the reliability of a subsequent velocity calculation improves.

$$\hat{r}_i = \sqrt{(x_i - x_{Taub})^2 + (y_i - y_{Taub})^2} \quad (6.5)$$

$$RMSE = \sqrt{\sum_{i=1}^n \frac{(\hat{r}_i - r_{Taub})^2}{n}} \quad (6.6)$$

The results of five networks trained on varying annotation styles are recorded in Table 6.1 according to annotation style ( $R_1$ ,  $R_2$ ,  $S_1$ ,  $S_2$ ,  $S_3$ ), average annotation area and Taubin RMSE. An additional annotation style, Lin, is also shown in Table 6.1, and will be detailed in the next subsection. It is shown that the first rectangular style ( $R_1$ ) which corresponds to the example shown in Figure 6.7(b) results in the largest Taubin RMSE. Reducing the area but maintaining the rectangular style, which corresponds to Figure 6.7(c), significantly reduces the experienced Taubin RMSE. In an effort to further reduce Taubin RMSE, three variants of the square annotation style were used, corresponding to Figure 6.7(d). Networks trained with square annotations reported lower values of Taubin RMSE, implying lower variation in wave speed calculations. Generally speaking, a trend is shown that as annotation area decreases, the Taubin RMSE is improved. The centroids predicted by the networks trained using the  $R_2$  and  $S_3$  style are plotted in Figure 6.8 overlaid on the corresponding Taubin fit circle. The figure highlights the consistency of predictions in relation to how tightly they fall along a given circumference for each annotation style. Although both data sets seem to tightly fit the Taubin circle, centroids associated with  $R_2$  show slightly more variance, contributing to the higher RMSE value shown in Table 6.1. Note that in previous studies <sup>46,44</sup> it was documented that in the experimental setup, a portion of the down-axis view (approximately  $60^\circ$ ) of the RDE is partially obstructed. As shown in Figure 6.8, in this region detonation waves are not imaged, and therefore not well detected.

Unfortunately, an expected fault of smaller square annotations is a loss of classification accuracy. By further inspecting the example annotation areas, Figure 6.9 shows the inherent variation of information contained within annotations of different sizes. As pixel area within annotations decreases, so do the contained features that can be extracted and therefore the network's ability to distinguish between CW and CCW waves. The resulting conclusion is

Annotation Style	Area (pixels)	Taubin RMSE
Rectangular (R <sub>1</sub> )	5070	3.391
Rectangular (R <sub>2</sub> )	809	2.311
Square (S <sub>1</sub> )	425	0.973
Square (S <sub>2</sub> )	318	0.907
Square (S <sub>3</sub> )	213	0.886
Linearized (Lin)	320	N/A

**Table 6.1:** Taubin RMSE for varying annotation styles and areas

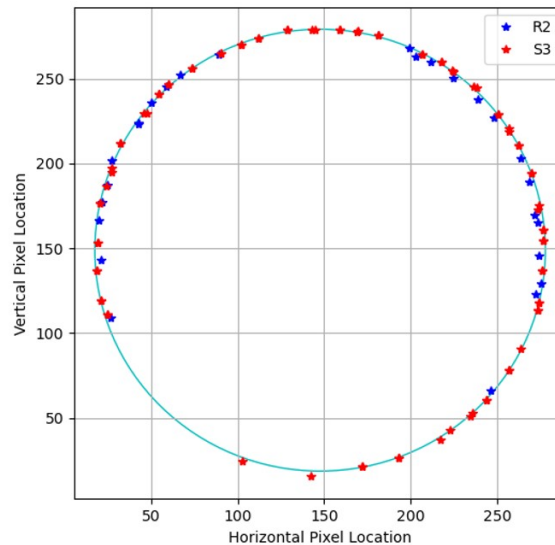


**Figure 6.8:** Annotation centroids predicted by annotation styles R<sub>2</sub> and S<sub>3</sub> and the corresponding Taubin fit circle

that each annotation style is beneficial in differing metrics. If wave direction classification is of most importance to a given study, the larger rectangular style (R<sub>1</sub>) is best suited. On the other hand, if wave velocity is of most importance to the user, a small square size such as S<sub>2</sub> or S<sub>3</sub> would be preferable. Because the final portion of this study is concerned with velocity calculations, and because determination of wave direction is still possible in post-processing, the model trained using style S<sub>3</sub> will be used to generate wave velocity results for the remainder of the text, with comparison to the R<sub>2</sub> style.

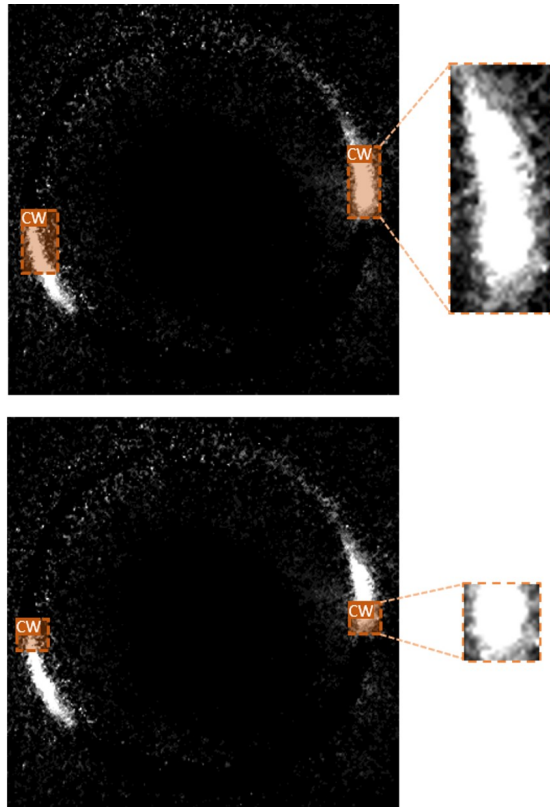


**Figure 6.9:** Highlighting features associated with varying annotation box areas

#### 6.4 CONSIDERATION OF LINEARIZED NETWORK

In an effort to address the errors associated with annotation coordinates and subsequent Taubin fit error, a final variation of the YOLO network is trained for linearized images, which attempt to "unwrap" the RDE annulus region. Linearized images eliminate unnecessary pixels outside of the RDE annulus, reducing total pixels passed to the network, and therefore further improving processing times. In general, square images sized 301x301 pixels are converted to linearized images of size 32x736 pixels according to the method outlined in Section 2.4.2. This pixel rearrangement leads to a 74% decrease in total pixel area. An example image is displayed with azimuthal lines and an S<sub>3</sub> annotation overlaid in Figure 6.10. The lin-

earized image, formed by extracting and concatenating the pixels along each line, the annulus is “unwrapped” to a rectangular format with x- and y-axes corresponding to  $\theta$  and  $(\hat{r}_i - r_{in})$ , respectively. Unfortunately, linearizing a hollowed circular region results in lost pixels, increasing in number with increasing radii. In the current format, 9.9% of the annulus region pixel area is forfeited. While selection of a more sparse angular sampling such as 360 lines would further reduce input image size, it would also result in 55.9% annulus region pixel area loss, which would likely be detrimental to wave feature preservation. The linearized version of the example quadrant and the translated annotation is shown in the lower portion of Figure 6.10, showing the conservation of wave features despite the pixel loss. Fully linearized images are shown in sequence in a later section.

The new annulus orientation enables an annotation style that reflects only the angular location of the wave, simplifying velocity calculations by circumnavigating Equations 6.2 and 6.3. Instead of determining the location of detonation waves in two spatial dimensions, the linear annotation style (Lin) aims to determine only the angular “bin” in which a wave front resides. Lin annotations span the full radius range and are consistently 10 pixels in width, corresponding to a width of  $4.89^\circ$  ( $0.0854$  rad) and an annotation area of 320 pixels. The width of 10 pixels is centered about the wave front to foster recognition of the profile edge. A comparison of an S<sub>3</sub> and Lin annotation is displayed in Figure 6.10. The linearized images are analyzed by an unaltered, flexible YOLO network employed consistently throughout the entire study, requiring only a minimum dimension of 32 pixels for filter compatibility. While it is possible to extract a 1D trace along the Taubin radius, spatial features of the wave front would be lost, likely leading to poor directional confidence and depreciation of velocity calculations. Additionally, object detection for the 1D signal would require a drastically different network architecture which does not align with the scope of the current study.

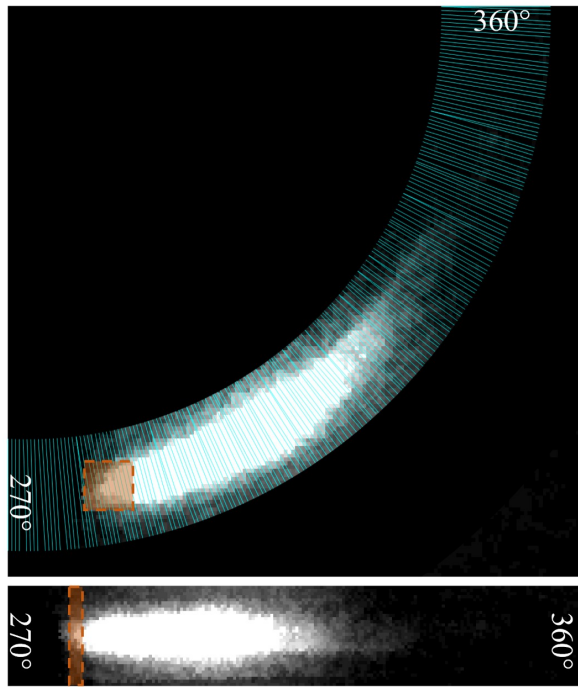


**Figure 6.10:** Example quadrant unwrapped to linearized image with translated annotation box

## 6.5 WAVE SPEED CALCULATIONS

For annotation styles applied to traditional down-axis images, the linear distance between centroids from frame to frame can be related to the circumferential distance traveled, and therefore wave velocity using Equations 6.2 - 6.4, outlined in the previous section. As mentioned in the previous subsection, annotations applied to linearized images (Lin) correspond directly to wave front angular locations. Therefore, these velocity calculations may be performed using only Equation 6.4 where  $\theta_i$  is the 1D shift of the Lin annotation between two consecutive frames. Because these calculations are performed between individual images, substantial fluctuations are expected. The average velocity can also be found as a steady-state measurement.

Using the  $S_3$  annotation style, velocity calculations were performed on a series of 50 images and are shown in Figure 6.11. Larger values like that experienced at frame 43 are associated with images where wave visibility is partially obstructed as an artifact of the experimental setup. With the exception of this outlier, the calculated velocities from frame to frame show more consistent values. To again highlight the benefits of the square annotation style compared to rectangular, velocity across the same set of images is calculated using the network trained using the  $S_3$  and  $R_2$  annotation sets, respectively, as shown in Figure 6.11 and Figure 6.12. While the velocity data shown in Figure 6.11 may not appear to offer drastic improvements to that in Figure 6.12, the lower variance is beneficial to a more accurate average velocity calculation as well as frame-to-frame velocities. Reduction in velocity variance associated with differing annotation styles do follow the trend suggested by the previously calculated Taubin RMSE. It is important to point out that while wave velocity calculations are not novel in the RDE community, this method attempts to perform these calculations with a timestep resolution of 20  $\mu\text{s}$  or 50 kHz frequency. Additionally, a reliable measure of average velocity can be found with as few as 10 frames, or a 200  $\mu\text{s}$  window of operation. Network output frames annotated with  $S_3$  style annotations used to calculate velocity values in Figure 6.11 are shown in Figures A.3 and A.4.

Eliminating the influence of the Taubin RMSE, velocity calculations using the linearized annotation style are shown in Figure 6.13. While the oscillation of calculated velocities may seem more extreme in this case, it can be attributed to a higher number of predicted annotations across the same number of frames as well as an apparent detection of physical wave behavior. Figure 6.14 displays the annotations predicted for frames 3-11 using the linearized annotation style. Visualizing lines fit to the annotation locations across the time and unwrapped circumferential axes is reminiscent of detonation surface plots <sup>44</sup>. Reiterating the

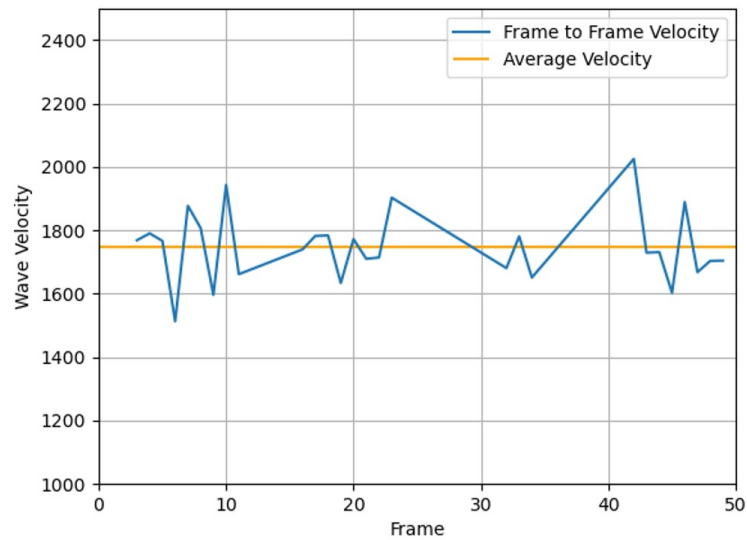


**Figure 6.11:** Wave velocity calculated across 50 frames using annotation S<sub>3</sub>

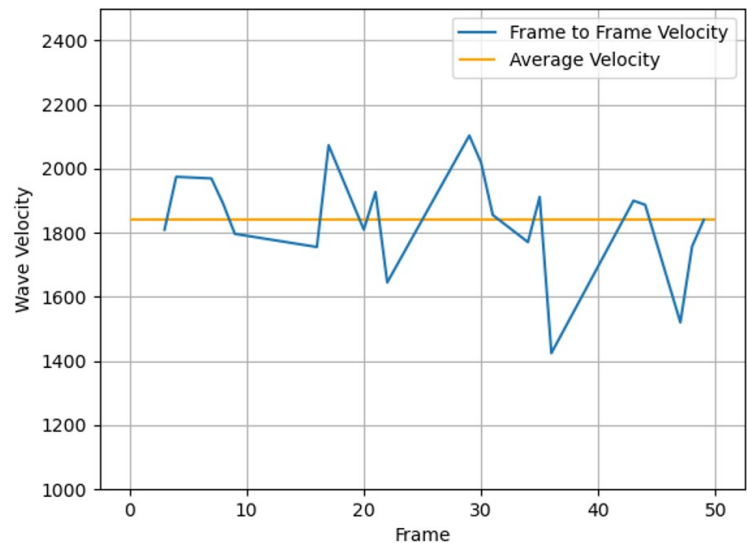


**Figure 6.12:** Wave velocity calculated across 50 frames using annotation R<sub>2</sub>

benefit of object detection proposed in this study, the annotations of each wave front offer a frame-to-frame velocity calculation that is more computationally efficient and requires less frames than the traditional detonation surface plotting method.

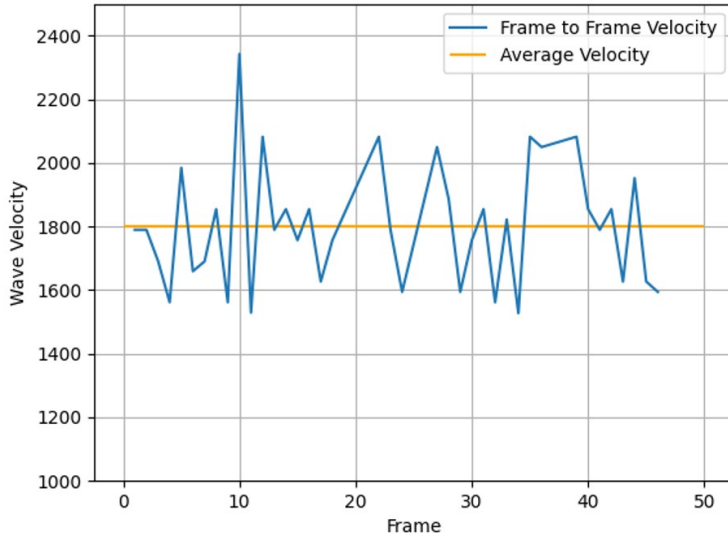


**Figure 6.13:** Wave velocity calculated across 50 frames using annotation Lin

The detonation wave propagating through Figure 6.14 appears to shorten and elongate, effecting the wave front locations and therefore introducing the velocity oscillations. The largest velocity peak shown in Figure 6.13 is at frame 10, corresponding to the velocity calculated between frames 10 and 11. From frame 9 to 10, the wave appears to shorten, reducing the velocity, and then from frame 10 to 11 the wave elongates and drastically increases the circumferential path traveled. This behavior could be an artifact of imaging, or a detection of short time scale galloping as a local response to the fill region or other phenomena. Further work to identify the causation of this frame-to-frame behavior is necessary. Nevertheless, Figure 6.14 shows that velocity oscillations plotted in Figure 6.13 can be attributed to the physical wave behavior captured in the high-speed images. All 50 frames processed as a Lin network output which are used to calculate velocity values in Figure 6.13 are shown in Figures A.5 and A.6.

With the trained network, object detection is performed at approximately 1.5 frames per second for 301x301 images and 9.5 frames per second for the linearized 32x736 images using

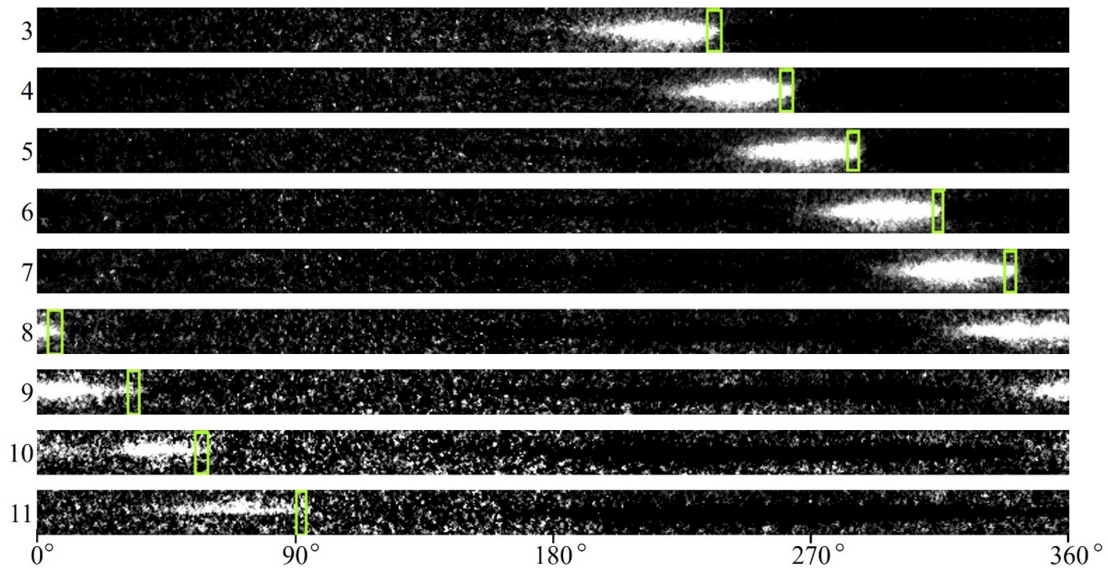


**Figure 6.14:** Linearized image annotation predictions for images 3-11

only the computer’s CPU. Undoubtedly, this speed could be drastically improved by utilizing the GPU if detection speeds were of enough importance to the given study. It should be noted that real-time operation does not require that wave speed be processed for every frame (at 50,000 fps), but rather at a speed sufficient to monitor wave velocity during steady operation. Compared to other object detection networks, the YOLO family relies on a single CNN, making high detection speeds possible. Based on the results outlined here and the experience related to other previous neural network success, it is believed that this method has produced a useful tool suitable for expedited post-processing, and serves to give further insight into the benefits of machine learning within the PGC community.

## 6.6 UNCERTAINTY ANALYSIS

Experimental uncertainty for the wave velocity was estimated based on the method outlined by Moffat<sup>127</sup> by introducing a bias uncertainty for each of the measured quantities and calcu-

lating a precision uncertainty based on test statistics. The bias uncertainties were determined based on manufacture specifications and engineering assumptions and were perturbed sequentially. The values which were perturbed in Equations 6.2- 6.4 for the S<sub>3</sub> and R<sub>2</sub> annotation boxes were the annotation box centroid locations ( $x$  and  $y \pm 1$  pixels), the Taubin radius ( $r_{Taub} \pm 1$  pixel), the camera frame rate ( $FR \pm 2\%$ ) and the RDE radius ( $r_{RDE} \pm 0.10$  mm). The  $x$  and  $y$  pixel uncertainties were assumed to be approximately 5% of the width of the annotation boxes, while the Taubin radius uncertainty is determine from the RMSE.

For the linearized annotation style relying only on Equation 6.4, values perturbed are angle of rotation ( $\theta_i \pm 0.00856$  rad), the camera frame rate ( $FR \pm 2\%$ ) and the RDE radius ( $r_{RDE} \pm 0.10$  mm). In the linearized format, only the angular bin is found from annotation centroid  $x$ -locations where each pixel width is equal to 0.00856 radians, and each annotation is 10 pixels wide. Remaining consistent, pixel uncertainties were assumed to be approximately 5% of the width of the annotation boxes. Because 5% of the 10 pixel annotation width is less than one pixel, perturbations utilize  $\pm 1$ pixel or as noted above  $\pm 0.00856$  rad. This reduction of variables perturbed through a lesser number of equations will directly reduce the bias uncertainty. The camera frame rate uncertainty was estimated based on data reported by Robbe, et al.<sup>128</sup> and the RDE radius accuracy was assumed based on machining tolerances, and considering that the centroid does not necessarily follow the centerline of the RDE annulus. Once all values had been perturbed, the positive perturbation and negative perturbation of each measurement were taken and their absolute values were averaged. These values are then used to find the root-mean-square (RMS) value of the bias uncertainty, which is assumed to be the same for the two annotation styles.

The second component is the precision uncertainty and is based on a student-t distribution based on the number of tests performed and test points collected (30 frames). Finally,

the total uncertainty,  $V_{uncertainty}$ , can be determined from the bias uncertainty,  $V_{bias}$ , and precision uncertainty,  $V_{precision}$ , shown in Equation 6.7 for the wave velocity.

$$V_{uncertainty} = \sqrt{V_{bias}^2 + V_{precision}^2} \quad (6.7)$$

The bias uncertainty was determined to be  $\pm 3.6\%$  for annotation styles S<sub>3</sub> and R<sub>2</sub>, and  $\pm 2.7\%$  for the Lin annotation style based on the measurement specifications discussed above. The precision uncertainty for the S<sub>3</sub>, R<sub>2</sub> and Lin annotation boxes, shown in Figures 6.11, 6.12 and 6.13, were  $\pm 2.4\%$ ,  $\pm 2.8\%$  and  $\pm 2.7\%$ , respectively. The total uncertainty was then determined to be  $\pm 4.3\%$  for the S<sub>3</sub> annotation boxes,  $\pm 4.6\%$  for the R<sub>2</sub> annotation boxes, and  $\pm 3.8\%$  for the Lin annotation style. The strength of the linear adaptation offers total uncertainty reductions of  $0.5\%$  and  $0.8\%$  compared to its S<sub>3</sub> and R<sub>2</sub> competitors, respectively.

## 6.7 SUMMARY OF RDE YOLO OUTCOMES

Detection and tracking of detonation waves present in an RDE annulus during combustor operation is critical to advance the monitoring of RDEs as they progress toward gas turbine engine integration. A methodology for wave detection in down-axis images using a computer vision You Only Look Once (YOLO) network was demonstrated in this chapter through analysis of high-speed camera images. The goal of this work was to use the YOLO architecture to report the location of each wave within the image as well as wave direction for multi-wave modal behavior in an experimental RDE. To do so, the YOLO network was first trained and validated using a chosen set of manually annotated, treated images. Separate efforts were outlined to alter Intersection over Union ( $IoU$ ) and confidence thresholds to improve the annotation outputs according to the physical understanding of the RDE. The trained network is equipped to predict annotation boxes around each detonation wave, and the centroid of

each annotation can be tracked through a series of images. The progression of annotation centroids is used to calculate wave velocity from frame to frame as well as through a series of images to determine an average wave velocity.

Sizes and proportions of annotation styles were found to have a substantial impact on reported centroids and their radial error respective to a Taubin fit circle. Increased radius variation associated with larger, rectangular annotations resulted in higher uncertainty for velocity calculations. Small, square annotations however experience higher classification error due to a reduction in wave features present within the annotation area. An additional network was trained to analyze linearized images containing only the RDE annulus pixels. The linear annotation style offered a higher volume of annotation predictions due to the more concise pixel arrangement, and reduced velocity uncertainty by reducing dependence on annotation coordinates to only angular location. Therefore, the resultant recommendation is that studies more interested in wave direction labeling utilize larger, rectangular annotations while studies interested more in wave velocity or processing speeds use linearized images with corresponding binned annotations. Because the goal of this study is wave speed calculations, the latter annotation style was selected and resulted in an overall uncertainty of  $\pm 3.8\%$ .

This work builds on the previous work in Chapter 4, and experience of training a neural network for analysis of high-speed down-axis RDE images <sup>46</sup>. Unlike the previous method, the current method does not rely on pressure data to determine wave velocities and is compatible with wave modes that do not exist in the training image set. Although both studies work to find wave velocity through image processing, which is an effort that is previously explored within the RDE/PGC community and documented in Chapter 3, both studies introduce computer vision to accelerate the process. However, the application of object detection will not achieve real-time RDE monitoring due to the need for sequential images

at high framerates which can't be acquired and analyzed at speeds comparable to the RDE timescale. Nevertheless, the RDE YOLO network offer drastic improvements compared to conventional techniques in both speed and velocity resolution. The current method calculates frame to frame velocity with a timestep resolution of 20  $\mu$ s or 50 kHz frequency and can process and annotate images at 1.5 frames per second for 301x301 images and 9.5 frames per second for the linearized 32x736 images. As computer vision and machine vision evolve alongside RDE technology, improved processing times and refined networks will allow for the progressive development of real-time monitoring of industrial RDEs. Benefits of object detection are expected to extend to wave strength and parasitic combustion quantification in future studies. This demonstrated approach offers another early example of neural network application to RDE research.

*Science progresses best when observations force us to alter our preconceptions.*

Vera Rubin, American astronomer and pioneer

# 7

## Time Series Classification of Ion Probe and Pressure Data

DUE TO THE TIMESCALE OF OBSERVABLE DETONATION BEHAVIORS, time series sensor data is studied for an experimental RDE at high sampling rates exceeding 250 kHz, which results in large volumes of data. This data most often requires post-processing deterministic

methods, which will likely never achieve real-time diagnostic speeds. In an effort to address this issue, a deep learning approach to time series classification (TSC) is proposed. Pressure and ion probe data collected near the RDE detonation plane is recorded and used to create 8 datasets of varying sample lengths: 200, 500, and 700 samples. These datasets, 6 univariate and 2 multivariate, are filtered and labeled according to the wave mode detected by simultaneous down-axis imaging. Further examining the effects of a TSC approach, each dataset is used to train three deep neural network architectures, an encoder, a fully convolutional network (FCN), and a residual network (ResNet), resulting in 24 uniquely trained networks. Networks are randomly initialized five times and trained over 250 epochs each time. The incremental network that minimizes loss is chosen as the finalized network. Among the results of the 24 finalized networks, shorter data lengths and multivariate data sets show the highest performances. The best performing individual network is a multivariate encoder, while ResNet achieves the highest overall average rank among the three architectures. According to the goal of the current study, which is to develop a component of a real-time RDE diagnostic, classification time is of high importance in the selection of a preferred network. Therefore, an FCN trained on a multivariate dataset with a data length of 200 samples is selected as a preferred network that is believed to best optimize classification time alongside validation accuracy, being 28.76 msec and 91.36% respectively. The chosen network's classification time corresponds to a classification rate of nearly 35 Hz, outperforming the speed of an RDE image classification network developed in a previous study by the current authors. It is believed that a reduced data acquisition time associated with the low dimensionality of time series data will enhance the viability of the TSC method and its contribution to a real-time RDE diagnostic.

In order to study the unsteady behavior of the detonation waves, high-speed images and temporal data from sensors such as ion probes and pressure transducers can be captured. For each sensor type, a variety of data analysis techniques have been developed and employed across the RDE community. However, as RDEs progress towards an applied technology, there is a greater need for real-time diagnostics that offer operational insights during RDE operation. High-speed imaging of RDEs typically requires extensive post-processing to provide useful information but has recently been advanced towards real-time speeds via Computer Vision techniques<sup>46</sup>. Similar to images, RDE time series data such as pressure and ion probe data offer features that suggest the active wave mode within the RDE. In many cases, those experimental data trends and features are visually intuitive to the experienced practitioner but are difficult or impossible to represent by a deterministic or analytical solution. As time series point measurements are widely common in research and across many industries, extensive work has been completed to develop more efficient means of analysis using deep learning approaches.

The current study aims to build on the recommendations of that progress through the training of a series of time series classification (TSC) networks which can classify the number and direction of waves within the RDE using univariate and multivariate pressure and ion probe datasets. Each dataset will span a range of experimental conditions and time frames, but with varying dimensionality, probe selection and normalization. The unique datasets will each be used to train three networks: a residual network (ResNet), an encoder, and a fully convolutional neural network (FCN) according to the DNN TSC framework shown in Figure 7.1 The effects of dataset size, probe selection, data treatment, and network selection will be investigated through comparison of network performance according to classification accuracy, classification speed and viability of real-time diagnostic integration. The final se-

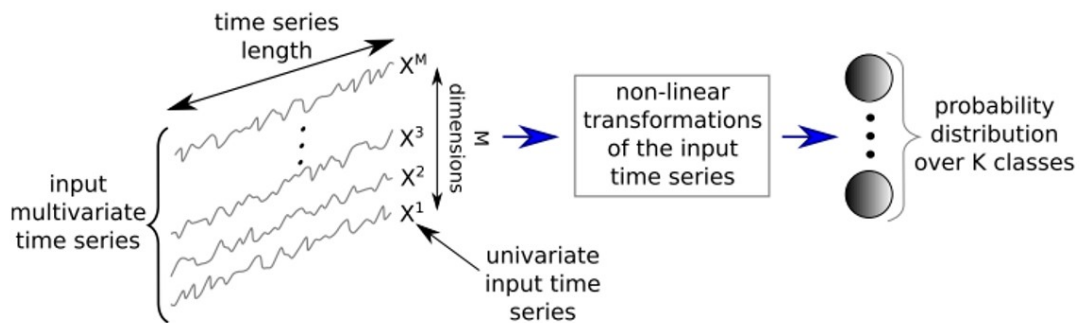


**Figure 7.1:** Generic DNN TSC framework for multivariate time series<sup>74</sup>

lected network may then be applied to live pressure data collected via the PyDAQ package within Python, and used as a real-time diagnostic offering wave classification during experimental RDE operation.

### 7.1 DATASET CREATION AND NORMALIZATION

In order to train a TSC network, a dataset must first be established. To explore the effects of data quality, dimensionality, and length, a series of datasets are created using previously recorded experimental RDE data. Data used throughout the chapter, is recorded from an Ion probe and PCB, at port locations C<sub>1</sub> and D<sub>1</sub> respectively, according to the nomenclature described by Figure 2.15. Each dataset is normalized using Z-normalizing, also referred to as Z-score. Z-normalization, or standardization, centers a dataset at mean  $\mu$  with a resultant standard deviation of 1. This standardization is a common option in data treatment for deep learning, as it improves learning capabilities by presenting data features as a normal distribution. The Z-normalization,  $x_{i,z}$ , of data point  $x_i$  is performed using Equation 7.1 where  $\mu_{global}$  and  $\sigma_{global}$  are the global mean and standard deviations of the training and validation data sets, respectively. Example windows of Ion and PCB traces across 200 samples which are

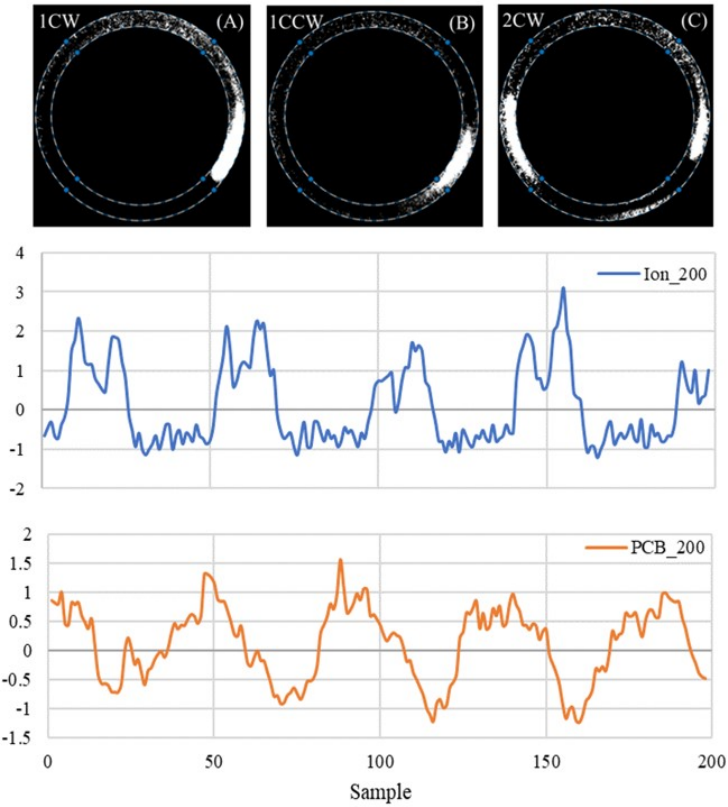


**Figure 7.2:** Example Down-axis images (A-C) and example Ion (D) and PCB (E) traces Z-normalized throughout a 200-sample window

Z-normalized signal, with an overlaid example down-axis image used to classify wave mode are plotted in Figure 7.2.

$$x_{i,z} = \frac{x_i - \mu_{global}}{\sigma_{global}} \quad (7.1)$$

As will be detailed in the next subsection, the DNN architectures considered include only end to end networks, therefore requiring labeled datasets. In order to create each dataset, windows of pressure and ion probe data are labeled according to the wave mode determined by imaging methods, either detonation surface or by image classification CNN<sup>44,46</sup>. Generating labels for time series data using down-axis imaging supplies modal certainty to labeling

that is otherwise complicated by complex wave modes when solely considering time series data. The datasets span operating windows that include 13 wave modes, simple and complex, experienced in the water-cooled NETL RDE. Wave modes included in the datasets are: 1CW, 1CCW, 2CR, 2CW, 2CCW, 3CR, 3CW, 5CR, 6CR, 6CCW, 7CCW, 7CW, 7CR with naming convention of wave count followed by directional indicator. Directions include clockwise (CW), counterclockwise (CCW), and counter rotating (CR). In the case of CR modes, the wave number indicates the number of counter-rotating pairs. Like all classification algorithms, the DNNs will only accurately classify data according to the labels present in the dataset. Therefore, the datasets must adequately sample every expected wave mode in a variety of operating conditions. The current dataset does not wholly survey every wave mode experienced in the RDE of interest, but adequately covers complex wave behaviors and multiplicity to study the proposed application of TSC. Resulting networks will offer the ability to properly identify co- and counter-rotating wave modes, which is critical to the previous and the current work. Future work will include expanding the dataset to include additional wave mode labels.

Univariate datasets are composed of time series having lengths of 200, 500, and 700 samples from pressure data or ion probe data. Multivariate datasets are composed of ion probe data in conjunction with pressure data with sample lengths of 200 and 500 samples. This results in 8 datasets (6 univariate, and 2 multivariate) uniquely representing a variety of detonation behaviors. To each of these datasets, three types of DNNs are applied: residual network (ResNet), encoder, and fully convolutional neural network (FCN). This parametric method will result in 24 trained networks offering insight to the benefits of various time series treatment and training aspects. Resultant recommendations can then be made regarding the future use of TSC applied to RDE data for real-time diagnostics. In order to develop a

collection of networks whose performance can be compared equitably, a strict network development method is followed.

## 7.2 RDE TSC NETWORK DEVELOPMENT

According to the dataset composition previously outlined, 6 of the datasets will be univariate while the remaining 2 datasets will be multivariate. In both cases, the method to develop each TSC DNN is conducted according to the flowchart in Figure 7.3. Each DNN considered is a discriminative, end-to-end network. This simply means the networks learn from input-output pairs, and are domain agnostic, removing bias of feature engineering. Therefore, the current method is universally applied and includes four major phases: Dataset, TSC DNN Training, TSC DNN Validation, and Inference.

While the Dataset phase is only performed once for each unique dataset, the remaining three phases must be performed to produce each of the 24 trained networks. In preparation for the TSC DNN Training phase, the chosen labeled time series dataset, whose generation was outlined in the previous subsection, is split into training and validation datasets with proportions of 70% and 30% respectively. Once split into respective datasets, the TSC DNN Training phase is initiated. Training data and labels from the given univariate or multivariate

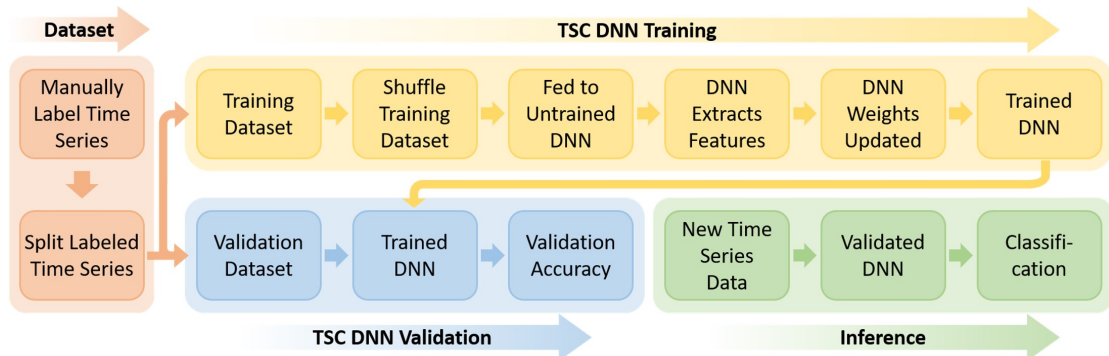


**Figure 7.3:** TSC DNN Development Method Flowchart

dataset are fed to an untrained DNN whose architecture must be determined and created beforehand with randomly initialized weights. As the network is presented with the dataset, parameterized weights are internally updated using a backward pass to propagate the error of model prediction through gradient descent. Simultaneously, the TSC DNN Validation phase is being performed to evaluate validation loss. In this process, the validation dataset is fed to the incrementally updated TSC DNN without labels. Each time the network is exposed to all data, an epoch is completed. For the current work, all network iterations are trained for 250 epochs. Once the network’s training loss is minimized alongside the validation loss, the DNN is considered a trained and validated network. This training and validation process must be performed for each desired network-dataset combination.

### 7.3 TSC NETWORK SELECTION AND USAGE

In an effort to obtain the most high-performing model, the training process is reinitialized and completed five times for each network, each time with newly randomized initial weights. Across the five iterations, a “best model” is retrieved and saved for end usage. The best model is not often at the final epoch, but instead a previous epoch at which the parameterized weights are found to minimize loss. In each case, a categorical cross-entropy loss function, also called SoftMax loss, is used to determine the best model among the five iterations. Categorical cross-entropy is a measure of similarity between two probability distributions. For classification problems, these are the incremental network’s output of a probability distribution for each label and the labeled data. In other words, for each classification attempt, the network outputs a probability distribution vector of length equal to the number of possible classifications. The maximum probability within the distribution determines the output label, which is compared to the label provided by the dataset generation process. The loss

function can be optimized by stochastic gradient descent (SGD) and is a low cost and effective choice for classification networks<sup>129</sup>.

A broad range of DNNs and an even larger selection of more traditional classifiers in categories such as NN or SVMs are available to train for the proposed study. The selection of deep learning architectures, based on their advantageous simplicity and previous successes in efforts similar to TSC, somewhat narrows the selection of potential architectures. To address a similar issue, Fawaz et al.<sup>74</sup> surveyed eight popular and proven methods in their ability to classify univariate and multivariate publicly available time series repositories<sup>130</sup>. Fawaz ranked architecture performance with respect to themes, dataset length, and training size. In each category corresponding to the current study (Theme: Sensor, Length: 251-700, Train size: >799), the top three performing networks were the same. Those networks, Encoder, FCN, and ResNet, are therefore chosen for the current study and will be briefly summarized.

The Encoder architecture is a computationally lightweight hybrid structure, whose output is summarized by a convolutional attention layer. The architecture begins with three convolutional blocks with max-pooling layers between each. Within each convolutional block is an instance normalization fed to a parametric rectified linear unit (PReLU) activation function, thought to be a possible improvement on the widely used rectified linear unit (ReLU) activation<sup>131</sup>. This varies from the somewhat similar FCN architecture, which relies on a global average pooling (GAP) layer instead of the encoder's attention layer. Both have three convolutional layers, but within the FCN convolutional block is a batch normalization fed to a ReLU activation function<sup>132</sup>. The ReLU activation function has brought much success to deep learning by overcoming the vanishing gradient issue associated with sigmoid and hyperbolic tangent activations. The final architecture, ResNet, is specifically designed to address the degradation problem where deeper networks experience saturated accuracies and become

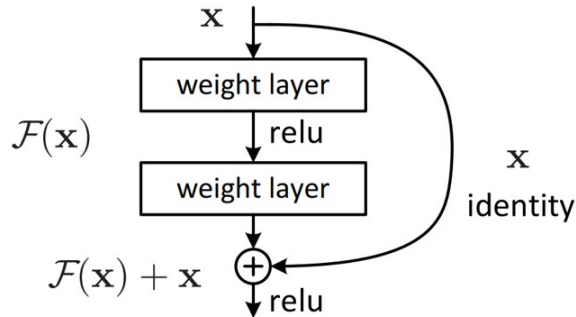


**Figure 7.4:** Generic ResNet residual block<sup>59</sup>

less effective than more shallow networks. This is accomplished by the residual block, depicted in Figure 7.4, which relies on a skip connection supplying information from earlier layers that would otherwise become too abstract<sup>59</sup>. The ResNet used in this study contains nine convolutional layers followed by a GAP layer<sup>132</sup>. Although the complexities and purposes of each network may seem dissimilar, they are all trained according to the method depicted in Figure 7.3.

The resulting best network(s) can then be used indefinitely within the Inference phase to classify the wave mode from new experimental time series data. Each trained network is only applicable to data arrangements identical to that of the initial training data, and viable for wave modes included in the training labels. To adapt the network to a new data arrangement or additional wave modes, the network development methodology can be applied from scratch, or transfer learning may be applied in some instances. Otherwise, the phase of Inference can be utilized as a TSC tool indefinitely.

For application as a real-time diagnostic technique, the networks may be used to classify “live” experimental data within the RDE lab environment. Using the PyDAQ package within Python, data windows can be collected from the appropriate sensors, and passed through the chosen TSC DNN. Similar to the technique proposed as an extension to the

previous image classification study<sup>46</sup> whose findings will be published in a future work, the DNN output of wave number and direction can drastically simplify calculation of other wave metrics. To generate diagnostic information, the same short window of sensor data fed to the DNN can be analyzed through a simple correlation method to determine wave speeds and frequencies. Informed of the wave mode via DNN output, the correlation, which is computationally cheap, can determine individual wave frequencies and velocities. This diagnostic output data, provided by the TSC and subsequent correlation method, is similar to that of an FFT but requires much less data while offering modal certainty that is otherwise elusive in time series dataset absent of optical verification. A second option, which may be considered in future work, combines the output of the current DNN with parameters derived through feature engineering of the time series signal. Each parameter, being fed to a regression network, could be used to estimate wave speed and frequency.

#### 7.4 PARAMETRIC CONSIDERATION OF TSC NETWORK PERFORMANCE

Three DNN architectures were trained on 8 unique datasets (6 univariate and 2 multivariate). Univariate datasets include data from either an ion probe or pressure reading at sample lengths 200, 500, and 700 samples. Multivariate datasets are made up of simultaneous ion and pressure data at sample lengths of 200 and 500 samples. Each dataset is labeled with wave modes extracted from down-axis high speed images. This combination results in 24 unique finalized networks. Finalized networks represent the model that best minimized categorical cross-entropy loss throughout five random initializations, with training durations of 250 epochs each. Results for the 24 models, including training accuracy, validation accuracy and classification time, are summarized in Table 7.1. Training and validation accuracies measure the model's ability to classify data windows from the training and validation datasets, respec-

tively. Classification time, reported in milliseconds, is the time it takes the model to analyze and predict a label for a single data window. Classification times reported in Table 7.1 are an average of 10 consecutive classifications. Intuitively, lesser classification times are preferred for downstream usage within a real-time diagnostic.

Architecture	Dimensionality	Data Length	Data Type	Training Accuracy	Validation Accuracy	Classification Times [msec]
Encoder	Univariate	200	Ion Probe	99.52%	77.56%	32.09
	Univariate	200	PCB Data	99.25%	71.44%	32.13
	Univariate	500	Ion Probe	99.94%	74.21%	33.78
	Univariate	500	PCB Data	99.92%	67.86%	33.64
	Univariate	700	Ion Probe	99.94%	71.88%	38.9
	Univariate	700	PCB Data	100.00%	66.12%	39.06
	Multivariate	200	Ion and PCB	100.00%	94.51%	35.77
	Multivariate	500	Ion and PCB	100.00%	88.13%	44.33
FCN	Univariate	200	Ion Probe	98.54%	82.62%	28.29
	Univariate	200	PCB Data	98.45%	73.26%	28.21
	Univariate	500	Ion Probe	97.57%	84.12%	29.07
	Univariate	500	PCB Data	96.02%	76.83%	29.11
	Univariate	700	Ion Probe	97.17%	87.23%	30.02
	Univariate	700	PCB Data	94.12%	82.58%	31.18
	<b>Multivariate</b>	<b>200</b>	<b>Ion and PCB</b>	<b>100.00%</b>	<b>91.36%</b>	<b>28.76</b>
	Multivariate	500	Ion and PCB	100.00%	89.89%	29.71
ResNet	Univariate	200	Ion Probe	99.95%	87.63%	36.25
	Univariate	200	PCB Data	99.98%	83.08%	39.1
	Univariate	500	Ion Probe	99.95%	87.63%	31.74
	Univariate	500	PCB Data	99.97%	86.63%	31.83
	Univariate	700	Ion Probe	99.91%	89.85%	32.65
	Univariate	700	PCB Data	100.00%	87.40%	33.21
	Multivariate	200	Ion and PCB	100.00%	94.24%	32.5
	Multivariate	500	Ion and PCB	100.00%	88.35%	31.66

**Table 7.1:** Results for tested CNN architectures

Generally speaking, a majority of the models achieve accuracies that may be suitable for end usage absent of competition. Additionally, the three architectures appear to each be competitive in various aspects. On average, ResNet achieves higher validation accuracies while the encoder achieves the highest accuracies by a single network. The FCN network

demonstrates overall higher accuracies than the encoder with better classification times. One consistent trend across each architecture is a higher performance on multivariate datasets, which will be further explained later in this section. Competing metrics between the three architectures highlight the absence of a clear optimal model choice or preexisting “formula” for model design for a given dataset. Effects of network depth and other design choices may suggest performance abilities to an experienced user. However, it is never fully known how one network may outperform another for any new dataset, and therefore a parametric comparison of various networks is necessary. Although the final results of the differing architectures seem incredibly similar, the progression of their learning process demonstrates the existence of their internal differences, which were detailed in the previous section.

Training accuracies are plotted against epochs for encoder, FCN and ResNet networks trained on univariate datasets in Figures 7.5 through 7.7. Training accuracies for all multivariate networks are plotted in Figure 7.8.

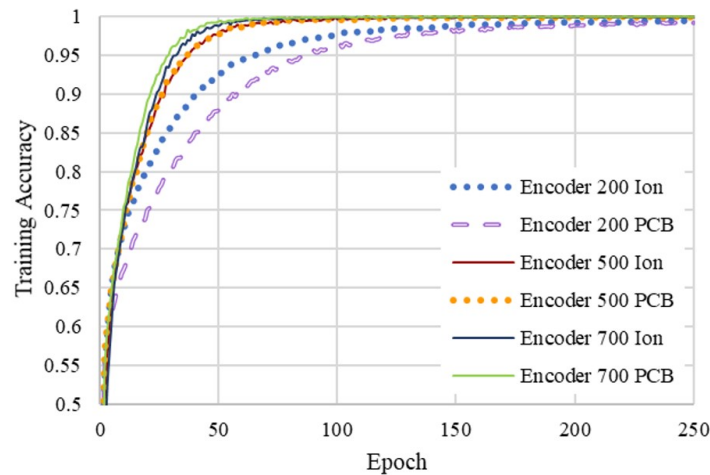


**Figure 7.5:** Training Accuracy for Univariate Encoder Networks versus Epochs

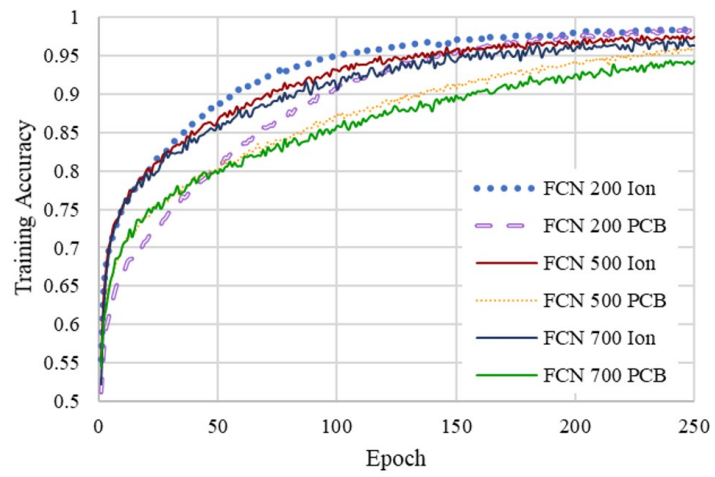


**Figure 7.6:** Training Accuracy for Univariate FCN Networks versus Epochs

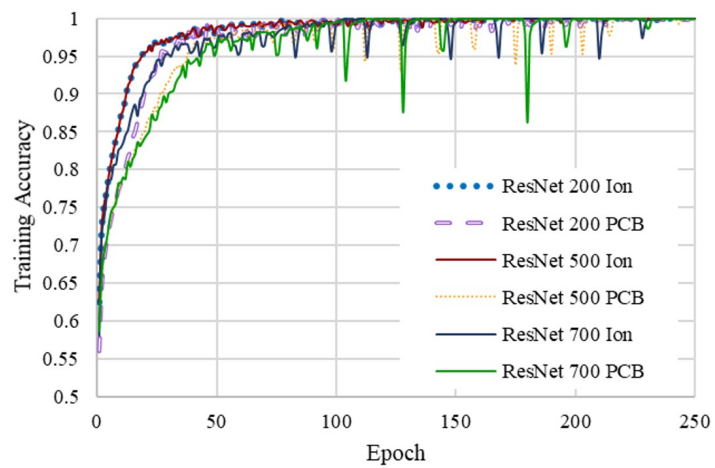


**Figure 7.7:** Training Accuracy for Univariate ResNet Networks versus Epochs

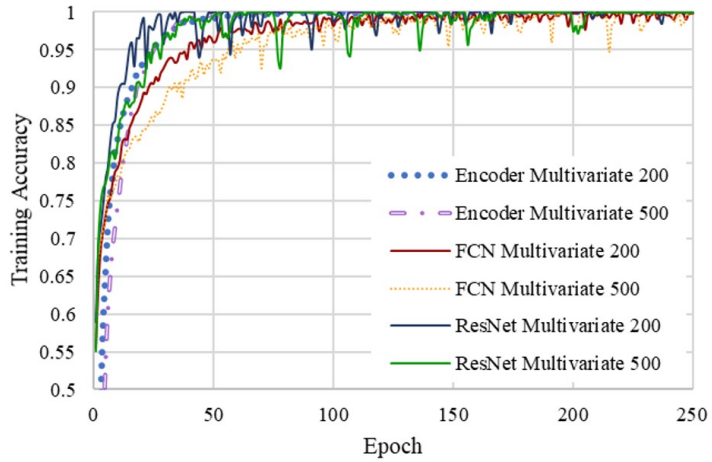


**Figure 7.8:** Training Accuracy for All Multivariate Networks versus Epochs

A multitude of behaviors can be observed in the plotted trends but will be discussed briefly as this is intended to be a demonstration of development of DNNs as tools for end-use in a lab environment. In Figure 7.5, it is shown that the encoder responds more quickly to longer data windows. For a given data length, the encoder does not consistently favor ion or pressure data. This is not true for the other univariate networks which all favor ion probe data. Higher accuracies associated with ion probe datasets are expected as a result of the more prominent trends in ion traces compared to the lesser quality of the pressure data, illustrated in Figure 7.2. Figure 7.6 highlights FCN networks' more gradual learning with the most prominent performance gap between ion and pressure data regardless of data length. Univariate ResNet achieves accuracies exceeding 95% in the fewest epochs, shown in Figure 7.7, but begins to overcorrect weights once the training accuracy is saturated. Each of these trends are echoed by the multivariate networks, shown in Figure 7.8.

Excluding the univariate encoder, all networks tend to perform better on shorter data lengths in early epochs. Without clarification, this may be incredibly counter-intuitive as “less data” should contain less characteristic information. Therefore, it is pertinent to acknowl-

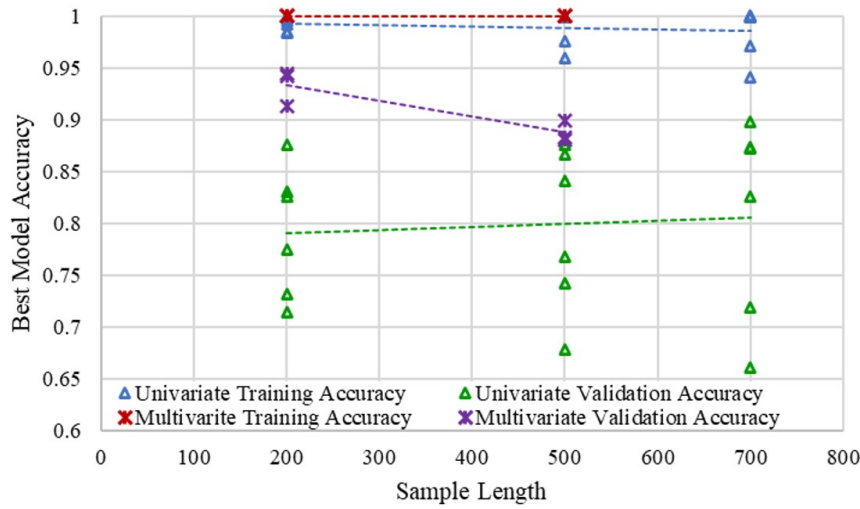


**Figure 7.9:** Training and Validation Accuracy for Univariate and Multivariate Networks versus Sample Length

edge that each dataset was created from the same pool of data, creating an exchange between data length and total datapoints. In other words, while data lengths of 500 may offer more informative features than data lengths of 200 within a single window, the latter dataset contains more than twice as many data windows with associated labels. It is likely that given an equal number of datapoints, larger data lengths would outperform their shorter counterparts with a negative impact of larger classification and data acquisition times. To study this relationship, a significant portion of labeled data would not be utilized in the shorter data length sets. This activity, wasting labeled experimental data, does not align with the current scope of work which aims to create the high-performing DNNs with the available data. To further consider impacts of sample lengths, Figure 7.9 shows training and validation accuracies of best models versus sample length.

While Figures 7.5 through 7.8 showed incremental training accuracies, Figure 7.9 summarizes the accuracies associated with the model that best minimizes loss, coinciding with the data reported in Table 7.1. In this format, the exchange between data length and datapoint

volume can be further quantified for the three sample lengths 200, 500, and 700 samples. For both training accuracies, univariate and multivariate, values are so high that little to no influence is attributed to sample length. Univariate validation accuracies are very scattered, but trend somewhat upward with larger sample lengths. Simultaneously, the lowest univariate validation accuracies worsen with larger sample lengths, likely a result of lesser validation datapoint volume. The most prominent trend is associated with multivariate validation accuracy, which is negatively impacted by increasing sample size. This exchange of data length and data volume is exacerbated in the multivariate cases as a result of an overall lower data volume available where ion and pressure data were both recorded at the port locations, C<sub>1</sub> and D<sub>1</sub>, chosen for this study. For this reason of sparsity, a multivariate dataset with sample length of 700 was not created.

Figure 7.9 also emphasizes the superior performance of multivariate networks over univariate at every sample length. Multivariate lengths of 200, having dimension of 2x200 equivalent to a reshaped 400 data length, outperform univariate lengths of 500 from a larger data pool. Again, this may seem illogical, but can be accounted for in the physical understanding of the sensor locations. Both sensors are located at axial locations closest to the detonation plane, or the base of the RDE. They are circumferentially separated by 60°, offering some degree of spatial variation in the data fed to the DNNs. Like any correlation method, information representing detonation behavior at various locations within the annulus greatly clarifies the wave mode. It is expected that a multivariate set where two sensors are circumferentially aligned and axially spaced would experience a lesser benefit as the additional spatial information would only respond to more vague behaviors such as wave height or combustion strength.

Beginning a process of selecting a preferred network or architecture to utilize as a real-time diagnostic component, Table 7.2 lists validation accuracy of each architecture and its respective rank amongst competitors for a given dataset. Validation accuracy, a measure of the network to classify unlabeled data, is the better accuracy indicator of a network's performance on new data. With data rearranged to the format of Table 7.2, it is abundantly clear that ResNet is the top performer for all univariate datasets. Likewise, FCN outranks the encoder in every univariate instance. For multivariate datasets, the three networks tie with an average rank of 2. Interestingly, the dataset for which the encoder achieves the top rank is the only instance of not exhibiting the lowest performance. Across all datasets, ResNet has the highest average rank of 1.25. Therefore, if TSC is to be performed on RDE sensor data with no access to supercomputing resources that allow a survey similar to that presented in the current study, ResNet is recommended to most likely achieve highest accuracies. However, a survey of architectures should be performed whenever possible.

Dataset Type	Data Source	Samp. Length	Encoder [Val. Acc. (Rank)]	FCN [Val. Acc. (Rank)]	ResNet [Val. Acc. (Rank)]
Univariate	Ion	200	77.56% (3)	82.62% (2)	87.63% (1)
Univariate	PCB	200	71.44% (3)	73.26% (2)	83.08% (1)
Univariate	Ion	500	74.21% (3)	84.12% (2)	87.63% (1)
Univariate	PCB	500	67.86% (3)	76.83% (2)	86.63% (1)
Univariate	Ion	700	71.88% (3)	87.23% (2)	89.85% (1)
Univariate	PCB	700	66.12% (3)	82.58% (2)	87.40% (1)
Multivariate	Ion + PCB	200	94.51% (1)	91.36% (3)	94.24% (2)
Multivariate	Ion + PBC	500	88.13% (3)	89.89% (1)	88.35% (2)
Overall Univariate Rank (Avg.)			(3)	(2)	(1)
Overall Multivariate Rank (Avg.)			(2)	(2)	(2)
Overall Rank (Avg.)			(2.75)	(2)	(1.25)

**Table 7.2:** Performance comparison of each network for given datasets with rank

Because the current study aims to develop a component of a real-time RDE diagnostic, classification time must be optimized alongside validation accuracy. Figure 7.10 is used to visualize those parameters for each architecture. It can be seen that FCN boasts the shortest

classification times with an overall minimum of 28.21 milliseconds (msec). ResNet, being the deepest network, experiences larger classification times in exchange for higher accuracies. In this format of consideration, the Encoder becomes a lessor competitor with lower accuracy and higher classification times.

Analyzing Figure 7.10, two networks appear to be viable choices. The first being the highest-accuracy FCN which achieves 91.36% validation accuracy and 28.76 msec classification time. The second choice is the highest-accuracy ResNet demonstrating 94.24% validation accuracy and a classification time of 32.50 msec. Consistent with the trends previously discussed, both contending networks are multivariate with data lengths of 200. Therefore, data acquisition setup and time are not deciding factors. Because validation accuracies of both options are very similar, the multivariate 200 sample length FCN network, also highlighted in Table 7.1, is chosen over the ResNet for the improved classification time. While less than 3% difference in accuracy is not expected to create drastic effects, a 13% slower ResNet may hinder real-time capabilities. At the chosen network's classification speed, new classifications can be generated at feedback rates just under 35 Hz, which exceeds current capabilities.

As a preliminary exercise of real-time diagnostic calculations, previously recorded ionization probe and PCB data were fed to the finalized network. The TSC classification output, which includes wave number, was utilized by a simplistic correlation method. Across 100 windows, each spanning 200 samples like the example traces in Figure 7.2, an average frequency and individual wave speed of 5556.6 Hz and 1298.8 m/sec were calculated, respectively. This frequency compares well to a frequency of 5617.3 Hz found using an FFT across 20,000 samples with a resolution of 61.035 Hz. In addition to calculations requiring much fewer samples, the TSC output provides wave number and directionality, which is typically estimated using a comparison of wave frequency proportional to the theoreti-

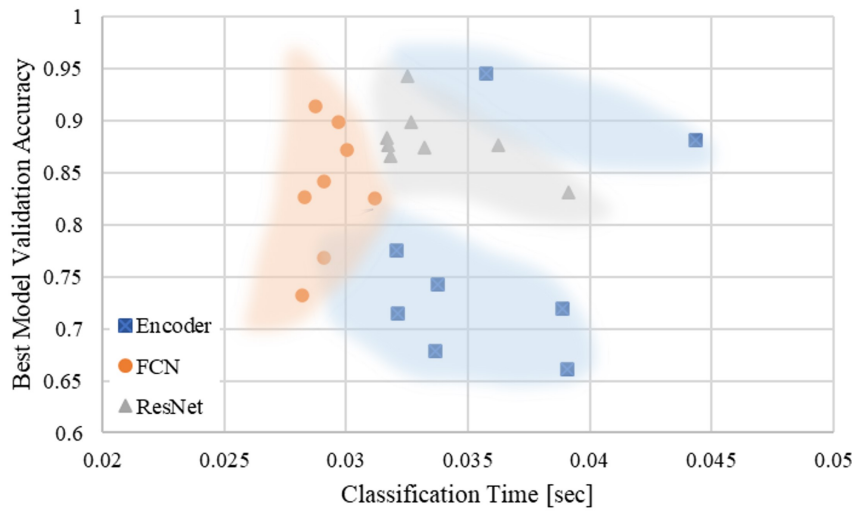


**Figure 7.10:** Validation Accuracy of three Architectures versus Classification Time

cal Chapman-Jouguet (CJ) velocity. Those estimations are further complicated by complex wave behaviors such as counter-rotating waves. The output of the TSCs developed in this study circumnavigate the CJ comparison in its entirety, resulting in an individual wave speed calculation at each iteration. Calculations of frequency and wave speed consume an average of 0.041 msec per iteration, barely impacting the diagnostic feedback rate. This exercise largely resembles diagnostic implementation in the lab environment, lacking only the addition of live data acquisition. Due to time constraints, full integration of the diagnostic with live experimental data acquisition will be performed as future work. However, the validity of TSC-output-informed correlation has been demonstrated by this preliminary exercise. Only the final diagnostic feedback rate will be affected due to the additional, but presumably small, data acquisition time per iteration. In the unexpected case of large data acquisition times, a univariate TSC may be preferred.

Fortunately, finalized network files and inference execution are formatted to be easily interchangeable if lab integration shifts preferences of accuracy and classification time. Ad-

ditional future work will include consideration of non-DNN machine learning algorithms identified as potential means to further reduce classification time, and therefore increase diagnostic feedback. It is worth noting that almost all FCN networks, including the preferred network, outperform the reported classification time of SqueezeNet, 29.9 msec, when applied to RDE images for image classification in a previous work. Although SqueezeNet is optimized for time, the total data within a single image is drastically larger than the sensor data used for the current TSC method. That larger data volume, however, offers more spatial resolution, resulting in a higher validation accuracy of 98.5%<sup>46</sup>. Paired with reduced acquisition time compared to imaging, during live RDE monitoring, the developed TSC method should prove a useful diagnostic tool and give further insight into the benefits of machine learning within the PGC community.

## 7.5 OUTCOME OF TSC EFFORT

In an effort to develop a functional component of a real-time RDE diagnostic, a multitude of deep neural networks (DNNs) were trained for time series classification using pressure and ion probe time series data collected from the NETL water-cooled RDE. Data labels were generated using down-axis high-speed imaging methods. Labels indicate the number and direction of detonation waves within the RDE annulus, or the wave mode, and include 13 unique wave modes in total. Labeled time series data was then used to generate 8 datasets, of which 6 were univariate with lengths of 200, 500, and 700 samples, consisting of either ion or pressure data. The 2 remaining datasets were multivariate with lengths of 200 and 500 samples, containing simultaneous ion and pressure data. Each dataset was used to train three time series classification (TSC) DNN architectures, being an encoder, an FCN, and a 10-

layer ResNet. This combination resulted in 24 final networks, each of which were optimized by a categorical cross-entropy loss function.

Training accuracy, validation accuracy, and classification time were reported and compared against epochs, data lengths, and one another for each finalized network. Various trends within the network performance analysis as well as recommendations for network selection and future implementation were presented. Excluding the univariate encoder, all networks more quickly responded to shorted data lengths, due to the increase in total data points and labels. Finalized training accuracies of multivariate networks responded most negatively to an increase in data length. In every case, multivariate networks outperformed univariate networks due to the added benefit of spatial resolution. When comparing the ranks of the three architectures, ResNet achieved the highest overall average rank of 1.25. For this reason, any new studies which must be performed in the absence of a DNN survey due to a lack of computational resources are recommended to start with a ResNet architecture. Otherwise, a survey of DNNs should be conducted for any new dataset to determine the network best suited for the parameters of highest interest.

Within the current chapter, which aimed to develop a TSC network as a component of an RDE real-time diagnostic, classification time was of highest importance when comparing networks. According to these priorities, a network with a slightly lesser accuracy than the highest-accuracy network was chosen for its 13% faster classification speed. An FCN trained on the 200 data length, multivariate ion and pressure dataset was chosen with final training accuracy, validation accuracy, and classification time of 100%, 91.36%, and 28.76 msec, respectively. A classification time of 28.76 msec, which corresponds to the time needed to predict a label for a new data window, results in a classification frequency of nearly 35 Hz, outperforming the image classification network developed in a previous study. As RDE tech-

nology progresses, and active control is developed, the required diagnostic feedback rate will become more well defined. While the presented TSC method should be further improved through future work, this new capability exceeds existing feedback rates. In combination with a smaller data acquisition time compared to that of imaging, this TSC method is expected to provide an improved means of real-time or near-real-time diagnostics within the experimental RDE environment. To perform this diagnostic, short windows of ion and/or pressure data will be collected using the PyDAQ package within Python. Live data will then be fed to a network developed by this study, which will predict a wave mode classification. That data, including the wave number and direction, are then fed to a lean correlation method that calculates wave velocity and frequency. This output information is widely available and commonly used in post-processing due to the larger data windows required by techniques like FFT. An ability to generate this information and other RDE performance metrics in real-time will be vital to the development of active control and gas turbine integration. It is believed that these goals can be met by a portfolio of artificial intelligence techniques, and that the results of the presented TSC method serve as another progressing step in the implementation of machine learning within pressure gain combustion technologies.

*A human must turn information into intelligence or knowledge. We've tended to forget that no computer will ever ask a new question.*

Grace Hopper, American computer scientist and  
computer programming pioneer

# 8

## Diagnostic Evaluation and Comparison

OF THE THREE METHODS DEVELOPED FOR REAL-TIME DIAGNOSTICS discussed throughout the manuscript, each offer various advantages which should be studied and compared. Throughout the chapter, image-based networks will be evaluated on their performance in analyzing external images. Afterward, external performance will be tabulated among other competing metrics to compare each diagnostic method. According to an overarching understanding of network strengths and limitations, which has informed the CNN types explored

throughout the text, no single network is expected to outperform others across the board in consideration of accuracies, feedback rates, access needs, and other metrics. Instead, certain networks will be more well-suited for particular applications and research needs, both justifying and underlining the need for an RDE machine learning portfolio.

## 8.1 EVALUATION OF EXTERNAL IMAGES

As has been mentioned, the strengths and capabilities of neural networks are inherently improved or restricted by dataset quality. Enabled by high frame rates, the current study is not limited by insufficient data volume, as is often the issue in machine learning application viability. The more likely limiting factor of the encompassed networks could instead be a consequence of data set isolation, resulting from shared RDE physical similarities. Data similarity may lead to networks applicable only in a setting identical to that used throughout training data set collection. If this be the case with the networks herein, an equal or similar application in another laboratory environment would require additional training (transfer learning), or complete reproduction of the CNN dataset generation, labeling, and training. For this potential need, each chapter presents a reproducible methodology which may be employed in any RDE environment with adequate data. However, a scenario in which the finalized networks created within this study may be directly applied to external data is more optimal. If network performance on external data is sufficient, model sharing should equip other research groups with real-time monitoring capacities, significantly expanding the impact of the current work.

The optimal solution achieving data similarity avoidance would likely be usage of an encompassing data set, representative of many many RDE geometries operated across the globe. Features may then be better generalized, as is the necessity of self-driving cars which rely on

vastly diverse representations, or YOLO’s ability to detect objects in more abstract scenes such as artwork<sup>72</sup>. While network architecture should not be understated as a major contributor to these applications, it is not likely that even the most effective network would properly inform a self-driving car traveling through the desert when it has been trained exclusively on data collected within wetlands. Unfortunately, a global RDE database does not exist to date. It is possible the adoption of machine learning will prompt the creation of such a collaborative product. However, in the meantime, datasets used throughout the manuscript do attempt to avoid large degrees of data similarity. Detailed in Chapter 2, datasets were generated using data from three RDE facilities (NETL Uncooled RDE, NETL Water-Cooled RDE, and Purdue University’s RDE), multiple annulus and injector geometries, various frame rates and a broad range of operating conditions. These variations, while not as vast as those among the optimally encompassing set, are expected to devise a more tolerant, valuable network collection.

Because methods presented throughout the manuscript intend to globally evolve RDE diagnostic capabilities beyond sole application in the NETL facility, the extent of data similarity restrictions must be quantified. Therefore, to evaluate the scope or necessary path of progression as a standard practice of machine learning in experimental RDE studies, external data should be evaluated. High-speed images were provided by Dr. Myles Bohon<sup>43,121,41</sup> capturing detonation waves within the experimental RDE at TU Berlin. Because they are the only data considered in this chapter, images provided by TU Berlin will be referred to as simply *external images*.

Regardless of network tolerance, input images should share aspects resulting from image treatment such as annulus centering, background subtraction if applicable, and a circular annulus representation. Due to mirror deformation, external images show a distorted or appar-

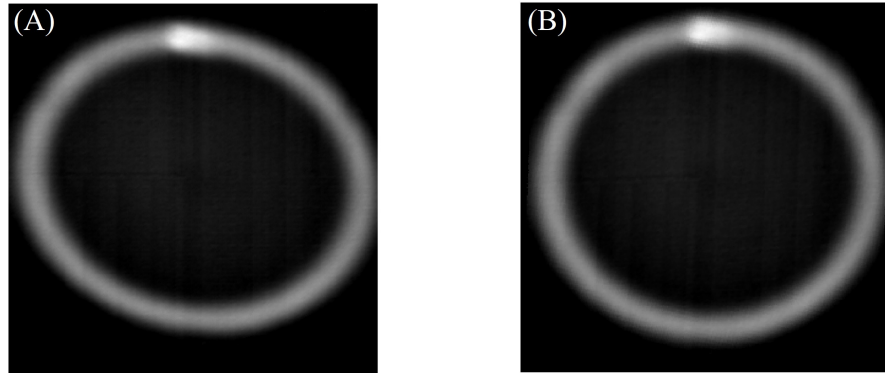


**Figure 8.1:** (A) Average image showing elliptical distortion, and (B) Corrected image to standard cylindrical proportions

ently warped annulus perimeter. Figure 8.1(A) shows an average image across 100 external images, highlighting the elliptical annulus shape. Because all image-based diagnostics rely on cylindrical coordinates and circular geometric relations to perform velocity calculations, the external images are corrected. By rotating the image stack matrix by a determined angle, in this case approximately  $28^\circ$ , such that the semi-major axis is closely aligned with the horizontal, "stretching" along the vertical axis through bicubic interpolation by a factor of 1.1, and rotating back to the original orientation, a corrected image stack is formed. The average image of the corrected image stack is shown in Figure 8.1.

Once the cylindrical proportions are established within the external images, the standard center-finding, Beta factor correction and cropping are performed according to the process outlined in Section 2.4. Those images will be used by detonation surface calculations as well as the image classification network. Additional steps of noise correction and contrast adjustment are necessary for images fed to the YOLO networks. Because the YOLO-adjusted images are more informative to the reader, offering higher contrast and a portion of pixels saturated, examples of those images are shown in Figure 8.2. Images shown in Figure 8.2 show a strong 1CW wave mode that does visibly differ in pixel variation and wave profile length

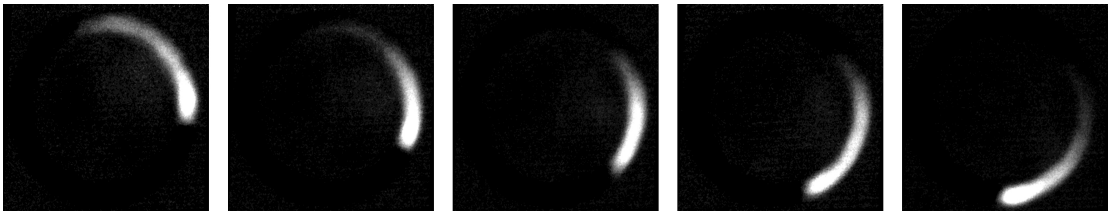


**Figure 8.2:** Example images of strong 1 CW wave mode provided by TU Berlin

compared to waves in NELL images. These images will be used for method comparisons and their evaluation of alternatively represented detonation wave profiles. It should be noted that while more complex wave modes would certainly pose a more challenging task to the networks, multiple waves introduce complexities which convolve velocity calculation interpretations. For example, even two co-rotational waves experience irregular spacing that fluctuates through time, termed galloping, resulting in oscillating velocities in short time-scales for each wave. The detonation surface method described in Chapter 3 outputs an average velocity value for each wave direction, while the YOLO method determines frame-to-frame velocities for each wave. To reduce the aspects of velocity interpretation influenced by modal complexities, the comparison of each diagnostic will use the simple case of the 1CW wave mode shown in Figure 8.2.

External images were collected on an 82.4 mm nominal diameter RDE with frame rate of 87,500 fps, both differing from the experimental setup outline in Chapter 2. It is known that the conventional detonation surface calculation is broadly immune towards varying geometries, frame rates and other factors. Therefore, values of wave number, direction and velocity obtained from detonation surface calculations will serve as the baseline for comparison. Using the method described in Chapter 3, a detonation surface is generated for 100 corrected external images, and is shown as a contour plot in Figure 8.3. Recall that negatively sloped wave traces correspond to CW directionality, and that a single column summarizes

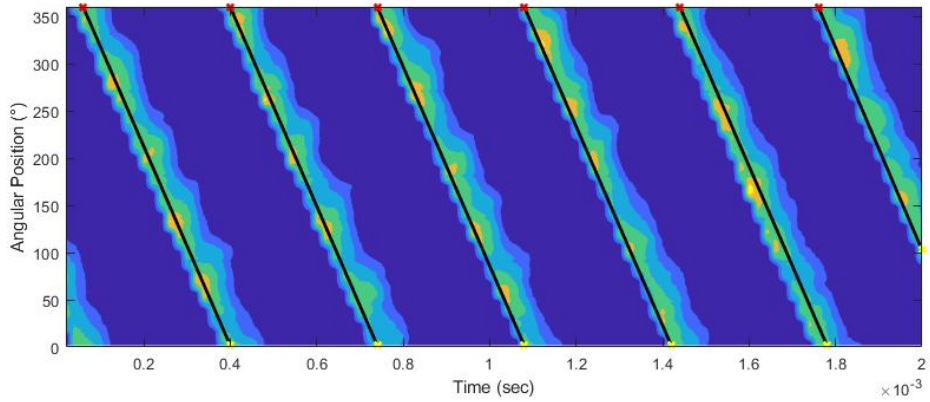


**Figure 8.3:** Detonation surface representing TU Berlin images, Hough transform lines overlaid

the instantaneous presence and location of waves within the unwrapped RDE annulus. For example, in Figure 8.3, the center column at 1 msec shows low values everywhere except the small angular region centered around approximately 120°. This indicates that at 1 msec, one wave is present in the annulus at the 120° location. Intuitively, if two waves were present, a trace traveling along a column would encounter two high-valued regions, expected to be somewhat evenly spaced throughout the 360° range, possibly at 120° and 300° locations.

To determine wave velocity, the line-detecting Hough transform is applied to the detonation surface. Hough lines, overlaid in Figure 8.3, are used to determine wave velocity by relation of median slopes to sampling rate and angular range. Velocity calculations using two-dimensional FFTs are common, but require at least 1000 images compared to the 100 images used currently. Hough lines displayed in Figure 8.3 are leveraged to determine a 1CW wave mode with an overall wave frequency of 5147.1 Hz, which in the TU Berlin RDE corresponds to a velocity of 1332.4 m/sec. This classification and velocity value will serve as the benchmark for network evaluation concerning external images.

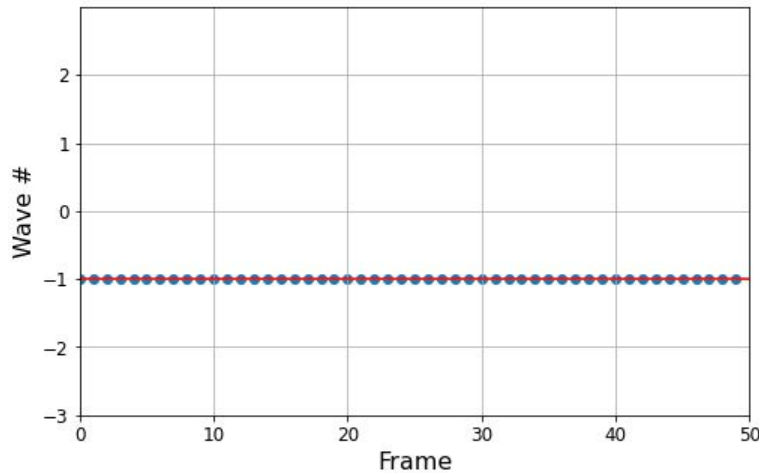


**Figure 8.4:** SqueezeNet classification of TU Berlin images, where (-) negative values correspond to CW waves, and (+) values to CCW directionality

The SqueezeNet image classification network is leveraged as a real-time diagnostic in Chapter 5. Unfortunately, the total diagnostic requires a window of simultaneously acquired ionization current signal which is not available to the author during the writing of the text. However, because calculations beyond the image classification output are simple auto-correlation, it is within reason to state that translation of the diagnostic relies almost solely on the translation of the network performance. To test the RDE SqueezeNet network, the same images used to generate the detonation surface are classified. The SqueezeNet network exhibits complete classification accuracy, as shown in Figure 8.4, where (-) negative classifications again correspond to CW directionality. Evaluation of the RDE SqueezeNet should be performed for more complex modes in external images in future work to quantify confusion across wave modes between the training and external datasets.

To next assess the performance of the YOLO object detection network on external images, contrast-adjusted images are supplied to the network for inference and annotation. Like the results shown in Chapter 6, outputs should indicate the location of the wave front. Although

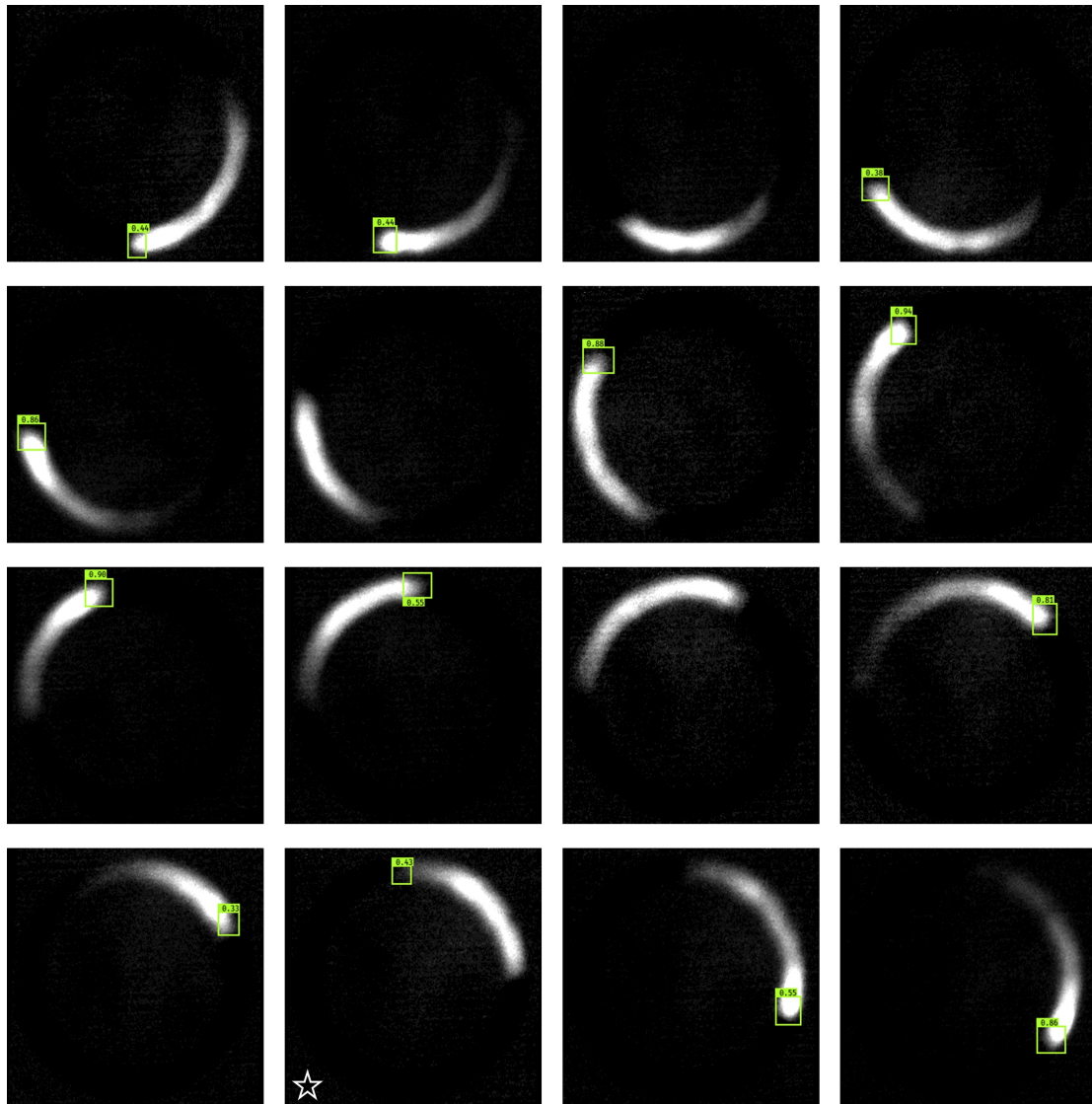


**Figure 8.5:** YOLO annotation subsampling using S<sub>3</sub> annotation style, showing examples of proper detection, absent detection, and an incorrect detection

the linear annotation style was found to be best performing in both detection speeds and velocity uncertainty, the YOLO S<sub>3</sub> annotation style is also evaluated for external square images. This is because the effort to adjust the initially distorted geometry is expected to result in imperfect unwrapped images, introducing an additional factor of uncertainty. A subsampling of external images through one wave revolution, annotated by the S<sub>3</sub> YOLO network are shown in Figure 8.5. In most cases, the network correctly detects the wave front. In a few instances, proportionally similar in frequency to that experienced in the annotation of internal images, no detections are output. Confusion between a wave front and the wave tail is exhibited within one image, indicated by an overlaid star, and is a unique type of misclassification thought to be an artifact of the wave profile effected by a secondary combustion behavior. Specifically, the wave shown in the starred image does not conform to the teardrop profile, and appears to more highly activated in an area closer to the tail. This is not an issue seen otherwise throughout the dataset, and will therefore have minimal effects not warranting retraining efforts.

Tracking of the annotations via Equations 6.2 through 6.4 enables frame-to-frame velocity calculations. Remaining consistent with averaged windows within Chapter 6, frame-to-frame and average velocities are plotted for 50 external images in Figure 8.6. Oscillations in frame-to-frame velocity may suggest cyclic galloping behavior or other alignment issues, but do not differ drastically from similar plots generated using internal images. YOLO velocity calculations in Chapter 6 as well as the current section, calculate values for two consecutive frames with annotations, and disregard outliers of directional difference. This means that velocity calculations across three frames to interpolate across a frame with no annotations, such as the third image in Figure 8.5, are not performed due to the compounding uncertainty across multiple frames. In other words, the first two velocities calculated for images

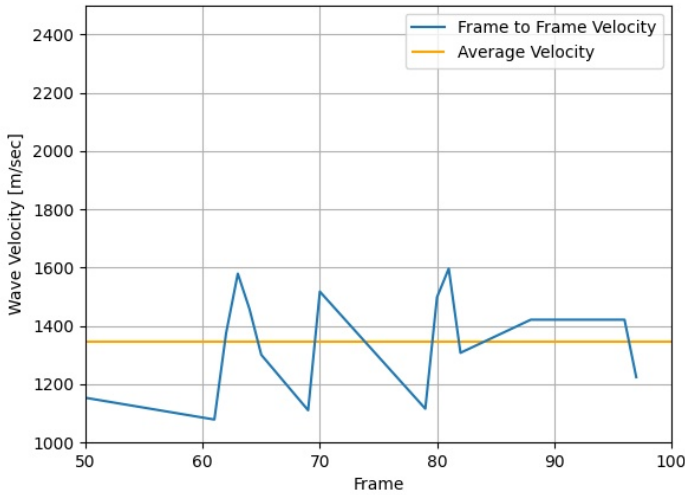


**Figure 8.6:** Frame-to-frame velocity and average velocity calculated with S3 annotations through 50 frames for TU Berlin images

in Figure 8.5 are for image pairs [1,2] and [4,5] because the third image has no annotation. Outliers of directional difference, such as the velocities which would result from the starred image in Figure 8.5, are disregarded by the algorithm. Through 50 frames, the YOLO S3 network measures an average velocity of 1346.9 m/sec. This compares very well to the baseline value of 1332.4 m/s using half as many images, while also offering valuable insights at a highly resolved time-step of 11.43  $\mu$ sec.

External images are also unwrapped to match the linearized format proposed in Section 6.4. In view of the limited usage of these external images relating to the current study, extensive efforts to perfectly correct the elliptical distortion are not undergone. Imperfect alignment of the annulus center and even more so imperfect circular proportions lead to unwanted oscillations in annulus center line positioning with respect to the linearized center axis. Still yet, the YOLO Lin network provides accurate annotations, shown in Figure 8.7 for a sub-sampling matching images shown in Figure 8.5. Through the same images and with the same

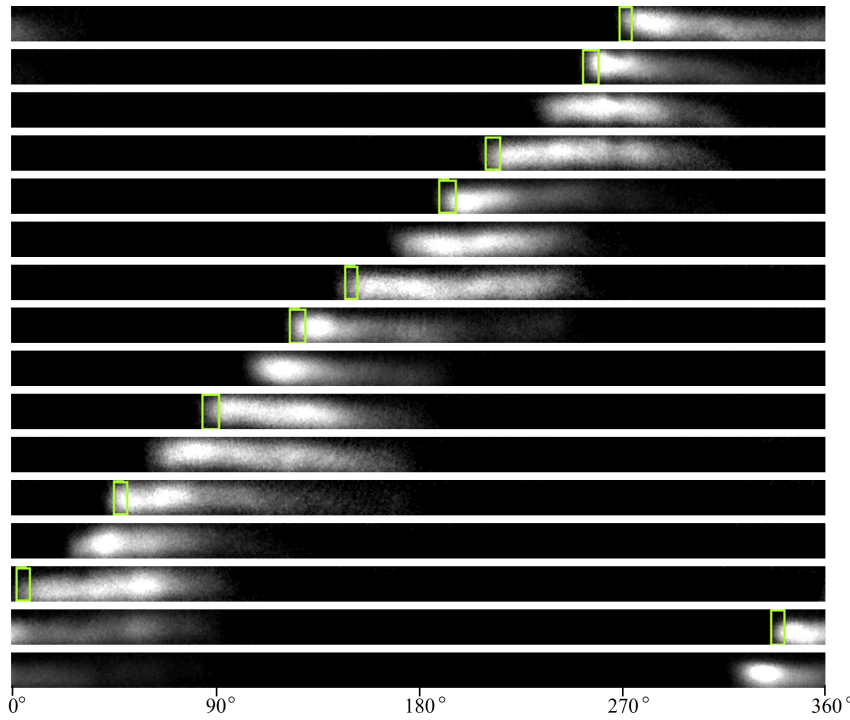


**Figure 8.7:** YOLO annotation subsampling using Lin annotation style, showing examples of proper detection, and absent detection

confidence threshold defined, YOLO Lin network produces less outputs but no incorrect annotations. Average velocity across the same 50 frames is found to be 1367.3 m/s. A slightly elevated velocity is thought to be a result of the flawed circular geometry, but still compares fairly well with the baseline value of 1332.4 m/sec.

As was extolled at the onset of the section, sufficient network performance on external data should allow model sharing across research facilities, enabling external research groups with real-time monitoring capabilities. Although data similarity was a potential road block for this achievement, the results in Figures 8.5 and 8.7 display a promising report for the finalized SqueezeNet, YOLO S<sub>3</sub>, and YOLO Lin networks. Additional modes and data sources are needed to further determine the transference limitations as a future work. For now, the limited

but proven classification, detection, and velocity calculation outputs, successfully evaluated on both internal and external images, significantly expands the impact of the current work.

## 8.2 OVERALL MODEL COMPARISON AND REQUIREMENTS

With knowledge of model performance on external images, a more comprehensive comparison is made possible. Specifically, this section considers the diagnostic packages capable of the total output, whose primary component is the CNN, and when applicable deployed in the lab. Each CNN-based diagnostic technique will be compared against the proven detonation surface method according to parameters targeting feasibility, external applicability, and performance. Addressing the former, Table 8.1 first details equipment and access information. These columns consider experimental setup and equipment, which may be limiting factors due to the relative feasibility of high-speed data acquisition or additional access points. Of the four methods, all require optical access except the TSC diagnostic, which requires only sensors near the detonation plane. Although the TSC diagnostic does not require optical access for operational usage, the TSC dataset does rely on labels informed by the spatial certainty offered by high-speed images. Reapplication of the TSC methodology in an environment without optical access would require an alternative means of modal classification. Optical access and sensors near the detonation plane are common throughout the RDE research community. Access requirements are likely to be more restricting at the turbine integration phase of technology development and eventually in production engines, where pressure or ion signals may be more standard than optical access.

All methods require processing in a numerical programming language such as MATLAB or Python. Equipment listed in Table 8.1 includes only experimental equipment, and no computing requirements since they can all be performed from a PC. Because detonation sur-

Method	Description	Equipment	Access	External Data Performance	New Mode Tolerance
<b>Detonation Surface</b>	100 images: Hough transform lines	High-speed chemiluminescent imaging	Optical access	✓	✓
<b>YOLO</b>	Object Detection: Linear annotations	High-speed chemiluminescent imaging	Optical access	✓	✓
<b>Squeeze-Net</b>	Image classification with Ion correlation integration	Low-speed chemiluminescent imaging NI cDAQ chassis	Optical access Sensor	✓	X
<b>TSC</b>	Time series classification: 200 sample length	NI cDAQ chassis	Sensor	NA	X
		NI cDAQ chassis	Sensor(s)	NA	X

**Table 8.1:** Comparison of four major diagnostic techniques - Application

faces and YOLO object detection rely solely on high-speed images to determine all diagnostic values of interest, equipment needed is limited to high-speed chemiluminescent imaging, as specified in Section 2.3. High-speed chemiluminescent images require a high-speed camera, intensifier, UV lens, and UV bandpass filter. All datasets generated for training throughout the text rely on high-speed imaging, while only detonation surfaces and YOLO object detection use them in the diagnostic phase. The SqueezeNet diagnostic, which uses network image classification outputs alongside time series correlation, utilizes a low-speed chemiluminescent imaging setup and sensor data acquisition via an NI cDAQ chassis, described in Section 2.3.1. Low-speed chemiluminescent imaging replaces the high-speed camera with a USB area scan camera, and relies on the short gate width imposed by the intensifier to capture images similar to those in the training dataset. The same NI cDAQ chassis is the only equipment needed for the TSC lab diagnostic.

The focus of the previous section addresses the second consideration for comparison, being external applicability. Table 8.1 indicates each diagnostics's abilities in external data performance and new mode tolerance. According to the findings of the previous section, detonation surfaces, YOLO object detection, and SqueezeNet image classification all perform well on external data. Unfortunately, external time series data is not available to the author at the writing of the text, leaving the external performance of the TSC diagnostic undetermined. Based on higher variation of sensor data features in the literature compared to more broad similarities in down-axis imaging, TSC is expected to be the least adept to external data classification amongst the competing methods. Classification networks cannot accurately classify modes which are not present in the training set, implying no new mode tolerance for both SqueezeNet and TSC. This has not been an issue within the current laboratory environment where wave modes are found to be fairly predictable and repetitive across the range of normal operating conditions. Creating additional labels in the training set would require adequate volume of representative data, which could possibly be addressed by a variational autoencoder or other method to synthetically generate datasets<sup>133</sup> across possible but unseen modes. YOLO object detection, concerned only with locating wave fronts can tolerate new modes as long as they are some combination of detonation waves. Detonation surfaces show the same degree of tolerance. This metric, while not directly mirroring external data performance, does indicate another layer of external applicability. For example, if a lab wished to apply the SqueezeNet diagnostic but regularly experienced a 5-wave mode, additional efforts of dataset labeling and training would be necessary, while another lab which observes the same modes seen in the NETL RDE could instantly apply the network with the coordinated experimental setup.

Finally, comparison of network performance, the primary focus of the preceding chapters, is tabulated in Table 8.2. Targeting the objective of the present study to advance diagnostic to more efficient, real-time capabilities Table 8.2 details various time requirements, diagnostic feedback rate and time-step resolution. Data acquisition time describes the time required in each diagnostic iteration to collect data necessary to output one set of diagnostic values. High-speed images are captured throughout a test duration, and saved between each test. Therefore, high-speed image analysis methods are limited to post-processing, listed as "Post", and do not correspond to a calculated value of data acquisition time. Diagnostic techniques applied in real-time include SqueezeNet, 200-sample univariate TSC, and 200-sample multivariate TSC, having data acquisition times of 0.2075, 0.176, and 0.342 seconds respectively. Recalling that a single SqueezeNet iteration requires one image and a sensor window equal to that used in a single iteration of the univariate TSC, it can be concluded that time series acquisition, instead of image acquisition, makes up a majority of the SqueezeNet data acquisition time. Requiring twice as much sensor data, multivariate TSC requires the largest data acquisition time among the real-time methods.

Once data is available to the analysis mechanism, classification and calculations are performed. Classification calculation times listed in Table 8.2 encompass time required to generate a single set of diagnostic outputs. While processing speeds of detonation surfaces are not commonly reported directly in the literature, the method employed in Chapter 3 is timed across 100 images and displays a classification speed of 0.5892 s/image. However, individual diagnostic points require the analysis of at least 100 sequential images, translating to 58.92 sec per classification, and a diagnostic feedback rate of 0.017 Hz in post. It is important to acknowledge that this timed classification is not optimized for efficient processing speeds, but boasts many strengths as a robust post-processing technique. Times reported in Table 8.2

correspond to the performance of YOLO Lin, which performs annotations and velocity calculations at 0.105 sec/frame. For a single velocity output, two images are needed, resulting in a classification calculation time of 0.210 sec. After the first velocity calculation, only a single additional image is needed for recurring velocity calculations, leading to a diagnostic feedback rate of 9.5 Hz in post. The YOLO networks are currently regarded as post-processing techniques as a result of camera limitations. High-speed images can not be read from the Photron camera while it continues to record additional images. If an alternate experimental setup allowed a short series of high-speed images to be captured and conveyed to the real-time data acquisition environment at each diagnostic step, the RDE YOLO networks could be operated as real-time diagnostics.

SqueezeNet exhibits the least efficient classification calculation time of 0.0425 sec due to the drastically larger data volume within a single image, despite its highly efficient Fire modules. Univariate and multivariate TSC configurations require increasing classification and calculation times of 0.024 and 0.038 sec, respectively. Data acquisition time and classification calculation time are combined to determine total diagnostic time. For all real-time methods, data acquisition makes up over 80% of the total diagnostic time. These trends, including the disproportionate time series acquisition time compared to an image of higher dimensionality, suggests major improvements may be realized by upgrading the NI cDAQ chassis, or another approach to sensor data acquisition. The inverse of total diagnostic time is the average diagnostic feedback rate, being competitive values of 4 and 5 Hz for SqueezeNet and TSC, respectively. In the laboratory environment, feedback rates are sometimes higher and can be improved by limiting benchmark data collected and stored for later evaluation.

The final performance metric listed in Table 8.2 is diagnostic time-step resolution. More simply, the final column states the window over which a single velocity value is calculated.

Unlike the other parameters, optimization of time-step resolution is not always one that is minimized or maximized for all applications. Instead, studies concerned with bulk behavior which may relate to overall device performance and exhaust flow properties may prefer a more averaged analysis offered by a larger time-step resolution. On the other hand, a study interested in short time scale phenomena such as galloping or counter-rotating interactions would likely benefit from more resolved calculations. All real-time arrangements share a time-step resolution of 8 msec, which is 60% more resolved than the detonation surface resolution of 2 msec. The finest resolution of 0.02 msec, or 20 $\mu$ sec, is achieved by the YOLO network and is dictated by framerate. A tabulated value of 0.02 msec reflects a framerate of 50 kfps, where the alternative 60 kfps results in resolution of 0.017 msec, and the TU Berlin framerate of 87.5 kfps a resolution of 0.011 msec. The speeds reported are determined using only CPUs on a local Dell Precision 7550 laptop with an Intel® Core™ i9-10885H CPU @ 2.40GHz and 64.0 GB of RAM).

Method	Data Acquisition Time (sec)	Classification Calculation Time (sec)	Total Diagnostic Time (sec)	Diagnostic Feedback Rate (Hz)	Diagnostic Time-step resolution (msec)
Detonation Surface	Post	58.92	–	0.017*	2
YOLO	Post	0.210	–	9.50*	0.02
SqueezeNet	0.2075	0.0425	0.25	4	0.8
TSC	Univariate 0.176	0.024	0.2	5	0.8
	Multivariate 0.342	0.038	0.38	2.63	0.8

**Table 8.2:** Comparison of four major diagnostic techniques - Performance

Leading remarks of the present chapter asserted the expectation that no single network should outperform its competitors in all facets. Each network, having unique strengths and limitations certainly presents as a well-suited solution to an aligned subset of experimental needs. Thus, each method occupies a worthwhile and earned place within the constructed RDE machine learning portfolio.

### 8.3 LIMITATIONS OF USAGE

In both classification networks, a broad range of operating conditions and geometries are represented in the training data set. Some of those operating condition envelopes are restated in Table 8.3. In addition to varying mass flows, equivalence ratios, back-pressures, and pre-heat temperatures, data covering operation of multiple injection schemes and RDE facilities is used. To illustrate the application of each network beyond the already broad scope of operating conditions at NETL, external images properly classified in the previous section were captured at a different pixel resolution, using a higher frame rate, on a smaller RDE, operating at an equivalence ratio beyond that of the envelope stated in Table 8.3. The major limitation of classification networks instead lies in the inability to classify new modes which are not present in the training set. Otherwise, as was shown in the previous subsection, data with comparable representation of detonation wave profiles are satisfactory to the trained network.

There certainly exists a critical point where wave representation decayed by elongated exposure times or poor image quality renders the current networks inapplicable. However, images captured throughout the RDE community and reported in the literature are all of similar quality and representation. In order to accommodate classification of images of drastically lesser quality, an additional network would need to be trained on a data set containing

similarly poor images. Such an effort was not conducted within this work, as image quality was comparable across multiple RDE facilities and operating conditions. Similarly, application of the trained networks is expected to be applicable only to OH\* chemiluminescence images, which are standard throughout the RDE community. Consideration of unfiltered images was not feasible at the time of this work, as high-speed images are utilized for various studies at NETL which require optimized detonation visualization via the targeting of OH\* chemiluminescence. Adaptation of this proposed methodology may be applicable to alternatively filtered images, but is certainly limited to facilities which can achieve short exposure times less than 20  $\mu$ sec, either by high-speed camera shutter speeds, or by intensifier gating. Images with elongated exposure times will excessively smear the detonation wave, to a critical point of an entirely illuminated annular gap, eliminating the primary features used to classify wave modes.

It is important to note that accuracies reported throughout the text are referred to as either *training* or *validation* accuracies. Those metrics, which achieve high values by the end of the training effort, reflect a network's final performance on training and validation data analysis, both of which are intentionally optimized throughout the training process. Analysis of new data not present in the training or validation data sets, specifically in the inference phase, will inherently show lesser performance. Some examples of this relationship, being that of *training* and *testing* accuracies, are depicted in Chapter 5 where the SqueezeNet network with a reported training accuracy of 99.6% achieves a testing accuracy of around 85% when classifying live images with a modified experimental setup. As the application of a trained network reaches the boundary of limitation, the training and validation accuracies do not change because they are a metric only of the training process. In this scenario, testing accuracy will certainly decrease with decreasing image similarity to an eventual critical point where train-

ing of a more representative network would be required. This point does necessarily mark a limitation of the contained methodology which can be easily reiterated, only a limitation of the finalized trained networks.

Air mass flow rate	0.52-0.7 kg/sec
Equiv. Ratio	0.5 - 0.9
Pressure (Pre-Combustion)	0 - 310 kPa
Temperature (Inlet Air)	340 - 480 K

**Table 8.3:** RDE operating conditions utilized for data set generation

As was mentioned earlier in the section, YOLO networks are currently limited to post-processing due to hardware constraints. Using a camera which can capture a short window of high-speed images, convey those images to the diagnostic environment, and continue to capture high-speed images at each diagnostic step, the YOLO networks could certainly be operated as real-time RDE diagnostics.

#### 8.4 SURVEY OF AI METHODS AND FUTURE WORK

Each network presented throughout the text is trained using a supervised learning approach. This simply indicates that the networks are trained with ground truth, manually labeled data. The supervised learning approach attempts to create a network that determines classifications or detections based on the features and patterns within the labeled data set. Throughout the work, classification of wave modes across large data volumes is simplified by the usage of detonation surfaces and image stacks played as videos for the human classifier, being the author. Manual classification ensures a standard and an account of label quality that specifically meets the needs of the objective.

Often, supervised learning is not practical for other studies due to the high costs or complete absence of domain expert labeling. In many cases, data volume is available cheaply but

lacks proper ground truth information. In those instances, unsupervised learning may be applied to a completely unlabeled data set to predict labels which reflect the clustering of input patterns based on a statistical structure. The outputs of unsupervised approaches do not correspond to any predetermined classifications, such as wave mode. For this reason, unsupervised learning is not a viable approach for the outlined objectives which rely heavily on specified modal classifications. However, unsupervised learning may prove valuable to the clustering of experimental RDE data, by possibly revealing shared features or patterns which are not apparent through explicit calculations or existing data processing techniques. Distinctions of choked vs. unchoked flow, galloping vs. equally spaced waves, or a number of unknown or unexpected correlations may be found using unsupervised learning in future work.

An alternative approach to both supervised and unsupervised learning is semi-supervised learning. Semi-supervised learning, addressing either classification or clustering, utilizes a partially labeled data set. In this format, output labels correspond to those present in the small portion of labelled data, which is much more applicable to the current objective than the abstract outputs of unsupervised learning. Self-training is a popular subset of semi-supervised learning in which a classifier is trained using the small portion of labeled data. The trained classifier then evaluates the larger portion of unlabeled data points, assigning confidence scores to each classification. Data points labeled with confidence scores exceeding a given threshold are added to the ground truth portion of the data set, which is then used to retrain the classifier. This sequence is performed repetitively until the classifier converges<sup>134</sup>. Semi-supervised learning is a unique solution for classification problems lacking ground truth labeling which has shown increased classification accuracies in some studies, but does not scale well with data volume, exhibiting cubic computational time complexity<sup>135</sup>. Because verifi-

cation of proper self-labeling requires additional efforts, and because visual classification of wave modes within disjointed images is much more difficult than considering a series of images, semi-supervised learning was not chosen as a preferred approach throughout this work. Future studies concerned with RDE behaviors which are more difficult to manually label in large volumes and whose architectural solution is less clear, such as deflagrative combustion detection in transverse images, may be best addressed by semi-supervised multi-view learning. In possible future studies where localized data sparsity, such as a wave mode that is very rarely experienced, semi-supervised low-density separation may be a suitable training style.

A supervised learning approach was chosen in each chapter based on a trade-off between data labeling, training time, model accuracy, and label verification. Unsupervised learning would have certainly required less labeling efforts, being none, but would not have offered satisfactory model accuracy or valuable outputs for new data. Semi-supervised may have achieved comparable accuracies with substantially less data labeling, but would have required more training time and an additional effort of label verification. Because the end product of each network is not simply proving that a model can be trained, but an operational component of a lab-deployed diagnostic, labels assigned to the larger portion of unlabeled data in the training set would need to be, at least in part but likely the whole, verified by the practitioner. Due to the nature of the RDE detonation waves, identification of the wave mode in a given image is much simpler and thought to be more accurate when classifying a series of images which can be described and visualized by detonation surfaces and/or image stack videos. While these trade-offs justify the preference of learning style utilized throughout the work, each certainly offers interesting means of studying RDE data in the future.

Reproduction of the diagnostic effort in an external laboratory should give strong consideration to both supervised and semi-supervised learning, as priorities elsewhere of domain

expert labeling may outweigh those of computational time and label verification. Unexplored machine learning techniques within the RDE community should be studied as means to offer valuable advancements in the future, either through the future work of the author or external studies. With thrust or pressure gain measurements available, regression may relate operating conditions or geometry parameters to overall performance more simply than what is described by deterministic methods. To that end, multi-dimensional trends relating injector geometry, operating conditions, or any other parameter to a similar performance metric may be optimized using machine learning linear programming or genetic algorithms. In the event that mode changes are found to be detrimental to RDE performance, or that a specific behavior such as detonation extinguishing is prevalent in production engines, time series forecasting may provide alerts to an active-control environment to prevent such unfavored events. These potential studies are a small subset of worthwhile machine learning applications to fundamental and applied RDE research. Exploration of such techniques by the RDE research community, each as an additional step building on the confidence of machine learning offered by this work, is strongly encouraged to more rapidly advance the technology maturation and achieve the targeted environmental impact as a whole.

For many RDE studies in the near-future, including many of those proposed in the previous paragraph, data will be treated and analyzed in post-processing. Optimizing injector schemes, quantifying parasitic combustion, clustering choking conditions and predicting or optimizing pressure gain for a set of parameters each hold value in their influence for RDE device improvements. Real-time diagnostics are not needed for those studies which require data volume over data velocity. In the years to come, if and when RDEs are fully integrated into gas turbines, real-time diagnostics will be necessary to actively control the subsystem. Therefore, upcoming studies more concerned with operational behaviors and response to

altered operating conditions, such as fuel flow, which are more reflective of future turbine integration, will in fact require real time diagnostics. It is important to note that real-time diagnostics should accomplish feedback rates comparable to active control loops, possibly 5 to 10 Hz. In order to do so, however, measurements with sampling rates capable of resolving the detonation wave timescale are necessary. In other words, images or time series sensor data must be captured with exposure times and sampling rates comparable to that of high-speed imaging and acquisition, but may only need to do so 5 to 10 times per second. This is exhibited in Chapter 5, where images are captured with a low-speed camera, 4 to 5 frames per second, but exposure time is gated by the intensifier to a short window of 12  $\mu$ sec, comparable to the exposure time of high-speed images. A similar process is performed in the text with time series sensor data, which was sampled at 250 kHz, but a short window of 200 samples was required only 4 to 5 times per second for the diagnostic. Longer exposure times and sampling rates which match the diagnostic feedback rate do not offer any valuable resolution of detonation behavior. It is thought to be possible that a more averaged parameter whose diagnostic feedback rate is a sufficient sampling rate, such as thrust, might be used to sufficiently diagnose operating characteristics of a final RDE design. However, until the accomplishment of the finalized RDE production design, resolution of detonation behaviors is necessary for both real-time and post-processing efforts.

The more immediate and direct application of diagnostics developed throughout this work will be performed as a future work in the development of an active control framework at NETL Morgantown. Real-time diagnostic outputs will be supplied to an active control loop, which will alter fuel mass flow and subsequently equivalence ratio in an ambitious effort to achieve intentional mode changes, to absolve galloping modes, to prevent mode changes and other behaviors towards a targeted modal condition. At the time of writing, a specific wave

mode has not been identified as the optimum mode of operation. Co-rotational and counter-rotational wave interactions with injectors, the fresh reactant region, and one another results in a complex relationship and unclear optimum. Future thrust and pressure gain measurements, which are already performed elsewhere in the RDE research community, will clarify some aspects of this issue. In the event that an additional parameter is found to more drastically impact RDE performance, such as back-flow indicated by plenum pressures, the current work provides a methodology that is widely adaptable across network types and data dimensionality. In addition to the diagnostic improvements of the current study and that of the upcoming active control work, the contained work to determine machine learning's applicability to highly abstract detonation wave characteristics, and to establish an adapted experimental setup for live data acquisition and processing, provides a suitable foundation for future RDE machine learning studies.

*The thing I'll remember most about the flight is that it was fun.*

Sally Ride, American physicist and NASA astronaut

# 9

## Conclusion

CLASSIFICATION OF DETONATION WAVE BEHAVIOR PRESENT IN A ROTATING DETONATION ENGINE (RDE) annulus during combustor operation is critical to advancing the control and integration of RDEs in gas turbine engines. The aim of this work is to advance the efficiency of RDE diagnostic techniques from conventional post-processing efforts to lab-deployed real-time methods, achieving highly efficient detonation characterization through

the application of convolutional neural networks (CNNs) to experimental RDE data. To accomplish this goal, six research tasks are proposed and executed.

Chapter 3 compares two conventional RDE diagnostics being cross-correlation of multiple transducer signals methods and high-speed image analysis resulting in detonation surface plots. Both prove capable of determining modal variations within an RDE, providing wave number, direction, frequency and velocity. While these conventional image processing methods provide reliable insights regarding detonation wave behaviors, extended processing times needed to deterministically analyze large data volumes eliminates the possibility of evolving toward real-time feedback capabilities. Values obtain using detonation surface plots serve as the baseline for CNN performance characterization.

Acknowledging a need for increased diagnostic speeds, Chapter 4 offers a methodology for wave mode classification through analysis of individual downstream high-speed chemiluminescent images using a CNN. Classified modes include clockwise and counterclockwise variants of one, two and three co-rotational detonation waves, single, double, and triple counter-rotating detonation waves as well as deflagration. After surveying and successfully training five publicly available CNN architectures, SqueezeNet was chosen for its classification speed of 0.0229 sec/frame. Achieving training and validation accuracies of 99.6% and 98.5% respectively, SqueezeNet demonstrated the ability to consistently classify the number of waves present as well as their direction in individual images and did so in a fraction of the time required by other common methods.

Chapter 5 extends the proposed methodology of Chapter 4 alongside conventional high-speed sensor data to achieve real-time detonation wave diagnostic capabilities, including wave velocity and frequency. The approach targets lab integration and acquisition of live experimental data, made possible by experimental equipment alterations allowing live acquisition

of short-gate low-speed images and simultaneous ionization current signal. Laboratory results show a diagnostic feedback of 3-5 Hz, with accurate and stable descriptions of wave behaviors. While this is well below the time scale of the detonation wave progression, it exceeds all existing capabilities in speed and adapted lab deployment, and offers a first step towards actively controlling an RDE toward favored modal operation.

In pursuit of additional diagnostics including wave velocity and frequency, Chapter 6 demonstrates a methodology for individual wave detection in down-axis images using a computer vision You Only Look Once (YOLO) network through analysis of high-speed images of standard and linearized proportions. The goal of this work was to use the YOLO architecture to report the location of each wave within the image as well as wave direction for multi-wave modal behavior in an experimental RDE. Separate efforts were outlined to alter Intersection over Union (IoU) and confidence thresholds to improve the annotation outputs according to the physical understanding of the RDE. Unfortunately, the YOLO network can not be considered as a real-time diagnostic due to its reliance on high-speed images, which cannot be retrieved from the high-speed camera during RDE operation. Still yet, annotation locations are tracked to determine frame-to-frame velocities, boasting time-step resolution of  $20 \mu\text{sec}$ . The finalized network can process and annotate images at 9.5 frames per second in post-processing. While this is not a real-time capability, it is certainly an advancement in RDE diagnostic efficiency in both post-processing speeds and drastically improved time-step resolution.

As RDE technology progresses towards production engine implementation, optical access may be limited or completely nonexistent. Chapter 7 outlines the creation of univariate and multivariate time series classification (TSC) networks, having the same modal classification capabilities as the image classification network while relying solely on time series pressure

and/or ionization current sensor data. Reduced data dimensionality of sensor data compared to images resulted in improved classification times. However, once integrated into the laboratory environment, acquisition speeds, which are disproportionately larger for high-speed sensor data than image collection, result in an average diagnostic feedback rate of 5 Hz, comparable to the lab deployed image classification diagnostic. The TSC effort parallels that of Chapters 4 and 5, providing an option for more easily integrated CNN-based diagnostic with equally resolved velocity calculations at 0.8 msec.

As a final evaluation, Chapter 8 compares each of the four diagnostic methods, being detonation surfaces, image classification, object detection, and time series classification, according to metrics effecting diagnostic feasibility, external applicability, and performance. External applicability was addressed through the study of external images, provided by TU Berlin. External images, captured in a different facility at a higher framerate and larger degrees of image distortion and smearing were treated in the same manor as those used in the training sets, and supplied to each image-based diagnostic. Image classifications, as well as wave speed calculations performed by the computer vision CNNs compared very well to the baseline detonation surface value. This suggested a degree of proper feature generalization, which may enable the direct application of these finalized models in other experimental facilities. Model transferability greatly increases the impact of the current work and the likelihood of widespread machine learning adoption needed to advance RDE monitoring and control. Comparisons found that no single diagnostic structure outperforms the others in all metrics. Instead, each method offers solutions uniquely beneficial to a given study based on primary objectives and constraints. This alone justifies the need for a portfolio of machine learning capabilities, begun herein, with networks tailored to specific needs throughout the research community.

Completion of the research tasks builds on the foundation of existing data analysis techniques and presents multiple computer vision and machine learning approaches to more efficient post-processing and real-time diagnostics, fully integrated in an experimental RDE facility. Each network offers new and unique benefits to the progression of RDE research efforts. As computer vision and machine vision evolve alongside and within RDE technology, improved processing times and refined networks have allowed for the progressive development of real-time monitoring, a crucial step in the development of an active control framework. The demonstrated approaches were uniquely developed for various RDE data types commonly used in the PGC community, and offer early and practical examples of neural network application to RDE research and diagnostics. When possible, diagnostic methods were successfully deployed in an altered laboratory environment, showing feedback rates expected to be satisfactory to the future development of an RDE active-control framework. This body of work, through the early applications of machine learning to RDE data, presents methods and insights which offer substantial and beneficial advancement of diagnostic techniques from post-processing to real-time speeds, a critical development in the progression of RDE technological maturation.

# A

Enlarged and Expanded Figures

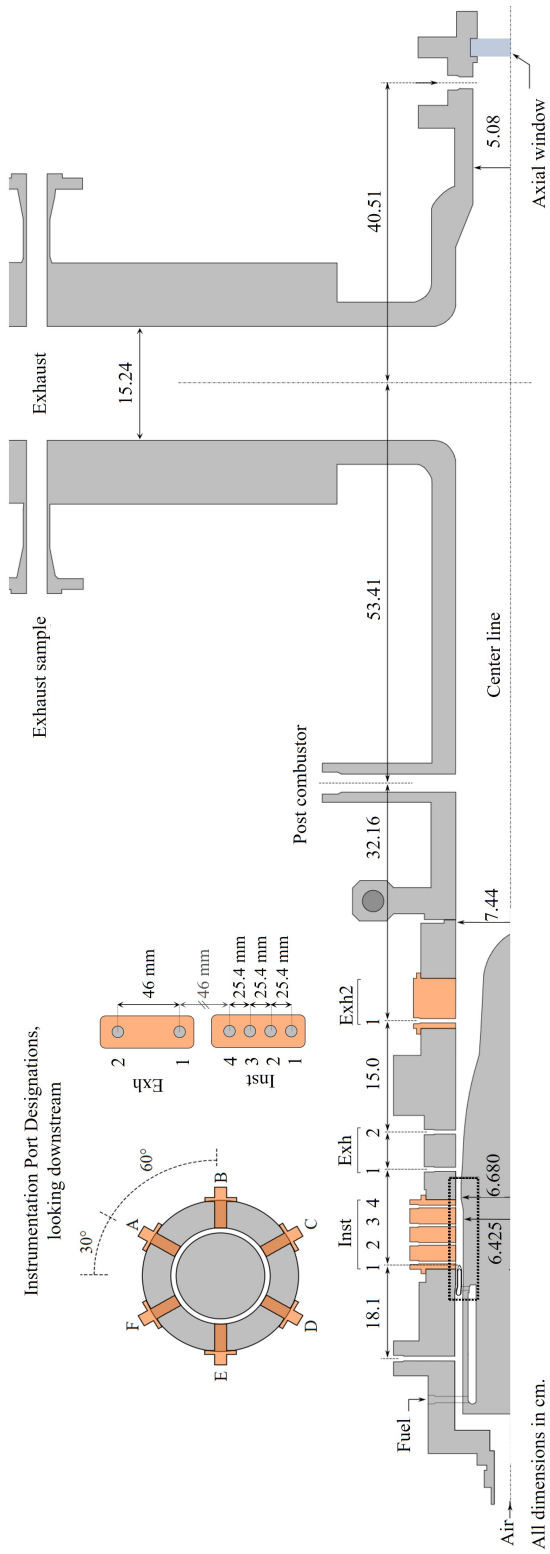


**Figure A.1:** Cross-section water-cooled RDE showing axial injection, sampling port circumferential and axial nomenclature, exit nozzle, and downstream diffuser. Box indicates boundary for Figure 2.8

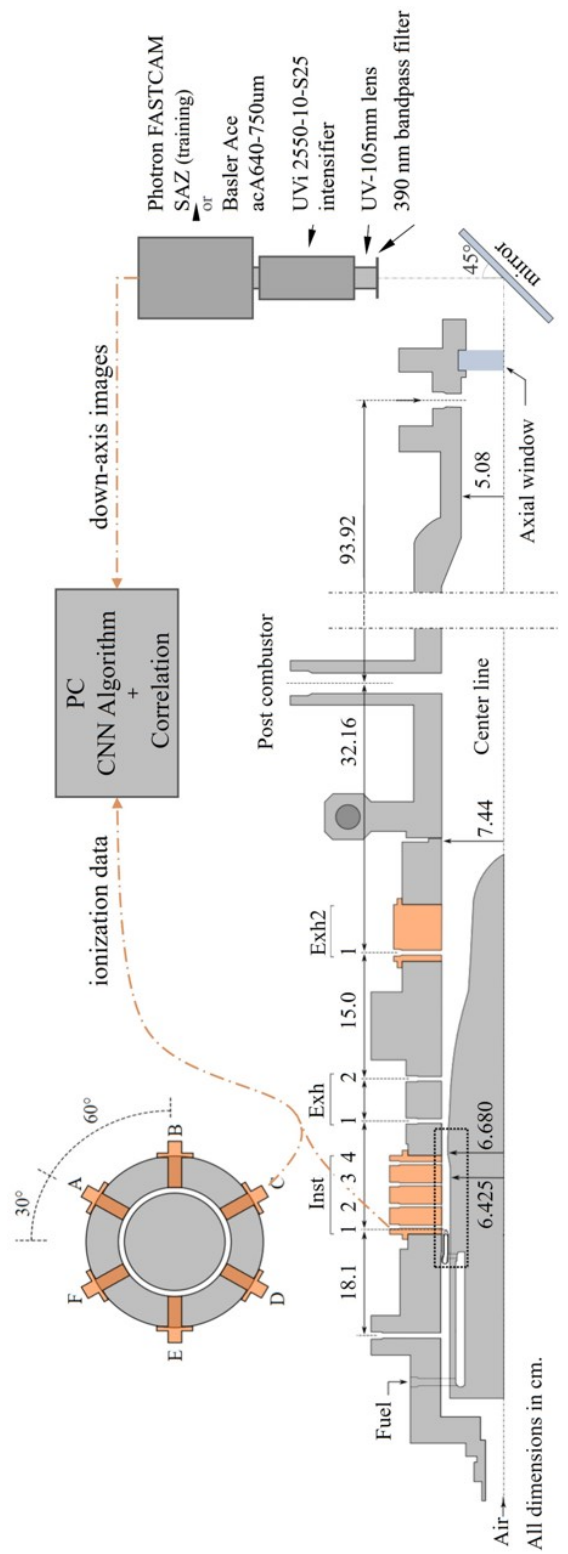


**Figure A.2:** Cross-section water-cooled RDE showing axial injection, sampling port nomenclature, exit nozzle, downstream diffuser, camera alignment, and real-time data acquisition setup. Box indicates boundary for Figure 2.8

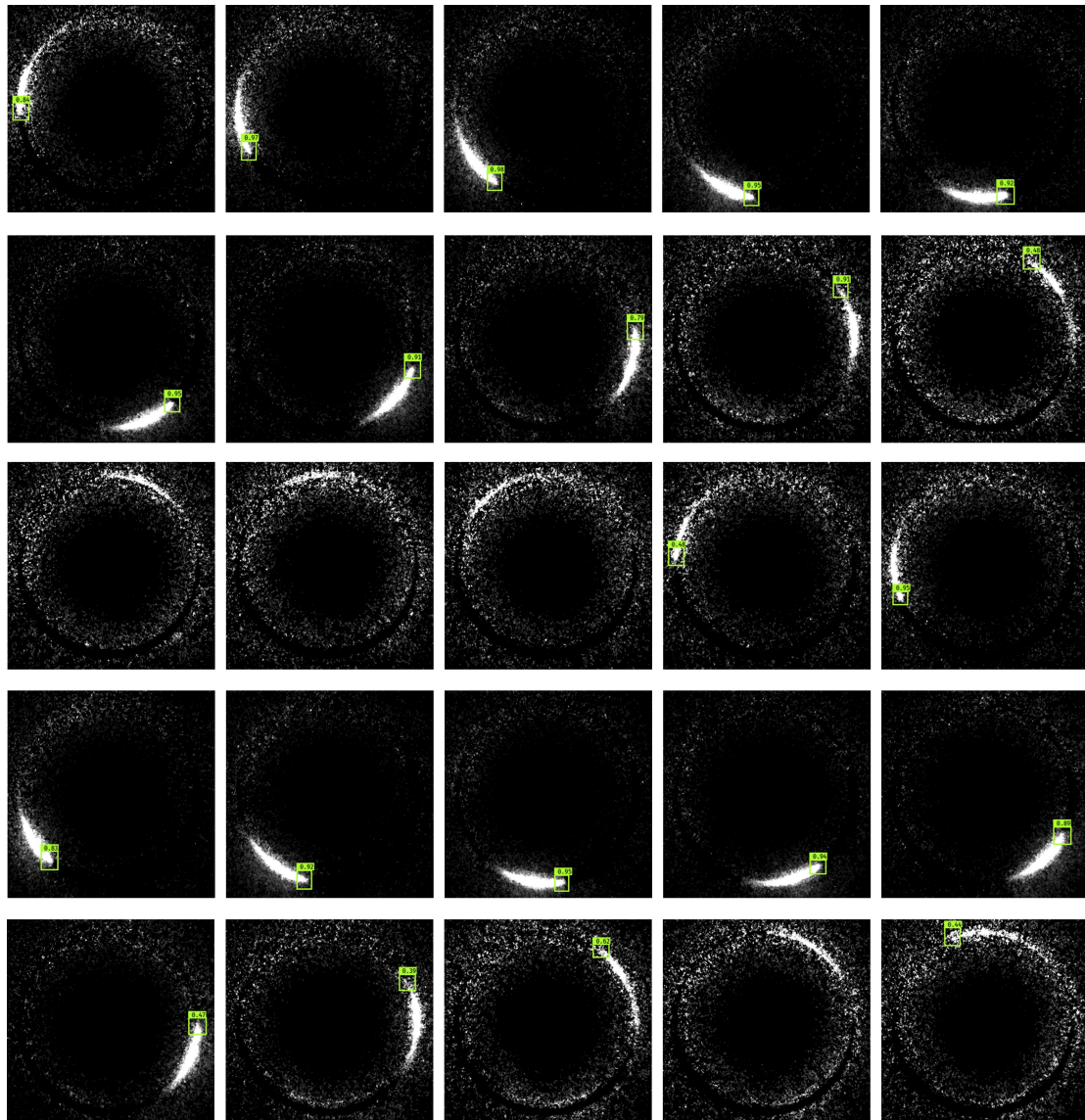


**Figure A.3:** YOLO object detection for S3 annotation for images 1-25, used for velocity calculation in Figure 6.11

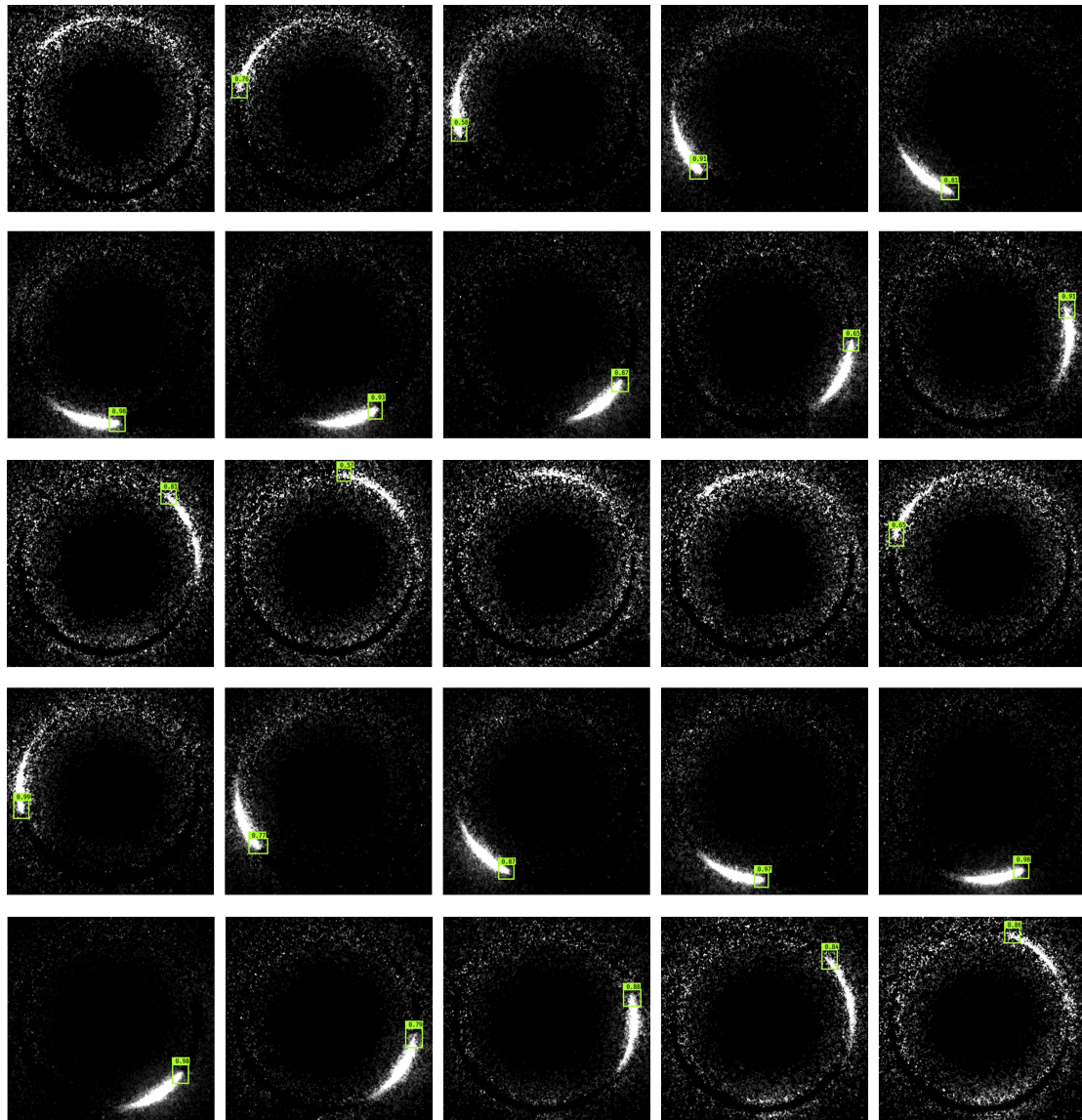


**Figure A.4:** YOLO object detection for S<sub>3</sub> annotation for images 26-50, used for velocity calculation in Figure 6.11

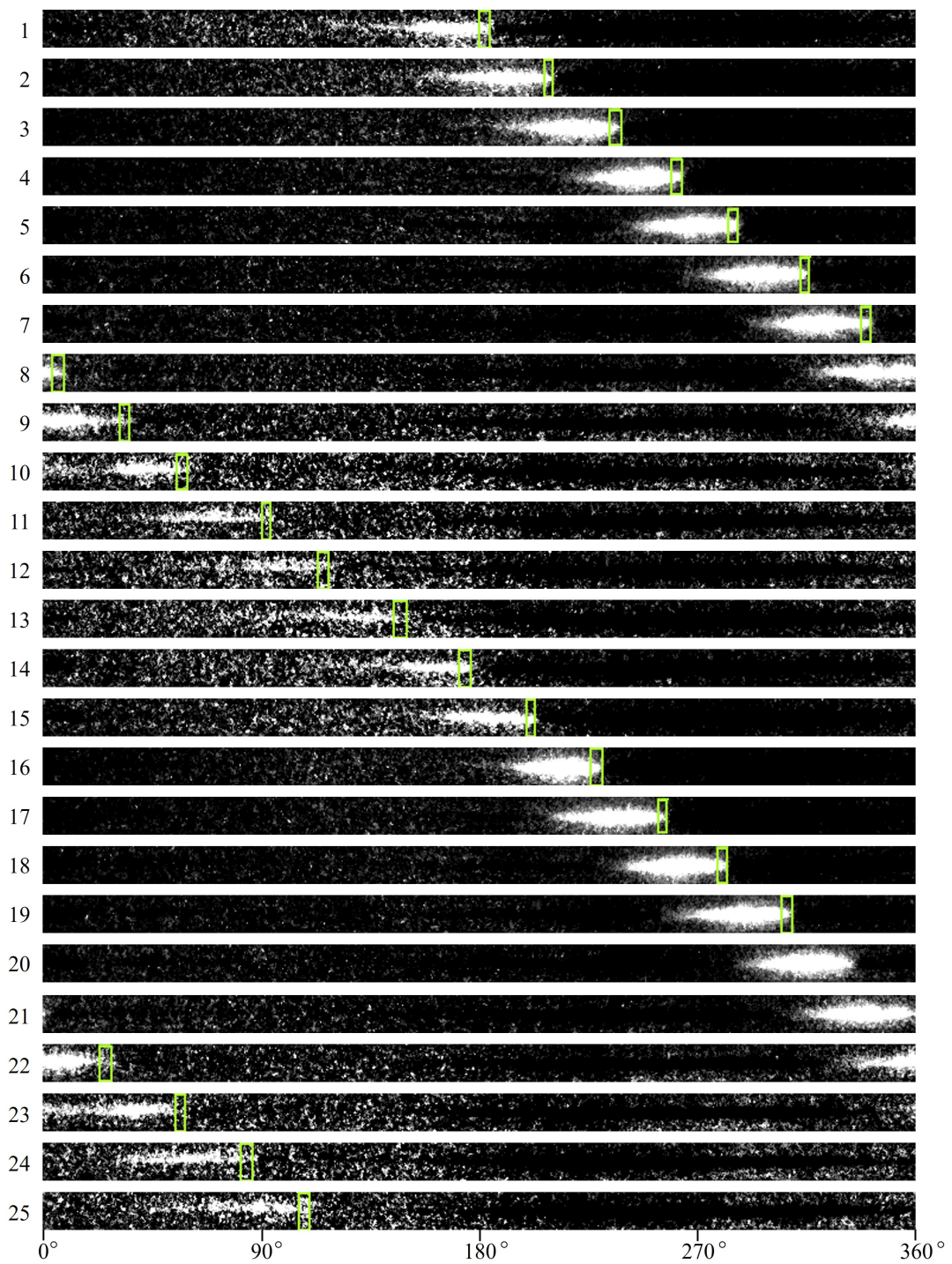


**Figure A.5:** YOLO object detection for Linearized images 1-25, used for velocity calculation in Figure 6.13

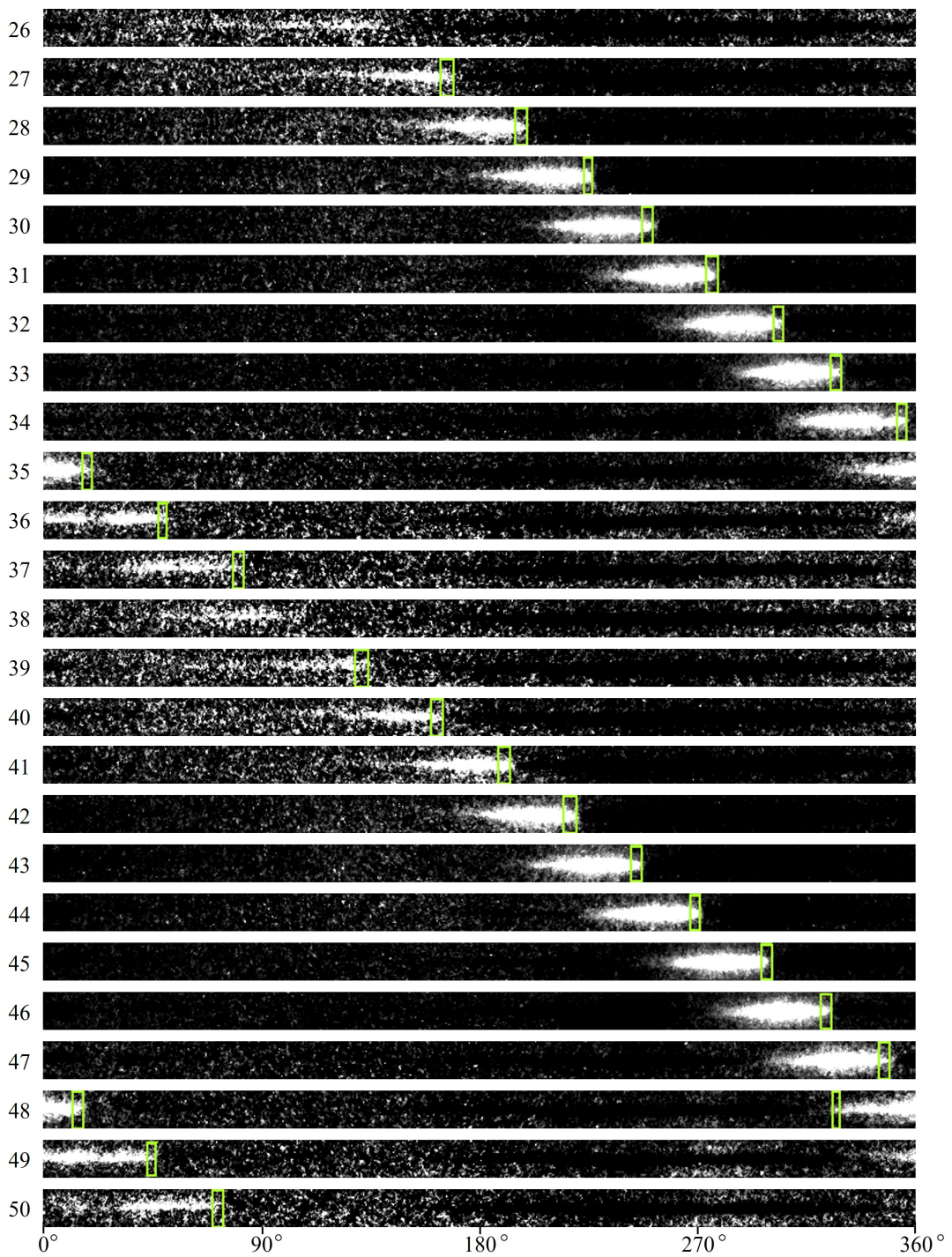


**Figure A.6:** YOLO object detection for Linearized images 26-50, used for velocity calculation in Figure 6.13

# B

## Model Summaries

Layer (type)	Output Shape	Param #	Connected to
<hr/>			
input_2 (InputLayer)	(None, 3, 224, 224)	0	
conv1 (Conv2D)	(None, 96, 112, 112)	14208	input_2[0][0]
maxpool1 (MaxPooling2D)	(None, 96, 55, 55)	0	conv1[0][0]
fire2_squeeze (Conv2D)	(None, 16, 55, 55)	1552	maxpool1[0][0]
fire2_expand1 (Conv2D)	(None, 64, 55, 55)	1088	fire2_squeeze[0][0]
fire2_expand2 (Conv2D)	(None, 64, 55, 55)	9280	fire2_squeeze[0][0]
concatenate_8 (Concatenate)	(None, 128, 55, 55)	0	fire2_expand1[0][0] fire2_expand2[0][0]
fire3_squeeze (Conv2D)	(None, 16, 55, 55)	2064	concatenate_8[0][0]
fire3_expand1 (Conv2D)	(None, 64, 55, 55)	1088	fire3_squeeze[0][0]
fire3_expand2 (Conv2D)	(None, 64, 55, 55)	9280	fire3_squeeze[0][0]
concatenate_9 (Concatenate)	(None, 128, 55, 55)	0	fire3_expand1[0][0] fire3_expand2[0][0]
fire4_squeeze (Conv2D)	(None, 32, 55, 55)	4128	concatenate_9[0][0]
fire4_expand1 (Conv2D)	(None, 128, 55, 55)	4224	fire4_squeeze[0][0]
fire4_expand2 (Conv2D)	(None, 128, 55, 55)	36992	fire4_squeeze[0][0]
concatenate_10 (Concatenate)	(None, 256, 55, 55)	0	fire4_expand1[0][0] fire4_expand2[0][0]
maxpool4 (MaxPooling2D)	(None, 256, 27, 27)	0	concatenate_10[0][0]
fire5_squeeze (Conv2D)	(None, 32, 27, 27)	8224	maxpool4[0][0]
fire5_expand1 (Conv2D)	(None, 128, 27, 27)	4224	fire5_squeeze[0][0]
fire5_expand2 (Conv2D)	(None, 128, 27, 27)	36992	fire5_squeeze[0][0]
concatenate_11 (Concatenate)	(None, 256, 27, 27)	0	fire5_expand1[0][0] fire5_expand2[0][0]
fire6_squeeze (Conv2D)	(None, 48, 27, 27)	12336	concatenate_11[0][0]

**Figure B.1:** SqueezeNet Model Summary<sup>63</sup>, continued in Figure B.2

fire6_expand1 (Conv2D)	(None, 192, 27, 27)	9408	fire6_squeeze[0][0]
fire6_expand2 (Conv2D)	(None, 192, 27, 27)	83136	fire6_squeeze[0][0]
concatenate_12 (Concatenate)	(None, 384, 27, 27)	0	fire6_expand1[0][0] fire6_expand2[0][0]
fire7_squeeze (Conv2D)	(None, 48, 27, 27)	18480	concatenate_12[0][0]
fire7_expand1 (Conv2D)	(None, 192, 27, 27)	9408	fire7_squeeze[0][0]
fire7_expand2 (Conv2D)	(None, 192, 27, 27)	83136	fire7_squeeze[0][0]
concatenate_13 (Concatenate)	(None, 384, 27, 27)	0	fire7_expand1[0][0] fire7_expand2[0][0]
fire8_squeeze (Conv2D)	(None, 64, 27, 27)	24640	concatenate_13[0][0]
fire8_expand1 (Conv2D)	(None, 256, 27, 27)	16640	fire8_squeeze[0][0]
fire8_expand2 (Conv2D)	(None, 256, 27, 27)	147712	fire8_squeeze[0][0]
concatenate_14 (Concatenate)	(None, 512, 27, 27)	0	fire8_expand1[0][0] fire8_expand2[0][0]
maxpool8 (MaxPooling2D)	(None, 512, 13, 13)	0	concatenate_14[0][0]
fire9_squeeze (Conv2D)	(None, 64, 13, 13)	32832	maxpool8[0][0]
fire9_expand1 (Conv2D)	(None, 256, 13, 13)	16640	fire9_squeeze[0][0]
fire9_expand2 (Conv2D)	(None, 256, 13, 13)	147712	fire9_squeeze[0][0]
concatenate_15 (Concatenate)	(None, 512, 13, 13)	0	fire9_expand1[0][0] fire9_expand2[0][0]
fire9_dropout (Dropout)	(None, 512, 13, 13)	0	concatenate_15[0][0]
conv10 (Conv2D)	(None, 6, 13, 13)	3078	fire9_dropout[0][0]
global_average_pooling2d_1 (Glo (None, 6)		0	conv10[0][0]
softmax (Activation)	(None, 6)	0	global_average_pooling2d_1[0][0]
=====			
Total params:	738,502		
Trainable params:	738,502		
Non-trainable params:	0		

Figure B.2: SqueezeNet Model Summary Cont.<sup>63</sup>

Layer (type)	Output Shape	Param #	Connected to
input_1 (InputLayer)	[(None, 200, 1)]	0	
conv1d (Conv1D)	(None, 200, 128)	768	input_1[0][0]
instance_normalization (InstanceNormal)	(None, 200, 128)	256	conv1d[0][0]
p_re_lu (PReLU)	(None, 200, 128)	128	instance_normalization[0][0]
dropout (Dropout)	(None, 200, 128)	0	p_re_lu[0][0]
max_pooling1d (MaxPooling1D)	(None, 100, 128)	0	dropout[0][0]
conv1d_1 (Conv1D)	(None, 100, 256)	360704	max_pooling1d[0][0]
instance_normalization_1 (InstanceNorm)	(None, 100, 256)	512	conv1d_1[0][0]
p_re_lu_1 (PReLU)	(None, 100, 256)	256	instance_normalization_1[0][0]
dropout_1 (Dropout)	(None, 100, 256)	0	p_re_lu_1[0][0]
max_pooling1d_1 (MaxPooling1D)	(None, 50, 256)	0	dropout_1[0][0]
conv1d_2 (Conv1D)	(None, 50, 512)	2753024	max_pooling1d_1[0][0]
instance_normalization_2 (InstanceNorm)	(None, 50, 512)	1024	conv1d_2[0][0]
p_re_lu_2 (PReLU)	(None, 50, 512)	512	instance_normalization_2[0][0]
dropout_2 (Dropout)	(None, 50, 512)	0	p_re_lu_2[0][0]
lambda_1 (Lambda)	(None, 50, 256)	0	dropout_2[0][0]
softmax (Softmax)	(None, 50, 256)	0	lambda_1[0][0]
lambda (Lambda)	(None, 50, 256)	0	dropout_2[0][0]
multiply (Multiply)	(None, 50, 256)	0	softmax[0][0] lambda[0][0]
dense (Dense)	(None, 50, 256)	65792	multiply[0][0]
instance_normalization_3 (InstanceNorm)	(None, 50, 256)	512	dense[0][0]
flatten (Flatten)	(None, 12800)	0	instance_normalization_3[0][0]
dense_1 (Dense)	(None, 13)	166413	flatten[0][0]

Total params: 3,349,901  
 Trainable params: 3,349,901  
 Non-trainable params: 0

**Figure B.3:** Encoder Summary - Univariate 200 Sample Length

Layer (type)	Output Shape	Param #	Connected to
input_2 (InputLayer)	[None, 499, 2]	0	
conv1d_3 (Conv1D)	(None, 499, 128)	1408	input_2[0][0]
instance_normalization_4 (InstanceNorm)	(None, 499, 128)	256	conv1d_3[0][0]
p_re_lu_3 (PReLU)	(None, 499, 128)	128	instance_normalization_4[0][0]
dropout_3 (Dropout)	(None, 499, 128)	0	p_re_lu_3[0][0]
max_pooling1d_2 (MaxPooling1D)	(None, 249, 128)	0	dropout_3[0][0]
conv1d_4 (Conv1D)	(None, 249, 256)	360704	max_pooling1d_2[0][0]
instance_normalization_5 (InstanceNorm)	(None, 249, 256)	512	conv1d_4[0][0]
p_re_lu_4 (PReLU)	(None, 249, 256)	256	instance_normalization_5[0][0]
dropout_4 (Dropout)	(None, 249, 256)	0	p_re_lu_4[0][0]
max_pooling1d_3 (MaxPooling1D)	(None, 124, 256)	0	dropout_4[0][0]
conv1d_5 (Conv1D)	(None, 124, 512)	2753024	max_pooling1d_3[0][0]
instance_normalization_6 (InstanceNorm)	(None, 124, 512)	1024	conv1d_5[0][0]
p_re_lu_5 (PReLU)	(None, 124, 512)	512	instance_normalization_6[0][0]
dropout_5 (Dropout)	(None, 124, 512)	0	p_re_lu_5[0][0]
lambda_3 (Lambda)	(None, 124, 256)	0	dropout_5[0][0]
softmax_1 (Softmax)	(None, 124, 256)	0	lambda_3[0][0]
lambda_2 (Lambda)	(None, 124, 256)	0	dropout_5[0][0]
multiply_1 (Multiply)	(None, 124, 256)	0	softmax_1[0][0] lambda_2[0][0]
dense_2 (Dense)	(None, 124, 256)	65792	multiply_1[0][0]
instance_normalization_7 (InstanceNorm)	(None, 124, 256)	512	dense_2[0][0]
flatten_1 (Flatten)	(None, 31744)	0	instance_normalization_7[0][0]
dense_3 (Dense)	(None, 13)	412685	flatten_1[0][0]
<hr/>			
Total params:	3,596,813		
Trainable params:	3,596,813		
Non-trainable params:	0		

**Figure B.4:** Encoder Summary - Multivariate 500 Sample Length

Layer (type)	Output Shape	Param #
input_1 (InputLayer)	[(None, 499, 1)]	0
conv1d (Conv1D)	(None, 499, 128)	1152
batch_normalization (BatchNormalization)	(None, 499, 128)	512
activation (Activation)	(None, 499, 128)	0
conv1d_1 (Conv1D)	(None, 499, 256)	164096
batch_normalization_1 (BatchNormalization)	(None, 499, 256)	1024
activation_1 (Activation)	(None, 499, 256)	0
conv1d_2 (Conv1D)	(None, 499, 128)	98432
batch_normalization_2 (BatchNormalization)	(None, 499, 128)	512
activation_2 (Activation)	(None, 499, 128)	0
global_average_pooling1d (GlobalAveragePooling1D)	(None, 128)	0
dense (Dense)	(None, 13)	1677

Total params: 267,405  
Trainable params: 266,381  
Non-trainable params: 1,024

**Figure B.5:** FCN Summary - Univariate 500 Sample Length

Layer (type)	Output Shape	Param #
input_1 (InputLayer)	[(None, 200, 2)]	0
conv1d (Conv1D)	(None, 200, 128)	2176
batch_normalization (BatchNormalization)	(None, 200, 128)	512
activation (Activation)	(None, 200, 128)	0
conv1d_1 (Conv1D)	(None, 200, 256)	164096
batch_normalization_1 (BatchNormalization)	(None, 200, 256)	1024
activation_1 (Activation)	(None, 200, 256)	0
conv1d_2 (Conv1D)	(None, 200, 128)	98432
batch_normalization_2 (BatchNormalization)	(None, 200, 128)	512
activation_2 (Activation)	(None, 200, 128)	0
global_average_pooling1d (GlobalAveragePooling1D)	(None, 128)	0
dense (Dense)	(None, 13)	1677

Total params: 268,429  
Trainable params: 267,405  
Non-trainable params: 1,024

**Figure B.6:** FCN Summary - Multivariate 200 Sample Length

Layer (type)	Output Shape	Param #	Connected to
<hr/>			
input_1 (InputLayer)	[None, 200, 2]	0	
conv1d (Conv1D)	(None, 200, 64)	1088	input_1[0][0]
batch_normalization (BatchNormalization)	(None, 200, 64)	256	conv1d[0][0]
activation (Activation)	(None, 200, 64)	0	batch_normalization[0][0]
conv1d_1 (Conv1D)	(None, 200, 64)	20544	activation[0][0]
batch_normalization_1 (BatchNormalization)	(None, 200, 64)	256	conv1d_1[0][0]
activation_1 (Activation)	(None, 200, 64)	0	batch_normalization_1[0][0]
conv1d_3 (Conv1D)	(None, 200, 64)	192	input_1[0][0]
conv1d_2 (Conv1D)	(None, 200, 64)	12352	activation_1[0][0]
batch_normalization_3 (BatchNormalization)	(None, 200, 64)	256	conv1d_3[0][0]
batch_normalization_2 (BatchNormalization)	(None, 200, 64)	256	conv1d_2[0][0]
add (Add)	(None, 200, 64)	0	batch_normalization_3[0][0] batch_normalization_2[0][0]
activation_2 (Activation)	(None, 200, 64)	0	add[0][0]
conv1d_4 (Conv1D)	(None, 200, 128)	65664	activation_2[0][0]
batch_normalization_4 (BatchNormalization)	(None, 200, 128)	512	conv1d_4[0][0]
activation_3 (Activation)	(None, 200, 128)	0	batch_normalization_4[0][0]
conv1d_5 (Conv1D)	(None, 200, 128)	82048	activation_3[0][0]
batch_normalization_5 (BatchNormalization)	(None, 200, 128)	512	conv1d_5[0][0]
activation_4 (Activation)	(None, 200, 128)	0	batch_normalization_5[0][0]
conv1d_7 (Conv1D)	(None, 200, 128)	8320	activation_2[0][0]
conv1d_6 (Conv1D)	(None, 200, 128)	49280	activation_4[0][0]
batch_normalization_7 (BatchNormalization)	(None, 200, 128)	512	conv1d_7[0][0]
batch_normalization_6 (BatchNormalization)	(None, 200, 128)	512	conv1d_6[0][0]
add_1 (Add)	(None, 200, 128)	0	batch_normalization_7[0][0] batch_normalization_6[0][0]
activation_5 (Activation)	(None, 200, 128)	0	add_1[0][0]
conv1d_8 (Conv1D)	(None, 200, 128)	131200	activation_5[0][0]
batch_normalization_8 (BatchNormalization)	(None, 200, 128)	512	conv1d_8[0][0]
activation_6 (Activation)	(None, 200, 128)	0	batch_normalization_8[0][0]
conv1d_9 (Conv1D)	(None, 200, 128)	82048	activation_6[0][0]
batch_normalization_9 (BatchNormalization)	(None, 200, 128)	512	conv1d_9[0][0]
activation_7 (Activation)	(None, 200, 128)	0	batch_normalization_9[0][0]
conv1d_10 (Conv1D)	(None, 200, 128)	49280	activation_7[0][0]
batch_normalization_11 (BatchNormalization)	(None, 200, 128)	512	activation_5[0][0]
batch_normalization_10 (BatchNormalization)	(None, 200, 128)	512	conv1d_10[0][0]
add_2 (Add)	(None, 200, 128)	0	batch_normalization_11[0][0] batch_normalization_10[0][0]
activation_8 (Activation)	(None, 200, 128)	0	add_2[0][0]
global_average_pooling1d (GlobalAveragePooling1D)	(None, 128)	0	activation_8[0][0]
dense (Dense)	(None, 13)	1677	global_average_pooling1d[0][0]
<hr/>			
Total params: 508,813			
Trainable params: 506,253			
Non-trainable params: 2,560			

Figure B.7: ResNet Summary - Multivariate 200 Sample Length

## References

- [1] Nordeen C, Schwer D, Schauer F, Hoke J, Cetegen B, Barber T. 2011 Thermodynamic Modeling of a Rotating Detonation Engine. In: *49th AIAA Aerospace Sciences Meeting including the New Horizons Forum and Aerospace Exposition*, Aerospace Sciences Meetings. (doi:10.2514/6.2011-803).
- [2] Gaydon AG, Hurle IR. 1963 *The Shock Tube in High Temperature Chemical Physics*. Reinhold Publishing Corporation.
- [3] Fickett W, Davis WC. 2000 *Detonation : Theory and Experiment*. Donver Publications.
- [4] D L Chapman. 1899 On the rate of explosion in gases. *The London, Edinburgh, and Dublin Philosophical Magazine and Journal of Science* **47**, 284, 90–104. (doi:10.1080/14786449908621243).
- [5] Jouguet E. 1905 On the Propagation of Chemical Reactions in Gases. *Journal de Mathématiques Pures et Appliquées* **2**, 6, 347–425.
- [6] Liu Y, Zhang W, Zhang Z. 2020. The propagating mechanism of chapman-jouguet deflagration. (doi:10.48550/ARXIV.2001.04738).
- [7] Akkerman V, Bychkov V, Kuznetsov M, Law CK, Valiev D, Wu MH. 2013 Fast flame acceleration and deflagration-to-detonation transition in smooth and obstructed tubes, channels and slits. In: *8th US National Combustion Meeting 2013*, pp. 970–978.
- [8] Akkerman V, Chaudhuri S, Law CK. 2013 Accelerative propagation and explosion triggering by expanding turbulent premixed flames. *Physical Review E - Statistical, Nonlinear, and Soft Matter Physics* **87**, 2, 1–7. (doi:10.1103/PhysRevE.87.023008).
- [9] Akkerman V, Law CK, Bychkov V, Eriksson LE. 2010 Analysis of flame acceleration induced by wall friction in open tubes. *Physics of Fluids* **22**, 5, 1–14. (doi:10.1063/1.3425646).

- [10] St George AC, Ganesh Kumar VA, Driscoll RB, Gutmark EJ. 2016 A Correlation-Based Method to Quantify the Operating State in a Rotating Detonation Combustor. In: *54th AIAA Aerospace Sciences Meeting*, January, pp. 1–15. (doi:10.2514/6.2016-1402).
- [11] Bluemner R, Bohon M, Paschereit CO, Gutmark EJ. 2018 Dynamics of Counter-Rotating Wave Modes in an RDC. In: *2018 Joint Propulsion Conference*. (doi:10.2514/6.2018-4572).
- [12] Zhou S, Ma H, Ma Y, Zhou C, Liu D, Li S. 2018 Experimental study on a rotating detonation combustor with an axial-flow turbine. *Acta Astronautica* **151**, 7–14. (doi:10.1016/J.ACTAASTRO.2018.05.047).
- [13] Anand V. 2018 *Rotating Detonation Combustor Mechanics*. Doctor of philosophy, University of Cincinnati.
- [14] Strakey PA, Ferguson DH, Sisler AT, Nix AC. 2016 Computationally quantifying loss mechanisms in a rotating detonation engine. In: *54th AIAA Aerospace Sciences Meeting*, pp. 1–14. (doi:10.2514/6.2016-0900).
- [15] Paxson DE. 2018 Examination of Wave Speed in Rotating Detonation Engines Using Simplified Computational Fluid Dynamics. In: *2018 AIAA Aerospace Sciences Meeting*, January, pp. 1–12. (doi:10.2514/6.2018-1883).
- [16] Paxson DE, Kaemming TATA. 2012 Foundational Performance Analyses of Pressure Gain Combustion Thermodynamic Benefits for Gas Turbines. In: *50th AIAA Aerospace Sciences Meeting including the New Horizons Forum and Aerospace Exposition*, May. (doi:10.2514/6.2012-770).
- [17] Gülen S. 2017 Pressure gain combustion advantage in land-based electric power generation. *Journal of the Global Power and Propulsion Society* **1**, 288–302. (doi:10.22261/JGPPS.K4MD26).
- [18] Roy GD, Frolov SM, Borisov AA, Netzer DW. 2004 Pulse detonation propulsion: Challenges, current status, and future perspective. *Progress in Energy and Combustion Science* **30**, 6, 545–672. (doi:10.1016/j.pecs.2004.05.001).
- [19] Zhdan SA, Bykovskii FA, Vedernikov EF. 2007 Mathematical modeling of a rotating detonation wave in a hydrogen-oxygen mixture. *Combustion, Explosion and Shock Waves* **43**, 4, 449–459. (doi:10.1007/s10573-007-0061-y).
- [20] Hoffmann N. 1940 Reaction Propulsion by Intermittent Detonative Combustion. *German Ministry of Supply*, Volkenrode Translation.

- [21] Voitsekhovskii B. 1960 Stationary Spin Detonation. *Soviet Journal of Applied Mechanics and Technical Physics* **3**, 157.
- [22] Nicholls JA, Cullen RE, Ragland KW. 1966 Feasibility studies of a rotating detonation wave rocket motor. *Journal of Spacecraft and Rockets* **3**, 6, 893–898. (doi:10.2514/3.28557).
- [23] Kailasanath K, Patnaik G. 2000 Performance estimates of pulsed detonation engines. *Proceedings of the Combustion Institute* **28**, 1, 595–601. (doi:10.1016/S0082-0784(00)80259-3).
- [24] Rasheed A, Tangirala VE, Vandervort CL, Dean AJ, Haubert C. 2004 Interactions of a Pulsed Detonation Engine with a 2D Turbine Blade Cascade. In: *42nd Aerospace Sciences Meeting and Exhibit*. (doi:10.2514/6.2004-1207).
- [25] Roy A, Ferguson DH, Sidwell T, O'Meara B, Strakey P, Bedick C, Sisler A. 2017 Experimental Study of Rotating Detonation Combustor Performance under Preheat and Back Pressure Operation. In: *55th AIAA Aerospace Sciences Meeting*, January, pp. 1–16. (doi:10.2514/6.2017-1065).
- [26] Shank JC. 2012 *Development and Testing of a Rotating Detonation Engine Run on Hydrogen and Air*. Ph.D. thesis, Air Force Institute of Technology.
- [27] Bykovskii FA, Zhdan SA, Vedernikov EF. 2006 Continuous Spin Detonations. *Journal of Propulsion and Power* **22**, 6, 1204–1216. (doi:10.2514/1.17656).
- [28] Heiser WH, Pratt DT. 2008 Thermodynamic Cycle Analysis of Pulse Detonation Engines. *Journal of Propulsion and Power* **18**, 1, 68–76. (doi:10.2514/2.5899).
- [29] Rankin BA, Fotia ML, Naples AG, Stevens CA, Hoke JL, Kaemming TA, Theuerkauf SW, Schauer FR. 2016 Overview of Performance, Application, and Analysis of Rotating Detonation Engine Technologies. *Journal of Propulsion and Power* **33**, 1, 131–143. (doi:10.2514/1.B36303).
- [30] Nordeen C. 2013 *Thermodynamics of a Rotating Detonation Engine*. Ph.D. thesis, University of Connecticut.
- [31] Lu FK, Braun EM, Massa L, Wilson DR. 2011 Rotating Detonation Wave Propulsion: Experimental Challenges, Modeling, and Engine Concepts (Invited). In: *47th AIAA/ASME/SAE/ASEE Joint Propulsion Conference & Exhibit*, August, pp. 464–470. (doi:10.2514/6.2011-6043).
- [32] Sousa J, Paniagua G, Collado Morata E. 2017 Thermodynamic analysis of a gas turbine engine with a rotating detonation combustor. *Applied Energy* **195**, 247–256. (doi:10.1016/j.apenergy.2017.03.045).

- [33] Naples AG, Hoke J, Battelle R, Schauer F. 2018 T63 Turbine Response To Rotating Detonation Combustor Exhaust Flow. In: *Proceedings of ASME Turbo Expo 2018 Turbomachinery Technical Conference and Exposition*, pp. 1–11. (doi:10.1115/1.4041135).
- [34] Zheng H, Qi L, Zhao N, Li Z, Liu X. 2018 A Thermodynamic Analysis of the Pressure Gain of Continuously Rotating Detonation Combustor for Gas Turbine. *Applied Sciences* **8**, 4, 535. (doi:10.3390/app8040535).
- [35] Ma JZ, Luan MY, Xia ZJ, Wang JP, Zhang SJ, Yao SB, Wang B. 2020 Recent progress, development trends, and consideration of continuous detonation engines. *AIAA Journal* **58**, 12, 4976–5035. (doi:10.2514/1.J058157).
- [36] Deng L, Ma H, Xu C, Liu X, Zhou C. 2018 The feasibility of mode control in rotating detonation engine. *Applied Thermal Engineering* **129**, 1538–1550. (doi:10.1016/j.aplthermaleng.2017.10.146).
- [37] Austin JM, Shepherd JE. 2003 Detonations in hydrocarbon fuel blends. *Combustion and Flame* **132**, 1–2, 73–90. (doi:10.1016/S0010-2180(02)00422-4).
- [38] Zipf RK, Gamezo VN, Sapko MJ, Marchewka WP, Mohamed KM, Oran ES, Kessler DA, Weiss ES, Addis JD, Karnack FA, et al. 2013 Methane-air detonation experiments at NIOSH Lake Lynn Laboratory. *Journal of Loss Prevention in the Process Industries* **26**, 2, 295–301. (doi:10.1016/j.jlp.2011.05.003).
- [39] Bennewitz JW, Bigler BR, Hargus WA, Danczyk SA, Smith RD. 2018 Characterization of detonation wave propagation in a rotating detonation rocket engine using direct high-speed imaging. In: *2018 Joint Propulsion Conference*. (doi:10.2514/6.2018-4688).
- [40] Chacon F, Gamba M. 2019 Study of Parasitic Combustion in an Optically Accessible Continuous Wave Rotating Detonation Engine. In: *AIAA Scitech 2019 Forum*. (doi:10.2514/6.2019-0473).
- [41] Bohon MD, Bluemner R, Paschereit CO, Gutmark EJ. 2019 High-speed imaging of wave modes in an RDC. *Experimental Thermal and Fluid Science* **102**, 28–37. (doi:10.1016/j.expthermflusci.2018.10.031).
- [42] Zahn A, Knight E, Anand V, Jodele J, Gutmark EJ. 2018 Examination of Counter-Rotating Detonation Waves Using Cross-Correlation. In: *2018 Joint Propulsion Conference*. (doi:10.2514/6.2018-4568).

- [43] Bohon MD, Bluemner R, Paschereit CO, Gutmark EJ. 2018 Cross-Correlation as a Tool for Measuring RDCWave Speed, Direction, and Complexity. In: *2018 Joint Propulsion Conference*. (doi:10.2514/6.2018-4569).
- [44] Johnson K, Ferguson DH, Nix A. 2020 Validation of Cross-Correlation Detonation Wave Mode Identification Through High-Speed Image Analysis. In: *AIAA Scitech 2020 Forum*. Reston, Virginia. (doi:10.2514/6.2020-1179).
- [45] Athmanathan V, Fisher JM, Ayers Z, Cuadrado DG, Andreoli V, Braun J, Meyer T, Paniagua G, Fugger CA, Roy S. 2019 Turbine-integrated High-pressure Optical RDE (THOR) for injection and detonation dynamics assessment. In: *AIAA Propulsion and Energy 2019 Forum*. Reston, Virginia. (doi:10.2514/6.2019-4041).
- [46] Johnson KB, Ferguson DH, Tempke RS, Nix AC. 2021 Application of a Convolutional Neural Network for Wave Mode Identification in a Rotating Detonation Combusotor Using High-Speed Imaging. *Journal of Thermal Science and Engineering Applications* 13, 6, 1–11. (doi:10.1115/1.4049868).
- [47] Theuerkauf SW, Schauer FR, Anthony R, Hoke JL. 2015 Experimental Characterization of High-Frequency Heat Flux in a Rotating Detonation Engine. In: *53rd AIAA Aerospace Sciences Meeting*, January, pp. 1–10. (doi:10.2514/6.2015-1603).
- [48] Paxson DE, Miki K. 2022 Computational Assessment of Inlet Backflow Effects on Rotating Detonation Engine Performance and Operability. In: *AIAA SciTech Forum*. (doi:10.2514/6.2022-1263).
- [49] Buyakofu V, Matsuoka K, Matsuyama K, Goto K, Kawasaki A, Watanabe H, Itouyama N, Ishihara K, Noda T, Kasahara J, et al. 2022 Flight Demonstration of Detonation Engine System Using Sounding Rocket S-520-31: Performance of Pulse Detonation Engine. In: *AIAA SciTech Forum*. (doi:10.2514/6.2022-0233).
- [50] Ferguson DH, O'Meara B, Roy A, Johnson K. 2020 Experimental measurements of NOx emissions in a Rotating Detonation Engine. In: *AIAA Scitech 2020 Forum*. ORlando, FL: American Institute of Aeronautics and Astronautics. (doi:10.2514/6.2020-0204).
- [51] Huang X, Chang PH, Li JM, Ngiam HK, Ruiqin S, Teo CJ, Khoo BC, Ngiam K, Shan R, Chiang J, et al. 2022 A Continuous Detonation Phenomenon: Shuttling Transverse Combustion. In: *AIAA SciTech Forum*. (doi:10.2514/6.2022-1457).
- [52] Ballard, D H, Brown C. 1982 *Computer Vision*. Englewood Cliffs, N.J.: Prentice-Hall.

- [53] Maqueda AI, Loquercio A, Gallego G, Garcia N, Scaramuzza D. 2018 Event-Based Vision Meets Deep Learning on Steering Prediction for Self-Driving Cars. In: *Proceedings of the IEEE Computer Society Conference on Computer Vision and Pattern Recognition*, Dl, pp. 5419–5427. (doi:10.1109/CVPR.2018.00568).
- [54] Kuo CM, Lai SH, Sarkis M. 2018 A compact deep learning model for robust facial expression recognition. In: *IEEE Computer Society Conference on Computer Vision and Pattern Recognition Workshops*, pp. 2202–2210. IEEE. (doi:10.1109/CVPRW.2018.00286).
- [55] Huang KT. 2019 Integrating computer vision and non-linear optimization for automated deformable registration of 3D medical images. *Physics in Medicine and Biology* **64**, 13. (doi:10.1088/1361-6560/ab2202).
- [56] Russakovsky O, Deng J, Su H, Krause J, Satheesh S, Ma S, Huang Z, Karpathy A, Khosla A, Bernstein M, et al. 2015 ImageNet Large Scale Visual Recognition Challenge. *International Journal of Computer Vision* **115**, 3, 211–252. (doi:10.1007/s11263-015-0816-y).
- [57] Krizhevsky BA, Sutskever I, Hinton GE. 2012 ImageNet Classification with Deep Convolutional Neural Networks. *Communications of the ACM* **60**, 6, 84–90.
- [58] Simonyan K, Zisserman A. 2015 Very deep convolutional networks for large-scale image recognition. *3rd International Conference on Learning Representations, ICLR 2015 - Conference Track Proceedings* pp. 1–14.
- [59] He K, Zhang X, Ren S, Sun J. 2016 Deep residual learning for image recognition. In: *Proceedings of the IEEE Computer Society Conference on Computer Vision and Pattern Recognition*. (doi:10.1109/CVPR.2016.90).
- [60] Dering ML, Tucker CS. 2017 A Convolutional Neural Network Model for Predicting a Product’s Function, Given Its Form. *Journal of Mechanical Design, Transactions of the ASME* **139**, 11, 1–14. (doi:10.1115/1.4037309).
- [61] Mao, X, Joshi, V, Miyanawala, T P and Jaiman RK. 2018 Data-Driven Computing with Convolutional Neural Networks for Two-Phase Flows: Application to Wave-Structure Interaction. In: *Proceedings of the ASME 2018 37th International Conference on Ocean, Offshore and Arctic Engineering*, p. Volume 2: CFD and FSI. Madrid, Spain. (doi:10.1115/OMAE2018-78425).
- [62] Xia M, Li T, Xu L, Liu L, De Silva CW. 2018 Fault Diagnosis for Rotating Machinery Using Multiple Sensors and Convolutional Neural Networks. *IEEE/ASME Transactions on Mechatronics* **23**, 1, 101–110. (doi:10.1109/TMECH.2017.2728371).

- [63] Iandola FN, Han S, Moskewicz MW, Ashraf K, Dally WJ, Keutzer K. 2016 SqueezeNet: AlexNet-level accuracy with 50x fewer parameters and <0.5 MB model size. pp. 1–13. arXiv. (doi:10.48550/ARXIV.1602.07360).
- [64] Görner M. 2020 Modern Convnets, SqueezeNet, with Keras and TPUs. In: <https://codelabs.developers.google.com/codelabs/keras-flowers-squeeze#0>.
- [65] Chen YS, Wang JY. 2018 Computer vision-based approach for reading analog multimeter. *Applied Sciences (Switzerland)* **8**, 8, 1–33. (doi:10.3390/app8081268).
- [66] Zhou L, Wei S, Cui Z, Ding W. 2019 YOLO-RD: A lightweight object detection network for range doppler radar images. *IOP Conference Series: Materials Science and Engineering* **563**, 4. (doi:10.1088/1757-899X/563/4/042027).
- [67] Kim TS, Choi SK, Ko MJ, Lee M, Choi HS, Lee SW, Park K, Park JW. 2012 Ultra-rapid Real-time PCR for the Detection of Tomato yellow leaf curl virus. *Research in Plant Disease* **18**, 4, 298–303. (doi:10.5423/rpd.2012.18.4.298).
- [68] Scheiner N, Kraus F, Appenrodt N, Dickmann J, Sick B. 2021 Object detection for automotive radar point clouds – a comparison. *AI Perspectives* **3**, 1. (doi:10.1186/s42467-021-00012-z).
- [69] Girshick R, Donahue J, Darrell T, Malik J. 2014 Rich feature hierarchies for accurate object detection and semantic segmentation. In: *Proceedings of the IEEE Computer Society Conference on Computer Vision and Pattern Recognition*, pp. 580–587. (doi:10.1109/CVPR.2014.81).
- [70] Girshick R. 2015 Fast R-CNN. In: *Proceedings of the IEEE International Conference on Computer Vision*, pp. 1440–1448. (doi:10.1109/ICCV.2015.169).
- [71] Ren S, He K, Girshick R, Sun J. 2017 Faster R-CNN: Towards Real-Time Object Detection with Region Proposal Networks. *IEEE Transactions on Pattern Analysis and Machine Intelligence* **39**, 6, 1137–1149. (doi:10.1109/TPAMI.2016.2577031).
- [72] Redmon J, Divvala S, Girshick R, Farhadi A. 2016 You only look once: Unified, real-time object detection. In: *Proceedings of the IEEE Computer Society Conference on Computer Vision and Pattern Recognition*, pp. 779–788. (doi:10.1109/CVPR.2016.91).
- [73] Lines J, Taylor S, Bagnall A. 2018 Time Series Classification with HIVE-COTE. *ACM Transactions on Knowledge Discovery from Data* **12**, 5, 1–35. (doi:10.1145/3182382).

- [74] Ismail Fawaz H, Forestier G, Weber J, Idoumghar L, Muller PA. 2019 Deep learning for time series classification: a review. *Data Mining and Knowledge Discovery* **33**, 4, 917–963. (doi:10.1007/s10618-019-00619-1).
- [75] Santos-Victor JA, Costeira JP, Tomé JA, Sentieiro JJ. 1993 A computer vision system for the characterization and classification of flames in glass furnaces. *IEEE Transactions on Industry Applications* **29**, 3, 470–478. (doi:10.1109/28.222414).
- [76] Tong MT. 2019 Using machine learning to predict core sizes of high-efficiency turbofan engines. *Journal of Engineering for Gas Turbines and Power* **141**, November, 1–7. (doi:10.1115/1.4044770).
- [77] Grogan KP, Ihme M. 2018 Identification of governing physical processes of irregular combustion through machine learning. *Shock Waves* **28**, 5, 941–954. (doi:10.1007/s00193-018-0852-y).
- [78] Barwey S, Prakash S, Hassanaly M, Ramen V. 2021 Data-driven Classification and Modeling of Combustion Regimes in Detonation Waves. *Flow, Turbulence & Combustion* **106**, 4, 1065–1089. (doi:10.1007/s10494-020-00176-4).
- [79] Rezzag T, Burke R, Ahmed K. 2021 A Kinematic Study of Individual Rotating Detonation Engine Waves Using K-means Algorithm. In: *ASME Turbo Expo 2021: Turbomachinery Technical Conference and Exposition*, p. 8. (doi:10.1115/GT2021-58814).
- [80] Johnson KB, Ferguson DH, Tempke RS, Nix AC. 2020 Application of a Convolutional Neural Network for Wave Mode Identification in a Rotating Detonation Com-bustor Using High-Speed Imaging. In: *ASME 2020 Turbomachinery Technical Conference & Exposition*, pp. 1–12. (doi:10.1115/GT2020-15676).
- [81] Johnson KB, Ferguson DH, Nix AC. 2022 Use of Convolutional Neural Network Image Classification and High-Speed Ion Probe Data Towards Real-Time Detonation Characterization in a Water-Cooled Rotating Detonation Engine. In: *Proceedings of the ASME 2022 Turbomachinery Technical Conference & Exposition*. To be published, manuscript accepted.
- [82] Johnson K, Ferguson DH, Nix AC. 2021 Individual Wave Detection and Tracking within a Rotating Detonation Engine through Computer Vision Object Detection applied to High-Speed Images. In: *AIAA SciTech 2021 Forum*. (doi:10.2514/6.2021-1382).
- [83] Johnson K, Ferguson DH, Nix AC. 2022 Time Series Classification within a Rotating Detonation Engine through Deep Convolutional Neural Networks applied to High-Speed Pressure Data. In: *AIAA SciTech 2022 Forum*. (doi:10.2514/6.2022-2371).

- [84] Nori V, Seitzman J. 2008 Evaluation of Chemiluminescence as a Combustion Diagnostic under Varying Operating Conditions. In: *46th AIAA Aerospace Sciences Meeting and Exhibit*. Reno, Nevada. (doi:10.2514/6.2008-953).
- [85] NETL. 2021. NETL's Private Infrastructure as a Service (IaaS) Cloud Computing Environment, Center for Artificial Intelligence & Machine Learning.
- [86] Fotia ML, Hoke J, Schauer F. 2017 Experimental study of the ignition process in rotating detonation engines. In: *AIAA SciTech Forum - 55th AIAA Aerospace Sciences Meeting*. (doi:10.2514/6.2017-1928).
- [87] Rankin BA, Richardson DR, Caswell AW, Naples A. 2015 Imaging of OH\* Chemiluminescence in an Optically Accessible Rotating Detonation Engine. In: *53rd AIAA Aerospace Sciences Meeting*, January, pp. 1–16. (doi:10.2514/6.2015-1604).
- [88] Fotia ML, Hoke J, Schauer F. 2017 Experimental Performance Scaling of Rotating Detonation Engines Operated on Gaseous Fuels. *Journal of Propulsion and Power* **33**, 5, 1–10. (doi:10.2514/1.B36213).
- [89] Sousa J, Paniagua G, Collado Morata E. 2017 Thermodynamic analysis of a gas turbine engine with a rotating detonation combustor. *Applied Energy* **195**, 247–256. (doi:10.1016/j.apenergy.2017.03.045).
- [90] Liu Z, Braun J, Paniagua G. 2018 Characterization of a Supersonic Turbine Downstream of a Rotating Detonation Combustor. In: *Proceedings of ASME Turbo Expo 2018 Turbomachinery Technical Conference and Exposition*, pp. 1–14. June 11–15, 2018, Oslo, Norway. (doi:10.1115/1.4040815).
- [91] Browne S, Ziegler J, Bitter N, Schmidt, B, Lawson, J and Shepherd J. 2018. Shock and Detonation Toolbox.
- [92] Goodwin, DG, Speth, RL, Moffat, HK and Weber B. 2018. Cantera: An Object-Oriented Software Toolkit for Chemical Kinetics, Thermodynamics, and Transport Processes.
- [93] Brophy CM, Codoni JR. 2019 Experimental Performance Characterization of an RDE Using Equivalent Available Pressure. In: *AIAA Propulsion and Energy 2019 Forum*. Indianapolis, IN. (doi:10.2514/6.2019-4212).
- [94] Walters IV, Journell CL, Lemcherfi A, Gejji R, Heister SD, Slabaugh CD. 2018 Experimental Investigation of a Piloted, Natural Gas-Air Rotating Detonation Wave Combustor. In: *2018 Joint Propulsion Conference*. (doi:10.2514/6.2018-4782).

- [95] Sick V. 2013 High speed imaging in fundamental and applied combustion research. *Proceedings of the Combustion Institute* **34**, 2, 3509–3530. (doi:10.1016/J.PROCI.2012.08.012).
- [96] Chambers J, Ahmed K. 2017 Turbulent flame augmentation using a fluidic jet for Deflagration-to-Detonation. *Fuel* **199**, 616–626. (doi:10.1016/j.fuel.2017.03.023).
- [97] Mustafa MA, Hunt MB, Parziale NJ, Smith MS, Marineau EC. 2017 Krypton tagging velocimetry (KTV) investigation of shock-wave/turbulent boundary-layer interaction. In: *AIAA SciTech 2017 Forum*. (doi:10.2514/6.2017-0025).
- [98] Wang Y, Capps C, Kulatilaka WD. 2017 Mixture fraction imaging using femtosecond TPLIF of krypton. In: *AIAA SciTech 2017 Forum*. (doi:10.2514/6.2017-0258).
- [99] Trindade T, Ferreira A, Fernandes E. 2014 Characterization of Combustion Chemiluminescence: An Image Processing Approach. *Procedia Technology* **17**, 194–201. (doi:10.1016/j.protcy.2014.10.228).
- [100] Rankin BA, Richardson DR, Caswell AW, Naples AG, Hoke JL, Schauer FR. 2017 Chemiluminescence imaging of an optically accessible non-premixed rotating detonation engine. *Combustion and Flame* **176**, 12–22. (doi:10.1016/j.combustflame.2016.09.020).
- [101] Feleo A, France J, White LW, Gamba M. 2019 Evaluation of OH Emission for Determining Operation of a Rotating Detonation Engine. In: *AIAA Scitech 2019 Forum*. San Diego, CA. (doi:10.2514/6.2019-2252).
- [102] Codoni JR, Cho KY, Hoke JL, Rankin BA, Schauer FR. 2018 Simultaneous mid-IR emission and OH chemiluminescence measurements within a RDE operating with and without backpressure. In: *2018 AIAA Aerospace Sciences Meeting*, January, pp. 1–13. (doi:10.2514/6.2018-1882).
- [103] Feleo A, Chacon F, Gamba M. 2019 Effects of Heat Release Distribution on Detonation Properties in a H<sub>2</sub>/Air Rotating Detonation Combustor from OH\* Chemiluminescence. In: *AIAA Propulsion and Energy 2019 Forum*. Reston, Virginia. (doi:10.2514/6.2019-4045).
- [104] Athmanathan V, Ayers Z, Fisher J, Braun J, Andreoli V, Cuadrado DG, Fugger CA, Roy S, Paniagua G, Slipchenko MN, *et al.* 2020 High speed imaging of injection backflow and recovery in a Turbine-integrated High-pressure Optical RDE (THOR). In: *AIAA Scitech 2020 Forum*. Reston, Virginia. (doi:10.2514/6.2020-1178).

- [105] Katta VR, Cho KY, Hoke JL, Codoni JR, Schauer FR, Roquemore WM. 2018 Effect of increasing channel width on the structure of rotating detonation wave. *Proceedings of the Combustion Institute* **37**, 3. (doi:10.1016/J.PROCI.2018.05.072).
- [106] Cho KY, Codoni JR, Rankin BA, Hoke JL, Schauer FR. 2017 Effects of lateral relief of detonation in a thin channel. In: *AIAA SciTech 2017 Forum*. (doi:10.2514/6.2017-0373).
- [107] Tobias J, Depperschmidt D, Welch C, Miller R, Uddi M, Agrawal AK, Jr RD. 2018 OH\* Chemiluminescence Imaging of the Combustion Products from a Methane-Fueled Rotating Detonation Engine. In: *Proceedings of ASME Turbo Expo 2018 Turbomachinery Technical Conference and Exposition*, pp. 1–14. June 11-15, 2018, Oslo, Norway.
- [108] Optics E. 2022. Hoya B390 (UV-VIS) 50.8mm Square, Colored Glass Bandpass Filter.
- [109] Optics E. 2022. SCHOTT UG11, 50mm Sq., 2mm Thick, Colored Glass Bandpass Filter.
- [110] Invisible Vision UVi. 2020. 25mm Format High Speed Video Camera Intensifier.
- [111] Basler. 2022 PyPylon: python wrapper for the Basler pylon Camera Software Suite. <https://github.com/basler/pypylon>.
- [112] CLADÉ P. 2021 PyDAQmx : a Python interface to the National Instruments DAQmx driver. <https://pythonhosted.org/PyDAQmx/>.
- [113] Bennewitz JW, Bigler BR, Schumaker SA, Hargus WA. 2018 Automated image processing method to quantify rotating detonation wave behavior. *Review of Scientific Instruments* **90**, 6. (doi:10.1063/1.5067256).
- [114] Taubin G. 1991 Estimation of planar curves, surfaces and nonplanar space curves defined by implicit equations, with applications to edge and range image segmentation. *IEEE Trans. Pattern Analysis Machine Intelligence* **13**, 1115–1138. (doi:10.1109/34.103273).
- [115] Chernov N. 2020 Circle Fit (Taubin method) . In: *MATLAB Central File Exchange*. <https://www.mathworks.com/matlabcentral/fileexchange/22678-circle-fit-taubin-method>.
- [116] Bluemner R, Bohon MD, Paschereit CO, Gutmark EJ. 2018 Single and Counter-Rotating Wave Modes in an RDC. In: *2018 AIAA Aerospace Sciences Meeting*, January. (doi:10.2514/6.2018-1608).

- [117] Chollet F. 2015 Keras. In: *GitHub Repository*. <https://github.com/keras-team/keras>.
- [118] LeCun Y, Bottou L, Bengio Y, Haffner P. 1998 Gradient-based learning applied to document recognition. *Proceedings of the IEEE* **86**, 11, 2278–2323. (doi:10.1109/5.726791).
- [119] Walters IV, Journell CL, Lemcherfi AI, Gejji R, Heister SD, Slabaugh CD. 2019 Parametric Survey of a Natural Gas-Air Rotating Detonation Engine at Elevated Pressure. In: *AIAA Scitech 2019 Forum*. Reston, Virginia. (doi:10.2514/6.2019-1510).
- [120] Walters IV, Lemcherfi A, Gejji RM, Heister SD, Slabaugh CD. 2020 Performance Characterization of a Natural Gas-Air Rotating Detonation Engine. *Journal of Propulsion and Power* **37**, 2, 1–13. (doi:10.2514/1.b38087).
- [121] Bohon M, Bluemner R, Paschereit CO, Gutmark EJ. 2018 Cross-correlation as a tool for measuring RDC wave speed, direction, and complexity. In: *2018 Joint Propulsion Conference*. (doi:10.2514/6.2018-4569).
- [122] Muehlemann A. 2019. TrainYourOwnYOLO: Building a Custom Object Detector from Scratch. (doi:10.5281/zenodo.5112375).
- [123] Everingham M, Van Gool L, Williams CK, Winn J, Zisserman A. 2010 The pascal visual object classes (VOC) challenge. *International Journal of Computer Vision* **88**, 2, 303–338. (doi:10.1007/s11263-009-0275-4).
- [124] Lin TY, Maire M, Belongie S, Hays J, Perona P, Ramanan D, Dollár P, Zitnick CL. 2014 Microsoft COCO: Common objects in context. In: *Computer Vision – ECCV 2014*, pp. 740–755. (doi:10.1007/978-3-319-10602-1\_48).
- [125] Rezatofighi H, Tsoi N, Gwak J, Sadeghian A, Reid I, Savarese S. 2019 Generalized intersection over union: A metric and a loss for bounding box regression. In: *Proceedings of the IEEE Computer Society Conference on Computer Vision and Pattern Recognition*, pp. 658–666. (doi:10.1109/CVPR.2019.00075).
- [126] Bodla N, Singh B, Chellappa R, Davis LS. 2017 Soft-NMS - Improving Object Detection with One Line of Code. In: *Proceedings of the IEEE International Conference on Computer Vision*, pp. 5562–5570. (doi:10.1109/ICCV.2017.593).
- [127] Moffat RJ. 1988 Describing the uncertainties in experimental results. *Experimental Thermal and Fluid Science* **1**, 1, 3–17. (doi:10.1016/0894-1777(88)90043-X).
- [128] Robbe C, Nsiampa N, Oukara A, Papy A. 2014 Quantification of the uncertainties of high-speed camera measurements. *International Journal of Metrology and Quality Engineering* **5**, 2. (doi:10.1051/ijmqe/2014007).

- [129] Bonacorso c/o Quandoo G. 2018 *Mastering Machine Learning Algorithms: Expert Techniques to Implement Popular Machine Learning Algorithms and Fine-Tune Your Models*. Birmingham: Packt Publishing.
- [130] Yanping Chen, Eamonn Keogh, Bing Hu, Nurjahan Begum, Anthony Bagnall AM, Batista G. 2015 The UCR Time Series Classification Archive. [www.cs.ucr.edu/~eamonn/time\\_series\\_data/](http://www.cs.ucr.edu/~eamonn/time_series_data/).
- [131] Serrà J, Pascual S, Karatzoglou A. 2018 Towards a Universal Neural Network Encoder for Time Series. *Frontiers in Artificial Intelligence and Applications* 308, 120–129. (doi:10.3233/978-1-61499-918-8-120).
- [132] Wang Z, Yan W, Oates T. 2017 Time series classification from scratch with deep neural networks: A strong baseline. In: *Proceedings of the International Joint Conference on Neural Networks*, pp. 1578–1585. (doi:10.1109/IJCNN.2017.7966039).
- [133] Tempke R, Musho T. 2022 Autonomous design of new chemical reactions using a variational autoencoder. *Communications Chemistry* 5, 1, 1–10. (doi:10.1038/s42004-022-00647-x).
- [134] Lighthart A, Catal C, Tekinerdogan B. 2021 Analyzing the effectiveness of semi-supervised learning approaches for opinion spam classification. *Applied Soft Computing* 101, 107023. (doi:<https://doi.org/10.1016/j.asoc.2020.107023>).
- [135] Reddy Y, Pulabaigari V, B E. 2018 Semi-supervised learning: a brief review. *International Journal of Engineering and Technology* 7, 81. (doi:10.14419/ijet.v7i1.8.9977).



**T**HIS DOCUMENT SERVES AS a dissertation in fulfillment of the requirements of the degree of Doctor of Philosophy in Mechanical Engineering submitted to West Virginia University Benjamin M. Statler College of Engineering and Mineral Resources, Department of Mechanical and Aerospace Engineering, under the advisement of Dr. Andrew C. Nix. This research is supported by an appointment under Dr. Donald Ferguson at the National Energy Technology Laboratory (NETL) Professional Internship Program, sponsored by the U.S. Department of Energy (DOE), and administered by the Oak Ridge Institute for Science and Education (ORISE). This work and accomplishment is dedicated to my greatest supporter and friend, my husband, Jason William.

ProQuest Number: 29283576

INFORMATION TO ALL USERS

The quality and completeness of this reproduction is dependent on the quality  
and completeness of the copy made available to ProQuest.



Distributed by ProQuest LLC (2022).

Copyright of the Dissertation is held by the Author unless otherwise noted.

This work may be used in accordance with the terms of the Creative Commons license  
or other rights statement, as indicated in the copyright statement or in the metadata  
associated with this work. Unless otherwise specified in the copyright statement  
or the metadata, all rights are reserved by the copyright holder.

This work is protected against unauthorized copying under Title 17,  
United States Code and other applicable copyright laws.

Microform Edition where available © ProQuest LLC. No reproduction or digitization  
of the Microform Edition is authorized without permission of ProQuest LLC.

ProQuest LLC  
789 East Eisenhower Parkway  
P.O. Box 1346  
Ann Arbor, MI 48106 - 1346 USA